April 2021

A Search for New Resonances Decaying into a Weak Vector Boson and a Higgs Boson in Hadronic Final States with the ATLAS Detector at the Large Hadron Collider

Zachary Alden Meadows
University of Massachusetts Amherst

A Search for New Resonances Decaying into a Weak Vector Boson and a Higgs Boson in Hadronic Final States with the ATLAS Detector at the Large Hadron Collider

Zachary Alden Meadows

A Search for New Resonances Decaying into a Weak Vector Boson and a Higgs Boson in Hadronic Final States with the ATLAS Detector at the Large Hadron Collider

A Dissertation Presented

by

ZACHARY ALDEN MEADOWS

Submitted to the Graduate School of the University of Massachusetts Amherst in partial fulfillment of the requirements for the degree of

DOCTOR OF PHILOSOPHY

February 2021

Department of Physics

A Search for New Resonances Decaying into a Weak Vector Boson and a Higgs Boson in Hadronic Final States with the ATLAS Detector at the Large Hadron Collider

A Dissertation Presented

By

ZACHARY ALDEN MEADOWS

Approved as to style and content by:

_____

Stephane Willocq, Chair

_____

Verena Martinez Outschoorn, Member

_____

Lorenzo Sorbo, Member

_____

Grant Wilson, Outside Member

_____

Narayanan Menon, Department Head

Department of Physics

I would like to dedicate this thesis to Daniel and his family, for paving the way.

ACKNOWLEDGEMENTS

It is truly impossible to accomplish any sufficiently large project on your own. Especially in a large collaboration such as ATLAS, support comes from many different directions and becomes a famiilar aspect of daily research life. There is no way I could list all those who have helped me along the way, so here I will single out only a few.

Firstly I would like to thank my advisor Stephane Willocq for the hundreds of discussions and pieces of sage advice, concerning physics or otherwise, which kept all the pieces of this research together and always moving forward. On top of this I credit him with an uncommon level of patience for gracefully tolerating my more stubborn moments as we encountered forks in the road.

Additionally I would like to thank the brilliant post-doctoral researchers I was fortunate enough to work closely with: Attilio Picazio, Inês Ochoa, and Nora Pettersson. Without their in-depth knowledge, fortitude, and willingness to share their time I might still be sitting at my desk wondering whose brilliant decision it was to admit me into an actual physics program.

Lastly I would like to thank my partner, Alissa, for absolutely everything.

ABSTRACT

A SEARCH FOR NEW RESONANCES DECAYING INTO A WEAK VECTOR BOSON AND A HIGGS BOSON IN HADRONIC FINAL STATES WITH THE ATLAS DETECTOR AT THE LARGE HADRON COLLIDER

FEBRUARY 2021

ZACHARY ALDEN MEADOWS

B.Sc., UNIVERSITY OF WISCONSIN - STEVENS POINT

Ph.D., UNIVERSITY OF MASSACHUSETTS AMHERST

Directed by: Professor Stephane Willocq

A search for heavy resonances decaying to a W or Z boson and a Higgs boson in the final state is described. The search uses 139 fb^{-1} of proton-proton collision data at $\sqrt{s}$ = 13 TeV collected by the ATLAS detector at the CERN Large Hadron Collider from 2015 to 2018. The results are presented in terms of constraints on a simplified model with a heavy vector triplet. Upper limits are set on the production cross-section times branching fraction for resonances decaying into a W/Z boson and a Higgs boson in the mass range between 1.2 to 5 TeV.

TABLE OF CONTENTS

LIST OF TABLES

Table **Page**

LIST OF FIGURES

Chapter 1

THEORETICAL BACKGROUND

The Standard Model (SM) of particle physics is the most successful theory in the history of human scientific endeavour[1]. It provides a unified framework describing the electromagnetic, weak, and strong interactions along with all known particles that participate in those interactions. The fundamental objects in the SM description are fields defined at all points in spacetime. The SM fields fall into four main categories:

1. Fermionic fields, Ψ, describing "matter": quarks and leptons;
2. Electroweak spin-1 boson fields,
   - W_1, W_2, W_3, B: before symmetry breaking.
   - W^+, W^-, Z^0, γ: after symmetry breaking.
3. Gluon fields, G_a;
4. The Higgs field, Φ.

The dynamics of these fields and their interactions are predicted via the mathematical framework of Quantum Field Theory (QFT). In this chapter a compact but complete overview of the mathematical framework of the Standard Model is given.

[1] According to physicists, of course.

1.1 Minkowski Spacetime

The arena in which all particles are embedded in the Standard Model is the pseudo-Riemannian manifold $\mathbb{R}^{3,1}$, otherwise known as *Minkowski space* or *Minkowski spacetime*. The spacetime location of any *event*, such as a particle collision or decay, can be encoded as a vector with four elements: $p = (ct, x, y, z)$, where c is the **speed of light**. From this point onwards the common particle physics convention of setting $c = 1$ will be used[2]. The distinction between normal four-dimensional Euclidean space $\mathbb{R}^4$ and Minkowski space $\mathbb{R}^{3,1}$ is necessary due to the discoveries of Hendrik Lorentz and Albert Einstein culminating in the special[3] theory of relativity, which proceeds from two postulates:

1. The laws of physics are invariant in all inertial (non-accelerating) frames of reference.

2. The speed of light in a vacuum is the same for all observers, *regardless* of the motion of the light source or observer.

The second postulate complicates the notion of transforming between frames of reference, which must be done carefully to ensure the validity of the first postulate. To address this Minkowski space is equipped with a metric η often referred to as the *Minkowski metric* which is used to compute the distance between two spacetime

[2] At the end of any calculation, dimensional analysis can be used to restore the true value of c to the result.

[3] General relativity, which accounts for gravity by including the possibility of curvature into spacetime, is not (yet) part of the Standard Model. This is, to put it mildly, an area of active interest for many theorists.

events in a manner slightly different than traditional Euclidean space:

$$\mu = \begin{bmatrix} 1 & 0 & 0 & 0 \\ 0 & -1 & 0 & 0 \\ 0 & 0 & -1 & 0 \\ 0 & 0 & 0 & -1 \end{bmatrix} \tag{1.1.1}$$

which can be used to define a bilinear form over arbitrary pairs of spacetime points p_1 and p_2,

$$p_1 \cdot p_2 \equiv p_1^T \, \eta \, p_2 = t_1 t_2 - x_1 x_2 - y_1 y_2 - z_1 z_2 \tag{1.1.2}$$

The **spacetime interval** Δs between any two events in the same inertial frame of reference, $p_1 \equiv (t_1, x_1, y_1, z_1)$ and $p_2 \equiv (t_2, x_2, y_2, z_2)$, can be expressed in terms of this bilinear form:

$$\begin{aligned} \Delta s(p_1, p_2) &\equiv \sqrt{(p_1 - p_2) \cdot (p_1 - p_2)} \\ &= \sqrt{(t_1 - t_2)^2 - (x_1 - x_2)^2 - (y_1 - y_2)^2 - (z_1 - z_2)^2} \end{aligned}$$

With some simple algebra it follows directly from the second postulate of special relativity that Δs must be invariant under changes of inertial reference frame. In other words, for two spacetime points in one inertial frame of reference (p_1, p_2) and their representation in a different inertial frame of reference (p_1', p_2'), it must hold that $\Delta s(p_1, p_2) = \Delta s(p_1', p_2')$ for *any* arbitrary pair of inertial reference frames.

1.1.0.0.1Einstein Notation In order to simplify expressions, summation over indices is often abbreviated in particle physics: $x_i y^i \equiv \sum_i x_i y^i$. For the case of four-vectors from Minkowski spacetime the summation notation implicitly carries the application of the Minkowski metric: $x_\mu y^\mu \equiv x \cdot y \equiv \sum_{\mu\nu} \eta_{\mu\nu} x^\mu y^\nu$. The distinction between lower (covariant) and upper (contravariant) indices is mathematically important but not necessary for our purposes here.

A very good question to ask at this point is: what types of transformations are allowed between inertial frames of reference? To state this question mathematically, if we write an arbitrary transformation as $p' = \Lambda p$, what are the range of possibilities for Λ which preserve the spacetime interval Δs? Intuitively we may have an idea of what these transformations will look like, but these must be mathematically codified. This is best accomplished via the mathematical framework of **group theory**.

Developing the language and concepts of group theory is beyond the scope of this dissertation, but it can be shown that the Λ objects mentioned above are the members of the **Poincaré group**, which is the *isometry group* of Minkowski space, i.e. the set of all bijective Δs-preserving maps from $\mathbb{R}^{3,1}$ to $\mathbb{R}^{3,1}$. These transformations fall into three categories:

- **translations** in time and/or space
- **rotations/reflections** in three-dimensional space
- **boosts** or constant shifts in velocity

These separate categories may be combined freely, which means the Poincaré group has ten dimensions: four for translations, three for rotations/reflections, and three for boosts. Any mathematical framework for making predictions about particle physics must be, at minimum, invariant with respect to these types of transformations.

1.2 Fields and the Action Principle

The foundation for making physical predictions about fundamental particle physics is the **action principle**, which provides a mathematical framework [1] for computing the probability amplitude for a system of particles to evolve from some initial quantum state $|\Psi_I\rangle$ at time $t = 0$ to a state $|\Psi_F\rangle$ at time $t = T$:

$$\langle \Psi_F | \, e^{-i\hat{H}T} \, |\Psi_I\rangle = \int_{\Psi_I}^{\Psi_F} \mathcal{D}_\Psi(t) \; \exp\left\{\frac{i}{\hbar} S\right\}, \tag{1.2.1}$$
$$S = \int_0^T dt \; L\left(\{\Psi\}, \{\partial_\mu \Psi\}\right)$$

where $\hat{H}$ is the Hamiltonian operator[4] corresponding to the total energy of the system of particles, S is the **action**, L is the **Lagrangian** which is an expression built from all the relevant particle fields $\{\Psi\}$ as well as their derivatives with respect to spacetime $\{\partial_\mu \Psi\}$, and $\mathcal{D}_\Psi(t)$ is the differential element for integrating over *all possible* system trajectories the system could take from $|\Psi_I\rangle$ to $|\Psi_F\rangle$. Thus the probability amplitude is computed as a *weighted sum* over all possible system trajectories, where the weight is $\exp\left\{\frac{i}{\hbar} S\right\}$. Once the Lagrangian is defined, arriving at the resulting physical predictions is only[5] a matter of carrying out the calculations to compute the relevant probability amplitudes.

One important job of the theoretical particle physicist is to construct a Lagrangian in such a way as to match and/or predict experimental results. In order to construct a Lagrangian one must put constraints on what sort of fields are allowed to enter into the expression and how those fields can be used in the expression. Following from work of Eugene Wigner [2], all the mathematical structures (fields) used to

[4] It may make intuitive sense to think of fields as smooth functions of spacetime. However, in actuality they are *operators* acting on the state space of the SM, here represented by $|\phi_I\rangle, |\phi_F\rangle$. The details and importance of this are beyond the scope of this dissertation.

[5] In practice this is *extremely* difficult and time consuming.

describe particles in the Standard Model must be part of a positive-energy irreducible unitary representation of the Poincaré group. This subset of the Poincaré group representations can be indexed by two properties possessed by every fundamental particle: mass[6] (a non-negative number) and spin (an integer or half integer such as $0, 1/2, 1, 3/2, \ldots$). The Lagrangian encodes the laws of physics for a particular theory, and we know that the laws of physics must be invariant under Poincaré transformations as discussed in the previous section. Therefore the Lagrangian itself must be invariant under these transformations. This severely restricts the types of terms that can be allowed in the Lagrangian.

Particles in the SM have *internal* properties which must be encoded in the Lagrangian as well. This means that the symmetry group under which the Lagrangian is invariant must actually be defined by the *direct product* of multiple groups, with some encapsulating global properties of spacetime itself (global symmetries), and others encoding the internal degrees of freedom of the particles embedded in this spacetime (local symmetries). There are three predominant local symmetries in the SM and each one is associated with special properties of a particular subset of SM particles. These local symmetries arise through the electromagnetic force associated with the $U(1)$ group, the weak force associated with the $SU(2)$ group, and the strong force associated with the $SU(3)$ group.

1.3 Gauge Invariance

Local symmetries lead to presence force-carrying particles in the Lagrangian through a requirement called **gauge invariance**. A **gauge** is a particular choice of values for any redundant degrees of freedom underlying the mathematical formalism of a

[6]The mass of a particle can of course be zero.

local symmetry group. A **gauge transformation** is a simultaneous change in these redundant degrees of freedom. A **gauge theory** is a physical model based on a Lagrangian to which gauge transformations can be applied, but with the important caveat that the *physical predictions remain the same* regardless of which gauge is used. The motivation for the concepts underlying gauge theory are largely analogous to the intuitive notion that physical predictions in classical mechanics remain the same regardless of which inertial frame of reference is used to perform the calculation.

For example, consider a single particle quantum mechanical system with time-independent Hamiltonian H and energy eigenstates $|n\rangle$. To make a physical prediction for the probability for some general solution to the Schroedinger equation $\left(|\phi\rangle = \sum_n c_n e^{-iE_n t/\hbar} |n\rangle\right)$ to be observed in eigenstate $|n\rangle$, one calculates the transition probability $\left|\langle n| H |\phi\rangle\right|^2$. However, if one were to transform all the eigenstates by $|n\rangle \rightarrow e^{i\theta_n} |n\rangle$, the probability would not change, even though you have ostensibly changed the eigenstates. In this case the *gauge* is a choice of values for θ_n and a *gauge transformation* would entail a change $\theta_n \rightarrow \theta_n + \Delta\theta_n$ for some arbitrary set of $\Delta\theta_n$.

In this sense, while the computations are performed in H, the physical states themselves actually reside in $P(H)$, the *projective* Hilbert space. This projective Hilbert space contains a set of all equivalence classes of states where $|n\rangle \sim e^{i\theta_n} |n\rangle$, for any θ_n. This should not be taken to mean that the redundant degrees of freedom in a gauge theory, like the complex phase factor above, are without meaning at all. While they are not themselves measurable, their presence in the theory has measurable *consequences*. For example, the presence of complex phase factors in QM is what leads to the famous double slit and Ahranov-Bohm effects. These consequences arise from the *difference* in phase factors between states that naturally arise throughout the calculation, but do not depend on the initial choices of θ_n. This is what is meant by the phrase *redundant degrees of freedom*.

In short, the necessity for gauge invariance is that the mathematical/computational framework of a theory may have its *own* internal machinery which contributes to the result, but has some arbitrary aspects which do not alter the final physical prediction. Once we include any purely computational degrees of freedom in our theory we must demand that our theory is invariant with respect to the most general possible change in them that does not alter the physical prediction. In the words of Murray Gell-Mann, "Everything not forbidden is compulsory", a sentiment at the heart of modern physics. To state it another way: any arbitrary element of a theory must be treated as *maximally* arbitrary in order to preserve its integrity.

One aspect left out of the simple quantum mechanics example above is the notion of a gauge which varies with respect to spacetime itself. To begin, imagine you have two n-dimensional vectors A and B in familiar Euclidean space R^n. In order to compare vector A to vector B, vector A must be *transported* so that the tails of A and B are located at the same point. Furthermore, this transport must be done while keeping A *parallel* to its original direction in order to preserve geometric information such as the relative angle betwen A and B. This process is precisely the same as the way in which you would bring two everyday objects together to compare them in the real world. The reason this works and is intuitive is that R^n is a flat space and maintaining the orientation and relevant properties of normal objects requires no special care to preserve when moving them around.

However, if one is operating on fields with a spacetime varying gauge corresponding to some local symmetry group, the notion of **parallel transport** must be refined in order to compare fields at separate points in spacetime. Consider an extension of the gauge invariance example from quantum mechanics above to a field with a spacetime varying gauge which can be arbitrarily transformed without altering the physical predictions: $\psi \rightarrow e^{i\alpha(x)}\psi$. This gauge $\alpha(x)$ is *non-physical* in

the same manner as the phase factors θ_n in the previous example. Due to the freedom of gauge choice, in order to compare the field values as different points of spacetime what is needed then is not just a measure of the change in a field, but a measure of the change in a field *relative* to the change that occurs purely due to the variations in the gauge itself. The **gauge covariant derivative** $D_\mu(x) \equiv \partial_\mu + \mathcal{A}_\mu(x)$ achieves precisely this. The extra spacetime-dependent term $\mathcal{A}_\mu(x)$ that addresses the effect of the spacetime-varying gauge of the local symmetry group is known as the **connection**. Somewhat mysteriously the *force-carrying* particles of the SM, such as photons, manifest through this connection.

Groups which are continuously parameterized by some number of real-valued parameters are called *Lie groups*, and all the local symmetry groups of the Standard Model fall into this category. In the case of a quantum field theory with a local symmetry Lie group, the connection is an element of the corresponding Lie Algebra[7] $\mathfrak{g}$. This means the connection can be written as a linear combination of the infinitesimal generators T_a of the Lie algebra. Thus $\mathcal{A}_\mu$ can be expanded as $\mathcal{A}_\mu \equiv A^a_\mu T_a$, where the different A^a_μ terms transform under the adjoint representation of the local symmetry group. In physics it is common notational practice to define $D_\mu \equiv \partial_\mu - igA^a_\mu T_a$, where g is a dimensionless *coupling constant*. The A^a_μ terms are referred to as *connection coefficients*. In fact these connection coefficients will turn out to be the fields for the "force-carrying" gauge bosons of the Standard Model.

1.3.0.0.1Notation Greek letters $\mu, \nu, \ldots$ will be used to index Minkowski space, and alphabetic characters $a, b, \ldots$ will be used to index the Lie algebra generator basis. Einstein summation notation is assumed throughout.

[7] A Lie Group G and its Lie Algebra $\mathfrak{g}$ are related by an *exponential map* which allows for any group element $X \in G$ to be written as e^{it} for some linear combination t of the elements of $\mathfrak{g}$.

1.4 Yang-Mills Theory

With the covariant derivative we can construct the **curvature form** $F_{\mu\nu} \equiv \frac{1}{g}\left[D_\mu, D_\nu\right]$. A simplified picture of the curvature is that it encodes the *strength* and geometric properties of the gauge field A_μ at each point in spacetime. For this reason, the curvature is usually referred to as the **field strength tensor** in physics and is always part of the Lagrangian.

The starting point for constructing the Standard Model is Yang-Mills gauge theory, which finds its fullest and most beautiful expression in the language of differential geometry. In the case of the Standard Model, we can dispense with some of the abstract notions of differential geometry and restrict our attention to theories taking place in Minkowski Space. The previous expression given for the curvature can be expanded as

$$F_{\mu\nu} = \partial_\mu \mathcal{A}_\nu - \partial_\nu \mathcal{A}_\mu + ig\left[\mathcal{A}_\mu, \mathcal{A}_\nu\right] \tag{1.4.1}$$

$$= \partial_\mu A^a_\nu T_a - \partial_\nu A^a_\mu T_a + ig\left[A^a_\mu T_a, A^b_\nu T_b\right] \tag{1.4.2}$$

$$\implies F^a_{\mu\nu} = \partial_\mu A^a_\nu - \partial_\nu A^a_\mu + ig f^a_{\ bc} A^b_\mu A^c_\nu \tag{1.4.3}$$

where $f^a_{bc} \equiv$ are the **structure constants** of the associated Lie algebra. If the associated Lie group is *abelian*, i.e. the generators commute, then the structure constants vanish. This is the case for $U(1)$, the local symmetry group associated with electromagnetism.

In this system of notation, the **Yang-Mills Action** can be written

$$S_{\text{YM}} = \int d^4x\ \mathcal{L}_{\text{YM}} \tag{1.4.4}$$

$$\text{where } \mathcal{L}_{\text{YM}} = -\frac{1}{4} F^a_{\mu\nu} F^{\mu\nu}_a \tag{1.4.5}$$

which is both Poincaré and gauge invariant. It is important to recognize that two bilinear forms are involved in the above expression, one acting over the indicies of the Lie algebra for the local symmetry group and one over indices of Minkowski space.

A Yang-Mills theory can be expanded by embedding more fields into Minkowski space

$$\mathcal{L} = \mathcal{L}_m \left(\{\mathbf{\Psi}\} , \left\{ D_\mu \mathbf{\Psi} \right\} \right) + \mathcal{L}_{\mathrm{YM}} \tag{1.4.6}$$

where $\{\mathbf{\Psi}\}$ is some set of new fields which transform under the fundamental representation of the internal symmetry group and, by virtue of D_μ, couple to the force-carrying particle associated with the relevant local symmetry. The new $\mathcal{L}_m$ term must be Poincaré and gauge invariant as well, which can be achieved by judicious use of bilinear covariants and substitution of the standard spacetime derivative ∂_μ with the covariant derivative D_μ.

1.5 The Standard Model

The Standard Model of particle physics is a Yang Mills gauge theory with local symmetry group $SU(3) \otimes SU(2) \otimes U(1)$. It describes the strong, weak, and electromagnetic interactions which occur via the exchange of the corresponding spin-1 gauge fields: eight massless gluons from $SU(3)$, three massive weak bosons ($W^\pm$, Z) from $SU(2)$ and one massless photon from $U(1)$. The matter fields of the SM are given by a three-tiered family of leptons and quarks as shown in Figure 1.1. Each family has identical properties other than the mass and *flavour* quantum number of the corresponding particles, which denotes which of the three families the particle belongs to.

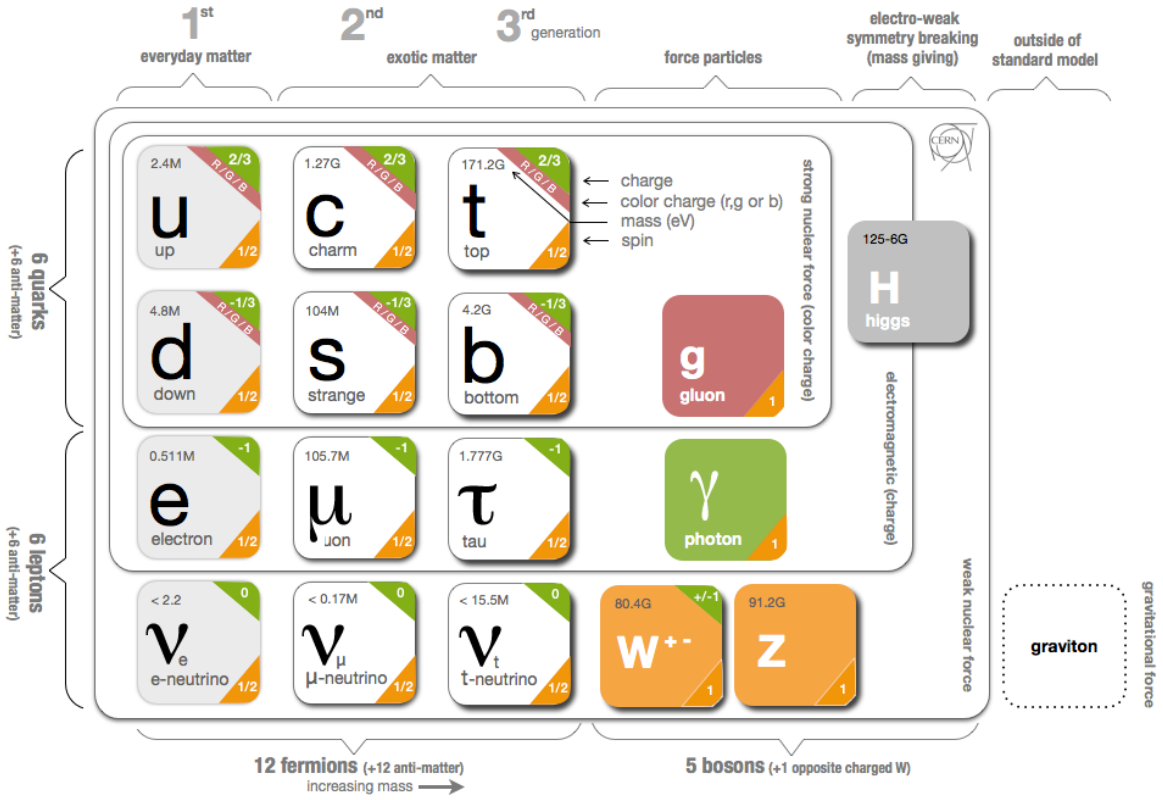

Fig. 1.1 Phenomenological breakdown of the Standard Model. © 2014 CERN

As mentioned previously all fields of the SM are constructed as positive-energy irreducible unitary representations of the Poincaré group. The particular representations used in the SM are subtle, accounting for the peculiarities of the nature of the interactions involved such as quark/lepton flavor, color, chirality, and spin. This results in significant complexity in the final representation, where for example the total fermionic field content of the SM has 96 complex-valued components. For the purposes of this dissertation the focus will be on the overall structure of the SM as it relates to the observed interactions in nature, as opposed to the full mathematical details.

1.5.1 Electroweak Interaction

The combined $SU(2) \otimes U(1)$ component of the Standard Model is known as the Electroweak interaction and consists of the unification of two fundamental interactions in nature: *electromagnetism* and the *weak interaction*.

The Lagrangian density for the electroweak interaction is given by

$$\mathcal{L}_{\text{EW}} = \sum_{\Psi} \bar{\Psi}(i\gamma^{\mu} D_{\mu})\Psi - \frac{1}{4} W_{a}^{\mu\nu} W_{\mu\nu}^{a} - \frac{1}{4} B^{\mu\nu} B_{\mu\nu} \tag{1.5.1}$$

$$D_{\mu} = \partial_{\mu} + igT_{a}W_{\mu}^{a} + i\frac{g'}{2}B_{\mu} \tag{1.5.2}$$

where $W_{\mu\nu}^{a}$ for $a \in (1, 2, 3)$ are field strength tensors for the local $SU(2)$ symmetry called **weak isospin**, $B^{\mu\nu}$ is the field strength tensor for the local $U(1)$ symmetry called **weak hypercharge**. The fields W_{μ}^{j} and B_{μ} are the corresponding connections for weak isospin and hypercharge, with coupling constants factored out as g and g'. Note that here we use the same base symbol (W and B) for both the connection coefficients and field strength tensor, whereas previously we used separate symbols: $F_{\mu\nu}$ and A_{μ}. The generators of $SU(2)$ are given by T_a and Y, respectively. Due to the simplicity of the $U(1)$ group, Y is simply a real number, whereas T_a for $a \in (1, 2, 3)$ are the 2×2 Pauli matrices. The Ψ fields are the fermions which are represented as *spinors* in the SM, which necessitates the use of the **gamma matrices** γ^{μ} to apply the covariant derivative D_{μ}.

There are a number of subtle complicating factors hidden in the definition of $\mathcal{L}_{\text{EW}}$. The weak isospin symmetry is *chiral* and only affects left-handed particles, where "handedness" depends on the orientation of the particle spin relative to its momentum[8]. Thus the Ψ fields outlined above are a combination of $SU(2)$ doublets

[8]This is an oversimplification of *chirality*, one of the more difficult aspects of the SM to understand.

for the left-handed fermions and singlets for the right-handed fermions.

$$\Psi = \begin{pmatrix} \nu_{l_i} \\ l_i \end{pmatrix}_L , \ (l_i)_R, \ \begin{pmatrix} u_i \\ d_i \end{pmatrix}_L , \ (u_i)_R, \ (d_i)_R \tag{1.5.3}$$

where the index $i \in (1, 2, 3)$ runs over the three families of quarks (u_i, d_i), charged leptons (l_i) and neutrinos (ν_{l_i}). The left-handed doublet quark fields in Ψ are not the same as the quark fields under the strong interaction, but rather a mixture of them, which are related by the Cabibbo-Kobayashi-Maskawa (CKM) matrix [3, 4].

1.5.2 Strong Interaction

Quantum Chromodynamics (QCD) is the theory of the *strong interaction* between quarks and gluons, which are the primary constituents of ordinary matter such a protons and neutrons, as well as less common hadrons such as the pion. The analogue of electric charge from QED is *color charge* in QCD, and the corresponding force-carrying particle is the gluon. The local symmetry group for QCD is SU(3), leading to the following Lagrangian:

$$\mathcal{L}_{\text{QCD}} = \sum_q \bar{\Psi}_q (i\gamma^\mu D_\mu)\Psi_q - \frac{1}{4} G_a^{\mu\nu} G^a_{\mu\nu} \tag{1.5.4}$$

$$D_\mu = \partial_\mu - i g_s G^a_\mu T_a \tag{1.5.5}$$

where $G_a^{\mu\nu}$ is the field strength tensor for $SU(3)$, T_a are the generators of $SU(3)$, and g_s is the coupling constant for the strong force. The connection coefficients G^a_μ are the eight[9] massless gluon gauge bosons. The quark fields Ψ_q are a three-dimensional vector representation of the Poincaré group which transforms under $SU(3)$, where

[9] The $SU(N)$ group has $n^2 - 1$ generators, thus $SU(3)$ has $3^2 - 1 = 8$ generators.

the three dimensions are indexed[10] by **color charge**:

$$\Psi_q \equiv \begin{pmatrix} \psi^q_{\text{red}} \\ \psi^q_{\text{green}} \\ \psi^q_{\text{blue}} \end{pmatrix}. \tag{1.5.6}$$

After expanding $\mathcal{L}_{\text{QCD}}$ there are three types of interaction vertices: ggg and $gq\bar{q}$ (proportional to g_s) and $gggg$ (proportional to g_s^2). The "strength" of the strong interaction is most-often described not in terms of g_s, but rather $\alpha_s \equiv \frac{g_s^2}{4\pi}$. In fact this coupling "constant" α_s is not constant at all. Due the peculiarities of quantum processes, all coupling constants depend on the energy scale of the interaction under consideration. This dependence on energy scale μ is encoded in the so-called **beta function**:

$$\beta(g) = \frac{\partial g}{\partial \ln \mu} \tag{1.5.7}$$

which is a differential equation that can be solved to relate the values of the coupling constant at one energy scale to their values at another energy scale. The beta functions and "running of the coupling" are vital for utilizing SM theory to understand experimental results.

For the case of the strong coupling constant, the beta function evaluated at leading order is

$$\beta(\alpha_s) = -\left(11 - \frac{2\ n_f}{3}\right)\frac{\alpha_s^2}{2\pi} \tag{1.5.8}$$

[10]The choice of red, green, and blue *colors* to index the vector representation is arbitrary. In the words of Richard Feynman: *The idiot physicists, unable to come up with any wonderful Greek words anymore, call this type of polarization by the unfortunate name of 'color,' which has nothing to do with color in the normal sense.*

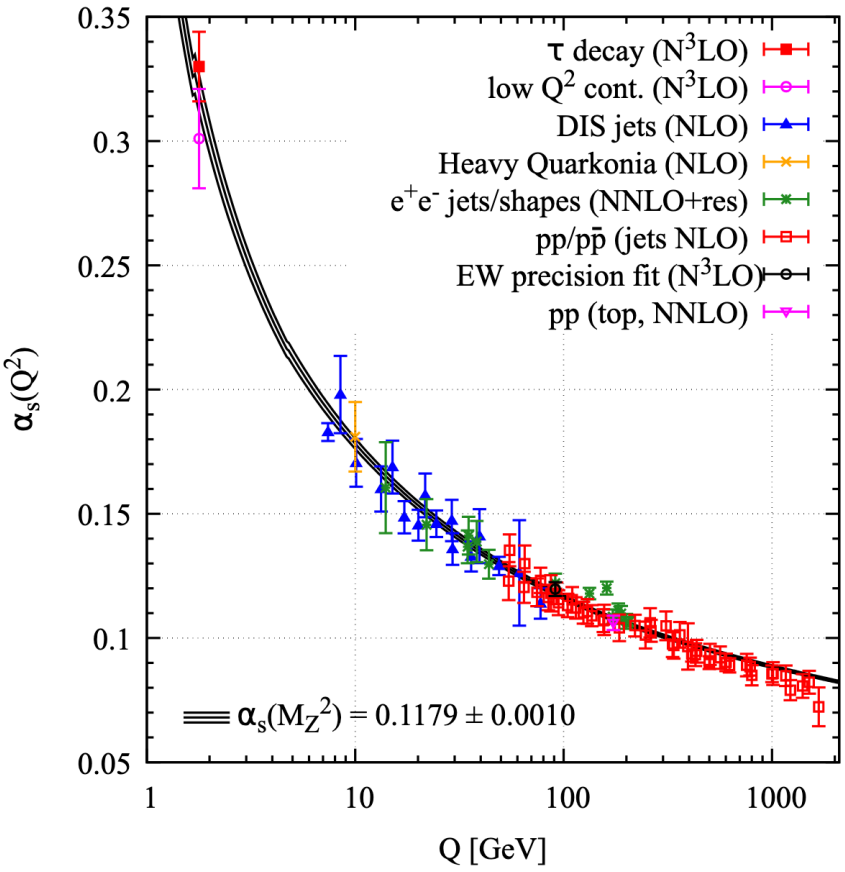

Fig. 1.2 Summary of measurements of the strong coupling α_s as a function of the energy scale Q. The respective order of QCD perturbation theory used in the extraction of α_s is indicated in parentheses. [5]

where n_f is the number of quark flavors. This beta function results in the following formula for α_s (at leading order):

$$\alpha_s(\mu^2) = \frac{12\pi}{(33 - 2\ n_f)\ln(\frac{\mu^2}{\Lambda^2_{\text{QCD}}})} \tag{1.5.9}$$

where Λ_{QCD} is the renormalization scale for QCD. Experimental results for α_s are shown in Figure 1.2.

This result shows that α_s *decreases* as the interaction scale increases, in stark contrast to the other interactions of the SM. Thus in the very high energy regime, QCD interactions become weaker, a phenomenon known as **asymptotic freedom**. The

inverse phenomenon, strong coupling in the low-energy regime, is known as **confinement**. This unique property of QCD is responsible for **fragmentation**, the process by which high energy **partons** (quarks/gluons) split into a shower of additional partons and **hadronization**, the process by which this parton shower recombines into colorless hadrons at lower energy. These effects make theory/computational efforts particularly difficult in QCD.

1.5.3 Higgs Mechanism

So far there are no mass terms, such as $-m_\Psi^2 \Psi^2$ for the fermions, in $\mathcal{L}_{\text{EW}}$ or $\mathcal{L}_{\text{QCD}}$. In all cases these terms would break local gauge invariance if no other changes were made. The solution to this problem is the inclusion of a complex-valued scalar[11] field in an $SU(2)$ doublet representation.

$$\mathcal{L}_{\text{H}} = \left|D_\mu \Phi\right|^2 - \mu^2 \Phi^\dagger \Phi + \lambda \left(\Phi^\dagger \Phi\right)^2 \tag{1.5.10}$$

$$\Phi = \begin{pmatrix} \phi^+ \\ \phi^0 \end{pmatrix} \tag{1.5.11}$$

where D_μ is the covariant derivative for the electroweak interaction as specified in Eq. 1.5.2. The last two terms in $\mathcal{L}_{\text{H}}$ define the Higgs potential, restricted to this form by the requirement that any new terms added to the SM Lagrangian density be both renormalizeable and invariant under the local $SU(2) \otimes U(1)$ symmetry group.

[11] Scalar here means the field transforms as a scalar under Poincaré transformations. This is distinctly different than the left-handed fermions, though they are also $SU(2)$ doublets but transform as spinors.

For the vacuum to be stable λ must be greater than zero. For the case where $\mu^2 > 0$ the scalar field Φ develops[12] a non-zero **vacuum expectation value** $\langle\Phi\rangle$. Since the potential only depends on $\Phi^\dagger\Phi$ there are an infinite number of degenerate states with minimum energy $\frac{\nu^2}{2}$ corresponding to this energy state. Due to the degeneracy and $SU(2)$ gauge invariance we can freely choose to write $\langle\Phi\rangle$ in a convenient form:

$$\langle\Phi\rangle = \frac{1}{\sqrt{2}}\begin{pmatrix}0\\ \nu\end{pmatrix} \tag{1.5.12}$$

and then by expanding around this minimum the Higgs field can be written as

$$\Phi(x) = \frac{1}{\sqrt{2}}\begin{pmatrix}0\\ \nu + h(x)\end{pmatrix}. \tag{1.5.13}$$

This way of encoding the Higgs field is called the *unitary gauge*. The remaining scalar field $h(x)$ is the massive, electrically neutral spin-0 Higgs boson. The usefulness of the unitary gauge is apparent when expanding the term from $\mathcal{L}_{\mathrm{H}}$ involving the covariant derivative:

$$\left|D_\mu\Phi\right|^2 = \left|\left(\partial_\mu + i\frac{g'}{2}YB_\mu + i\frac{g}{2}T_aW_\mu^a\right)h(x)\right|^2 \tag{1.5.14}$$

$$= \frac{\nu^2}{8}\left[g^2\left\{(W_\mu^1)^2 + (W_\mu^2)^2\right\}^2 + (gW_\mu^3 - g'B_\mu)^2\right]. \tag{1.5.15}$$

[12]It is important to note here that there is no mathematical motivation for the value of μ and the presence of this vacuum expectation value for the Higgs field. This is a case where the Lagrangian is constrained by experimental observations rather than mathematical constraints.

At this stage one can define new fields as linear combinations of the previous B_μ and W_μ^a fields to simplify the above expression:

$$W_\mu^\pm \equiv \frac{1}{\sqrt{2}}\left(W_\mu^1 \mp iW_\mu^2\right) \tag{1.5.16}$$

$$Z_\mu \equiv \frac{1}{\sqrt{g^2+g'^2}}\left(gW_\mu^3 - g'B_\mu\right) \tag{1.5.17}$$

$$A_\mu \equiv \frac{1}{\sqrt{g^2+g'^2}}\left(g'W_\mu^3 + gB_\mu\right) \tag{1.5.18}$$

where each of these new fields now have familiar $\frac{m^2}{2}x^2$-type mass terms in the Lagrangian, leading specifically to masses of:

$$m_{W^\pm} = \frac{gv}{2}, \tag{1.5.19}$$

$$m_Z = \frac{v}{2}\sqrt{g^2+g'^2}, \tag{1.5.20}$$

$$m_A = 0. \tag{1.5.21}$$

By choosing this gauge three of the four real scalar fields of Φ have disappeared, but they have re-emerged as components of the new W, Z, and A fields which correspond to the Standard Model weak $W^\pm/Z$ bosons and the photon A. This process just described by which the ground state of the Higgs field Φ breaks the $SU(2)\otimes U(1)$ gauge symmetry is called **spontaneous symmetry breaking**.

Even though the entire Lagrangian still retains $SU(2)\otimes U(1)$ symmetry, if re-written in terms of perturbations *around* the asymmetric vacuum state, the Lagrangian re-organizes itself to represent a different set of particles. Do not be mislead though, it is still the same Standard Model Lagrangian that describes the fundamental particle interactions (except gravity) both before and after spontaneous symmetry breaking, it is only the "ground state" of the universe that changes. The general consensus is that the spontaneous breaking of the $SU(2)\otimes U(1)$ symmetry by the accumulation

of $\langle\Phi\rangle$ is an event that actually occurred during the early moments following the big bang, specifically when the temperature dropped below 159.5 ± 1.5 GeV [6].

So far we have only shown how spontaneous symmetry breaking gives rise to the masses of the gauge bosons $W^{\pm}$, Z and A. In order to incorporate mass terms for the fermions, new terms must be added to the Lagrangian which involve the coupling of the Higgs field to the left *and* right-handed fermions with a form proportional to $\bar{\Psi}_L h \Psi_R$. The reason these new coupling terms must be added is simple: because they are *possible* under all the contraints of Poincaré invariance, gauge invariance and renormalization, thus we cannot ignore them. These new terms involve the **Yukawa coupling constants** f_Ψ for each fermion, and after spontaneous symmetry breaking contribute fermion mass terms to the SM Lagrangian with the following form:

$$\mathcal{L}_{\text{Yuk}} = \frac{f_\Psi v}{\sqrt{2}} \left(\bar{\Psi}_L \Psi_R + \bar{\Psi}_R \Psi_L\right) \tag{1.5.22}$$

for each fermion Ψ where $m_\Psi = \frac{f_\Psi v}{\sqrt{2}}$.

1.6 Hadronic Collisions

An accurate mathematical description of the physics processes in a pp collision, such as the example outlined in Figure 1.3, is extremely complicated. For example, either of the incoming or outgoing partons may radiate to produce initial state radiation (ISR) or final state radiation (FSR). These types of complications that arise are labelled as the **underlying event**, a generic term for the combined impact of colored beam remnants, additional pp interactions from the same bunch crossing, ISR, FSR, pileup, noise, and more. In most cases of interest to particle physics research, only particles coming from high-p_T processes are studied and the underlying event serves in practice as a challenge to both experimental and theoretical methods.

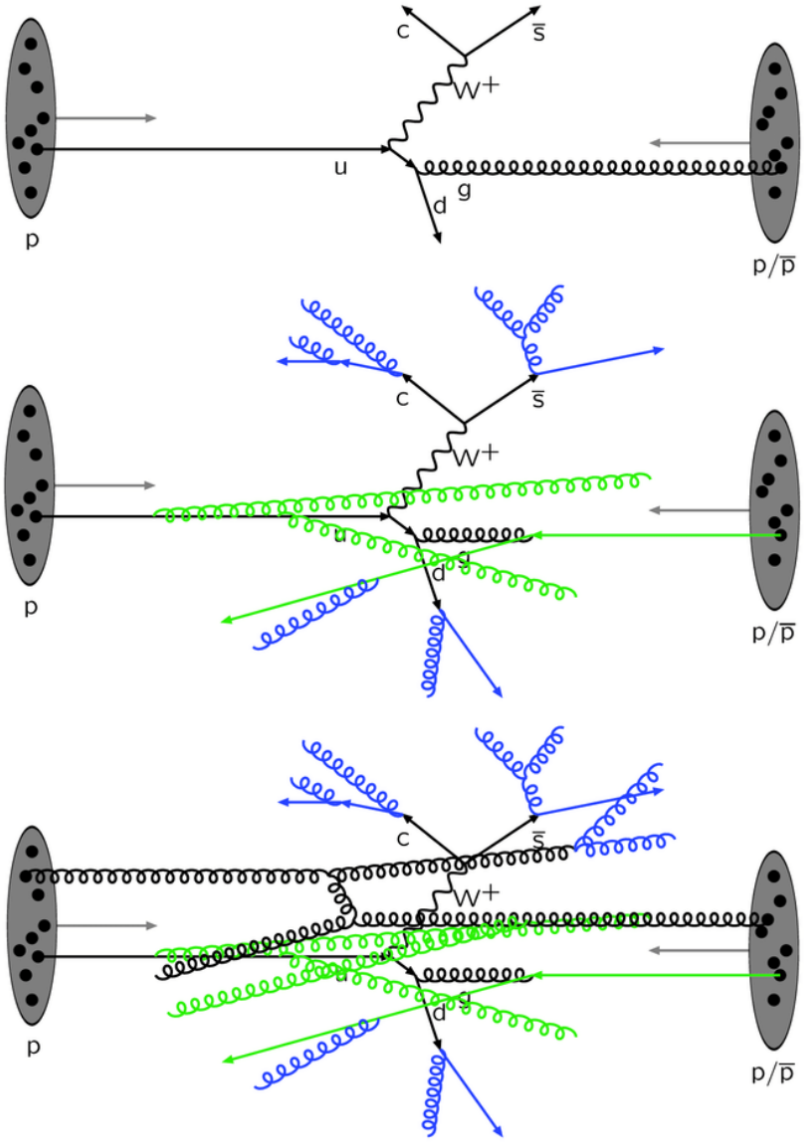

Fig. 1.3 Sketch of a proton-proton collision at high energies with increasing levels of detail: (top) the hard scatter process only, (middle) including initial and final state radiation, and (bottom) inclusion of the underlying event, itself with additional initial and final state radiation [7].

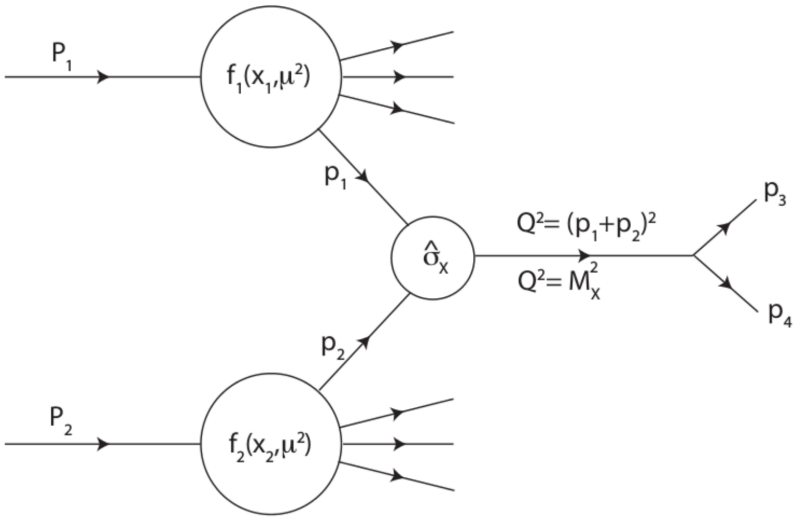

Fig. 1.4 Schematic diagram outlining the factorization theorem for the hard scattering of two protons with momentum P_1 and P_2. The parton distribution functions $f_i(x_i, \mu^2)$ give the probability to have a parton with a fraction x_i of the proton momentum, and $\hat{\sigma}_x$ gives the cross section for the parton level interaction for two incoming partons with momentum p_1 and p_2. [8]

The outgoing partons from the hard scatter event undergo **fragmentation** and **hadronization**, complex processes which involve different regimes of QCD which require different computation methods. These processes of fragmentation and hadronization are a directly result of two fundamental properties of QCD discussed earlier: asymptotic freedom and confinement. Luckily, the **factorization theorem** shows that the cross section for a scattering process between two partons i and j leading to the final state X can be calculated by separating the high energy scale perturbative part of the interaction from the low energy scale non-perturbative part and treating them independently.

What this means in practice is that the cross section for $pp \rightarrow X$ production can be computed using the cross section for the single parton-parton interaction of interest, weighting it with the probability for each parton to carry a given proportion of the proton momentum and integrating over all possible combinations of momentum

fraction and initial state partons:

$$\sigma(P_1, P_2 \to X) = \sum_{i,j} \int \mathrm{d}x_1 \, \mathrm{d}x_2 \, f_i(x_1, \mu^2) \, f_j(x_2, \mu^2) \, \hat{\sigma}_{ij \to X} \left(p_1, p_2, \alpha_s(\mu^2), Q^2/\mu^2 \right) \tag{1.6.1}$$

where P_1 and P_2 are the four momenta of the incoming protons. The four-momentum transferred between the partons during the hard scattering is Q. The **parton distribution functions** f_1 and f_2 encode the probability for each initial state parton (i, j) to possess a certain fraction of the proton momentum x_1 and x_2 and they must be measured experimentally. Thus the momentum of each parton can be written as $p_1 = x_1 P_1$ and $p_2 = x_2 P_2$. The factorization scale μ is a purely computational quantity resulting from *renormalization*, an aspect of QFT required to make physical predictions particularly in the case of dealing with infinities that arise due to the effects of self interaction. The cross section for $i, j \to X$ production is given by $\hat{\sigma}_{ij \to X}$, which depends on the strong coupling α_s and must take into account the factorization scale μ used in the PDF expressions. A schematic of the factorization theorem is shown in Figure 1.4.

The total cross section is the sum of all cross sections for all possible pp interactions that could be involved. These interactions can be either elastic or inelastic. Elastic collisions occur when both protons are preserved and no additional particles are produced. Inelastic collisions result when at least one of the incoming protons is destroyed and the outgoing particles differ from the incoming particles. Inelastic collisions are of predominant interest in particle physics as they probe fundamental interactions.

1.7 Monte Carlo Simulation

In order to interpret and understand experimental results from the ATLAS detector, comparisons to theoretical predictions must be made. These predictions are often (but not always) necessary for predicting background rates, optimizing analysis selection, determining detector measurement resolution for various physical quantities, and more. For collider physics, simulation involves not only the prediction of the underlying collision physics, but the interaction of the collision products with the detector itself. In order to achieve this, the ATLAS experiment utilizes simulation based on Monte Carlo (MC) methods which rely on random sampling.

The ATLAS MC simulation proceeds in a serial manner where each step relies only on the output of the prior step. An example illustration of a common pp collision event outlining these steps is shown in Fig. 1.5. These steps are (in order):

1. Hard Scatter Event Generation
2. Underlying Event Generation
3. Parton Showering
4. Hadronization
5. Detector Simulation

Simulation begins with the hard-scatter process, or in other words, evaluation of a set of Feynman diagrams for some particular $2 \rightarrow n$ process. In order to simulate collisions, parton distribution functions (PDF) must be used. A parton refers to the strongly interacting particles (quarks and gluons) which protons are composed of. These distribution functions describe the probability of finding a parton carrying a given fraction of the proton momentum. These Feynman diagrams are used to compute the so-called *Matrix Element* (ME) for the process via a perturbative

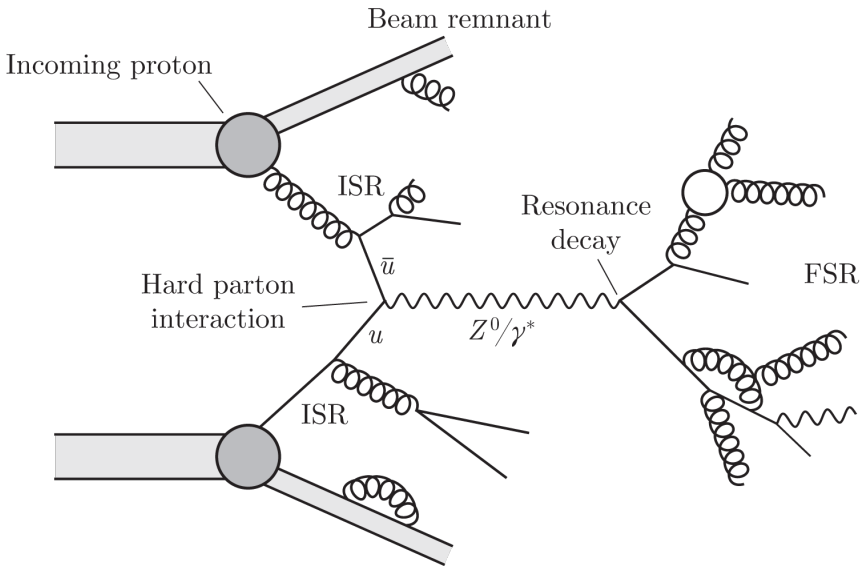

Fig. 1.5 Illustration of an LHC proton-proton collision. © 2011 Chris Blanks

expansion in powers of (α_s). An intrinsic and unavoidable property of QCD known as "asymptotic freedom" asserts that this type of perturbative expansion is only valid at very high energies, or in other words, only for the immediate hard scatter event. This breakdown occurs when the momentum scale of the collision products becomes ≈ 1 GeV or less. In this "soft regime" another simulation must pick up where the perturbative ME expansion left off.

In addition to the hard interaction generated, the interaction between the incoming proton remnants must be taken into account. This is typically modelled through multiple $2 \rightarrow 2$ scattering processes occurring at a momentum scale of a few GeV. The UE can include additional hard interactions and soft processes which cannot be computed perturbatively.

The ME method above works very well to describe hard parton interactions but is unable to correctly simulate the evolving collection of lower energy products that emerge from the products of the hard scatter. In a manner similar to how accelerated electric charges radiate bremsstrahlung due to the rules of QED, colored partons emit QCD radiation in the form of gluons. These radiated gluons can continue

to radiate more gluons or split into quark-antiquark pairs. This successive series of radiation/splitting results in a formation termed the "parton shower" which follows the evolution of the collision products momenta from the scale defined by the hard-scatter interaction down to the infrared scale at ≈ 1 GeV at which point QCD becomes non-perturbative and confinement of the partons into hadrons takes place.

As the shower approaches the QCD confinement scale (Λ_{QCD}) the coupling forces become significant and the outgoing colored partons transform into colorless hadrons with a typical mass scale of ≈ 1 GeV. The hadronization process is also non-perturbative and relies on models which are tuned by experimental data, such as the Lund string model used by PYTHIA and clustering models used by HERWIG and SHERPA.

To simulate the interaction of the simulated collision products with the ATLAS detector, the simulation results must be passed to a tool such as GEANT 4. The detector simulation reproduces the effects of the particles passing through the various layers of the sub-detector components and relies on a detailed specification of the geometry, materials, and magnetic field inside the detector. The physics processes involved in this detector simulation include ionization, bremsstrahlung, photon conversion, multiple scattering, scintillation, absorption, transition radiation, and more. The last step in the simulation involves digitizing the output of the various detector components. This is necessary to accurately reflect the raw data output of real events from the detector. After digitization, simulated events may be fed to the reconstruction algorithms described in Chapter 3 and processed exactly as if they were recorded data events.

Chapter 2

THE LHC AND THE ATLAS DETECTOR

The **ATLAS** (**A T**oroidal **L**HC **A**pparatu**S**) is one of four primary detectors constructed to explore the high energy/intensity frontier of modern particle physics by utilizing the **LHC** (Large Hadron Collider) at the **CERN** (Conseil Européen pour la Recherche Nucléaire) laboratory in Geneva, Switzerland.

2.1 The Large Hadron Collider

The LHC is the world's highest energy particle accelerator and the largest machine ever built by humans. It is composed of over a thousand superconducting magnets, sixteen radio frequency (RF) accelerating cavities, large scale cryogenic systems, and support structures within a circular 27 kilometer subterranean ring. Its purpose is to accelerate two beams of protons or heavy ions travelling in opposite directions around the ring in ultra-high vacuum (UHV) conditions to 99.9999991% of the speed of light (c) and collide them into one another at four separate interaction points (IP).

Four large detectors reside at each of these interaction points: ATLAS, CMS (Compact Muon Solenoid), ALICE (A Large Ion Collider Experiment), and LHCb

(LHC Beauty). Vast amounts of data describing the collision products are collected by these detectors and studied by thousands of scientists across the globe. The ATLAS and CMS detectors are general purpose detectors intended to study the Standard Model, in particular the properties of the Higgs boson, as well as search for new physics beyond the Standard Model (BSM). The ALICE and LHCb detectors are more specialized, with ALICE focusing on heavy ion collisions to study quark-gluon plasma and LHCb investigating physics involving hadrons containing b-quarks and the matter-antimatter asymmetry of the universe. The relative positions of these detectors around the ring can be seen in Figure 2.1.

2.1.1 Proton Accelerator Chain

Before the protons reach the detectors or the LHC ring itself they pass through a chain of prior accelerators as outlined in Figure 2.1. The protons themselves are obtained from a simple bottle of hydrogen gas. An electric field is used to strip the hydrogen atoms of their electrons to yield bare protons. The first accelerator in the chain, LINAC2, accelerates these bare protons up to 50 MeV. The beam is then injected into the Proton Synchotron Booster (PSB) and accelerated to 1.4 GeV, followed by the Proton Synchotron (PS) itself which accelerates the beam to 25 GeV.

Starting with the PSB the protons begin to assemble into "bunches" of 1.15×10^{11} protons each as they synchronize with the RF cavity acceleration frequency. As the protons pass through the PS acceleration stage, the bunching is modified several times and ultimately results in a time separation between bunches of 25 ns. In the final step before arriving at the LHC, the protons are accelerated by the Super Proton Synchotron (SPS) up to 450 GeV. A variety of filling schemes were used by the LHC during stable data-taking periods during Run 2, where the number of bunches per

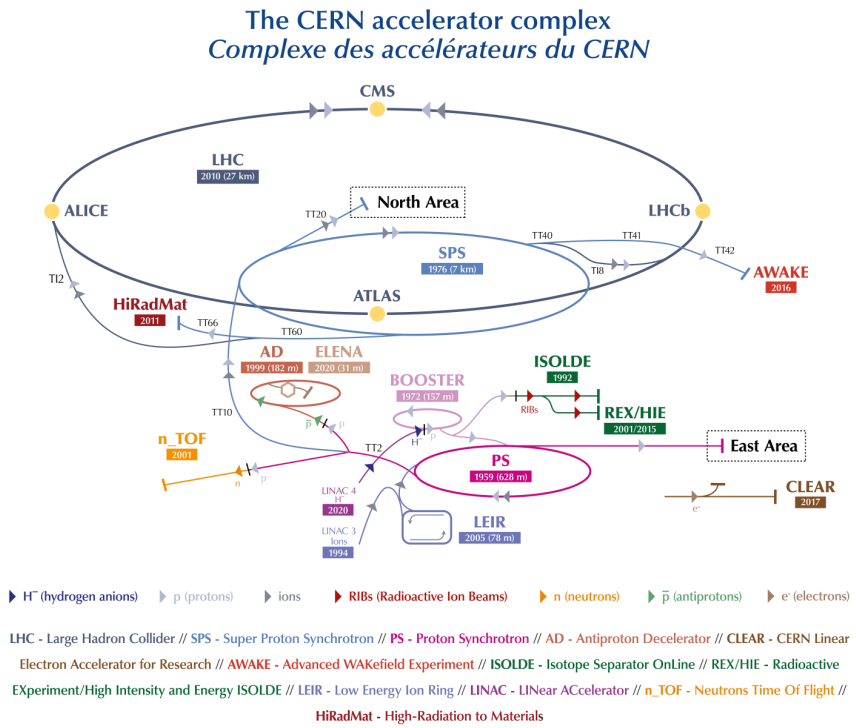

Fig. 2.1 The CERN accelerator complex. © 2019-2020 CERN.

injection varied from 48 to 144, with a maximum of 2556 bunches recorded in the ring at once. It takes 4 minutes and 20 seconds to fill each of the two LHC beam pipes and an additional 20 minutes to accelerate the protons to their maximum energy of 6.5 TeV for Run 2. This results in a center-of-mass energy of $\sqrt{s} = 2 \times 6.5$ TeV = 13 TeV.

Most of the physical processes of interest to high energy physics (HEP) are extremely rare. This necessitates that the overarching goal of collider experiments be to maximize the amount of collisions observed. At the LHC this is achieved via an elaborate scheme called Batch Compression Merging and Splitting (BCMS) that determines when and how the proton bunches are split and the beam is compressed at each stage of the proton accelerator chain described above.

2.1.2 Luminosity

The scientific potential of a particle collider experiment can be quantified by its center-of-mass energy and the number of inelastic collisions it produces per unit time

$$R_{\text{inelastic}} = \mathcal{L}_{\text{inst}}\, \sigma_{\text{inelastic}}, \tag{2.1.1}$$

where $\mathcal{L}_{\text{inst}}$ is the *instantaneous luminosity* and $\sigma_{\text{inelastic}}$ is the *inelastic scattering cross section* of the particle collisions. The units of $\mathcal{L}_{\text{inst}}$ are events per time per area, and the units of $\sigma_{\text{inelastic}}$ are area per event. In classical terms $\sigma_{\text{inelastic}}$ represents the area transverse to the relative motion of the two scattering particles within which they must meet in order to scatter from each other. From the perspective of QFT, $\sigma_{\text{inelastic}}$ is more accurately described as the scattering event probability. Given these definitions, $\mathcal{L}_{\text{inst}}$ quantifies the part of the collision rate that is determined by the collider itself. The peak instantaneous luminosity delivered to the ATLAS detector during Run-2 of the LHC was 21.0×10^{33} cm^{-2} s^{-1}.

In terms of the properties of storage rings like the LHC the rate can also be written as

$$R_{\text{inelastic}} = n_b f_{\text{rev}} \langle \mu \rangle \tag{2.1.2}$$

where f_{rev} is the revolution frequency of the ring[1], n_b is the number of colliding bunches and $\langle \mu \rangle$ is the average number of simultaneous inelastic interactions per bunch crossing. Thus the instantaneous luminosity can be re-written as

$$\mathcal{L}_{\text{inst}} = \frac{n_b f_{\text{rev}} \langle \mu \rangle}{\sigma_{\text{inelastic}}}. \tag{2.1.3}$$

[1] At the LHC the protons traverse the ring at a revolution frequency of 11245.5 Hz.

An alternative way to express $\mathcal{L}_{\text{inst}}$ in terms of beam quantities allows the luminosity to be measured[9]. In the case of symmetric, Gaussian beams the instantaneous luminosity can be expressed as

$$\mathcal{L}_{\text{inst}} = \frac{n_b f_{\text{rev}} N_1 N_2}{4\pi \Sigma_x \Sigma_y}, \tag{2.1.4}$$

where Σ_x, Σ_y are the convolved beam size $\left(\Sigma_{x/y} = \sqrt{\sigma^2_{x/y,1} + \sigma^2_{x/y,2}}\right)$ in the x/y plane and N_1/N_2 are the number of protons in each bunch. The values for $\Sigma_{x/y}$ are measured with the ATLAS detector during special data-taking periods [10] using techniques known as van der Meer scans, during which a small separation is induced and varied along the axes transverse to the collisions. In addition to the quantities shown in Eq. 2.1.4 and Eq. 2.1.3, the optimization of $\mathcal{L}_{\text{inst}}$ at the LHC includes consideration of beam properties such as the crossing angle (θ_c) and longitudinal compression (β^*) around the interaction point (IP).

Ultimately the *integrated luminosity* L determines the number of events observed by a collider experiment.

$$L = \int \mathcal{L}_{\text{inst}}(t)\, dt \tag{2.1.5}$$

where the integral is over the total stable data-taking uptime of the detector. For a given rare physics process x the expected number of observed events for a given integrated luminosity L is

$$N^x_{\text{events}} = \epsilon_x \sigma_x L \tag{2.1.6}$$

where σ_x is the cross section (fixed by Nature), ϵ_x is the detection efficiency which is a product of both the geometrical coverage of the detector and analysis selection efficiency. Optimization of ϵ_x for both SM measurements and BSM searches is one of the primary focal points for most HEP researchers, but the primary limitation will always be the integrated luminosity delivered by the particle collider.

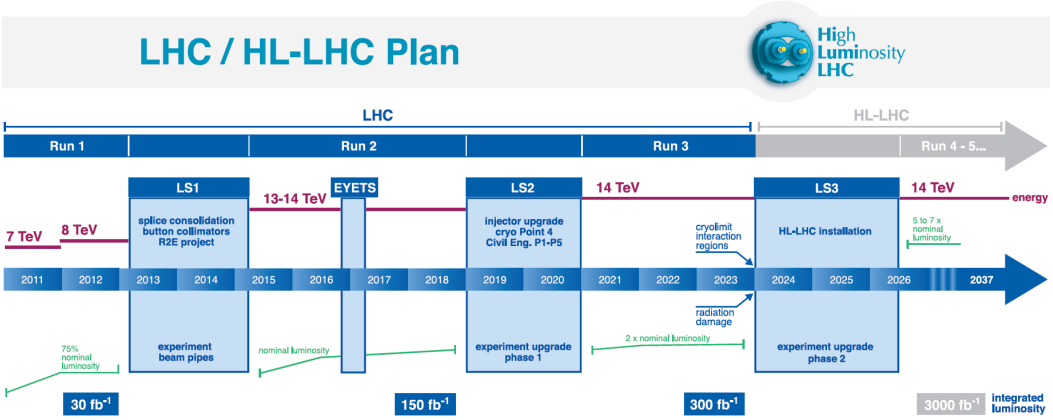

Fig. 2.2 Timeline of the LHC program up to the high-luminosity LHC (HL-LHC). © CERN

2.1.3 Operational History

The LHC experimental program follows a detailed timeline of data taking periods known as "Runs" interspersed with longer shutdown periods used to repair and upgrade the experiments and the accelerator. At the LHC these data-taking periods typically take place between April and November during non-shutdown years. Since Run 1 began in 2011 the LHC has followed a gradual trend of increasing center-of-mass energy ($\sqrt{s}$) and instantaneous luminosity. The nominal design luminosity has already been surpassed by a factor of two, and the nominal design value of $\sqrt{s} = 14$ TeV will be achieved for Run 3 and beyond. In 2016 the CERN Council approved a roadmap (see Fig. 2.2) for twenty more years of LHC physics which will ultimately surpass the nominal design luminosity by up to a factor of seven. At the time of the writing of this thesis the LHC is in the midst of the second long shutdown (LS2).

The cumulative luminosity delivered to the ATLAS detector so far as a function of time for each separate year can be seen in Fig. 2.3. The final measured integrated luminosity luminosity values for Run-2, along with their uncertainties, are shown in Table 2.1.

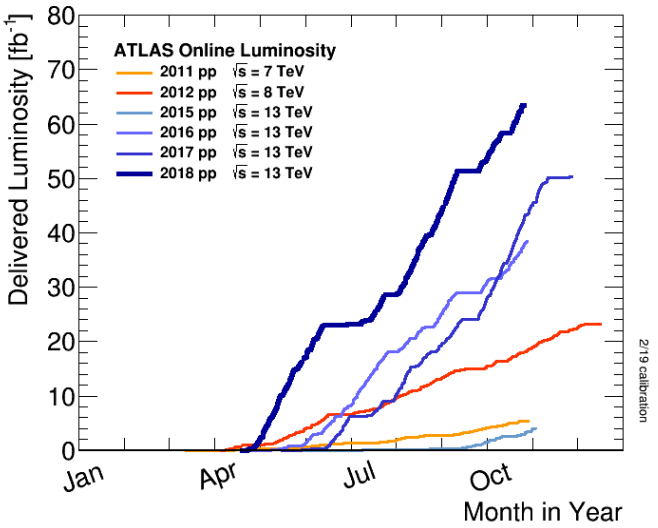

Fig. 2.3 Cumulative luminosity versus day delivered to ATLAS during stable beams for high energy p-p collisions. © CERN

Period	Luminosity [fb^{-1}]
2015+16	36.2 ± 0.8
2017	44.3 ± 1.0
2018	58.5 ± 1.2
Run-2	139.0 ± 2.4

Table 2.1 The total luminosity delivered by the LHC to the ATLAS detector during Run-2. Values are taken from the ATLAS online luminosity determination measurements described in Ref. [10].

2.2 ATLAS Detector

2.2.1 Overview

The ATLAS detector is the largest volume detector ever constructed for a particle collider. It is cylindrically shaped with a diameter of 25 m, a length of 46 m, and located 100 m underground at the first IP of the LHC. The total weight of the detector is 7,000 metric tonnes, which is equivalent to almost ten thousand Volkswagen Beetles. The major ATLAS detector components can be seen in Fig. 2.4.

The ATLAS detector is composed of several subdetectors which measure different properties of the particles which emerge from the proton-proton collisions around the IP. The subdetectors closest to the beam line are the inner tracking detectors (Sec. 2.2.3) which measure with high precision the flight paths of charged particles. Continuing outwards, the next subdetectors are the calorimeters (Sec. 2.2.4), of which there are two types: electromagnetic and hadronic. These calorimeters measure the energy deposited by both charged and neutral particles as they are slowed or, most often, completely stopped by the calorimeter detector material. The muon spectrometer (Sec. 2.2.5) is the outermost subdetector and provides additional measurements along trajectory of muons.

2.2.2 Coordinate System

The ATLAS detector uses a right-handed coordinate system as illustrated in Fig. 2.5. The x-axis points towards the center of the LHC ring, the y axis points upwards away from the center of the earth and the z-axis points along the beam line. When describing the products of a collision event it is often more useful to use a set of polar coordinates defined relative to this Cartesian coordinate system.

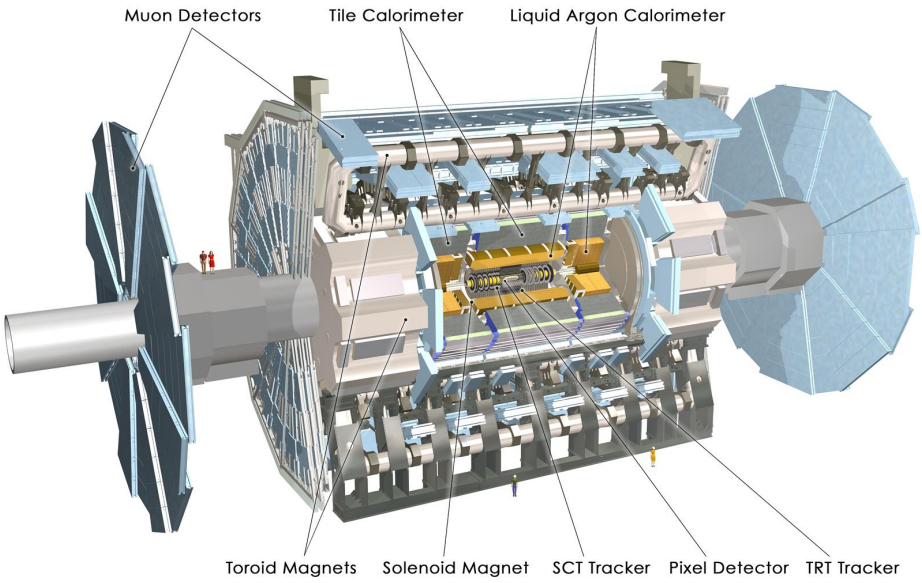

Fig. 2.4 A computer-generated cutout view of the ATLAS detector illustrating all of the various subdetector components. Note the human beings included for scale on the left. © 2008 CERN.

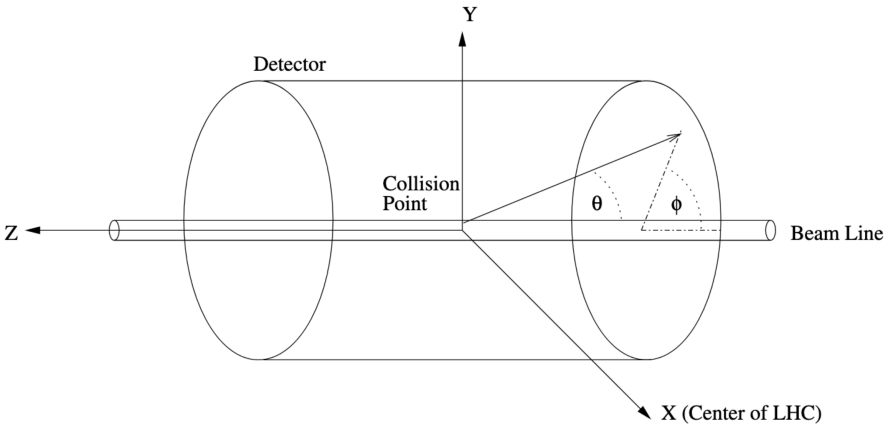

Fig. 2.5 Illustration of the ATLAS coordinate system [11].

These polar coordinates are defined as follows:

$$\phi = \arctan\left(\frac{y}{x}\right) \tag{2.2.1}$$

$$\theta = \arctan\left(\frac{z}{\sqrt{x^2 + y^2}}\right) \tag{2.2.2}$$

where θ is the *polar* angle and ϕ is the *azimuthal* angle. The polar angle θ is not convenient for use in particle physics because it is not invariant under boosts along the beam line axis. For this reason a related quantity called the *rapidity* (y) is defined as

$$y = \frac{1}{2}\ln\left(\frac{E + p_z}{E - p_z}\right) \tag{2.2.3}$$

and is invariant under boosts along the z-axis. However, due to the dependence of y on energy/momentum, a purely geometric quantity called *pseudorapidity* is most often used in its place, defined by

$$\eta = -\ln\left(\tan\left(\frac{\theta}{2}\right)\right) \tag{2.2.4}$$

which is equivalent to rapidity in the case of massless or highly energetic particles. A visualization of the distribution of η values is illustrated in Fig. 2.6. A measure of distance[2] between particles in the $\eta - \phi$ "plane" is commonly used and defined as

$$\Delta R = \sqrt{(\Delta\eta)^2 + (\Delta\phi)^2} \tag{2.2.5}$$

When measuring the properties of collision products, the momentum they possess along the beam line is less important than their momentum perpendicular to the beam line. This is because the momentum of the colliding particles along the beam

[2]The radial distance from the beam center $\left(R = \sqrt{x^2 + y^2}\right)$ is also commonly used in discussing tracking and the Inner Detector.

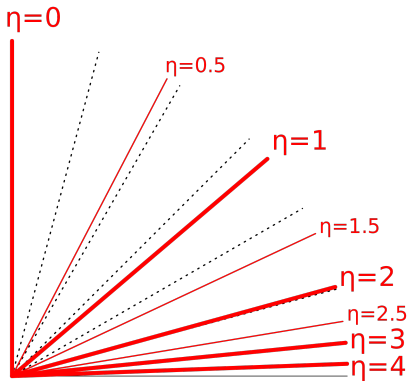

Fig. 2.6 Example values of pseudorapidity. The value of η approaches infinity as the beam line (z-axis, towards the right) is approached. A value of $\eta = 0.5$ corresponds to a polar angle of 27.5 degrees, $\eta = 1.0$ corresponds to 49.6 degrees, $\eta = 1.5$ corresponds to 64 degrees, $\eta = 4$ corresponds to 87.9 degrees.

line is unknown, while the perpendicular momentum is purely a consequence of whatever physics occurred during the collision due to conservation of momentum. For this reason the *transverse momentum* and *transverse energy* are more often used instead, and defined as

$$p_T = \sqrt{p_x^2 + p_y^2} \tag{2.2.6}$$

$$E_T = E\sin(\theta) = E\sinh(\eta). \tag{2.2.7}$$

Both of these quantities are invariant with respect to boosts along the beam axis.

2.2.3 Inner Detector

The ATLAS Inner Detector (ID) [12] [13] is a tracking detector that records the paths taken by charged particles as they emerge from the collisions around the IP. Two of the primary design goals for the ID are to provide a transverse momentum resolution

of $\frac{\sigma_{p_T}}{p_T} = 0.05\% \times p_T \oplus 1\%$ and a transverse impact parameter resolution of 10μm for high momentum partices in the central pseudorapidity region [13].

The ID is itself composed of four separate concentric detectors: The Insertable B-Layer (IBL), the Pixel detector, the Semiconductor Tracker (SCT), and the Transition Radiation Tracker (TRT). These individual subdetectors can be seen in Fig. 2.7. A more detailed view of the sensor components from each subdetector within the Inner Detector is shown in Fig. 2.8. The active area of the Inner Detector extends up to $|\eta|< 3$ for the IBL, $|\eta|< 2.5$ for the Pixel/SCT, and $|\eta|< 2.0$ for the TRT.

The entire Inner Detector is immersed in an axial symmetric $2T$ magnetic field provided by an enclosing solenoid magnet. The magnet is 5.3 m long, 2.4 m in diameter, 4.5 cm thick and weighs approximately 5 metric tonnes. The purpose of the magnetic field is to bend the trajectories of charged particles[3] in the $x-y$ plane as they move through the detector so that momentum and charge can be deduced from the resulting path curvature. The path of charged particles with low momentum (< 400MeV) are so tightly curved by the magnetic field that they never move far enough from the IP in the radial direction to interact with even the first detector layer.

The IBL, Pixel and SCT detectors all operate via the same underlying detection technology: excitation of p-n junctions in silicon. When a charged particle passes through a portion of the silicon and deposits energy via collision, silicon is ionized and electron-hole pairs are created. These electrons then drift and create a current due a bias voltage that is applied across the silicon. The magnitude of the current produced depends on the energy of the incident particle, as more electron-hole pairs are produced for a higher momentum particle.

[3]This bending is achieved via the Lorentz Force, which bends charged particle motion in the plane perpendicular to that of a magnetic field.

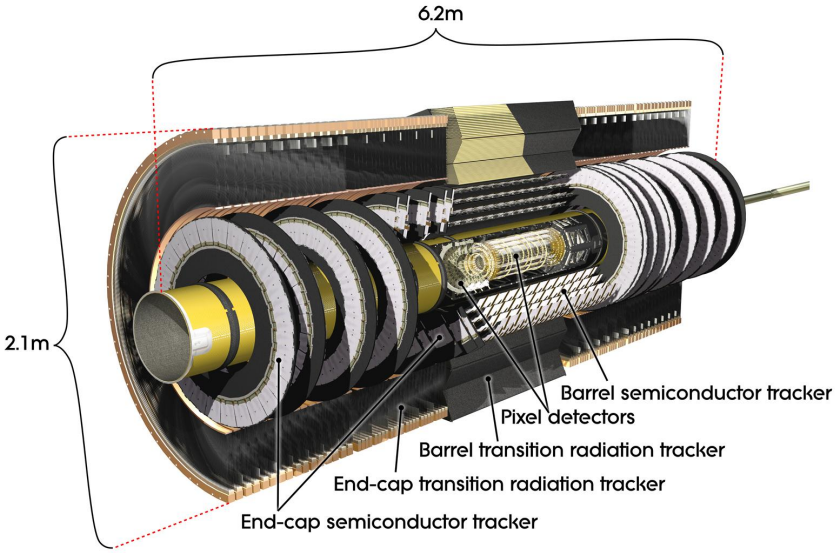

Fig. 2.7 A computer generated cutaway image displaying the components of the ATLAS Inner Detector. © 2014 CERN.

The reconstruction of the particle trajectory is of utmost importance because the curvature of the particle path allows for the determination of both the charge and momentum of the particle. One of the primary reasons the Inner Detector is situated as the closest subdetector to the beamline is so that it may reconstruct the trajectory of even short-lived particles that decay before reaching the outer layers of the detector. This improves the quality of primary vertex reconstruction and makes it possible to reconstruct secondary vertices.

The IBL [14, 15] is the innermost and newest layer of the Inner Detector, installed in 2014 during the first long shutdown period of the LHC. The purpose of the IBL is primarily to improve the measurement resolution of the transverse and longitudinal impact parameters of tracks, particularly in the face of increased pileup and luminosity during the HL-LHC phase. These impact parameters are of crucial importance for vertex reconstruction and the identification of b-jets.

The IBL is located at an average radial distance of 33 mm from the center of the beam pipe, covers 332mm in the z-direction, and extends the active tracking

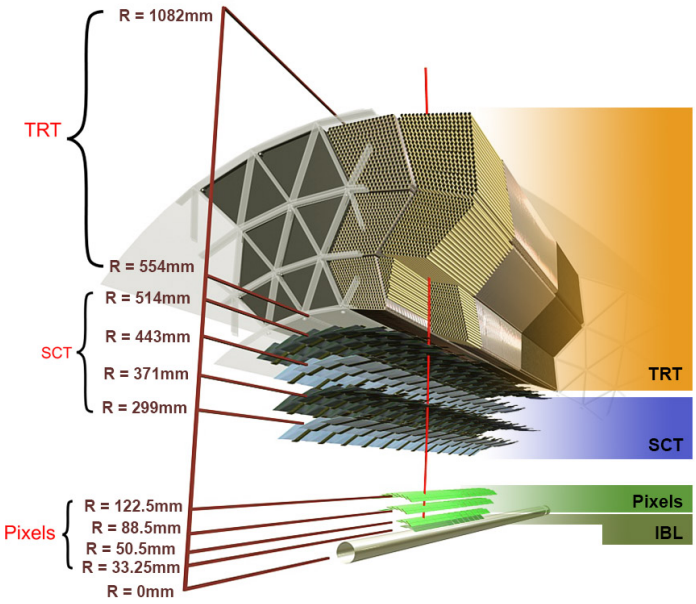

Fig. 2.8 Exploded view of the sensor components of the IBL, Pixel, SCT, and TRT layers of the ATLAS Inner Detector. © 2014 CERN.

area up to $|\eta|< 3$ compared to the $|\eta|< 2.5$ coverage of the ID without the IBL. The planar pixel sensors in the central $|\eta|$ region of the IBL have an instrinsic resolution of approximately 0.01 to 0.04mm in $R-\phi$ and 0.6 to 1.8mm in z, which allows for precise measurements of charged particle momentum.

The Pixel detector barrel is composed of three concentric cylindrical layers of silicon semiconductor staves at radial distances of 50.5, 88.5 and 122.5 mm which extend to $|z|\approx$ 400 mm on either side. Two end-cap sections consisting of three semiconductor disks are situated at each end perpendicular to the beam axis at $|z|= 495, 580, 650$ mm. The Pixel detector contains over 80 million sensors in total, each with an intrinsic resolution of approximately 8μm in $R-\phi$ and 75μm in z. These pixel sensors are divided into 1744 modules of 46080 pixels each with an area of $\approx$ 10cm, covering a total area of 1.7 m^2. The barrel layers cover $|\eta|< 2$ and contain 1456 modules, while the end caps extend coverage to $|\eta|< 2.5$ and contain

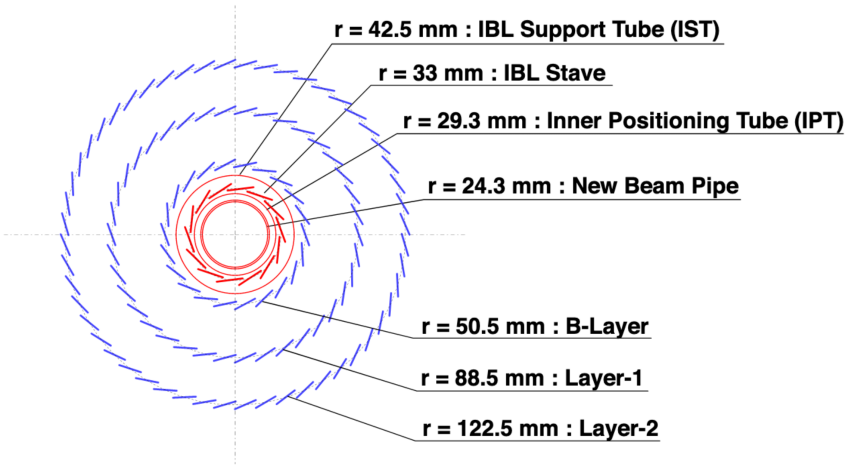

Fig. 2.9 Radial placement of concentric pixel barrels, beam pipe, and carbon-fiber support cylinders (IST, IPT). [16]

288 modules. The barrel layers are arranged in a turbine-like fashion with an overlap in ϕ, as shown in Fig. 2.9.

The Semiconductor Tracker (SCT) is a silicon microstrip detector with 4088 modules arranged in four concentric barrels (2112 modules) and two endcaps (988 modules per endcap) of nine disks each. The use of strips with dimension $63.56 \times 63.96\text{mm}^2$ instead of pixels is required due to the much larger coverage area (63 m^2 vs. 1.7 m^2) of the SCT when compared compared to the Pixel detector. The silicon-strip detector technology further differs from pixels by requiring the combination of two measurements from separate strips aligned at stereo angles for each particle position measurement. The SCT typically provides eight strip measurements (four position measurements) for each particle, with an intrinsic resolution of 17μm perpendicular to the strips in the $R - \phi$ plane (barrel) and 580 μm parallel to the beam in z (barrel) and R (end-cap).

The Transition Radiation Tracker (TRT) detector is composed of carbon fiber reinforced Kapton drift tubes called "straws" with diameter of 4mm. Inside of the straws reside 31 μm diameter gold-plated tungsten wires. These tubes are interleaved

with polypropyline or polyethylene fibers, which gives rise to so-called *transition radiation* of the particles as they pass through alternating materials with different refractive indices. Since transition radiation is more prominent in high-momentum, low-mass particles [17], this property underlies the primary use of the TRT in ATLAS: electron identification.

2.2.4 Calorimeters

The calorimeter system measures particle energy and is located directly outside the solenoidal magnet surrounding the ID (Fig. 2.10). The ATLAS calorimeter system is designed to fully absorb both charged and neutral particles[4] such that they deposit their full energy into the calorimeter detector material. Each separate ATLAS calorimeter technology provides granular coverage segmented in both η and ϕ. Though they can provide some information about the direction of particles, the $\eta - \phi$ granularity of the calorimeter does not compare to that of the ID.

The ATLAS calorimeter system is composed of two types of calorimeters: electromagnetic and hadronic. Both are sampling calorimeters which use alternating layers of active sampling material and inactive absorbing material. When high energy particles interact with the dense absorbing layers, a shower of lower energy particles is created which interacts with the adjacent sampling material. This results in a signal (electric current) proportional to the initial energy, which is then summed across all layers of the calorimeter system to measure the total energy of the particle. The shape of the shower can also be determined by comparing the energy deposited in each layer, which results in some of the most useful particle identification information for ATLAS event reconstruction.

[4]There are a few exceptions to this: muons, neutrinos, and extremely high energy particles that may "punch through".

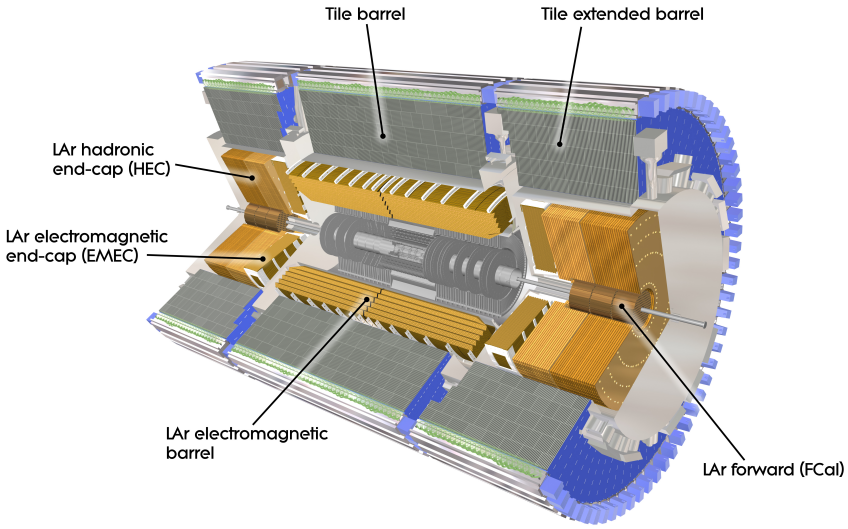

Fig. 2.10 The ATLAS calorimeter system. The Inner Detector (visible, but greyed out) is enclosed by the Calorimeter system. © 2014 CERN.

2.2.4.1 Electomagnetic Calorimeters

The Electromagnetic (EM) calorimeter is the innermost layer of the calorimeter system and used for measuring the energy of electrons and photons. It consists of a high-granularity lead-liquid argon (LAr) EM sampling calorimeter which covers the $|\eta|< 3.2$ region. The energy deposits in the EM calorimeter primarily result from the charged particles in jets, bremsstrahlung radiation produced by electrons, and pair-produced electrons resulting from photons interactions within the calorimeter material.

The EM calorimeter is divided into a Barrel part (EMB) covering $|\eta|< 1.475$ and two End-Caps (EMEC) covering $1.375 < |\eta| < 3.2$. Three separate cryostats are installed to to keep the liquid argon below its boiling point, and the services that compose the End-Cap cryostat necessitate a loss of EM calorimeter coverage in the $1.37 < |\eta| < 1.52$ region. The EMB has three layers, each with slightly different purpose and segmentation granularity, as shown in Fig. 2.11. The first layer is

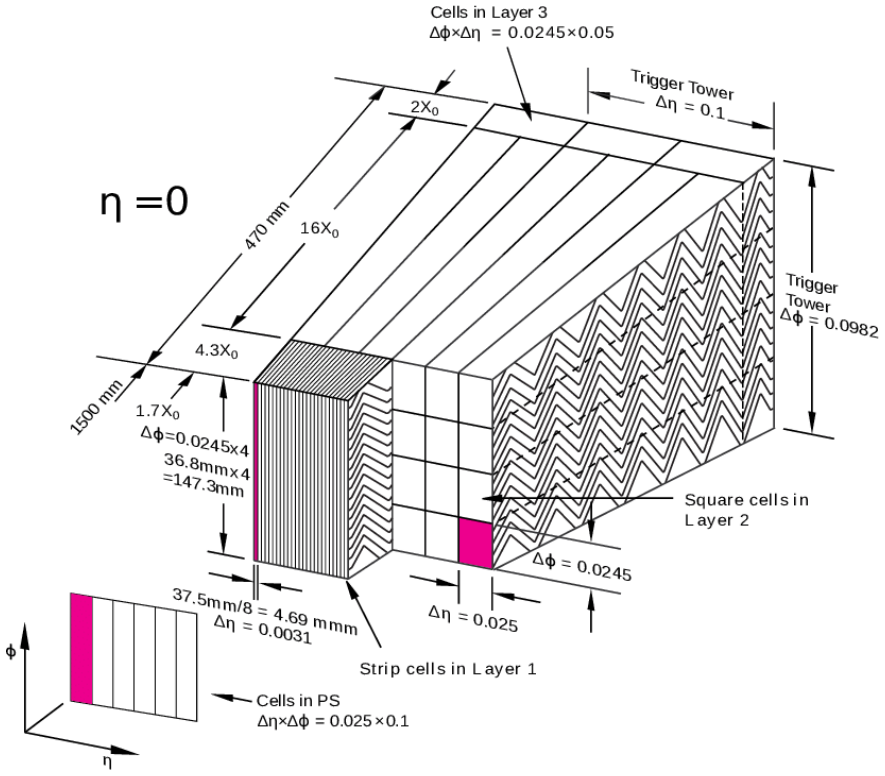

Fig. 2.11 Sketch of the ATLAS EM barrel calorimeter segmentation around $|\eta|= 0$. The X_0 quantity is known as the *radiation length* and quantifies the rate of energy loss with respect to traversed distance as a particle passes through a specific material. ATLAS Experiment © 2018 CERN.

composed of narrow (in η) strips which provide precise measurements during the initial showering process. The second layer is composed of square cells and is designed to fully capture moderate energy ($E < 50$ GeV) photons and electrons. The final layer of the EMB is less granular and meant to provide additional information about the longitudinal shower development for higher energy photons and electrons. The EMEC follows the EMB segmentation design up until the end of tracking acceptance ($|\eta|< 2.5$), after which it becomes coarser-grained with only two sampling layers. Additionally there is a *pre-shower* detector based on silicon sensors placed in front of the end-caps to improve in particular the discrimination between photons and pions in this region.

2.2.4.2 Hadronic Calorimeters

The hadronic calorimeters are composed of two different technologies in different $|\eta|$ regions of the detector. In the barrel region ($|\eta|< 1.7$) resides the Tile Calorimeter composed of alternating layers of plastic active scintillator tiles and steel absorbing plates. Like the EM calorimeter, particle showers are induced by the absorbing layer and particle showers are produced. Unlike the EM calorimeter, strong force interactions play a role in addition to the electromagnetic interactions, resulting in the presence of hadrons in the showers. When these hadrons pass through the plastic scintillator material, photons are emitted and detected by photomultipler tubes (PMTs) in order to produce the electrical signals which are then recorded and converted to an energy measurement. The tile calorimeter is composed of three sections: one central barrel section ($|\eta|< 1.0$) and two extended barrels sections ($0.8 < |\eta|< 1.7$).

The Hadronic End-Cap (HEC) calorimeter provides hadronic energy measurements in the forward ($1.5 < |\eta|< 3.2$) region. Like the EM calorimeter it uses liquid argon as the active material, but copper plates as the absorbing material. Each wheel of the HEC system is composed of two longitudinal layers, both located directly behind the end-cap cryostats.

2.2.4.3 Forward Calorimeter

The forward region ($3.1 < |\eta| < 4.9$) is covered by the Forward Calorimeter (FCal) which measures both electromagnetic and hadronic energy. The FCal is composed of three concentric cylindrical modules which are themselves composed of a series of rods and tubes, where liquid argon fills the gaps between the rod and tubes as the active medium. The first modules (closest to the beam line) use copper as an absorber and performs the electromagnetic energy measurement, while the second

and third modules use tungsten as the absorber and perform the hadronic energy measurement.

2.2.4.4 Calorimeter Resolution

The calorimeter energy resolution can be generically parameterized as

$$\frac{\sigma(E)}{E} = \frac{a}{\sqrt{E}} \oplus \frac{b}{E} \oplus c \tag{2.2.8}$$

where a is a stochastic/sampling term representing an intrinsic resolution limit due to particle fluctuations within the shower, b is a noise term determined primarily by electronics noise and pileup, and c is a constant term which dominates at high incident particle energy which is due to non-linearities in calorimeter response caused by inhomogeneity in detector materials, leakage due to un-absorbed particles from the shower, and calibration imperfections. Each of these quantities a, b, and c depend on the specific calorimeter detector technology under consideration. The $\oplus$ operator denotes that each contributing term is summed in quadrature to estimate the final resolution.

The a and c quantities have been carefully measured for the ATLAS calorimeters [18–21] and are summarized in Table 2.2. The degradation of performance when moving towards higher values of $|\eta|$ is due primarily to the increased presence of pileup in these more forward regions closer to the beam line. The electronics/pileup noise (b) for each type of calorimeter is shown in Fig. 2.12. Increased noise is acceptable in the more forward regions because the higher (on average) incident particle energy there diminishes the effect of the first two terms in Eq. 2.2.8.

Region	a [%]	c [%]
EM Barrel	10.1 ± 0.1	0.17 ± 0.04
EM End-Cap	13.5 ± 0.5	0.7 ± 0.1
EM Forward	29.3 ± 0.7	3.0 ± 0.1
Hadronic Barrel	52.9 ± 0.9	5.7 ± 0.2
Hadronic End-Cap	88.0 ± 5.0	6.8 ± 0.4
Hadronic Forward	98.5 ± 4.0	6.4 ± 0.04

Table 2.2 Measured test beam resolution parameters for the ATLAS calorimeters. Each measurement is performed at specific impact points for each separate region: $0 < |\eta| < 0.7$ for the Barrel, $|\eta| = 2.8$ for the End-Caps and $|\eta| = 3.65$ for the Forward region.

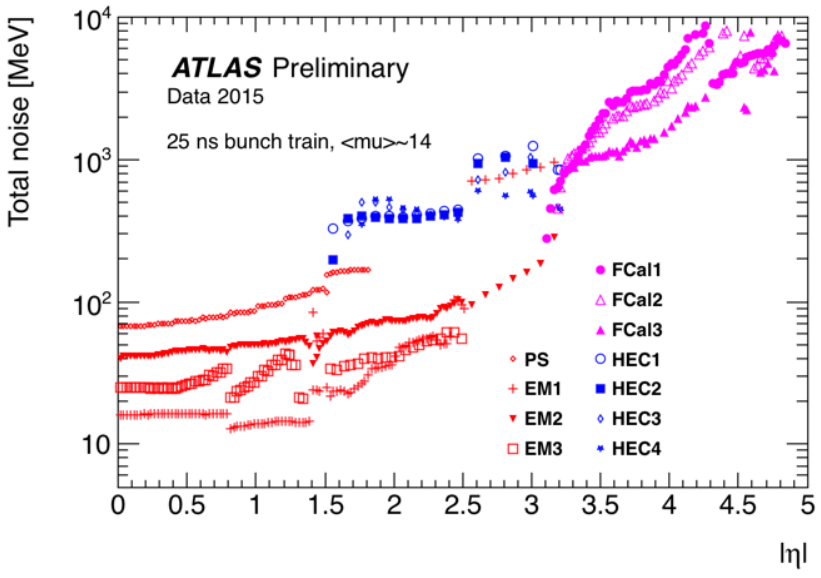

Fig. 2.12 Total electronics/pileup noise vs. $|\eta|$ at the electron scale, measured in data with 25ns bunch spacing and $\langle\mu\rangle = 14$. ATLAS Experiment © 2015 CERN.

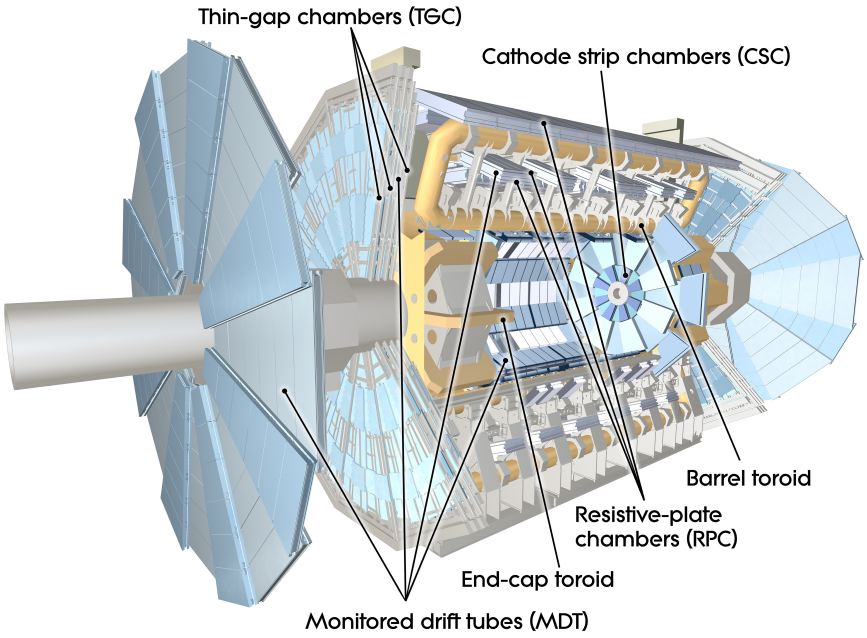

Fig. 2.13 ATLAS Experiment Muon Spectrometer. © 2014 CERN

2.2.5 Muon Spectrometer

Muons are unique among the common Standard Model p-p collision products by virtue of their long lifetime ($2.2\mu s$), weakly interacting nature, high production momentum and high mass ($\approx 200 \times m_e$). Due to these properties, muons pass through the ATLAS calorimeters without depositing a significant portion of their energy and leave only a weak ionization trail behind. This necessitates the existence of the final outermost layer of the ATLAS detector: the Muon Spectrometer (MS) [22], shown in Figure 2.13.

The MS consists of three air-core superconducting toroidal magnet systems (see Figure 2.14) and four separate types of tracking chambers covering a region of up to $|\eta|< 2.7$, extending from a radius of 4.25m to 11m. The magnet system of the MS serves to bend the trajectories of muons in the $R - z$ plane. The large barrel toroid

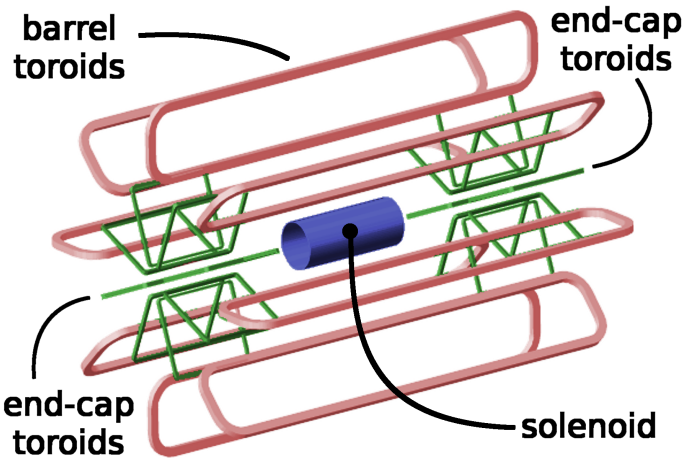

Fig. 2.14 Illustration of the ATLAS magnet system. [23] The barrel region toroid magnet is shown in red and the two end-cap toroid magnets are shown in green. The inner solenoid is shown in blue, which is parallel to the beam pipe. © 2013 Jet Goodson

magnet strength depends strongly on ϕ and is active for $|\eta|< 1.6$. The two smaller end-cap magnets (1 T) are active in the range $1.6 < |\eta| < 2.7$.

The MS is composed of several different types of detector technologies which are designed for two separate use-cases: (1) extending the precision tracking of each individual muon beyond the ID measurements and (2) fast readouts for the ATLAS trigger system. Monitored Drift Tube Chambers (MDT) and Cathode Strip Chambers (CSC) are used for the high precision tracking measurements, while Resistive Plate Chambers (RPC) and Thin Gap Chambers (TGC) are less precise but provide a much faster readout, on the scale of nanoseconds, for the trigger system. A cross section of the muon spectrometer highlighting the various sub-components is shown in Figure 2.15. The tracking coverage ($|\eta|< 2.7$) of the MS is more complete than the trigger coverage ($|\eta|< 2.4$). Like the other major ATLAS detector components, the MS is split into separate barrel ($|\eta|< 1.05$) and endcap ($1.05 < |\eta|< 2.7$) regions.

The MDT chambers are used for precision tracking of the $R - z$ plane curvature of muons. They consist of 3-8 layers of 30mm diameter drift tubes between 0.8m

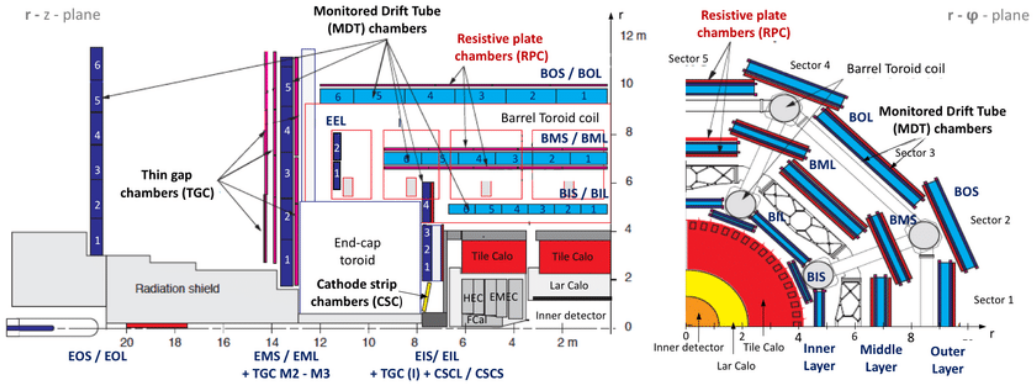

Fig. 2.15 Cross-section of a quadrant of the ATLAS Muon Spectrometer [24] in the $R-z$ plane (left) and the $R-\phi$ plane (right) comprising all detector modules. The naming of MDT chambers is based on their location in the barrel or end-cap (B,E), in the inner, middle, or outer layer (I, M, O) and in either the a large or a small sector (L,S). © CERN

and 6.5m long, filled with a mixture of Ar/CO_2 gas held at a pressure of three atmospheres. Whenever the gas inside the drift tube is ionized by a passing muon, the resulting free electrons drift towards a 50 μm W-Rh anode wire held at a voltage of 3kV in the center of the tube. The precision tracking data from the barrel is measured by MDT chambers that cover the $|\eta|<2$ range in the first layer, and up to $|\eta|<2.7$ in the two outer layers. There are three concentric barrel layers composed of MDT and RPC chambers at radii of 5m, 7.5m, and 10m.

The RPC chambers measure the non-bending coordinate (ϕ) of muons. They are composed of a set of parallel plate capacitors separated by a 2mm insulating space filled with a gas mixture of predominantly tetrafluoroethane ($C_2H_2F_4$). The plates have high resistance and are held at a constant high voltage, with metallic strips attached to their outer faces. The fast response time of the RPC technology (1.5ns) makes it a prime candidate for the muon trigger system. The RPC chambers are attached to the MDT chambers in the barrel and cover the central $|\eta|<1.05$ region.

The CSC chambers replace the MDTs in the forward region of the first endcap layer of the MS in order to account for the high interaction rate in this region that

would otherwise cause significantly degraded performance of the MDTs in this region ($2 < |\eta| < 2.7$)). The CSC detector region is organized into two disks of sixteen chambers each. Each CSC chamber consists of both a multi-wire proportional drift chamber as well as interleaved cathode strips placed parallel and perpendicular to the anode multi-wire layers. The parallel cathode strips provide precision tracking measurement in the bending plane, while the perpendicular cathode strips provide measurements of ϕ.

The TGC chambers are similar to the CSC chambers in design and consist of 50 μm gold-plated tungsten anode wires, but with smaller gaps between electrodes for faster readouts. They provide measurements of the R-z and ϕ coordinates, covering the $1.0 < |\eta| < 2.4$ region.

2.2.6 Trigger and DAQ

The LHC currently operates at a collision rate of 40 MHz. Given that each event requires approximately 1.5 MB of disk storage, it is impractical to attempt to record every collision event observed by the ATLAS detector. Not only would this require a bandwidth of > 60 TB/s, but only a small fraction of events are of interest to current HEP research efforts. For this reason the trigger system [25] is used to reduce the recorded event rate to a more manageable level of approximately 1-2 kHz, which reduces the bandwidth requirement to 1 GB/s or less. The trigger system operates in real-time at both hardware and software levels and ensures only events of interest to ongoing research are recorded by the ATLAS data acquisition system (DAQ). For Run-2 ATLAS uses a two-tier trigger system: a hardware-based "level-1" (L1) trigger followed by a software based "high-level" (HLT) trigger. Each trigger in the chain significantly reduces the data rate. Only the events selected by the HLT are actually

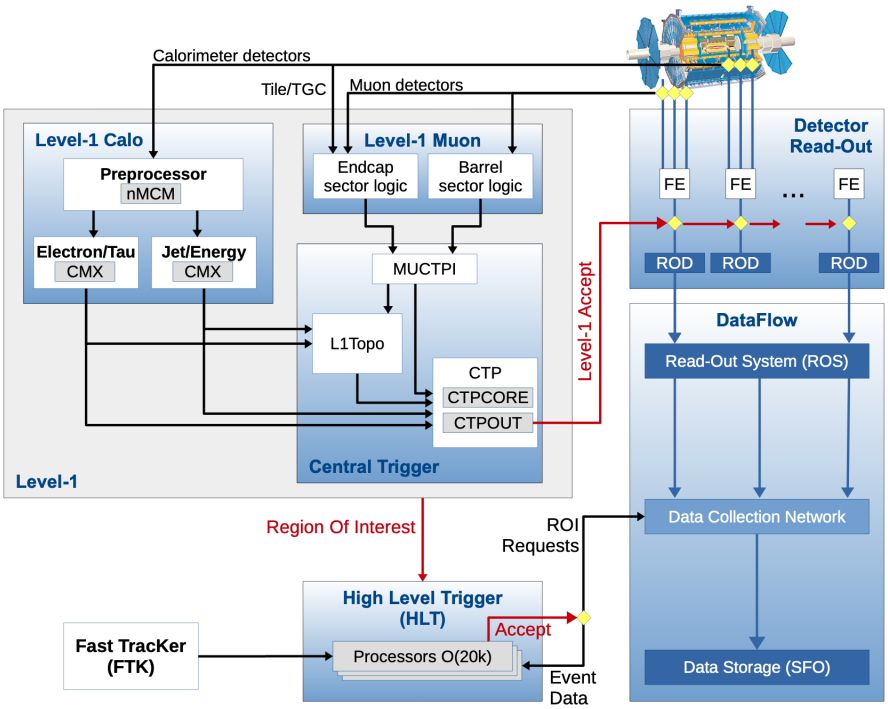

Fig. 2.16 Schematic layout of the ATLAS trigger and data acquisition system for Run-2. [25]

stored for offline processing/analysis. A schematic of the full ATLAS trigger/DAQ system is shown in Figure 2.16.

The L1 Trigger is a distributed electronics system located within the ATLAS detector which has sub-components that communicate with hardware from both the calorimeter (L1Calo) and muon spectrometer (L1Muon). The L1Muon trigger processor interfaces directly with the dedicated muon trigger chamber hardware described in Section 2.2.5. The L1Calo trigger processor, on the other hand, relies on a form of modified calorimeter output called *calorimeter trigger towers*. These trigger towers consist of energy and timing sums for calorimeter regions with reduced granularity ($\Delta\eta \times \Delta\phi$) ranging from 0.1×0.1 in the central region to 0.4×0.4 in the forward region. A newer hardware-based L1 trigger labeled L1Topo analyzes kinematic/geometric relationships between different objects.

The Central Trigger Processor (CTP) receives all the information in real-time from the L1Muon, L1Calo, and L1Topo processors. The CTP first synchronizes the trigger inputs with the LHC collision clock in order to correctly associate each event with the correct bunch crossing. All trigger inputs are then compared to different sets of trigger thresholds on the transverse momentum and various detector signatures, defined for each separate type of physics being targeted by ATLAS. The choice of trigger thresholds is ultimately determined by the maximum allowed L1 output rate of 100 KHz, which represents a factor of 400 reduction from the 40 MHz event rate at the LHC. If any set of trigger thresholds are passed, the CTP flags the event as accepted and notifies all sub-detectors. Upon receiving this "L1 Accept" (L1A) notification, all the data from each sub-detector is read out and propagated to the next step in the trigger process: the High Level Trigger.

The HLT is a software based trigger that refines set of events passing the L1 trigger using the full information available from the ATLAS detector, as opposed to the low granularity data used by the L1 trigger. For example, the HLT uses tracking information from the ID to locate the primary vertex (PV) and various particle candidates. The HLT reduces the data rate from 100 KHz to approximately 1 KHz. Since the HLT is software based it is limited primarily by the CPU processing time and must be highly optimized to process each event in approximately 0.1 - 1.0 seconds. An example of such an optimization is that track reconstruction is only performed within ROIs defined by the L1 trigger.

2.2.7 Computing

The raw data for all events passing the ATLAS trigger system is sent to the CERN Data Center where the process of archiving, distributing, processing and analyzing

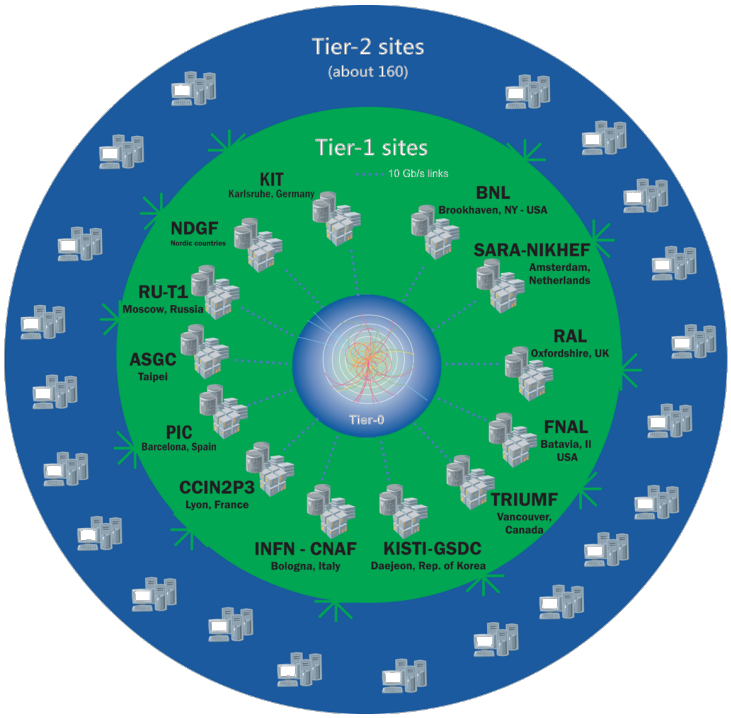

Fig. 2.17 Schematic diagram of the Worldwide LHC Computing Grid tier system. © 2020 CERN.

begins. However, this is only the starting point of an international network of LHC computing resources [26] known as the Worldwide LHC Computing Grid (WLCG) or simply "the grid". The WLCG is a layered system made up of three separate "tiers" as shown in Figure 2.17.

The CERN Data Center (**Tier-0**) provides around 20% of the total compute capacity of the LHC, with the other 80% coming from institutions around the world. The next layer of support (**Tier-1**) is composed of thirteen large computing centers with round-the-clock support and massive storage capacity. They are responsible for large-scale reprocessing, storage and safe-keeping of a significant proportion of raw and reconstructed data from the LHC. Furthermore, Tier-1 centers share these resources with the next link in the chain (Tier-2). Tier-1 centers are typically national laboratories such as BNL, INFN, and TRIUMF.

The next link in the chain (**Tier-2**) is composed primarily of universities and other scientific institutions which possess enough storage and computing power for a combination of analysis tasks, simulated event production and reconstruction. Individual scientists connect to the grid via the last tier (**Tier-3**) which consists of local computing resources such as small local clusters belonging to individual Physics departments or even individual PCs.

Chapter 3

ATLAS OBJECT RECONSTRUCTION AND PARTICLE IDENTIFICATION

A large number of particles is produced during a pp collision event. These include charged particles such as electrons ($e^{\pm}$), muons ($\mu^{\pm}$), tau leptons $\tau^{\pm}$ and charged hadrons (e.g. $\pi^{\pm}$) as well as electrically neutral particles such as photons (γ), neutrinos (ν_e, ν_μ, ν_τ) and neutral hadrons (π^0). In order to achieve the wide range of physics goals of the ATLAS experiment, all of these particles must be reconstructed and identified with high efficiency. Furthermore, the properties of these objects must be measured with a high degree of precision and accuracy. This requires maximal utilization of the output from all ATLAS subdetectors.

3.1 Tracks

The reconstruction of charged particle trajectories within the ATLAS detector is important for nearly all physics object identification and reconstruction. These reconstructed trajectories are referred to as *tracks* and the procedure for identifying

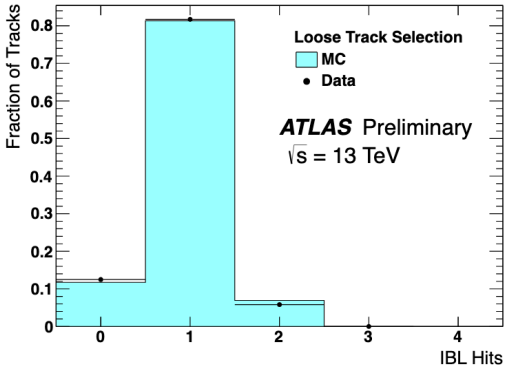

(a) Number of IBL Hits

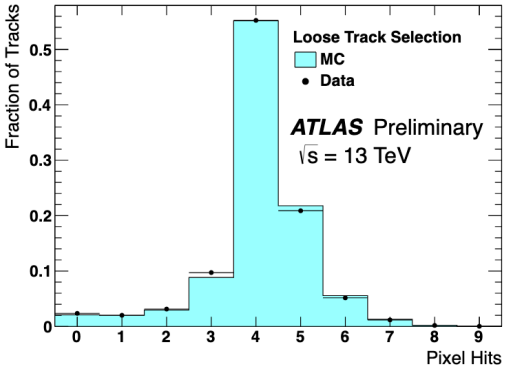

(b) Number of Pixel Hits

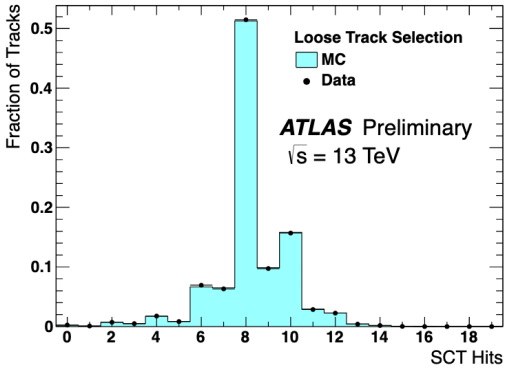

(c) Number of SCT Hits

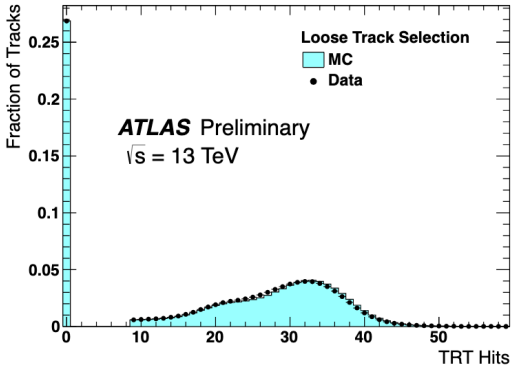

(d) Number of TRT Hits

Fig. 3.1 Comparison of the number of (a) IBL, (b) Pixel, (c) SCT, and (d) TRT tracking hits distributions in data and simulation for the Loose track selection. The distributions are normalized to one so that the bin contents represent track fraction. [27]

and reconstructing all the charged particle trajectories in each event is called *tracking*. Tracking begins with the measurement of the particles position at multiple points within the ID (Section 2.2.3) each referred to as a *hit*. A comparison of the number of hits per ID sub-detector in MC simulation and data is given in Figure 3.1.

The tracking procedure for ATLAS is divided into four separate stages [28]:

1. **Data Preparation and Space Point Formation**

   When a charged particle passes through the active silicon material of the various

ID sub-detectors, it leaves behind *clusters* of energy deposits resulting in raw data output spanning multiple nearby sensors. The first tracking stage consists of finding these connected clusters and associating them together into a single three-dimensional location. The difficulty of this process is compounded by the fact that nearby particle trajectories can in many cases *merge* together into the same cluster. This is particular common in the case of high p_T jets, covered in Chapter 4. This necessitates the use of a neural network based cluster splitting routine for the Pixel detector. After clusters are identified and (potentially) split, their locations are transformed from the local sub-detector coordinate system to the global ATLAS coordinate system and referred to as *space points*.

2. **Space Point Seeded Track Finding**

   The process of converting space points into actual tracks begins by forming track *seeds* built from triplets of space points. These triplets may come from any combination of space points from either of two innermost ID sub-detectors: Pixel and SCT. To reduce the number of potential seeds, each individual space point is restricted to appear in only a small number of seeds. Seeds which pass a set of loose initial requirements are passed to a *track finding algorithm* which utilizes the Kalman Filter [29] technique. The goal at this stage is to produce a set of *track candidates*, consisting only of space points within the Pixel/SCT detectors, to pass forward to the next tracking stages.

3. **Ambiguity Solving**

   At this stage, some of the track candidates may be *fake* or *duplicates*. Fake tracks result from a random combination of space points that manage to pass the loose quality requirements of the track seeding described above. Because space points are allowed to be shared between different track candidates, it is also possible for the same charged particle to manifest as two separate track

candidates. At this stage it is necessary to reject as many of these fake/duplicate tracks as possible. The *ambiguity solving algorithm* achieves this by scoring track candidates. Positive scores are gained by track candidates that possess unique (non-shared) space points and good fit quality from the Kalman Filter algorithm. Negative scores are assigned to track candidates which possess shared hits or missing hits (called *holes*) in a Pixel/SCT layer where they would be expected.

4. **TRT Extension**

   After passing the ambiguity resolution stage, the final set of track candidates are extended to include hits from the TRT, the outermost ID sub-detector. This process is only performed for track candidates within the acceptance of the TRT. When the TRT extension is successful, the momentum resolution is significantly improved.

These resulting tracks are then individually fit with a χ^2 minimization routine [30] which accounts for the magnetic field strength in each region of the detector, the position error on each hit as well as the possibility of mulitple scattering. This final track fitting produces an estimate of the *track parameters*.

The track selection requirements are

1. **Loose**

   - $p_T > 400$ MeV
   - $|\eta| < 2.5$
   - number of silicon (IBL + Pixel + SCT) hits ≥ 7
   - number of shared modules ≤ 1
   - number of silicon holes ≤ 2
   - number of pixel holes ≤ 1

2. **Tight** [1]

   - if $|\eta| \leq 1.65$, number of silicon hits ≥ 9
   - if $|\eta| > 1.65$, number of silicon hits ≥ 11
   - either one IBL or next-to-innermost-Pixel-layer hit
   - no Pixel holes

3.2 Vertices

In order to perform physics analysis it is vital to determine the location of the individual proton-proton collisions in each event at the ATLAS detector. The *vertex finding* algorithm is divided into four major steps which are iterated numerous times to reconstruct each vertex in the event [31]:

1. The arithmetic mode of the z_0 impact parameter for all (remaining) tracks in an event is computed in order to produce an initial *seed* vertex.
2. Tracks compatible with the seed are grouped together for fitting.
3. The adaptive vertex fitting algorithm is used to estimate the position and uncertainty of the vertex.
4. Remaining tracks that are incompatible with this new vertex are removed and used to repeat the entire procedure again, starting by computing a new seed.

This vertex finding algorithm is tuned to balance two competing difficulties: (1) Splitting a real vertex into multiple reconstructed vertices and (2) merging two proton-proton interactions into the same reconstruction vertex. The vertex with the largest $\sum p_T^2$ for all associated tracks is termed the hard-scatter vertex. In general all

[1] The Tight selection requirements are applied *on top of* the Loose requirements.

physics analysis work considers only objects associated to this vertex, while all other reconstructed vertices are considered to be the result of pile-up.

3.3 Electrons

Electrons interact primarily with the EM calorimeters (described in Section 2.2.4) by leaving a signature in groups of neighboring cells. The reconstruction of electrons is performed by matching reconstructed tracks from the ID with these calorimeter deposits. Electron reconstruction in the central region of the ATLAS detector ($|\eta| < 2.47$) proceeds in several steps [32]:

1. **Seed-Cluster Reconstruction**

   A 3×5 sliding window[2] is used to search for electron cluster *seeds*. For position of the sliding window the total energy is summed across all longitudinal layers for each contained cell, forming a so-called *tower*. If the sum of transverse energy from the towers in the window is greater than 2.5 GeV, a seed cluster is formed. If the seed cluster passes certain quality requirements a *Region of Interest* (ROI) is specified surrounding the location of the cluster.

2. **Track Reconstruction**

   Several intricacies of the track-fitting (described in Section 3.1) are modified in order to assist with the reconstruction of electrons. By default the ATLAS tracking procedure assumes tracks correspond to particles with an energy loss model corresponding to pions. However, this model can be substituted for an alternative model that allows for up to 30% energy loss at each intersection of the track with the ID material. This alternative model accounts for the

[2]The sliding window grid has has units of 0.025×0.025 in (η, ϕ) space, which corresponds to the granularity of the middle layer of the EM calorimeter.

possibility of bremsstrahlung. During the execution of the tracking algorithm, if a track seed with $p_T > 1$ GeV cannot be extended into a full track with at least seven hits using the pion energy loss model, a second attempt is performed using the electron energy loss hypothesis. Furthermore, if a track candidate is produced with the pion hypothesis but fails the final Global χ^2 track fit, it is then refit with the electron hypothesis. Tracks utilizing the electron hypothesis are tagged as such and utilized in the next steps of the electron reconstruction process.

3. **Electron-Specific Track Fit**

   The tracks obtained in the previous step are then loosely matched to the EM clusters based on their separation in the $\eta - \phi$ plane. In order to perform this matching the trajectory of the track is extended into the center of the EM calorimeter. Tracks with ≥ 4 pixel layer hits which are loosely associated to electron clusters are refit using an optimized Gaussian Sum Filter (GSF) [33] which is specialized to account for non-linear bremsstrahlung effects. A similar but stricter matching as the one described above is performed again with the refitted track.

4. **Electron Candidate Reconstruction**

   If multiple tracks fulfill the matching criteria for the same EM cluster, one of them is chosen as the *primary* track. The choice is based upon a number of criteria: (1) cluster-track distance in the $\eta - \phi$ plane, (2) number of hits in the Pixel detector and (3) the presence of a hit in the first silicon layer. If a cluster is not associated to any tracks at this point, it is removed and considered as a photon candidate. The efficiency of electron identification is shown in Figure 3.2. The energy of the clusters is then calibrated to match that of the original electron energy using multivariate techniques based on simulated MC

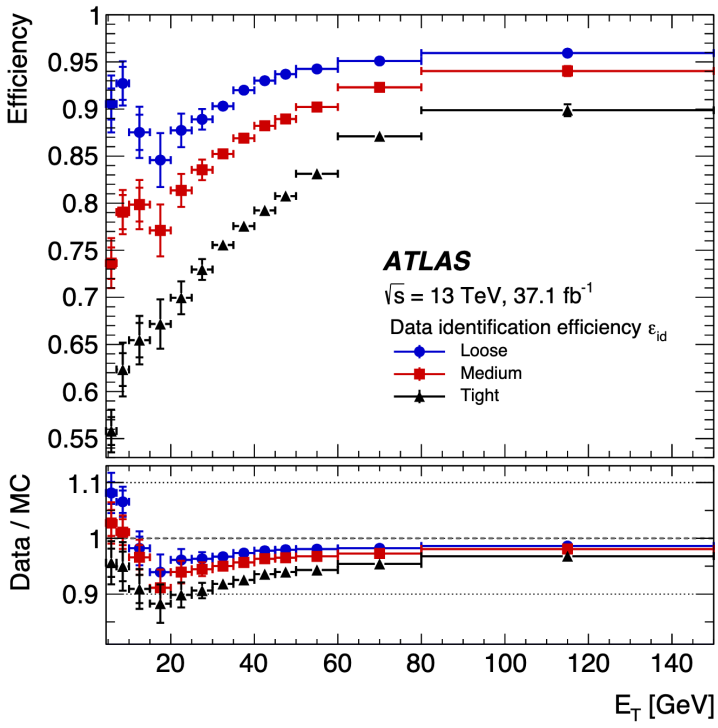

Fig. 3.2 The electron identification efficiency in $Z \rightarrow ee$ events in data as a function of transverse energy (E_T) for the Loose, Medium, and Tight working points. The efficiency in data is obtained by applying data-to-simulation efficiency ratios that are measured in $J/\psi \rightarrow ee$ and $Z \rightarrow ee$ events to the $Z \rightarrow ee$ simulation. [34]

samples [34]. The four-momentum of the electron is then computing using the energy information from the final calibrated energy of the cluster and directional information (η, ϕ) from the best track matched to the original seed cluster.

3.4 Muons

Muons are minimum ionizing particles that interact weakly with the ATLAS calorimeter system, depositing approximately 3-4 GeV there on average [35]. Thus, as discussed in Section 2.2.5, muons are reconstructed primarily by combining tracking

information from the ID and MS. Within the ID, tracks from muons are not treated any differently than any other type of charged particle. Within each sub-detector region of the MS (MDTs, CSCs, etc) a Hough transform [36] is used to search for hits aligned in the bending plane of the detector (produced by the magnetic field) and produce muon *track candidates*. Track candidates are formed by combining hits from different track segments via a combinatorial search [37]. After this an overlap removal algorithm is run to find the most optimal track assignment. The final track candidates are fit with a global χ^2 minimization algorithm, similar to ID track reconstruction. Finally, a hit recovery and track re-fit are performed if necessary.

Four types of muons emerge from the reconstruction process, depending on which sub-detectors are involved:

- **Combined Muons (CB)**

  A global fit is used to combine hits form both the ID and the MS while accounting for energy loss in the calorimeter. The track from the MS is used as the primary starting point and extrapolated inward and matched to a single ID track. These are the most common types of reconstructed muons used in physics analyses, as they have the highest purity and best kinematic resolution.

- **Segment-Tagged Muons (ST)**

  Like the CB muons, ST muons are constructed by combining ID and MS hits. However, in the case of ST muons, a local track segment from either the MDT or CSC chambers is used in place of a full MS track. This strategy is necessary for reconstructing muons which cross only one layer of the MS chambers. This typically occurs when the muon possesses low p_T and passes through only one region of the MS.

- **Calorimeter-Tagged Muons (CT)**

  In the case where an ID track can be matched to a deposit in the calorimeter

system which is compatible with a minimum ionizing particle, some muons can be reconstructed in regions where the MS has low acceptance around $|\eta| \approx 0$.

- **Extrapolated Muons (ME)**

  In the region beyond the ID acceptance but still within the MS acceptance ($2.5 < |\eta| < 2.7$) some muons can still be reconstructed by utilizing only MS tracks. A loose requirement is placed to ensure the MS track points towards the IP.

As with electrons, muon candidates are categorized according to purity: "Loose", "Medium", and "Tight". The muon reconstruction efficiency at ATLAS is nearly 100%, as seen in Figure 3.3.

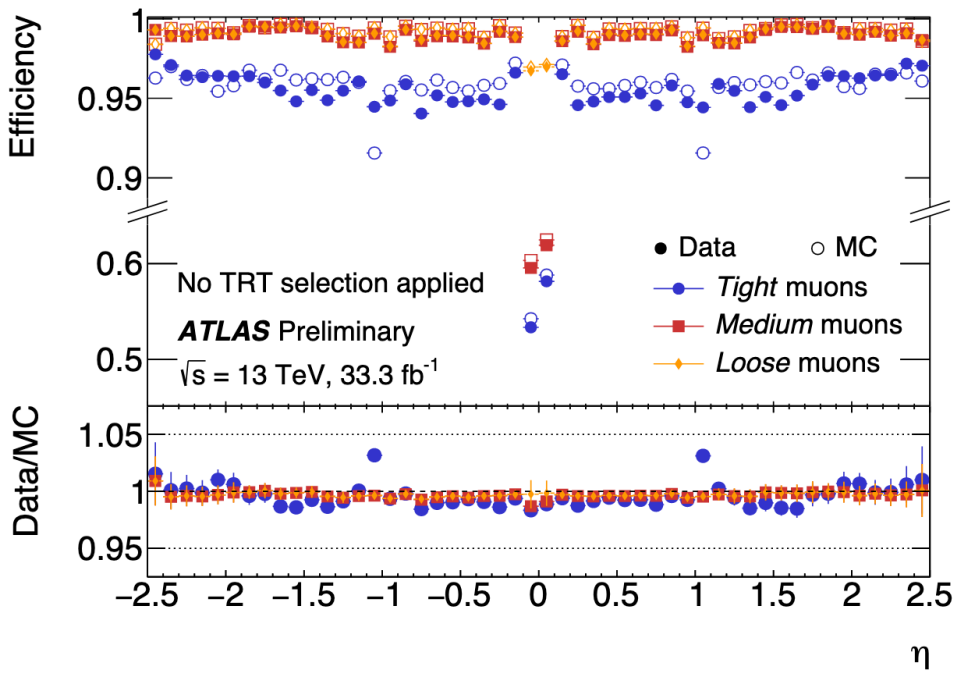

Fig. 3.3 Muon reconstruction efficiencies for the Loose/Medium/Tight identification algorithms measured in $Z \rightarrow \mu\mu$ events as a function of the muon pseudorapidity (η) for muons with $p_T > 10$ GeV. The prediction by the detector simulation is depicted as open circles, while filled dots indicate the observation in collision data with statistical errors. The bottom panel shows the ratio between expected and observed efficiencies: the effiency scale factor. The errors in the bottom panel show the quadratic sum of statistical and systematic uncertainty. [38]

Chapter 4

JETS

As discussed in Section 1.7, partons created during pp collisions undergo a showering process where they produce cascades of additional strongly interacting particles through gluon radiation and splitting. As this showering process concludes and the products approach a sufficiently low energy ($\approx$ 1 GeV) the resulting partons hadronize and produce a spray of colorless hadrons called a "jet" which interacts with both the tracking and calorimeter systems of the ATLAS detector. Jets are reconstructed by employing *jet clustering algorithms* which take from the event a set of constituent inputs representing the products of parton showering and combine them to output a set of jets, ideally representing the original partons from the hard scatter event. At the ATLAS experiment jets may be constructed using only tracks as inputs, only calorimeter clusters as inputs, or a combination of both.

4.1 Jet Constituents

All jet clustering algorithms take as input a set of four-vectors representing all the products of parton showering and hadronization, known as *constituents*. These constituents compose *all* the potential jets in the event, and it is the job of the jet clustering algorithm to convert these to a set of four-vectors representing only

the corresponding jets from the event. These constituents can be created with information from any particular ATLAS sub-detector or combination thereof, as long as they encode the four-vectors of the particles produced during the jet showering/hadronization process. The most relevant constituent types for this analysis are outlined below.

4.1.1 Calorimeter Clusters

The information quality contained within a collection of calorimeter signals of a given collision event can be increased by grouping the signals into *topologically connected cell clusters*. This strategy helps to reduce the impact of background electronic noise and other sources of calorimeter fluctuation such as the presence of pile-up. The finely segmented lateral (η-ϕ) readout together with the longitudinal sampling layers allows the ATLAS calorimeter system to resolve spatial signal patterns relevant for jet reconstruction while efficiently removing insignificant signals caused by noise.

These topo-clusters are formed by a growing-volume algorithm [39] which begins with a calorimeter cell possessing a highly significant *seed signal*, where significance is defined as the ratio of the cell signal magnitude over the expected noise:

$$\varsigma^{\mathrm{EM}}_{\mathrm{cell}} = \frac{E^{\mathrm{EM}}_{\mathrm{cell}}}{\sigma^{\mathrm{EM}}_{\mathrm{noise,cell}}} \tag{4.1.1}$$

The growth of the topo-cluster proceeds iteratively by connecting nearby cells, where the seeding, growth, and boundary conditions are controlled by placing bounds on the cell significance (Eq. 4.1.1), as shown in Figure 4.1. The four-vector corresponding to each topo-cluster is computed by a weighted combination of all cells contained in the topo-cluster. The weights are necessary because each cell is allowed to contribute (unevenly) its energy to two separate topo-clusters.

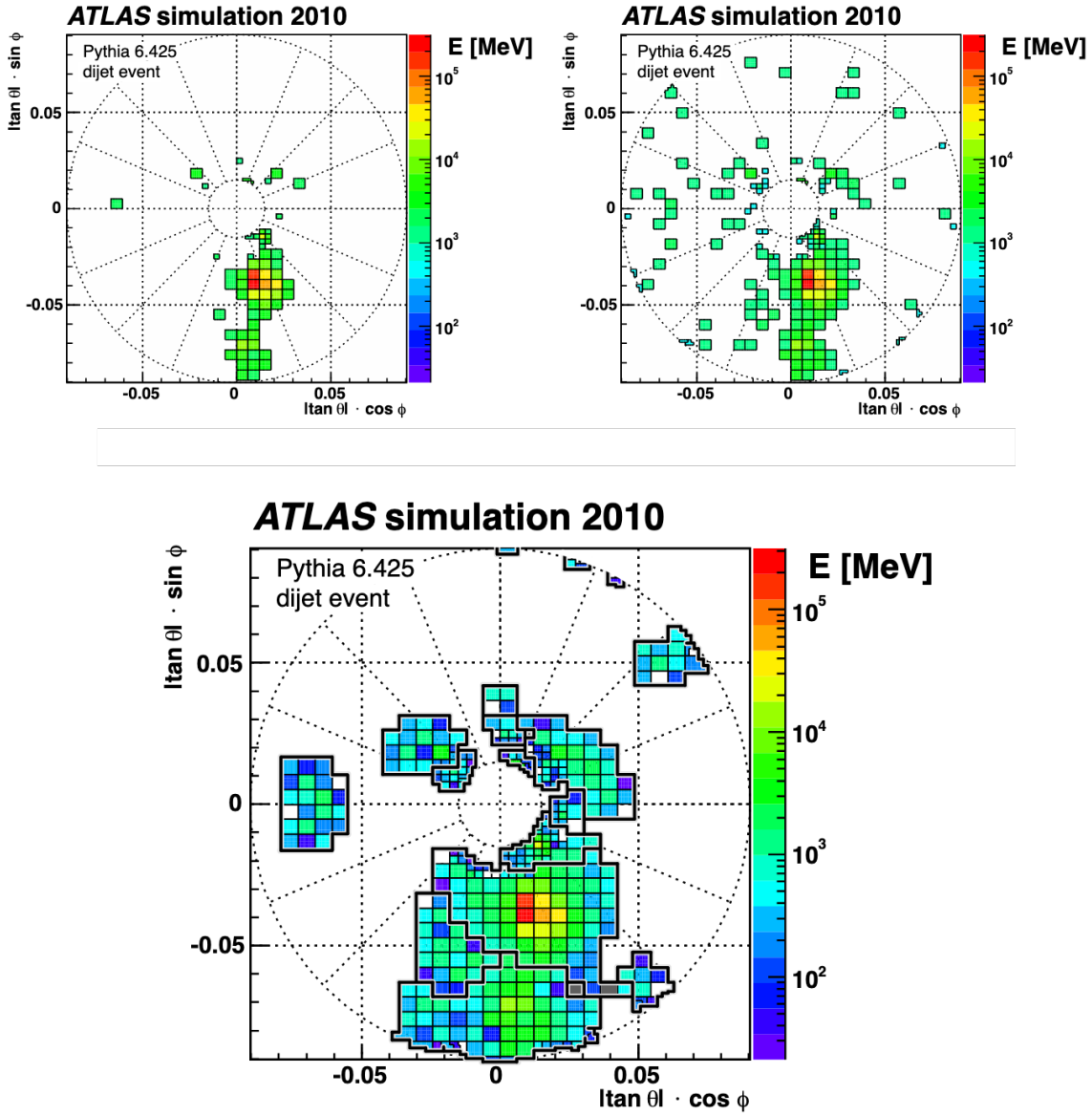

Fig. 4.1 Stages of topo-cluster formation in the FCAL calorimeter for a simulated dijet event. Cells with $\varsigma_{\text{cell}}^{\text{EM}} > 4$ (top left) are used in the seeding, cells with $\varsigma_{\text{cell}}^{\text{EM}} > 2$ (top right) control the topo-cluster growth. The final set of topo-clusters (bottom) is shown with black outlines around each cluster. Adapted from Ref. [39].

4.1.2 Tracks

The more energetic or "boosted" a jet-initiating particle is, the more collimated the showering/hadronization process becomes. At a certain point the calorimeter spatial resolution is no longer fine-grained enough to fully resolve the individual jet constituents. On the other hand, the ID has excellent angular resolution and track reconstruction efficiency even at very high energy with dense clusters of charged particles [40]. Since jet clustering algorithms are indifferent to the origin of the inputs, only requiring a set of four-vectors as input, they can be applied to tracks just as well as calorimeter clusters. In particular, utilizing ID information during jet clustering allows for a more detailed view of the internal structure of jets, which is particularly useful in the context of jet substructure (Section 4.4) and b-tagging (Section 4.5).

4.1.3 Track-Calo Clusters

While using tracks as inputs to the jet clustering improves the angular resolution, there are two primary downsides: (1) only charged particles interact with the ID, and (2) the energy resolution of the tracking detector degrades at very high energy. In order to achieve the best of both worlds, tracking and calorimeter information can be combined. One of the first ways in which ATLAS explored this possibility was by improving the calorimeter jet mass (m^{calo}) measurement by incorporating information about nearby associated tracks to produce the so-called *track-assisted jet mass* [41].

The four-vector of a jet is simply the sum of the four-vectors of its constituents. For a calorimeter jet J with calorimeter cell cluster constituents i, each with momentum

$\vec{p}_i$, the calorimeter mass (m^{calo}) is defined (by the basic rules of special relativity) as:

$$m^{\text{calo}} = \sqrt{\left(\sum_{i \in J} E_i\right)^2 - \left(\sum_{i \in J} \vec{p}_i\right)^2} \tag{4.1.2}$$

where each calorimeter cluster is assumed to result from particles with zero mass. The track-assisted jet mass is defined as:

$$m^{\text{TA}} = \frac{p_T^{\text{calo}}}{p_T^{\text{track}}} \times m^{\text{track}} \tag{4.1.3}$$

where p_T^{calo} is the transverse momentum of a calorimeter jet, p_T^{track} is the transverse momentum of the four-vector sum of tracks associated to the calorimeter jet and m^{track} is the invariant mass of this four-vector sum. The improvement in jet mass resolution observed with m^{TA} is shown in Figure 4.2.

While the jet mass resolution is notably improved by utilizing m^{TA} in many cases, a more rigorous unification of tracking and calorimeter information was desired to yield benefits in *all* observable jet properties at a wider range of energies. One method to achieve this is the definition of a new type jet input constituent which unifies tracks and calorimeter deposits into new "Track-Calo Cluster" (TCC) objects, designed to maximally exploit the strengths of each detector.

To build TCC constituents for each event, good quality tracks matched to the selected hard scatter primary vertex are extrapolated to the calorimeter and matched to corresponding topo-clusters, as shown in Figure 4.3. The error on this extrapolation accounts for both the original ID measurement of the track parameters, as well as additional uncertainty accumulated as the particle passes through additional detector elements. The typical extrapolated angular uncertainty of a track is significantly

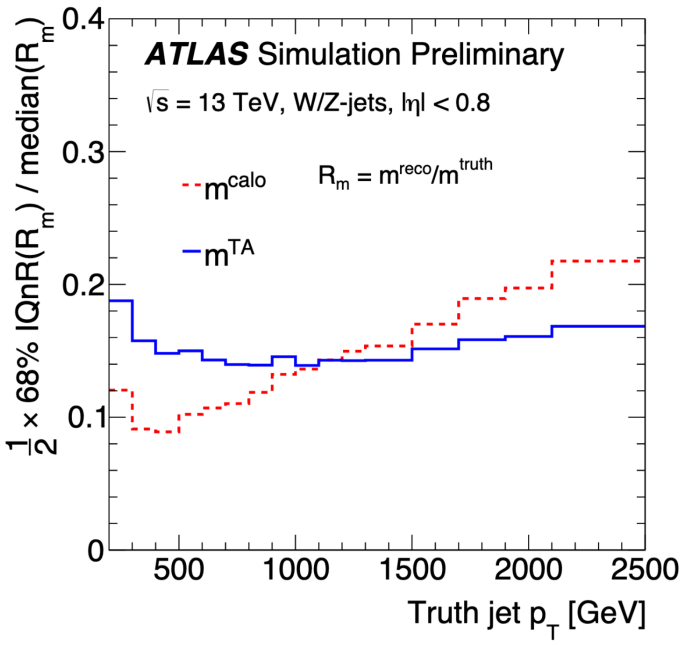

Fig. 4.2 The resolution of the jet mass response as a function of truth jet p_T for simulated W and Z boson jets for calorimeter-based jet mass (dashed red line) and track-assisted jet mass (blue solid line). The half of the 68% interquartile range (IQnR) divided by the median of the jet mass response is used as an outlier-insensitive measure of the resolution. [41]

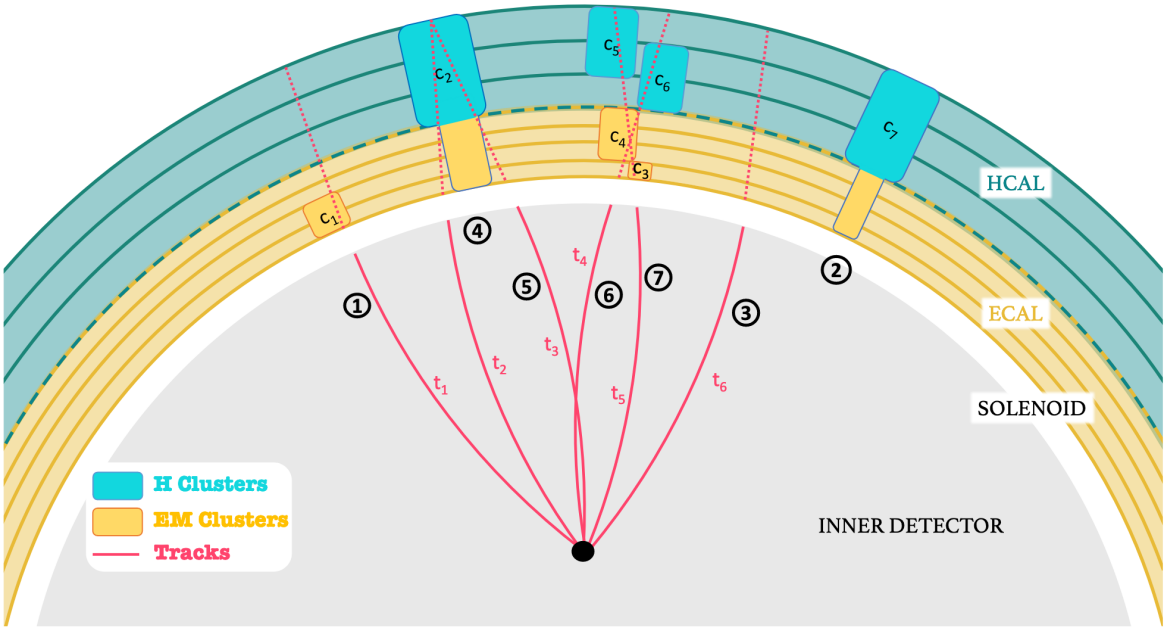

Fig. 4.3 A schematic demonstration the creation of seven TCC objects representing ① a simple track-cluster match, ② a topo-cluster without a matching track, ③ a track without a matching cluster, ④ and ⑤ are each tracks matching a single cluster but sharing that cluster's energy, and ⑥ and ⑦ showing a much more complex scenario with multiple track-cluster matches. [42]

smaller than the size of the average topo-cluster across the detector, particularly for moderate to high p_T tracks.

Fully matched track/topo-cluster combinations are referred to as "combined". Un-matched topo-clusters and tracks are not discarded, but rather grouped into separate sets of TCC constituents. TCC objects created with an un-matched track are referred to as "charged", and TCC objects created with an un-matched topo-cluster are referred to as "neutral". Within the acceptance of the ID the "combined" type composes > 95% of all reconstructed TCC, whereas outside the acceptance of the ID the "neutral" type dominates, as shown in Figure 4.4.

In order to combine the track and/or topo-cluster into a single object, a scheme must be devised for defining the resulting four-vector in terms of the four-vectors of

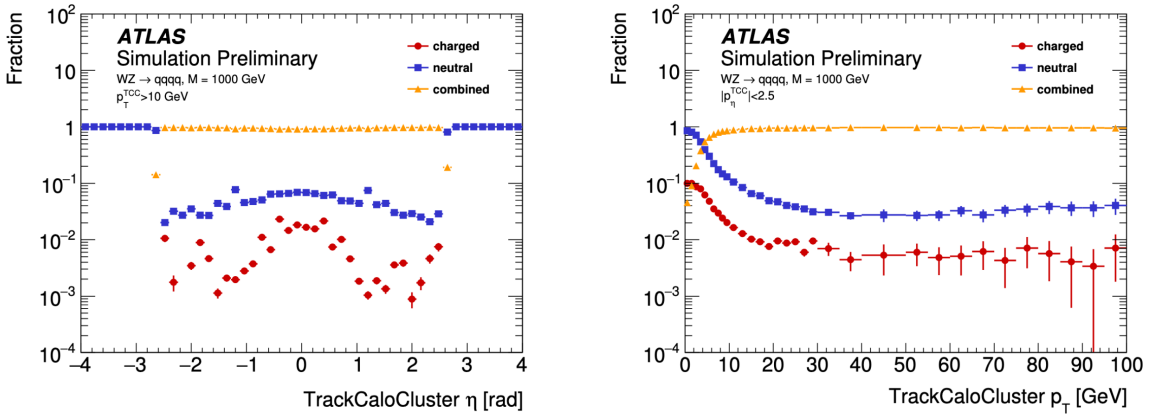

(a) η dependence

(b) p_T dependence

Fig. 4.4 The fractions of different TCC types are shown as a function of (a) the TCC η and (b) the TCC p_T. Combined objects (triangles) represent tracks for the selected hard scatter primary vertex which are matched to topo-clusters, neutral objects (squares) are for topo-clusters not matched to tracks for any primary vertex, and charged objects (circles) are tracks from the selected hard scatter primary vertex not matched to any topo-cluster. [42]

the track and topo-cluster. This is done in a straight-forward manner as follows:

$$\vec{p}_{\text{TCC}}^{\,\text{combined}} \equiv (p_T^{\text{calo}}, \eta^{\text{track}}, \phi^{\text{track}}, m^{\text{calo}}) \tag{4.1.4}$$

$$\vec{p}_{\text{TCC}}^{\,\text{charged}} \equiv (p_T^{\text{track}}, \eta^{\text{track}}, \phi^{\text{track}}, m^{\text{track}}) \tag{4.1.5}$$

$$\vec{p}_{\text{TCC}}^{\,\text{neutral}} \equiv (p_T^{\text{calo}}, \eta^{\text{calo}}, \phi^{\text{calo}}, m^{\text{calo}}) \tag{4.1.6}$$

which combines calorimeter energy/mass measurements and track angular information for the combined TCC objects. For dealing with cases where multiple tracks are matched to the same topo-cluster (or vice versa) a more complicated formula accounting for energy-sharing is required [42].

4.2 Clustering Algorithms

Due to their aggregate nature, the notion of a *jet* is not as immediately or clearly interpreted as are other physics objects such as electrons, muons, and photons. This allows for a significant amount of freedom in how jets are defined and reconstructed in collider experiments. Furthermore the manner in which individual constituents are combined, and the characteristic size of the resulting jets (in the η-ϕ plane) can be altered on a per-algorithm basis. To deal with this ambiguity a set of properties that must be met by any standardized jet definition were outlined in December of 1990 [43] as follows:

1. Simple to implement in an experimental analysis.
2. Simple to implement in a theoretical calculation.
3. Defined at any order of QCD perturbation theory.
4. Yield finite cross section at any order of perturbation theory.
5. Yield a cross section that is *relatively* insensitive to hadronization.

This set of rules allows for better comparison of experimental results and theoretical predictions, as well as better comparison of results between different collider experiments.

The most common category of jet clustering algorithm used by ATLAS is *sequential recombination* [44]. These algorithms are carefully designed to be insensitive to the present of soft (sometimes called "infrared") and collinear gluon emission and thus usable in perturbation theory calculations. These recombination algorithms work iteratively by attempting to work in reverse through the history of the parton shower, starting with the softer final products of the showering/hadronization process

recorded by the detector, and working back (ideally) to the original hard collisions product(s) which initiated the jet.

The primary quantities of interest in these algorithms are a distance measure between separate objects d_{ij} and between each object and the "beam" d_{iB}.

$$d_{ij} = \min\left(p_{T_i}^{2P}, p_{T_j}^{2P}\right) \times \frac{\Delta R_{ij}^2}{R^2} \tag{4.2.1}$$

$$d_{iB} = p_{T_i}^{2P} \tag{4.2.2}$$

where ΔR_{ij} is the angular distance between the i-th and j-th objects: $\Delta R_{ij}^2 = \Delta\eta_{ij}^2 + \Delta\phi_{ij}^2$, p_T is the transverse momentum of the object, and the parameters P and R are algorithm parameters which regulate the evolution of the clustering. Starting with the full set of constituents as objects, the algorithm proceeds by identifying the smallest of all the distance measures d_{ij} or d_{iB}. If the smallest is d_{ij} for some particular i/j then it combines the four-vectors of i and j into a new object, otherwise if it is d_{iB} then object i is added to the set of jets to be output at the end of the clustering and discarded from the rest of the calculation. New distances are calculated accounting for combined objects and the process is repeated until no objects are left, or in other words, all constituents in the event have been recombined into jets.

Different jet clustering algorithms in the sequential recombination family are distinguished by different values for the parameters P and R mentioned above. The k_T algorithm [44] for $P = 1$ causes softer (lower p_T) particles to be merged first. This introduces a strong sensitivity to small fluctuations of the energy density in the particle shower. For this reason it is rarely used in a modern context. The *Cambridge-Aachen* (C/A) algorithm [45] for $P = 0$ works only with the angular component of the jets by sorting the objects without any reference to p_T in d_{ij}.

The *anti-k_T* algorithm [46] for $P = -1$ causes soft particles to cluster together with nearby hard particles before they cluster between themselves. This reduces sensitivity to small fluctuations of energy within the parton shower, the primary (undesirable) characteristic of the k_T algorithm. This property causes a hard particle with no hard neighbors within a distance of $2R$ to accumulate all nearby soft particles within a circle of radius R. This leads to a stability in jet area which is helpful for jet calibration and analysis, which has resulted in anti-k_T being used as the default algorithm for the majority of ATLAS research.

The choice of jet clustering algorithm parameters as well as constituent type depends in part upon the physics analysis goals in question. In particular circumstances two separate jet algorithms may be used to reconstruct the same event to pick out separate features. For example, for identifying the decay products of the two-pronged decay of a Standard Model vector boson ($W/Z \rightarrow q\bar{q}^{(\prime)}$), the anti-$k_T$ algorithm with a large radius parameter of $R = 1$ is used to capture the full jet corresponding to the inclusive W/Z decay. However, jets with a smaller radius parameter can be used to capture the features of the jets corresponding to the individual quark jets.

In particular for the case of capturing and reconstructing the b-quarks from a $H \rightarrow b\bar{b}$ decay, a special modification the jet clustering algorithms discussed above can be made to produce jets with variable radius (VR) [47]. This entails modifying the radius parameter R to depend on jet p_T in the following way:

$$R \rightarrow R_{\text{eff}}(p_T) \equiv \frac{\rho}{p_T} \tag{4.2.3}$$

where the new constant parameter ρ determines how quickly the effective jet size decreases as the jet p_T increases. Additionally the VR jet clustering algorithm also imposes a minimum (R_{min}) and maximum (R_{max}) bound on the radius which prevents the jet radii from becoming pathologically small or large.

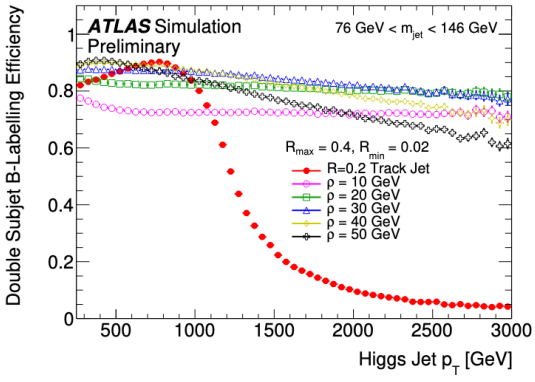

(a)

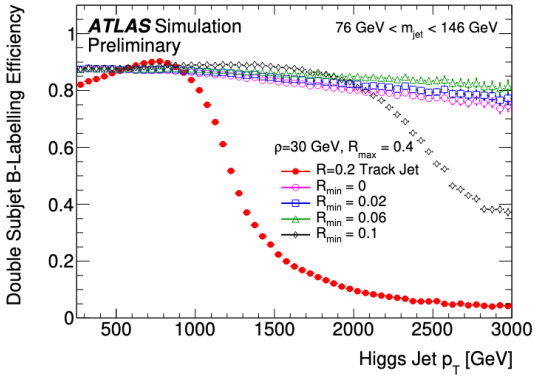

(b)

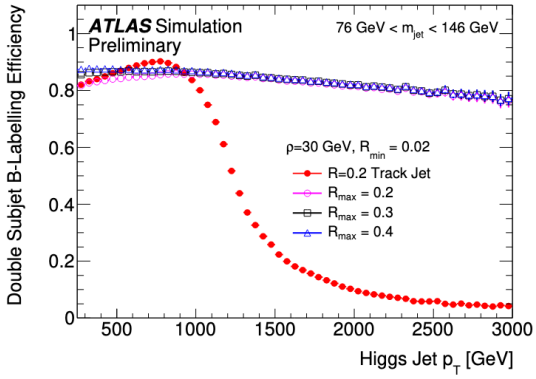

(c)

Fig. 4.5 Efficiency of subjet double b-labelling at the truth level for Higgs jets as a function of Higgs jet p_T. (a) The efficiency for VR track jets with $R_{\text{min}} = 0.02$ and $R_{\text{max}} = 0.4$ for several different ρ values. (b) The efficiency for VR track jets with $\rho = 30$ GeV and $R_{\text{max}} = 0.4$ for several different values of R_{min}. (c) The efficiency for VR track jets with $\rho = 30$ GeV and $R_{\text{min}} = 0.02$ for several different values of R_{max} The efficiency for standard $R = 0.2$ track jets is also included in all of the plots. [48]

In practice the VR modification has only been widely used on ATLAS for anti-k_T jets reconstructed with track constituents, in particular for reconstructing the individual b-jets from an $H \longrightarrow b\bar{b}$ decay process. The values $\rho = 30$ GeV, $R_{\text{min}} = 0.02$, and $R_{\text{max}} = 0.4$ are used in ATLAS and were derived by scanning each parameter for simulated Higgs jets and maximizing the truth b-quark matching efficiency for each subjet as shown in Figure 4.5.

4.3 Calibration

The jets reconstructed by any particular clustering algorithm may not correctly match the true four-vector of the original parton. There are a number of factors responsible for this, such as:

- **Dead Material**: Some of the products of the showering process may be absorbed by inactive detector elements and thus not be present as constituents.
- **Leakage**: Some energy may fall outside or "punch through" the calorimeter.
- **Out-of-cone Effects**: Some particles may fall outside the reconstructed jet due to imperfect clustering.
- **Thresholds/Efficiency**: A proportion of the total jet energy may be lost in reconstruction. For example by falling below the noise threshold in some calorimeter cells.

In order to compensate for these effects the jet energy, η and mass is corrected based upon studies utilizing MC simulated events. The full calibration scheme is outlined in Figure 4.6. For each simulated event, jets are reconstructed and groomed as described in the preceding sections. However, a second collection of jets is also clustered using truth particles from the simulation. These "truth" or "particle-level" jets suffer from none of the issues described above and match the true parton four-vector much more closely. By matching together each reconstructed jet with its truth-level counterpart, the difference between the truth four-vector and the reconstructed four-vector can be quantified.

Reconstructed jets are matched to particle-level jets with a simple angular matching procedure that minimizes their separation $\Delta R = \sqrt{(\Delta\eta)^2 + (\Delta\phi)^2}$. The energy *response* is defined as $E_{\text{reco}}/E_{\text{truth}}$, where E_{reco} is the reconstructed jet energy

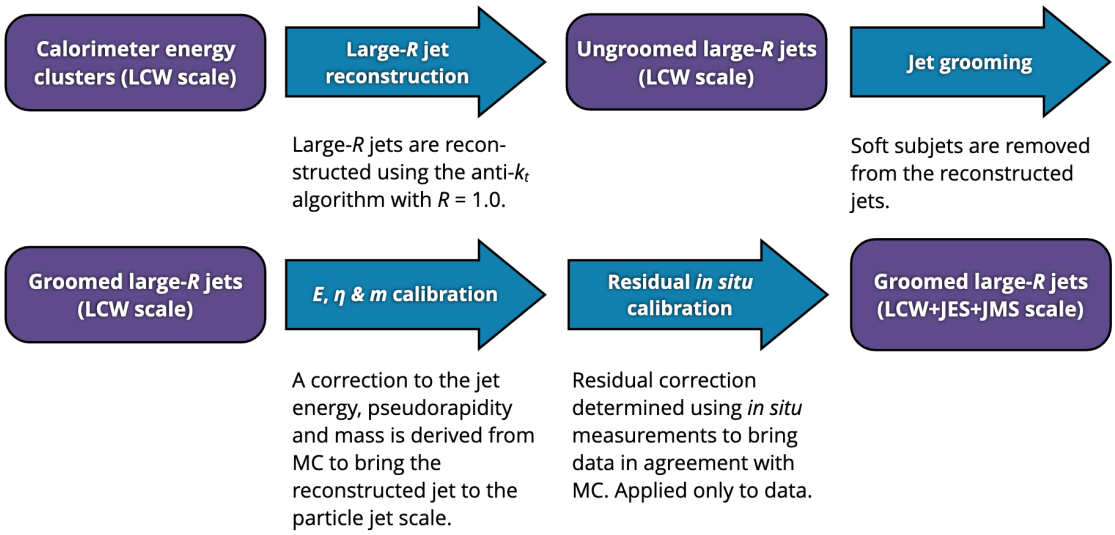

Fig. 4.6 Overview of the large-R jet reconstruction/calibration procedure, as described in [49]. Note that for the TCC jets used in the analysis covered by this thesis, the inputs are Track-Calo Clusters (TCCs) instead of calorimeter clusters as specified in this chart.

prior to calibration and E_{truth} is the energy of the corresponding truth-level jet. The mass response is defined similarly as $m_{\text{reco}}/m_{\text{truth}}$. The response is parameterized as a function of jet energy and η_{reco}, and an average is computed ($R_E = \langle E_{\text{reco}}/E_{\text{truth}} \rangle$) using a Gaussian fit of the response. The jet energy response for TCC jets is shown in Figure 4.7.

The energy correction derived this way (c_{JES}) is typically on the order of 5-10% with only a weak dependence on the jet energy and a structure in η_{reco} that clearly reflects the detector technology and geometry. The mass correction (c_{JMS}) is close to unity for jets with p_T between 200 and 800 GeV, but can be as large as 1.5 for very energetic jets with low mass.

In addition to this jet energy scale (JES) and jet mass scale (JMS) calibration, a small correction $\Delta\eta$ is applied to correct for a bias relative to truth-level jets, but only in certain regions of the detector [50]. At this point we refer to the uncalibrated quantities with subscript zero (E_0, η_0, etc), and the calibrated quantities with subscript

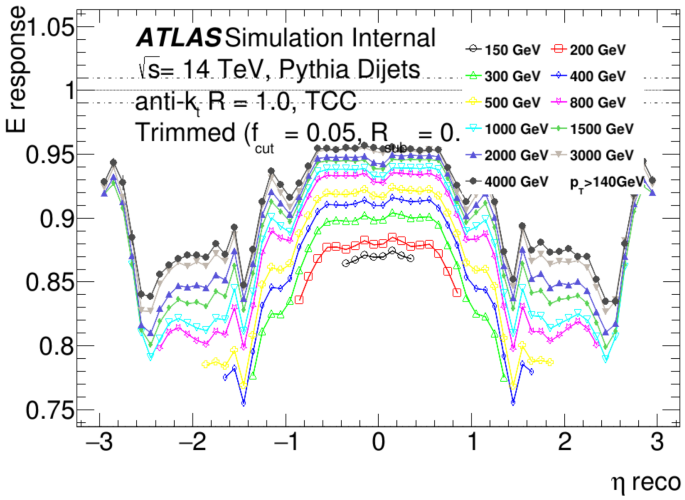

Fig. 4.7 The jet energy response (before calibration) for TCC jets is presented as a function of jet pseudorapidity for several values of truth jet energy ranging from 150 GeV to 4 TeV.

"reco". The final JES+JMS scale calibrated large-R jet energy, mass, η and p_T can then be written as

$$E_{\text{reco}} = c_{\text{JES}}\, E_0 \tag{4.3.1}$$

$$m_{\text{reco}} = c_{\text{JES}}\, c_{\text{JMS}}\, m_0 \tag{4.3.2}$$

$$\eta_{\text{reco}} = \eta_0 + \Delta\eta \tag{4.3.3}$$

$$p_T^{\text{reco}} = c_{\text{JES}} \sqrt{E_0^2 - c_{\text{JMS}}^2 m_0^2} \;/\; \cosh\left(\eta_0 + \Delta\eta\right) \tag{4.3.4}$$

4.4 Jet Substructure

The primary goal of jet reconstruction is to accurately measure the four-vectors of the outgoing partons resulting from the hard scatter event. However, a significant amount of additional information can be obtained by analyzing the internal structure

of the jet constituents. For example they may tend to be diffuse and evenly spread in the case of a gluon-initiated jet. On the other hand, in the case of a $Z \rightarrow q\bar{q}$ or $H \rightarrow b\bar{b}$ decay there will often be two distinct "prongs". It is often the case that the sensitivity of jet-based searches can be improved by accounting for these differences in the internal structure of jets which differs for background and signal, because a single jet containing all the decay products of a massive particle (such as a W or Z boson) has significantly different internal structure than a jet (of the same p_T) originating from a light quark or gluon.

The details of jet substructure can be more clearly resolved if the contribution from soft radiation and pileup is removed from the jet beforehand using a process generally referred to as *jet grooming*. For the large-R TCC jets used for this thesis a technique called "trimming" is used which relies on the fact that the contamination from pile-up, multiple parton interactions (MPI) and initial state radiation (ISR) in the reconstructed jet is often much softer than the showering products of the partons associated with the outgoing hard-scatter products. During the trimming procedure soft constituents are removed by using their p_T ratios as the metric for removal.

The trimming procedure uses a k_T algorithm with a smaller radius parameter R_{sub} to reconstruct all constituents from a single large-R jet into a set of smaller contained "subjets". Any subjets with $p_{T_i}/p_T^{\text{jet}} < f_{\text{cut}}$ are removed from the original large-R jet, where p_{T_i} is the transverse momentum of the i^{th} subjet and f_{cut} is an adjustable parameter of the trimming procedure. This process is illustrated in Figure 4.8. For this thesis values of $R_{\text{sub}} = 0.2$ and $f_{\text{cut}} = 0.05$ are used. A variety of alternative jet grooming procedures have been studied by ATLAS [51] as well, including methods that involve modifying the jet clustering algorithm itself.

After jet grooming has been applied to enhance the quality of information contained within the constituents of a jet, the aggregate properties of these constituents

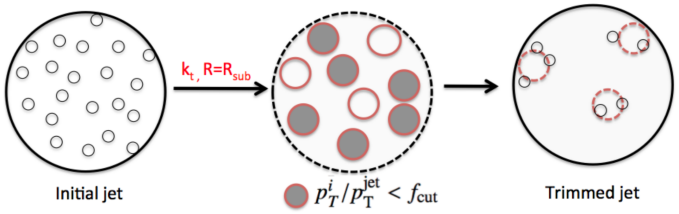

Fig. 4.8 Diagram depicting the jet trimming procedure. [51]

can be computed with so-called *jet substructure variables*. In the past the more commonly used jet substructure variables were computed by analyzing the jet clustering algorithm history (k_T "splitting scales" [52]) or properties of the re-clustered subjets (N-subjettiness [53]).

Presently, as is the case for the work covered in this thesis, the so-called *Energy Correlation Functions* (ECF) [54, 55] have become the de facto standard and are computed by summing certain expressions over all constituents contained within a jet as follows:

$$e_2^{(\beta)} = \sum_{1 \le i < j \le n_J} z_i z_j \theta_{ij}^{\beta} \tag{4.4.1}$$

$$e_3^{(\beta)} = \sum_{1 \le i < j < k \le n_J} z_i z_j z_k \theta_{ij}^{\beta} \theta_{ik}^{\beta} \theta_{jk}^{\beta} \tag{4.4.2}$$

$$e_4^{(\beta)} = \sum_{1 \le i < j < k < l \le n_J} z_i z_j z_k z_l \theta_{ij}^{\beta} \theta_{ik}^{\beta} \theta_{jk}^{\beta} \theta_{il}^{\beta} \theta_{jl}^{\beta} \theta_{kl}^{\beta} \tag{4.4.3}$$

where n_J is the number of constituents in the jet, β is an adjustable parameter, z_i is the ratio of the p_T of the i^{th} constituent of the jet over the total jet p_T, and $\theta_{ij} = (\phi_i - \phi_j)^2 + (y_i - y_j)^2$ is the angular separation of constituents i and j. These ECF expressions form the basis for constructing higher-level jet substructure observables where $e_{N+1}^{(\beta)}$ captures the N-prong nature of a jet. For example, the high level jet substructure observable that quantities how compatible a jet is with a 2-prong

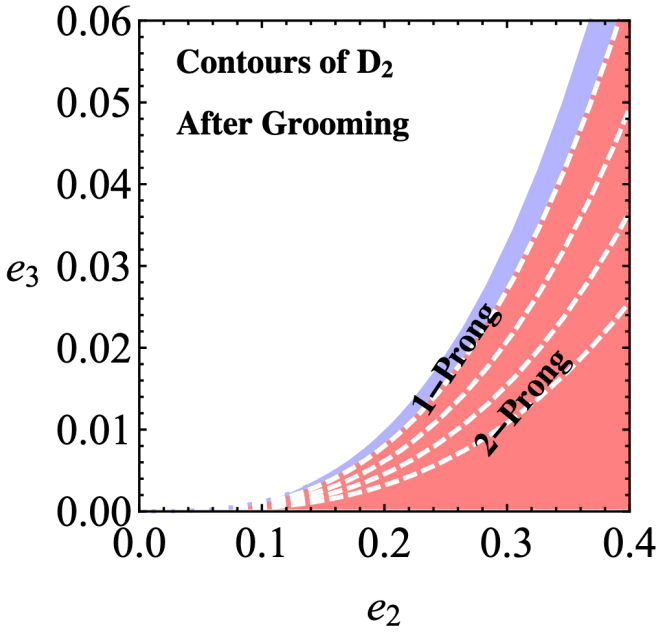

Fig. 4.9 Schematic depiction of the phase space for the energy correlation functions e_2 and e_3 which compose D_2. Contours of the D_2 variable are shown as white dashed curves. The D_2 variable is explicitly defined to cleanly separate the 1-prong and 2-prong regions of this phase space. [55]

structure is

$$D_2^{(\beta)} = \frac{e_3^{(\beta)}}{\left(e_2^{(\beta)}\right)^3} \tag{4.4.4}$$

The e_2 vs. e_3 phase space distributions of 1-prong (light quark/gluon) and 2-prong ($W/Z \to q\bar{q}^{(\prime)}$, $H \to b\bar{b}$) jets are shown in Figure 4.9. The value $\beta = 1$ is standard in ATLAS as it results in the highest sensitivity across a wide range of jet mass and p_T.

4.5 B-Jet Identification

In general jet reconstruction algorithms proceed without special consideration of the "flavor" of a jet: light quark, charm (c) or bottom (b). However, the identification of jets containing b-hadrons (often simply called *b-jets*) is of utmost importance not only

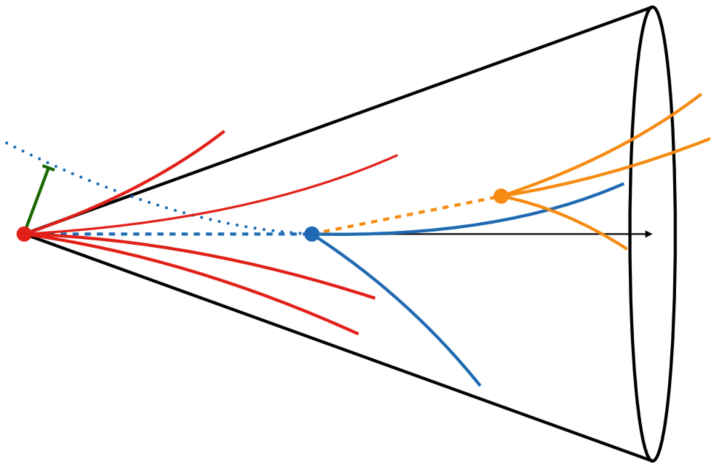

Fig. 4.10 Cartoon of a b-jet decay containing a b-hadron decay vertex (blue dot) displaced from the primary pp vertex (red dot) and a c-hadron decay vertex (orange dot) further displaced and often close to the b-hadron flight axis. The tracks emerging from the secondary (blue dot) and tertiary (orange dot) vertices have large impact parameters (green line) with respect to the primary hard scatter vertex (red dot). ©2017 Andy Chisholm.

for this thesis, but for the majority of the most ambitious physics goals of the ATLAS experiment. In particular the precision measurements of Higgs boson properties and searches for BSM physics rely heavily on an ability to pick out or *tag* b-jets and distinguish them from light quark jets. The algorithms used to perform this tagging are referred to as *b-tagging algorithms*.

The relatively long lifetime of b-hadrons (approximately 1.5 picoseconds) gives them a characteristic flight path of approximately 5 mm from the primary hard-scatter vertex before undergoing secondary decay. This flight distance is quite often large enough that the decay chain can be resolved by the ID and the secondary decay vertex (SV) can be identified. Furthermore, roughly 90% of the time a tertiary vertex (TV) from a c-quark will be present as well. These properties, depicted in Figure 4.10, are exploited by the b-tagging algorithms.

The primary b-tagging algorithm developed for ATLAS during Run 2, referred to as MV2c10, utilizes a machine learning technique called a boosted decision tree (BDT). This is multivariate algorithm which uses inputs from a variety of other algorithms which utilize both tracking and calorimeter information pertinent to each jet under consideration. These include:

- Jet p_T and η.
- A likelihood-based combination of the transverse and longitudinal impact parameter significances.
- The presence and properties of a secondary vertex.
- Reconstruction of a b-hadron decay chain using a Kalman filter to search for a common direction connecting the primary vertex to both the bottom and tertiary charm decay vertices.

The MV2c10 machine learning algorithm is trained on a set of events from a simulated $t\bar{t}$ sample, where b-jets are labelled as "signal" and c-jets and light quark jets are labelled as "background". Ultimately the MV2c10 algorithm produces a single output discriminating variable for each jet, as shown in Figure 4.11.

In order to utilize the MV2c10 output discriminant in a physics analysis, two tasks must be accomplished: (1) Cuts on the MV2c10 discriminant called "working points" (WP) must be defined, with a specified signal efficiency in simulated events and (2) scale factors to correct for small discrepancies between simulation and data must be derived along with their uncertainties. The ATLAS experiment produces these scale factors by studying a very pure $t\bar{t}$ sample in data using two complementary methods: a "tag-and-probe" approach (T&P) and a combinatorial likelihood approach (LH). These methods both rely on the fact that the $t \to Wb$ branching fraction is close to 100%. Two oppositely charged leptons resulting from the leptonic W boson decays

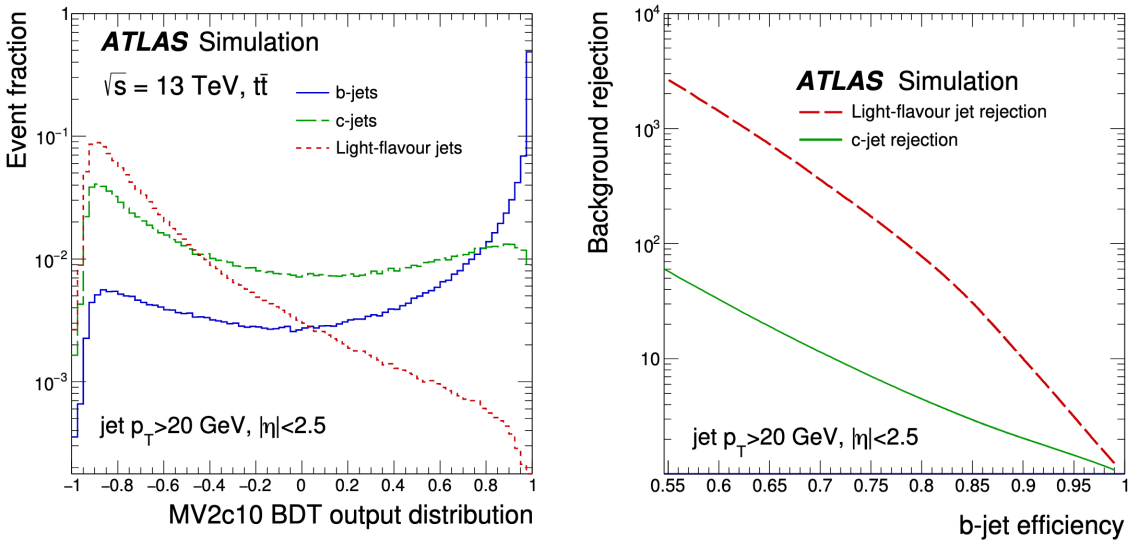

Fig. 4.11 The MV2c10 output (left plot) for b-jets (solid line), c-jets (dashed line) and light quark jets (dotted line) in simulated $t\bar{t}$ events, as well as the background rejection for light quarks (dashed line) and c-jets as a function of the b-jet tagging efficiency (right plot). This performance was evaluated on simulated $t\bar{t}$ events. [56]

are required in each event ($e\mu$, ee or $\mu\mu$). By selecting only events where both W bosons (from each top quark) decay leptonically, the number of non b-jets in these events is greatly reduced. The T&P and LH methods differ in the restrictions they place on the lepton flavors of the final state. The resulting b-tagging efficiencies and scale factors are shown in Figure 4.12 for the 70% WP.

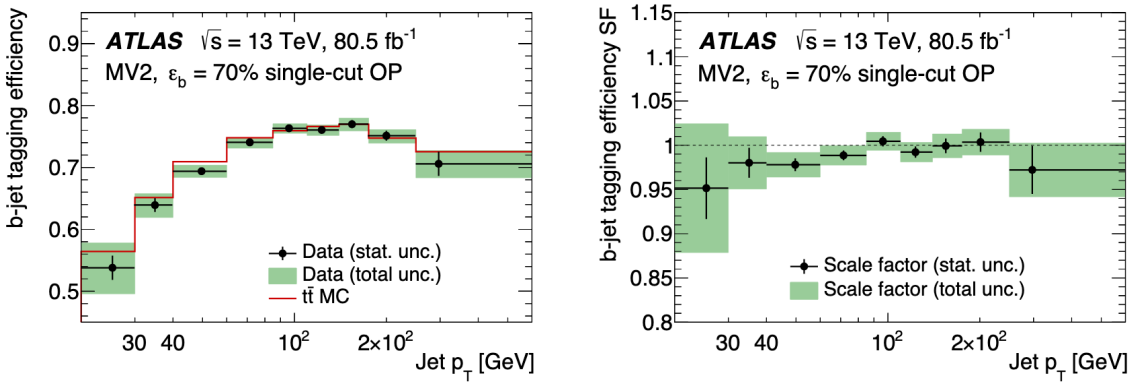

(a) (b)

Fig. 4.12 The (a) b-jet tagging efficiency and (b) b-jet tagging efficiency simulation-to-data scale factors for the ε_b=70% single-cut WP of the MV2 tagger as a function of jet p_T. The efficiency measurement is shown together with the efficiency derived from simulated $t\bar{t}$. Vertical error bars include data statistical uncertainties only while the green bands correspond to the sum in quadrature of statistical and systematic uncertainties. The dots are located at the mean of the b-jet $p_T$distribution in each p_T bin. [57]

Chapter 5

FULLY-HADRONIC VH RESONANCE SEARCH

5.1 Overview

This thesis presents the ATLAS search for new resonances decaying to a vector boson ($V = W, Z$) and a Higgs boson H, in the fully hadronic channel where both the H and V boson decay to quarks producing a $q\bar{q}^{(\prime)}b\bar{b}$ final state[1]. This search focuses on new resonances with mass ≥ 1.5 TeV. In terms of the H and V decay products, the mass of such a resonance can be written as

$$m_{JJ} \equiv \sqrt{(E_H + E_V)^2 - \left|\vec{p}_H + \vec{p}_V\right|^2}. \tag{5.1.1}$$

where the common particle physics convention of setting the speed of light (c) to unity is used. See Figure 5.1 for a tree-level Feynman diagram illustrating the basic production/decay of the signal model under consideration. Some of the most

[1]The specific final states are $W \to q\bar{q}'$, where the prime symbol denotes that the quark and anti-quark have different flavor, and $Z \to q\bar{q}$, where both the quark and anti-quark have the same flavor. The expression $q\bar{q}^{(\prime)}b\bar{b}$ is used to denote the general final state resulting from either W or Z boson decay accompanied by an $H \to b\bar{b}$ decay.

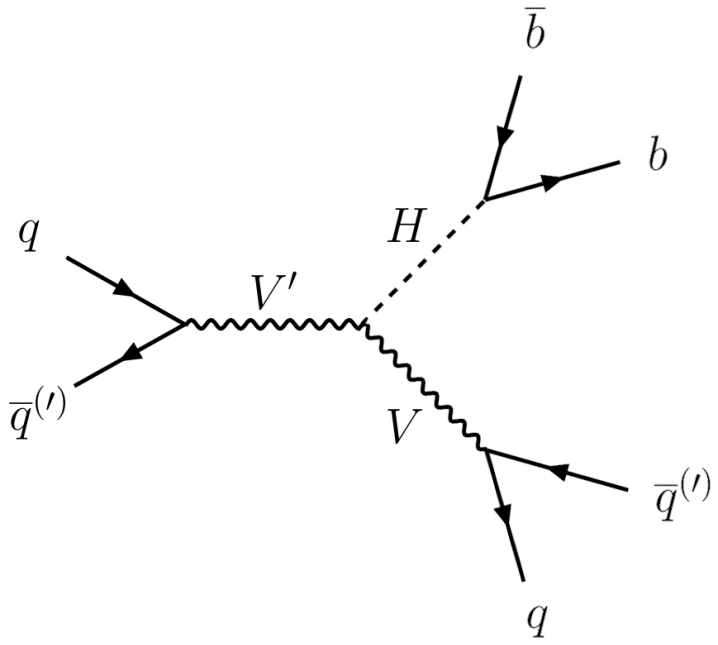

Fig. 5.1 Feynman diagram illustrating the $pp \to V' \to VH$ production/decay chain searched for by this analysis. The initial state quarks originate from the two protons involved in the hard scatter event.

relevant properties of W and Z bosons are outlined in Tables 5.1 and 5.2. The branching fractions for the Higgs boson decay modes are detailed in Figure 5.2.

The V and H bosons that are produced in the decay of such theoretical heavy resonances are highly boosted and the resulting decay products of each boson are likely to be collimated and merged into a single large radius jet. The dijet invariant mass (m_{JJ}) spectrum of the two large radius jets is then used as the discriminant variable, where the signature of the new heavy resonance decay yields a resonant peak structure on top of the smoothly falling background. The dominant background ($\approx 90\%$) corresponds to multijet QCD processes, with much smaller contributions from other non-resonant SM backgrounds: $t\bar{t}$ and V + jets. After reconstructing the V and H boson candidates as large radius jets, the tools of jet substructure (Section 4.4) and b-tagging (Section 4.5) are applied to heavily suppress the dominant background of multijet events. Due to the challenges associated with modelling

this background with MC simulated samples, a fully data-driven method is used to provide a background estimation method.

W Boson Property	Measured Value
mass	80.379 ± 0.012 GeV
Γ_{total}	2.085 ± 0.042 GeV
$\Gamma(e^+\bar{\nu}_e)/\Gamma_{\text{total}}$	10.71 ± 0.16 [%]
$\Gamma(\mu^+\bar{\nu}_\mu)/\Gamma_{\text{total}}$	10.63 ± 0.15 [%]
$\Gamma(\tau^+\bar{\nu}_\tau)/\Gamma_{\text{total}}$	11.38 ± 0.21 [%]
$\Gamma(\text{hadrons})/\Gamma_{\text{total}}$	67.41 ± 0.27 [%]
$\langle N_{\text{charged}} \rangle$	19.39 ± 0.08

Table 5.1 W Boson properties computed from global averages of experimental results by the Particle Data Group (PDG). [5]

Z Boson Property	Measured Value
mass	91.1876 ± 0.0021 GeV
Γ_{total}	2.4952 ± 0.0023 GeV
$\Gamma(e^+e^-)/\Gamma_{\text{total}}$	3.3632 ± 0.0042 [%]
$\Gamma(\mu^+\mu^-)/\Gamma_{\text{total}}$	3.3662 ± 0.0066 [%]
$\Gamma(\tau^+\tau^-)/\Gamma_{\text{total}}$	3.3696 ± 0.0083 [%]
$\Gamma(\text{invisible})/\Gamma_{\text{total}}$	20.000 ± 0.055 [%]
$\Gamma(\text{hadrons})/\Gamma_{\text{total}}$	69.911 ± 0.056 [%]
$\langle N_{\text{charged}} \rangle$	20.76 ± 0.16

Table 5.2 Z Boson properties computed from global averages of experimental results by the Particle Data Group (PDG). [5]

A simplified theoretical model [59] fulfilling only SM symmetry constraints is used to provide a model-independent Lagrangian for a heavy resonance search. This framework incorporates Heavy Vector Triplets (HVT), a common SM extension with an isospin $SU(2)_L$ triplet formed of a neutral Z' and two charged $W'^{\pm}$ bosons, from which two explicit models will be considered as benchmarks to evaluate the relative sensitivity of this analysis to $W'^{\pm}$ and Z' signals: Models A and B [59], where weakly and strongly coupling scenarios are described, respectively. The couplings of the new vector bosons $W'^{\pm}$, Z' to the H and V bosons are defined as a combination of

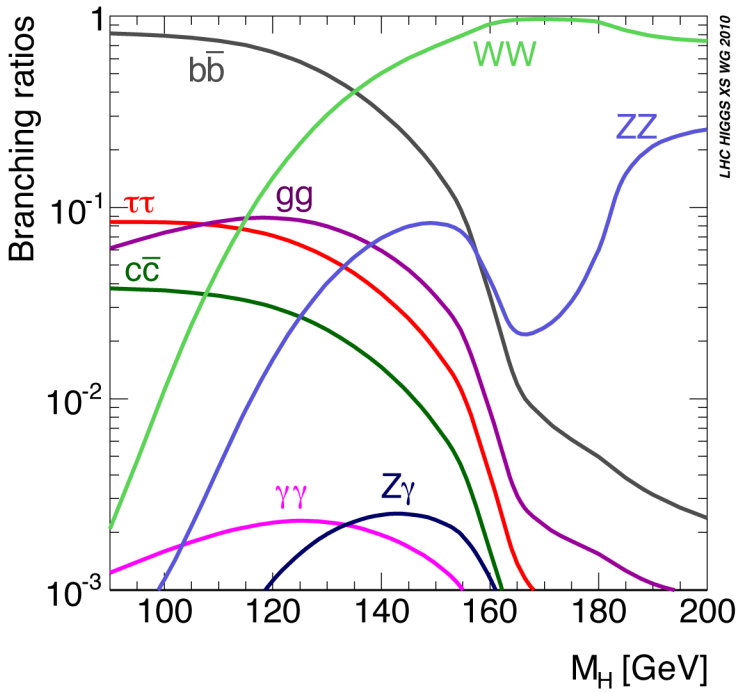

Fig. 5.2 Standard Model predictions for Higgs boson decay branching ratios. [58]

parameters $g_V c_H$, while the couplings to fermions are defined as $(g^2/g_V)c_F$, where g^2 is the SM $SU(2)$ gauge coupling, g_V represents the strength of the new vector boson interaction and c_H (c_F) represents the coupling to the Higgs boson (fermions). In Model A, the branching fractions to fermions and gauge bosons are comparable, whereas in Model B the fermionic couplings are suppressed. Within the ATLAS experiment a simplified pair of coupling constants is typically used: $g_H = g_V c_H$ and $g_f = g^2 c_F / g_V$.

A search for heavy vector resonances decaying to VH in the fully hadronic final state was previously performed in ATLAS using 36.1 ± 1.0 fb^{-1} of pp collision data at 13 TeV taken during 2015 and 2016 [60]. The largest excess was observed in the ZH channel at $m_{JJ} \sim 3.0$ TeV with a local significance of 3.3 σ, and a global significance of 2.2 σ. Upper limits on the production cross-section times branching ratio to the $q\bar{q}^{(\prime)}b\bar{b}$ final state were set for resonance masses in the range between 1000 and 3800

GeV with values ranging between 107 to 3 fb and 97 to 2 fb (at 95% CL) for WH and ZH resonances, respectively. The corresponding excluded HVT Model B signal mass ranges are 1000-2500 GeV for WH resonances, and 1000 - 2600 GeV for ZH resonances.

Searches for heavy vector resonances decaying to VH in the V boson leptonic decay channels have been performed in ATLAS using 36.1 ± 1.0 fb^{-1} of pp collision data at 13 TeV [61]. For HVT Model A W' (Z') masses have been excluded up to 2.67 TeV (2.65 TeV), while for Model B, W' (Z') masses of up to 2.86 TeV (2.83 TeV) have been excluded.

The CMS collaboration has published a search for new heavy resonances decaying to VH in the fully hadronic mode using 19.7 fb^{-1} of 8 TeV data from Run 1 of the LHC. Resonance masses up to 1.7 TeV were excluded in the combined W' and Z' search (1.1 TeV in $Z' \rightarrow ZH$, 1.5 TeV in $W' \rightarrow WH$), using the HVT Model B benchmark [62]. The search was also performed by CMS using 35.9 fb^{-1} of 13 TeV data from Run 2 of the LHC, excluding W' (Z') bosons with masses up to 3.15 TeV (2.26 TeV, except 1.19-1.21 TeV) in Model B [63].

This chapter is structured as follows: Section 5.2 describes the contents and motivation behind the HVT model; Section 5.3 describes the data and simulated samples used; Sections 5.4 and 5.5 describe the object definitions, event selection criteria and corresponding optimization studies; Section 5.6 describes the strategy for background estimation; Section 5.7 describes the statistical method used to interpret the results; Section 5.8 describes the systematic uncertainties considered in this search. The results and conclusions of the search are provided in Chapter 6.

5.2 Theoretical Framework/Motivation

In order to search for any BSM signature in a particle collider experiment, a model with explicit predictions is necessary. No particular model has emerged as the most compelling or well-motivated possibility to single out for search efforts, but producing explicit results[2] for each model would be prohibitively difficult and time consuming for HEP researchers. However, the case of a heavy resonance search simplifies the matter because it is not sensitive to all the specific details and free parameters of any underlying model, but only the restricted set of parameters which control the mass of the resonance and any interactions involved in its production and decay.

For this reason a so-called *bridge model* has been developed called the Heavy Vector Triplet (HVT) model [59]. It employs a simplified model of the resonance where only the mass parameters and relevant couplings to SM particles are retained. Aside from known SM symmetry constraints this simplified Lagrangian model does not need to fulfill any particular theoretical requirements. With this simplified model, experimental results can be presented only in terms of the parameter space of this simplified Lagrangian. In this way experimental results can be easily translated by theorists into constraints on parameters of any particular model. Due to the careful construction of the HVT model this can be done analytically and not just via numerical simulations, which eliminates the need for knowledge (on the theorists part) of the experimental details of the search results.

Conceptually this method can be represented by a bridge as seen in Figure 5.3. The central pillar represents the simplified model with Lagrangian $\mathcal{L}_S$ and parameters $\vec{c}$. The likelihood $L(\vec{c})$ is used by the experimental analysis (see Section 5.7) to derive

[2] A *result* here consists of a set of experimentally-derived statistical constraints on model parameters related to the heavy resonance.

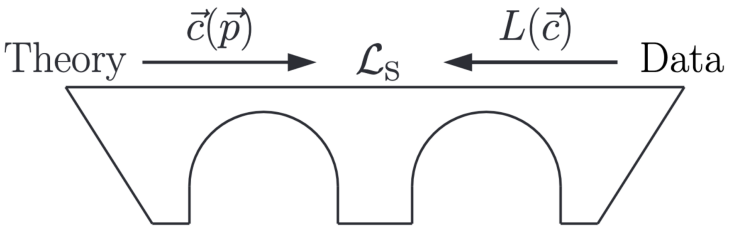

Fig. 5.3 Pictorial view of the HVT bridge method. [59]

constraints on the simplified model parameters $\vec{c}$. Once the experimental constraints on $\vec{c}$ are known they can be translated into the free parameters $\vec{p}$ of any explicit theoretical model by computing their analytic relationship to the simplified model parameters: $\vec{c}(\vec{p})$.

Due to its nature as a simplified model rather than a complete description of Nature, some care must be taken to ensure the HVT model is not applied outside the realm of its validity. Most importantly the HVT model is constructed to only describe *on-shell* resonance production and decay. Thus a corresponding experimental search should only be sensitive to the on-shell process and insensitive to any off-shell effects.

The HVT model Lagrangian is constructed beginning with the SM Lagrangian and incorporating a real vector V_μ^a, $a = 1, 2, 3$, in the adjoint representation of $SU(2)_L$ with vanishing hypercharge. These new additions describe two charged ($V_\mu^\pm$) and one neutral (V_μ^0) heavy spin-one particles with the charge eigenstate fields defined by the following relations:

$$V_\mu^\pm = \frac{V_\mu^1 \mp iV_\mu^2}{\sqrt{2}}, \quad V_\mu^0 = V_\mu^3. \tag{5.2.1}$$

The impact on the choice of model A/B on the branching ratios of the two body decays and total width of the neutral V^0 boson is shown in Figure 5.4.

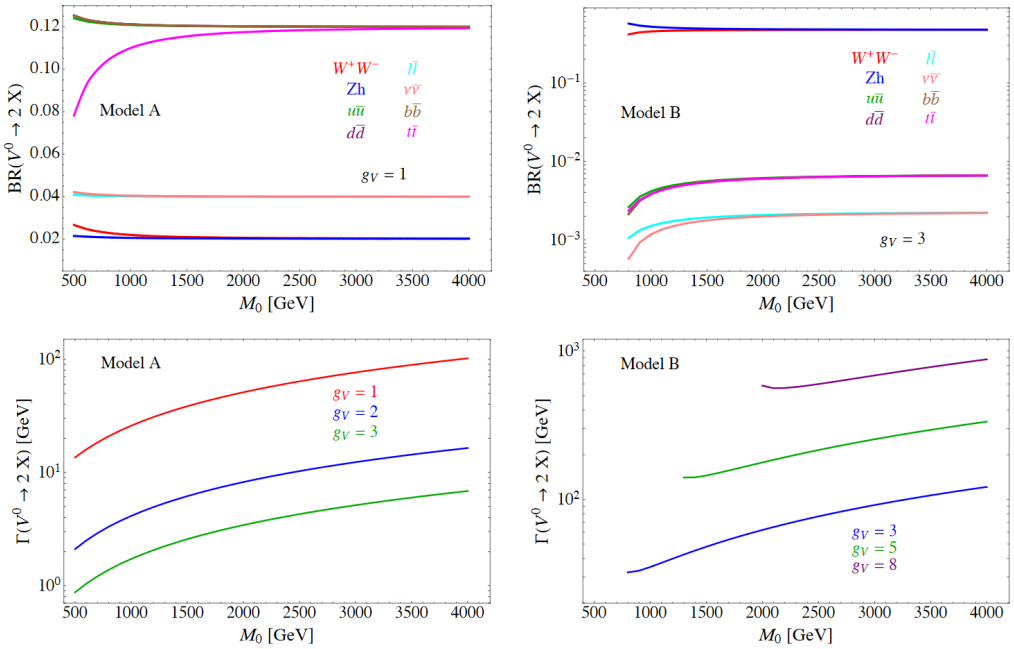

Fig. 5.4 Upper panel: Branching Ratios for the two body decays of the neutral vector V_0 for the benchmark model A with $g_V = 1$ (left) and model B $g_V = 3$ (right). Lower panel: Total widths corresponding to different values of the coupling g_V in the models A (left) and B (right). [59]

5.3 Data and Monte Carlo Simulation

5.3.1 Signal

The Heavy Vector Triplet (HVT) Model A with $g_V = 1$ samples are used as a benchmark model to interpret the results of this analysis. Under the assumption that there are no differences[3] between Model A and Model B in terms of the relevant kinematics of the event, the results interpreted with the Model A samples can be directly translated to Model B by scaling the relevant branching fraction and cross section values. The MC samples are generated at leading order in α_S with MadGraph 5_aMC@NLO 2.2.2 [64] interfaced to Pythia 8.186 [65] for parton shower and hadronization, with the NNPDF23 PDF set [66] and the ATLAS A14 tune [67]. Tables 5.3 and 5.4 show the cross-sections and sample information for the HVT Model A samples, generated at different mass points in the range of 1 to 5 TeV. Only $H \to b\bar{b}$ and $H \to c\bar{c}$ decays are included for the Higgs boson, corresponding to a branching ratio of 0.569 + 0.0287 [68]. Tables 5.3 and 5.4 summarize the properties of the HVT Model A signal samples generated and used for this analysis, while Tables 5.5 and 5.6 describe HVT Model B.

5.3.2 Data

This search is performed with 139 fb^{-1} of $\sqrt{s}$ = 13 TeV data collected by the ATLAS experiment in 2015, 2016, 2017, and 2018 LHC pp runs, in the 25 ns running configuration. Only data selected in the ATLAS good runs lists (GRL) below are used, ensuring that all the relevant elements of the ATLAS detector were fully operational and efficient while the data were collected.

[3]The width of the HVT resonance is dominated entirely by experimental resolution

DSID	Process	Generator	σ [fb]	k-factor	ϵ_{filter}	Events
302321	HVT $W' \to WH \to qq'(b\bar{b} + c\bar{c})$ Model A, m = 1000 GeV	MadGraph v2.2.2 + Pythia v8.186 + EvtGen v1.2.0	4.334e+02	1.0	1.0	110000
302322	HVT $W' \to WH \to qq'(b\bar{b} + c\bar{c})$ Model A, m = 1100 GeV	MadGraph v2.2.2 + Pythia v8.186 + EvtGen v1.2.0	2.901e+02	1.0	1.0	110000
302323	HVT $W' \to WH \to qq'(b\bar{b} + c\bar{c})$ Model A, m = 1200 GeV	MadGraph v2.2.2 + Pythia v8.186 + EvtGen v1.2.0	1.995e+02	1.0	1.0	110000
302324	HVT $W' \to WH \to qq'(b\bar{b} + c\bar{c})$ Model A, m = 1300 GeV	MadGraph v2.2.2 + Pythia v8.186 + EvtGen v1.2.0	1.401e+02	1.0	1.0	95000
302325	HVT $W' \to WH \to qq'(b\bar{b} + c\bar{c})$ Model A, m = 1400 GeV	MadGraph v2.2.2 + Pythia v8.186 + EvtGen v1.2.0	1.002e+02	1.0	1.0	125000
302326	HVT $W' \to WH \to qq'(b\bar{b} + c\bar{c})$ Model A, m = 1500 GeV	MadGraph v2.2.2 + Pythia v8.186 + EvtGen v1.2.0	7.283e+01	1.0	1.0	80000
302327	HVT $W' \to WH \to qq'(b\bar{b} + c\bar{c})$ Model A, m = 1600 GeV	MadGraph v2.2.3 + Pythia v8.186 + EvtGen v1.2.0	5.367e+01	1.0	1.0	110000
302328	HVT $W' \to WH \to qq'(b\bar{b} + c\bar{c})$ Model A, m = 1700 GeV	MadGraph v2.2.2 + Pythia v8.186 + EvtGen v1.2.0	3.999e+01	1.0	1.0	110000
302329	HVT $W' \to WH \to qq'(b\bar{b} + c\bar{c})$ Model A, m = 1800 GeV	MadGraph v2.2.3 + Pythia v8.186 + EvtGen v1.2.0	3.012e+01	1.0	1.0	110000
302330	HVT $W' \to WH \to qq'(b\bar{b} + c\bar{c})$ Model A, m = 1900 GeV	MadGraph v2.2.2 + Pythia v8.186 + EvtGen v1.2.0	2.289e+01	1.0	1.0	70000
302331	HVT $W' \to WH \to qq'(b\bar{b} + c\bar{c})$ Model A, m = 2000 GeV	MadGraph v2.2.2 + Pythia v8.186 + EvtGen v1.2.0	1.753e+01	1.0	1.0	105000
302332	HVT $W' \to WH \to qq'(b\bar{b} + c\bar{c})$ Model A, m = 2200 GeV	MadGraph v2.2.2 + Pythia v8.186 + EvtGen v1.2.0	1.049e+01	1.0	1.0	110000
302333	HVT $W' \to WH \to qq'(b\bar{b} + c\bar{c})$ Model A, m = 2400 GeV	MadGraph v2.2.2 + Pythia v8.186 + EvtGen v1.2.0	6.427e+00	1.0	1.0	110000
302334	HVT $W' \to WH \to qq'(b\bar{b} + c\bar{c})$ Model A, m = 2600 GeV	MadGraph v2.2.2 + Pythia v8.186 + EvtGen v1.2.0	4.008e+00	1.0	1.0	110000
302335	HVT $W' \to WH \to qq'(b\bar{b} + c\bar{c})$ Model A, m = 2800 GeV	MadGraph v2.2.2 + Pythia v8.186 + EvtGen v1.2.0	2.537e+00	1.0	1.0	110000
302336	HVT $W' \to WH \to qq'(b\bar{b} + c\bar{c})$ Model A, m = 3000 GeV	MadGraph v2.2.2 + Pythia v8.186 + EvtGen v1.2.0	1.624e+00	1.0	1.0	50000
302337	HVT $W' \to WH \to qq'(b\bar{b} + c\bar{c})$ Model A, m = 3500 GeV	MadGraph v2.2.2 + Pythia v8.186 + EvtGen v1.2.0	5.534e-01	1.0	1.0	65000
302338	HVT $W' \to WH \to qq'(b\bar{b} + c\bar{c})$ Model A, m = 4000 GeV	MadGraph v2.2.2 + Pythia v8.186 + EvtGen v1.2.0	1.953e-01	1.0	1.0	100000
302339	HVT $W' \to WH \to qq'(b\bar{b} + c\bar{c})$ Model A, m = 4500 GeV	MadGraph v2.2.2 + Pythia v8.186 + EvtGen v1.2.0	7.015e-02	1.0	1.0	80000
302340	HVT $W' \to WH \to qq'(b\bar{b} + c\bar{c})$ Model A, m = 5000 GeV	MadGraph v2.2.2 + Pythia v8.186 + EvtGen v1.2.0	2.543e-02	1.0	1.0	85000

Table 5.3 HVT Model A ($g_V = 1$) WH samples used in the analysis. The dataset ID, MC generator, production cross-sections, k-factor, filter efficiency and total number of generated events are shown.

- `data15_13TeV.periodAllYear_DetStatus-v105-pro22-13_Unknown_PHYS_StandardGRL_All_Good_25ns.xml`
- `data16_13TeV.periodAllYear_DetStatus-v105-pro22-13_Unknown_PHYS_StandardGRL_All_Good_25ns_WITH_IGNORES.xml`
- `data17_13TeV.periodAllYear_DetStatus-v105-pro22-13_Unknown_PHYS_StandardGRL_All_Good_25ns_Triggerno17e33prim.xml`

- `data18_13TeV.periodAllYear_DetStatus-v105-pro22-13_Unknown_PHYS_StandardGRL_All_Good_25ns_Triggerno17e33prim.xml`

Additional quality requirements are applied, as recommended by the ATLAS Data Preparation group. These include the rejection of incomplete events, as well as events with LAr noise bursts and LAr or Tile data corruption.

DSID	Process	Generator	σ [fb]	k-factor	ϵ_{filter}	Events
302371	HVT $Z' \to ZH \to q\bar{q}(b\bar{b} + c\bar{c})$ Model A, m = 1000 GeV	MadGraph v2.2.2 + Pythia v8.186 + EvtGen v1.2.0	2.179e+02	1.0	1.0	50000
302372	HVT $Z' \to ZH \to q\bar{q}(b\bar{b} + c\bar{c})$ Model A, m = 1100 GeV	MadGraph v2.2.3 + Pythia v8.186 + EvtGen v1.2.0	1.446e+02	1.0	1.0	110000
302373	HVT $Z' \to ZH \to q\bar{q}(b\bar{b} + c\bar{c})$ Model A, m = 1200 GeV	MadGraph v2.2.2 + Pythia v8.186 + EvtGen v1.2.0	9.855e+01	1.0	1.0	80000
302374	HVT $Z' \to ZH \to q\bar{q}(b\bar{b} + c\bar{c})$ Model A, m = 1300 GeV	MadGraph v2.2.2 + Pythia v8.186 + EvtGen v1.2.0	6.871e+01	1.0	1.0	70000
302375	HVT $Z' \to ZH \to q\bar{q}(b\bar{b} + c\bar{c})$ Model A, m = 1400 GeV	MadGraph v2.2.2 + Pythia v8.186 + EvtGen v1.2.0	4.881e+01	1.0	1.0	95000
302376	HVT $Z' \to ZH \to q\bar{q}(b\bar{b} + c\bar{c})$ Model A, m = 1500 GeV	MadGraph v2.2.2 + Pythia v8.186 + EvtGen v1.2.0	3.525e+01	1.0	1.0	100000
302377	HVT $Z' \to ZH \to q\bar{q}(b\bar{b} + c\bar{c})$ Model A, m = 1600 GeV	MadGraph v2.2.2 + Pythia v8.186 + EvtGen v1.2.0	2.581e+01	1.0	1.0	55000
302378	HVT $Z' \to ZH \to q\bar{q}(b\bar{b} + c\bar{c})$ Model A, m = 1700 GeV	MadGraph v2.2.3 + Pythia v8.186 + EvtGen v1.2.0	1.913e+01	1.0	1.0	110000
302379	HVT $Z' \to ZH \to q\bar{q}(b\bar{b} + c\bar{c})$ Model A, m = 1800 GeV	MadGraph v2.2.2 + Pythia v8.186 + EvtGen v1.2.0	1.434e+01	1.0	1.0	104000
302380	HVT $Z' \to ZH \to q\bar{q}(b\bar{b} + c\bar{c})$ Model A, m = 1900 GeV	MadGraph v2.2.2 + Pythia v8.186 + EvtGen v1.2.0	1.084e+01	1.0	1.0	95000
302381	HVT $Z' \to ZH \to q\bar{q}(b\bar{b} + c\bar{c})$ Model A, m = 2000 GeV	MadGraph v2.2.2 + Pythia v8.186 + EvtGen v1.2.0	8.271e+00	1.0	1.0	110000
302382	HVT $Z' \to ZH \to q\bar{q}(b\bar{b} + c\bar{c})$ Model A, m = 2200 GeV	MadGraph v2.2.2 + Pythia v8.186 + EvtGen v1.2.0	4.916e+00	1.0	1.0	85000
302383	HVT $Z' \to ZH \to q\bar{q}(b\bar{b} + c\bar{c})$ Model A, m = 2400 GeV	MadGraph v2.2.3 + Pythia v8.186 + EvtGen v1.2.0	2.994e+00	1.0	1.0	110000
302384	HVT $Z' \to ZH \to q\bar{q}(b\bar{b} + c\bar{c})$ Model A, m = 2600 GeV	MadGraph v2.2.2 + Pythia v8.186 + EvtGen v1.2.0	1.859e+00	1.0	1.0	105000
302385	HVT $Z' \to ZH \to q\bar{q}(b\bar{b} + c\bar{c})$ Model A, m = 2800 GeV	MadGraph v2.2.2 + Pythia v8.186 + EvtGen v1.2.0	1.173e+00	1.0	1.0	70000
302386	HVT $Z' \to ZH \to q\bar{q}(b\bar{b} + c\bar{c})$ Model A, m = 3000 GeV	MadGraph v2.2.2 + Pythia v8.186 + EvtGen v1.2.0	7.497e-01	1.0	1.0	90000
302387	HVT $Z' \to ZH \to q\bar{q}(b\bar{b} + c\bar{c})$ Model A, m = 3500 GeV	MadGraph v2.2.2 + Pythia v8.186 + EvtGen v1.2.0	2.554e-01	1.0	1.0	110000
302388	HVT $Z' \to ZH \to q\bar{q}(b\bar{b} + c\bar{c})$ Model A, m = 4000 GeV	MadGraph v2.2.2 + Pythia v8.186 + EvtGen v1.2.0	9.049e-02	1.0	1.0	75000
302389	HVT $Z' \to ZH \to q\bar{q}(b\bar{b} + c\bar{c})$ Model A, m = 4500 GeV	MadGraph v2.2.2 + Pythia v8.186 + EvtGen v1.2.0	3.274e-02	1.0	1.0	100000
302390	HVT $Z' \to ZH \to q\bar{q}(b\bar{b} + c\bar{c})$ Model A, m = 5000 GeV	MadGraph v2.2.2 + Pythia v8.186 + EvtGen v1.2.0	1.198e-02	1.0	1.0	110000

Table 5.4 HVT Model A ($g_V = 1$) ZH samples used in the analysis. The dataset ID, MC generator, production cross-sections, k-factor, filter efficiency and total number of generated events are shown.

The integrated luminosity of the runs is estimated following the methodology described in [69]. This corresponds to an integrated luminosity of 3.2 fb^{-1} in 2015, 33.0 fb^{-1} in 2016, 44.3 fb^{-1} in 2017, and 58.5 fb^{-1} in 2018. The mean number of pp interactions per crossing was not constant for Run-2 and is shown for each data period in Figure 5.5. The mean number of interactions per crossing corresponds to the mean of the poisson distribution of the number of interactions per crossing calculated

DSID	Process	Generator	σ [fb]	k-factor	ϵ_{filter}	Events
302321	HVT $W' \to WH \to qq'(b\bar{b} + c\bar{c})$ Model B, m = 1000 GeV	MadGraph v2.2.2 + Pythia v8.186 + EvtGen v1.2.0	5.016e+02	1.0	1.0	110000
302322	HVT $W' \to WH \to qq'(b\bar{b} + c\bar{c})$ Model B, m = 1100 GeV	MadGraph v2.2.2 + Pythia v8.186 + EvtGen v1.2.0	3.634e+02	1.0	1.0	110000
302323	HVT $W' \to WH \to qq'(b\bar{b} + c\bar{c})$ Model B, m = 1200 GeV	MadGraph v2.2.2 + Pythia v8.186 + EvtGen v1.2.0	2.646e+02	1.0	1.0	110000
302324	HVT $W' \to WH \to qq'(b\bar{b} + c\bar{c})$ Model B, m = 1300 GeV	MadGraph v2.2.2 + Pythia v8.186 + EvtGen v1.2.0	1.943e+02	1.0	1.0	95000
302325	HVT $W' \to WH \to qq'(b\bar{b} + c\bar{c})$ Model B, m = 1400 GeV	MadGraph v2.2.2 + Pythia v8.186 + EvtGen v1.2.0	1.440e+02	1.0	1.0	125000
302326	HVT $W' \to WH \to qq'(b\bar{b} + c\bar{c})$ Model B, m = 1500 GeV	MadGraph v2.2.2 + Pythia v8.186 + EvtGen v1.2.0	1.077e+02	1.0	1.0	80000
302327	HVT $W' \to WH \to qq'(b\bar{b} + c\bar{c})$ Model B, m = 1600 GeV	MadGraph v2.2.3 + Pythia v8.186 + EvtGen v1.2.0	8.128e+01	1.0	1.0	110000
302328	HVT $W' \to WH \to qq'(b\bar{b} + c\bar{c})$ Model B, m = 1700 GeV	MadGraph v2.2.2 + Pythia v8.186 + EvtGen v1.2.0	6.181e+01	1.0	1.0	110000
302329	HVT $W' \to WH \to qq'(b\bar{b} + c\bar{c})$ Model B, m = 1800 GeV	MadGraph v2.2.3 + Pythia v8.186 + EvtGen v1.2.0	4.733e+01	1.0	1.0	110000
302330	HVT $W' \to WH \to qq'(b\bar{b} + c\bar{c})$ Model B, m = 1900 GeV	MadGraph v2.2.2 + Pythia v8.186 + EvtGen v1.2.0	3.648e+01	1.0	1.0	70000
302331	HVT $W' \to WH \to qq'(b\bar{b} + c\bar{c})$ Model B, m = 2000 GeV	MadGraph v2.2.2 + Pythia v8.186 + EvtGen v1.2.0	2.827e+01	1.0	1.0	105000
302332	HVT $W' \to WH \to qq'(b\bar{b} + c\bar{c})$ Model B, m = 2200 GeV	MadGraph v2.2.2 + Pythia v8.186 + EvtGen v1.2.0	1.723e+01	1.0	1.0	110000
302333	HVT $W' \to WH \to qq'(b\bar{b} + c\bar{c})$ Model B, m = 2400 GeV	MadGraph v2.2.2 + Pythia v8.186 + EvtGen v1.2.0	1.067e+01	1.0	1.0	110000
302334	HVT $W' \to WH \to qq'(b\bar{b} + c\bar{c})$ Model B, m = 2600 GeV	MadGraph v2.2.2 + Pythia v8.186 + EvtGen v1.2.0	6.689e+00	1.0	1.0	110000
302335	HVT $W' \to WH \to qq'(b\bar{b} + c\bar{c})$ Model B, m = 2800 GeV	MadGraph v2.2.2 + Pythia v8.186 + EvtGen v1.2.0	4.234e+00	1.0	1.0	110000
302336	HVT $W' \to WH \to qq'(b\bar{b} + c\bar{c})$ Model B, m = 3000 GeV	MadGraph v2.2.2 + Pythia v8.186 + EvtGen v1.2.0	2.698e+00	1.0	1.0	50000
302337	HVT $W' \to WH \to qq'(b\bar{b} + c\bar{c})$ Model B, m = 3500 GeV	MadGraph v2.2.2 + Pythia v8.186 + EvtGen v1.2.0	8.918e-01	1.0	1.0	65000
302338	HVT $W' \to WH \to qq'(b\bar{b} + c\bar{c})$ Model B, m = 4000 GeV	MadGraph v2.2.2 + Pythia v8.186 + EvtGen v1.2.0	2.969e-01	1.0	1.0	100000
302339	HVT $W' \to WH \to qq'(b\bar{b} + c\bar{c})$ Model B, m = 4500 GeV	MadGraph v2.2.2 + Pythia v8.186 + EvtGen v1.2.0	9.789e-02	1.0	1.0	80000
302340	HVT $W' \to WH \to qq'(b\bar{b} + c\bar{c})$ Model B, m = 5000 GeV	MadGraph v2.2.2 + Pythia v8.186 + EvtGen v1.2.0	3.149e-02	1.0	1.0	85000

Table 5.5 HVT Model B ($g_V = 3$) WH samples used in the analysis. The dataset ID, MC generator, production cross-sections, k-factor, filter efficiency and total number of generated events are shown.

for each bunch. It is calculated from the instantaneous per bunch luminosity as $\mu = L_{\text{bunch}}\sigma_{\text{inel}}/f_r$ where L_{bunch} is the mean per bunch instantaneous luminosity, σ_{inel} is the inelastic cross section which we take to be 80 mb for 13 TeV collisions, and f_r is the LHC revolution frequency. The luminosity shown represents the initial 13 TeV luminosity estimate and includes all 13 TeV pp data recorded up to 2018.

DSID	Process	Generator	σ [fb]	k-factor	ϵ_{filter}	Events
302371	HVT $Z' \to ZH \to q\bar{q}(b\bar{b} + c\bar{c})$ Model B, m = 1000 GeV	MadGraph v2.2.2 + Pythia v8.186 + EvtGen v1.2.0	2.641e+02	1.0	1.0	50000
302372	HVT $Z' \to ZH \to q\bar{q}(b\bar{b} + c\bar{c})$ Model B, m = 1100 GeV	MadGraph v2.2.3 + Pythia v8.186 + EvtGen v1.2.0	1.888e+02	1.0	1.0	110000
302373	HVT $Z' \to ZH \to q\bar{q}(b\bar{b} + c\bar{c})$ Model B, m = 1200 GeV	MadGraph v2.2.2 + Pythia v8.186 + EvtGen v1.2.0	1.358e+02	1.0	1.0	80000
302374	HVT $Z' \to ZH \to q\bar{q}(b\bar{b} + c\bar{c})$ Model B, m = 1300 GeV	MadGraph v2.2.2 + Pythia v8.186 + EvtGen v1.2.0	9.864e+01	1.0	1.0	70000
302375	HVT $Z' \to ZH \to q\bar{q}(b\bar{b} + c\bar{c})$ Model B, m = 1400 GeV	MadGraph v2.2.2 + Pythia v8.186 + EvtGen v1.2.0	7.236e+01	1.0	1.0	95000
302376	HVT $Z' \to ZH \to q\bar{q}(b\bar{b} + c\bar{c})$ Model B, m = 1500 GeV	MadGraph v2.2.2 + Pythia v8.186 + EvtGen v1.2.0	5.359e+01	1.0	1.0	100000
302377	HVT $Z' \to ZH \to q\bar{q}(b\bar{b} + c\bar{c})$ Model B, m = 1600 GeV	MadGraph v2.2.2 + Pythia v8.186 + EvtGen v1.2.0	4.006e+01	1.0	1.0	55000
302378	HVT $Z' \to ZH \to q\bar{q}(b\bar{b} + c\bar{c})$ Model B, m = 1700 GeV	MadGraph v2.2.3 + Pythia v8.186 + EvtGen v1.2.0	3.020e+01	1.0	1.0	110000
302379	HVT $Z' \to ZH \to q\bar{q}(b\bar{b} + c\bar{c})$ Model B, m = 1800 GeV	MadGraph v2.2.2 + Pythia v8.186 + EvtGen v1.2.0	2.292e+01	1.0	1.0	104000
302380	HVT $Z' \to ZH \to q\bar{q}(b\bar{b} + c\bar{c})$ Model B, m = 1900 GeV	MadGraph v2.2.2 + Pythia v8.186 + EvtGen v1.2.0	1.752e+01	1.0	1.0	95000
302381	HVT $Z' \to ZH \to q\bar{q}(b\bar{b} + c\bar{c})$ Model B, m = 2000 GeV	MadGraph v2.2.2 + Pythia v8.186 + EvtGen v1.2.0	1.348e+01	1.0	1.0	110000
302382	HVT $Z' \to ZH \to q\bar{q}(b\bar{b} + c\bar{c})$ Model B, m = 2200 GeV	MadGraph v2.2.2 + Pythia v8.186 + EvtGen v1.2.0	8.102e+00	1.0	1.0	85000
302383	HVT $Z' \to ZH \to q\bar{q}(b\bar{b} + c\bar{c})$ Model B, m = 2400 GeV	MadGraph v2.2.3 + Pythia v8.186 + EvtGen v1.2.0	4.958e+00	1.0	1.0	110000
302384	HVT $Z' \to ZH \to q\bar{q}(b\bar{b} + c\bar{c})$ Model B, m = 2600 GeV	MadGraph v2.2.2 + Pythia v8.186 + EvtGen v1.2.0	3.078e+00	1.0	1.0	105000
302385	HVT $Z' \to ZH \to q\bar{q}(b\bar{b} + c\bar{c})$ Model B, m = 2800 GeV	MadGraph v2.2.2 + Pythia v8.186 + EvtGen v1.2.0	1.934e+00	1.0	1.0	70000
302386	HVT $Z' \to ZH \to q\bar{q}(b\bar{b} + c\bar{c})$ Model B, m = 3000 GeV	MadGraph v2.2.2 + Pythia v8.186 + EvtGen v1.2.0	1.226e+00	1.0	1.0	90000
302387	HVT $Z' \to ZH \to q\bar{q}(b\bar{b} + c\bar{c})$ Model B, m = 3500 GeV	MadGraph v2.2.2 + Pythia v8.186 + EvtGen v1.2.0	4.046e-01	1.0	1.0	110000
302388	HVT $Z' \to ZH \to q\bar{q}(b\bar{b} + c\bar{c})$ Model B, m = 4000 GeV	MadGraph v2.2.2 + Pythia v8.186 + EvtGen v1.2.0	1.369e-01	1.0	1.0	75000
302389	HVT $Z' \to ZH \to q\bar{q}(b\bar{b} + c\bar{c})$ Model B, m = 4500 GeV	MadGraph v2.2.2 + Pythia v8.186 + EvtGen v1.2.0	4.673e-02	1.0	1.0	100000
302390	HVT $Z' \to ZH \to q\bar{q}(b\bar{b} + c\bar{c})$ Model B, m = 5000 GeV	MadGraph v2.2.2 + Pythia v8.186 + EvtGen v1.2.0	1.589e-02	1.0	1.0	110000

Table 5.6 HVT Model B ($g_V = 3$) ZH samples used in the analysis. The dataset ID, MC generator, production cross-sections, k-factor, filter efficiency and total number of generated events are shown.

5.3.3 Backgrounds

The dominant contribution to the background in this search originates from dijet QCD processes and contributes approximately 92-98% of the total background yield depending on the region under consideration, as shown in Table 5.17. QCD MC samples do not have enough enough events in the high mass region to model this

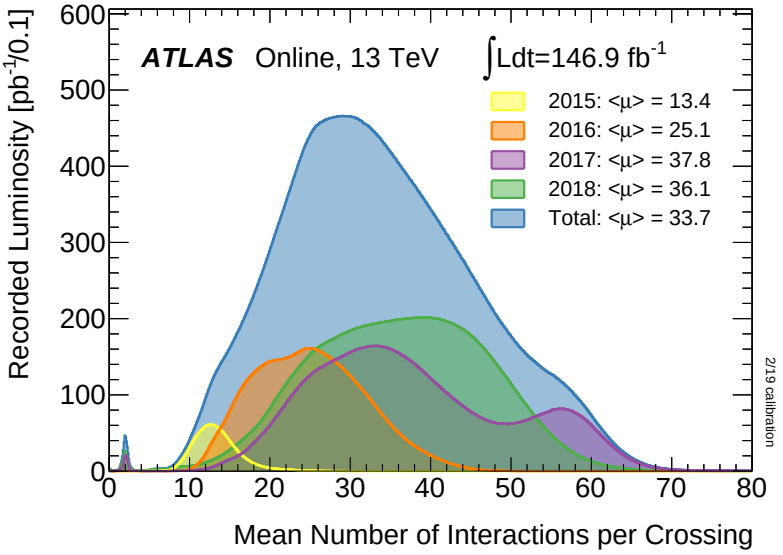

Fig. 5.5 Shown is the luminosity-weighted distribution of the mean number of interactions per crossing for the 2015-2018 pp collision data at 13 TeV centre-of-mass energy. All data recorded by ATLAS during stable beams is shown, and the integrated luminosity and the mean mu value are given in the figure. © 2019 CERN

process in the regions of interest, especially given the high background rejection that is achieved with the V and H tagging techniques. Therefore, the multijet background is estimated from data, in order to avoid problems associated with theoretical mismodelling and low statistics.

Other contributions to the background composition come primarily from $t\bar{t}$ and V+jets, totaling from 2 to 10% of the background, depending on the region. Since the background prediction is fully data-driven, these MC samples are only used for a limited set of studies. Standard Model VV, VH and $H \to gg$ contributions are considered negligible.

5.3.3.1 QCD

For studies with simulated QCD events, the nominal MC samples used are generated with PYTHIA 8.186, with the NNPDF23LO PDF and the ATLAS A14 tune for the

underlying event. Events are generated in bins of p_T of anti-k_T R=0.6 truth jets, as listed in Table 5.7.

DSID	Process	Generator	$\sigma \times$ BR [fb]	k-factor	ϵ_{filter}	Events
361023	JZ3W $160 < p_T^{jet} < 400$ GeV	Pythia v8.186 + EvtGen v1.2.0	2.645e+10	1.0	0.00032012	31758000
361024	JZ4W $400 < p_T^{jet} < 800$ GeV	Pythia v8.186 + EvtGen v1.2.0	2.546e+08	1.0	0.00053137	31900000
361025	JZ5W $800 < p_T^{jet} < 1300$ GeV	Pythia v8.186 + EvtGen v1.2.0	4.554e+06	1.0	0.00092395	31985000
361026	JZ6W $1300 < p_T^{jet} < 1800$ GeV	Pythia v8.186 + EvtGen v1.2.0	2.575e+05	1.0	0.0009427	35714400
361027	JZ7W $1800 < p_T^{jet} < 2500$ GeV	Pythia v8.186 + EvtGen v1.2.0	1.622e+04	1.0	0.0003928	31099500
361028	JZ8W $2500 < p_T^{jet} < 3200$ GeV	Pythia v8.186 + EvtGen v1.2.0	6.250e+02	1.0	0.010176	31986000
361029	JZ9W $3200 < p_T^{jet} < 3900$ GeV	Pythia v8.186 + EvtGen v1.2.0	1.964e+01	1.0	0.012077	28507000
361030	JZ10W $3900 < p_T^{jet} < 4600$ GeV	Pythia v8.186 + EvtGen v1.2.0	1.196e+00	1.0	0.0059083	29973000
361031	JZ11W $4600 < p_T^{jet} < 5300$ GeV	Pythia v8.186 + EvtGen v1.2.0	4.226e-02	1.0	0.0026761	31941000
361032	JZ12W $p_T^{jet} > 5300$ GeV	Pythia v8.186 + EvtGen v1.2.0	1.037e-03	1.0	0.00042592	31635600

Table 5.7 Nominal QCD weighted (JZXW) simulated samples used in the analysis. The dataset ID, MC generator, production cross-sections, k-factor, filter efficiency and total number of generated events are shown.

5.3.3.2 V+jets

The W+jets and Z+jets events are generated with Sherpa 2.1.1 [70] interfaced with the CT10 PDF set [71]. Matrix elements of up to 4 extra partons are calculated at next-to-leading order in α_S. Only the hadronic decays of the W and Z are included. The samples are split by boson p_T, as listed in Table 5.8.

5.3.3.3 $t\bar{t}$

The $t\bar{t}$ samples are generated with Powheg-Box v2 [72] with the NNPDF30 PDF, interfaced with Pythia 8 with NNPDF23 PDF and A14 tune for parton shower. EvtGen v1.2.0 [73] is used for properties of bottom and charm hadron decays. In

DSID	Process	Generator	$\sigma \times$ BR [fb]	k-factor	ϵ_{filter}	Events
304307	$W \to q\bar{q}' + 0,1,2,3,4$ partons $280 < p_T^W < 500$ GeV	SHERPA v2.1.1	2.949e+04	1.0	1.0	490000
304308	$W \to q\bar{q}' + 0,1,2,3,4$ partons $500 < p_T^W < 1000$ GeV	SHERPA v2.1.1	2.164e+03	1.0	1.0	170000
304309	$W \to q\bar{q}' + 0,1,2,3,4$ partons $p_T^W > 1000$ GeV	SHERPA v2.1.1	4.609e+01	1.0	1.0	115000
304707	$Z \to q\bar{q} + 0,1,2,3,4$ partons $280 < p_T^Z < 500$ GeV	SHERPA v2.1.1	1.262e+04	1.0	1.0	250000
304708	$Z \to q\bar{q} + 0,1,2,3,4$ partons $500 < p_T^Z < 1000$ GeV	SHERPA v2.1.1	9.027e+02	1.0	1.0	144000
304709	$Z \to q\bar{q} + 0,1,2,3,4$ partons $p_T^Z > 1000$ GeV	SHERPA v2.1.1	1.823e+01	1.0	1.0	90000

Table 5.8 W+jets and Z+jets samples used in the analysis. The dataset ID, MC generator, production cross-sections, k-factor, filter efficiency and total number of generated events are shown.

order to keep statistical fluctuations small across the dijet mass spectrum, additional $t\bar{t}$ samples are used which are generated in slices of $t\bar{t}$ invariant mass, starting from 1.1 TeV. Double-counting is avoided by explicitly cutting out events in the inclusive sample that have a $t\bar{t}$ mass greater than 1.1 TeV. The samples are listed in Tables 5.9 and 5.10. The cross-section of the $t\bar{t}$ process is normalized to NNLO+NNLL in QCD, as calculated by TOP++ 2.0 [74]. The POWHEG HDAMP parameter [75] is set to 1.5 times the top mass.

DSID	Process	Generator	$\sigma \times$ BR [fb]	k-factor	ϵ_{filter}	Events
410471	all-hadronic $t\bar{t}$	POWHEG + PYTHIA v8.230 + EvtGen v1.6.0	7.298e+05	1.0	0.45623	109738000

Table 5.9 The $t\bar{t}$ inclusive sample used in the analysis. The dataset ID, MC generator, production cross-sections, k-factor, filter efficiency and total number of generated events are shown.

DSID	Process	Generator	$\sigma \times$ BR [fb]	k-factor	ϵ_{filter}	Events
410284	all-hadronic $t\bar{t}$ $1.1 < m_{t\bar{t}} < 1.3$ TeV	POWHEG + PYTHIA v8.230 + EvtGen v1.6.0	7.298e+05	1.0	0.0038853	2045000
410285	all-hadronic $t\bar{t}$ $1.3 < m_{t\bar{t}} < 1.5$ TeV	POWHEG + PYTHIA v8.230 + EvtGen v1.6.0	7.298e+05	1.0	0.0015782	777000
410286	all-hadronic $t\bar{t}$ $1.5 < m_{t\bar{t}} < 1.7$ TeV	POWHEG + PYTHIA v8.230 + EvtGen v1.6.0	7.298e+05	1.0	0.00069112	389300
410287	all-hadronic $t\bar{t}$ $1.7 < m_{t\bar{t}} < 2.0$ TeV	POWHEG + PYTHIA v8.230 + EvtGen v1.6.0	7.298e+05	1.0	0.00042428	335740
410288	all-hadronic $t\bar{t}$ $2.0 < m_{t\bar{t}} < 14$ TeV	POWHEG + PYTHIA v8.230 + EvtGen v1.6.0	7.298e+05	1.0	0.00023803	187700

Table 5.10 Additional $t\bar{t}$ samples used in the analysis. The dataset ID, MC generator, production cross-sections, k-factor, filter efficiency and total number of generated events are shown.

5.4 Object Selection

5.4.1 Large Radius Jets

In order to identify and reconstruct potential vector boson and Higgs boson candidates, large radius parameter ("large-R") jets are used. In prior years the de facto jet algorithm in this circumstance was the anti-k_T algorithm with a radius parameter of $R = 1.0$ utilizing locally weighted topological cell clusters (LCTopo) [76] for constituents. A new jet type of jet constituent known as Track-CaloCluster (TCC) has been developed [42] which combines calorimeter and tracking data in such a way as to leverage the most performant aspects of both. In practice TCC jets exploit the superior spatial resolution of the tracker and the energy measurement of the calorimeter. This approach is particularly beneficial for recovering angular information from highly boosted jet constituents that would otherwise merge and be lost due to the resolution limitations when using the calorimeter alone. A comparison of jet mass and D_2 resolution is shown in Figure 5.6. For these reasons TCC jets are used in this analysis rather than LCTopo. Refer to Section 4.1 for more details.

Pileup dependence is significantly negated by jet trimming [77] with parameters $f_{\text{cut}} = 0.05$ and $R_{\text{sub}} = 0.2$, as described in Section 4.4. A Monte Carlo based particle-level calibration is applied to the jets used in this analysis, which corrects on average the reconstructed mass and p_T of the jets to their true values, as described in Section 4.3.

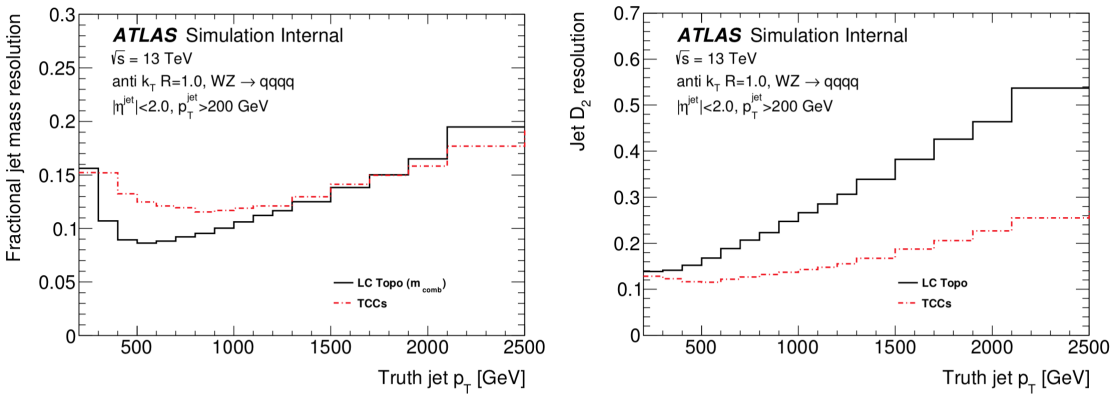

(a) (b)

Fig. 5.6 A comparison of the fractional jet (a) mass and (b) D_2 resolution for LCTopo (solid black lines) and TCC (dashed red lines) as a function of truth jet p_T. © CERN

All large-R jets are required to have a p_T of at least 200 GeV in order to ensure they fall within the region of phase space where the jet calibration is well understood. Furthermore, each large-R jet is required to have $|\eta| < 2.0$ to ensure that the track-jets associated with it are contained within the ID acceptance. The leading large-R jet must also have a p_T greater than 500 GeV, ensuring that the large-R jet is in the trigger efficiency plateau for triggers used in 2015, 2016, 2017, and 2018 datasets. The large-R jet reconstruction, calibration, and selection parameters are summarized in Table 5.11.

Parameter	Value
Algorithm	anti-k_T
Radius	1.0
Constituent Type	TrackCaloClusters
Grooming Algorithm	Trimming ($f_{\text{cut}} = 0.05, R_{\text{trim}} = 0.2$)
Calibration Sequence	η + JES + JMS
p_T Cut	> 500 GeV (leading), > 200 GeV (sub-leading)
$\lvert\eta\rvert$ Cut	< 2.0

Table 5.11 Summary of jet reconstruction and selection parameters for this analysis.

5.4.2 Track-jets

Track-jets are built by clustering Inner Detector tracks using the anti-k_T algorithm. All tracks used are required to be associated with the primary vertex of the event, defined as the vertex with the largest $\sum p_T^2$. The selected tracks are required to have p_T greater than 500 MeV and pass the "Loose" tracking quality cuts. In this analysis the variable-radius track jet collection is used, where the radius parameter is a function of the jet p_T as $R = \rho/p_T$. The parameter ρ is set to 30 GeV, and the minimum and maximum values for the radius are set to 0.02 and 0.4, respectively [48].

When compared to calorimeter jets, the smaller R parameters in track-jets coupled with the fact that tracks have better angular resolution than calorimeter clusters, mean that the decay products of highly boosted heavy objects can still be resolved. After clustering, track-jets are then associated to the large-R calorimeter jets via ghost-association [78], a procedure that treats them as four-vectors of infinitesimal magnitude during the jet reconstruction and assigns them to the jet with which they are clustered.

A b-tagging algorithm is used to identify track-jets which are likely to contain b-hadrons from the Higgs boson decay. The MV2 algorithms exploit the relatively

long lifetime and large mass of b-hadrons with respect to lighter hadrons, as well as the kinematics of the charged particle tracks.

Optimization studies were performed in order to determine the best b-tagging algorithm and working point for this search. The MV2c10 algorithm is used with the 77% fixed efficiency working point, as measured from b jets in $t\bar{t}$ events, which corresponds to a background rejection of $1/5$ for c jets and $1/112$ for light jets.

5.4.3 Leptons

Based on the lepton veto applied in the ATLAS $Z' \to ZH \to \nu\bar{\nu}b\bar{b}$ analysis, events with at least one loose lepton are rejected. Loose muons are required to have $p_T > 7$ GeV and fall in the central region of the detector ($|\eta| < 2.5$). They are identified with the "loose" quality working point. Track quality requirements are applied such that $|d_0/\sigma(d_0)| < 3$ and $|z_0 \sin\theta| < 0.5$ mm, where d_0 and z_0 are the transverse and longitudinal track impact parameters. Loose electrons are also required to have $p_T > 7$ GeV, with a pseudorapidity requirement such that $|\eta| < 2.47$. As with muons, requirements on the transverse and longitudinal impact parameters of the associated tracks are made. In terms of isolation, both loose electrons and loose muons are required to be "LooseTrackOnly", where a cone with radius $r(p_T^\ell) = \min(0.2, 10\text{ GeV}/p_T^\ell)$ (0.3 for muons) is constructed around each lepton and for which the p_T-sum of all tracks with $p_T > 500$ MeV defines the isolation I_ℓ. A cut on $I_\ell/p_T^\ell < I_0$ is imposed, and I_0 is such that a flat efficiency of 99% as a function of p_T and η is obtained for lepton candidates in $Z \to \ell\ell$ events.

5.5 Event Selection

5.5.1 Pre-Selection

5.5.1.1 EXOT3 Derivation: xAOD → DxAOD

All data and MC samples are initially produced in xAOD format. In order to reduce the file size of these samples, the derivation framework is used to remove both objects and entire events of no interest to the analysis. The EXOT3 derivation is used[4]. Beyond reducing file size, the derivation is also responsible for the production of nonstandard jet collections, such as the fat jet collections needed for this analysis.

A *slimming* procedure is applied in order to remove all but the essential variables for calibration of the following objects:

- `Electrons`
- `Muons`
- `MET_Reference_AntiKt4LCTopo`
- `InDetTrackParticles`
- `PrimaryVertices`
- `AntiKt4EMTopoJets`

A *thinning* procedure is applied in order to remove some objects based on the following criteria:

- `InDetTrackParticles`: must be associated with
  - An electron

[4] `https://gitlab.cern.ch/atlas/athena/blob/21.2/PhysicsAnalysis/DerivationFramework/DerivationFrameworkExotics/share/EXOT3.py`

  - A muon
  - An AntiKt10LCTopoJet with p_T> 150 GeV and $|\eta|$< 2.8.
  - An AntiKt10TrackCaloCluster jet

- `LCOriginTopoClusters`: must be associated with
  - An AntiKt10LCTopoJet with p_T> 150 GeV and $|\eta|$< 2.8.
  - An AntiKt10TrackCaloCluster jet

A *skimming* procedure is also applied to remove entire events from the xAOD with the following criteria:

- Topological large-R jet selection
  - >2 calibrated offline AntiKt10LCTopoTrimmedPtFrac5SmallR20Jets jets with
    * p_T > 100 GeV
    * $|\eta|$ < 2.8
    * m > 30 GeV for jets with $p_T < 1.0\ TeV$
- Events must be required to pass one of a long list of jet-related ATLAS triggers.

In total the combined EXOT3 skimming, thinning, and slimming reduces the file size to 2% of the original size for data.

5.5.1.2 Event Cleaning

Non-collision backgrounds originating from calorimeter noise, beam halo interactions or cosmic rays can lead to spurious calorimeter signals and the reconstruction of "bad" jets. This effect can be suppressed by applying a standard jet cleaning procedure, which has been developed for 2015 data to reject jets based on their shape and timing

information [79] . Events are rejected if they contain at least one small radius jet (anti-k_T, with $R = 0.4$) classified as "bad-loose" by the aforementioned jet cleaning criteria. Additional vetos are applied to reject events where Tile or LAr calorimeter errors occur, as well as single event upsets in the SCT. These cuts are applied by accessing information via special flags recorded by each subdetector on a per-event basis. Incomplete events are also flagged and rejected by inspecting similar flags. Events are also required to have at least one primary vertex with at least two tracks.

Due to the nature of the VR track jet reconstruction it is possible for one VR track jet (i) to be fully contained within another (j) in terms of their angular separation. This overlap condition can be expressed with the following inequality:

$$\Delta R(i, j) < \min(R_i, R_j) \tag{5.5.1}$$

Any VR track jets matching this criterion are removed from consideration. This prevents the utilization of track jets with an ambiguous association of tracks for b-tagging, because in these cases it is likely that the b-tagging calibration scale factors are not correct. See Figure 5.7 for an illustration of this phenomenon.

5.5.2 Trigger Requirements

For the analysis of the 2015 dataset, a high p_T, unprescaled large-R jet trigger is used to trigger events: HLT_j360_a10_lcw_sub_L1J100. During the 2016 data taking, given the increase in instantaneous luminosity, the trigger with a higher threshold is used: HLT_j420_a10r_L1J100. For the 2017 and 2018 datasets an even higher threshold is used: HLT_j460_a10t_lcw_jes_L1J100. The 2015/2016 triggers listed above fire on the untrimmed jet p_T, while the 2017/2018 trigger fires on the trimmed jet p_T and applies a subsequent jet energy scale calibration.

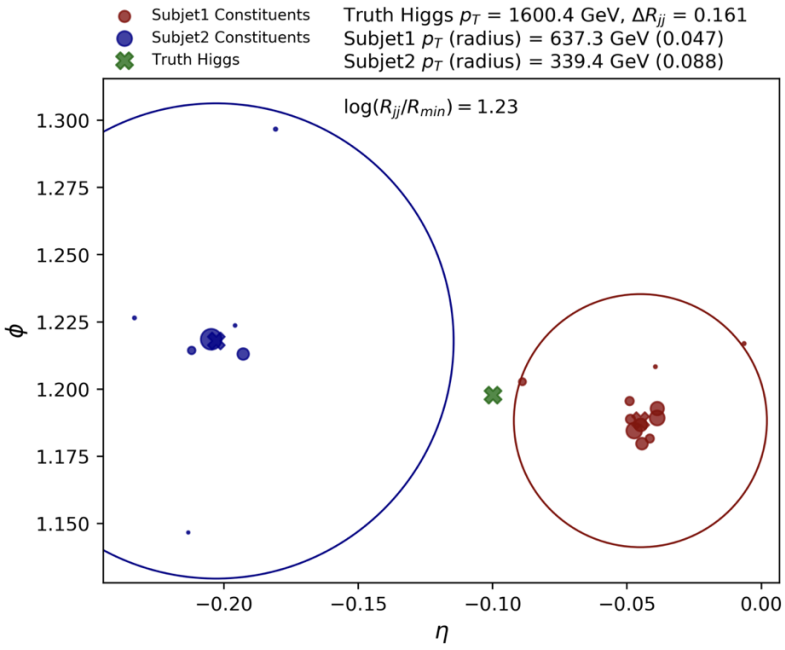

(a)

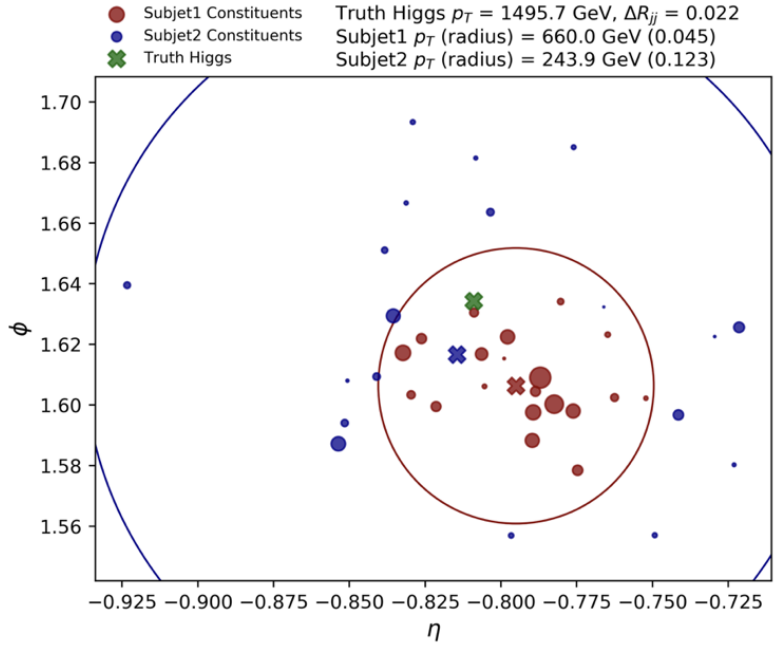

(b)

Fig. 5.7 $\eta - \phi$ distribution (from simulation) of constituents of the two leading p_T VR track jets ghost associated to a truth large-R Higgs jet. Two illustrative cases are shown: (a) clean separation of track jet constituents and (b) pathological overlap. The radii of the filled red/blue circles are proportional to log p_T of the corresponding track jet constituent.

For all datasets the offline selection is chosen to produce nearly 100% efficiency. No trigger-related scale factors are needed in MC simulation to match the efficiency obtained in data. The efficiency of the relevant triggers as a function of leading large-R jet p_T are shown in Figure 5.8.

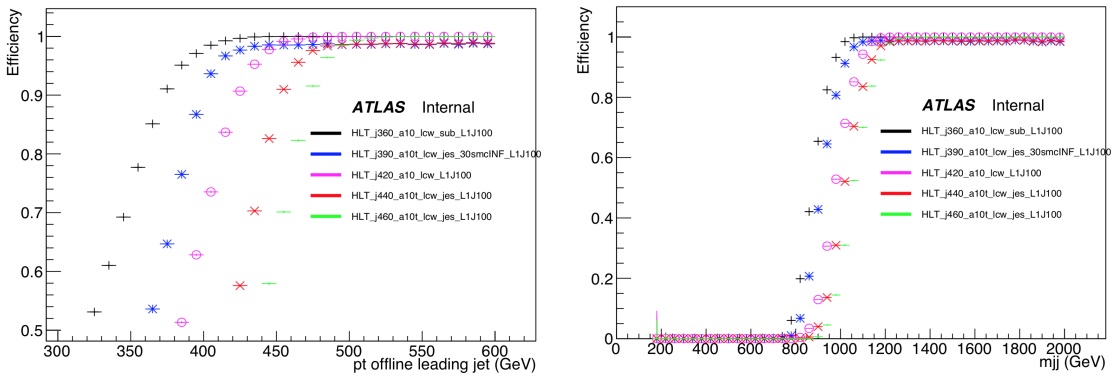

Fig. 5.8 The efficiency of a range of HLT large-R jet triggers as a function of the leading large-R jet p_T (left) and dijet mass (right). The dijet mass (right) plot is produced after applying a flat leading jet p_T cut of 500 GeV. © CERN

5.5.2.1 Jet Selection

At least two large-R jets are required to be present in the event which pass the kinematic cuts explained in Section 5.4. In order to ensure full trigger efficiency, a cut of 500 GeV is placed on the leading large-R jet p_T along with a cut on the dijet mass (m_{JJ}> 1.3 TeV). The two leading jets in the event will correspond to a vector boson and a Higgs boson candidate, the assignment of which is made based on their invariant masses: the heaviest jet is chosen as the Higgs candidate and the lightest as the W/Z candidate. The remaining H or W/Z specific cuts described below apply to each jet according to this assignment. Figure 5.9 shows the fraction of events that are correctly matched with this V/H assignment, by checking that the jets chosen for vector and Higgs boson candidates match the truth-level bosons in the signal samples, as a function of the resonance mass. The truth matching requirement is

defined as $\Delta R < 1.0$ between the untrimmed parent of the reconstructed large radius jet and the truth boson.

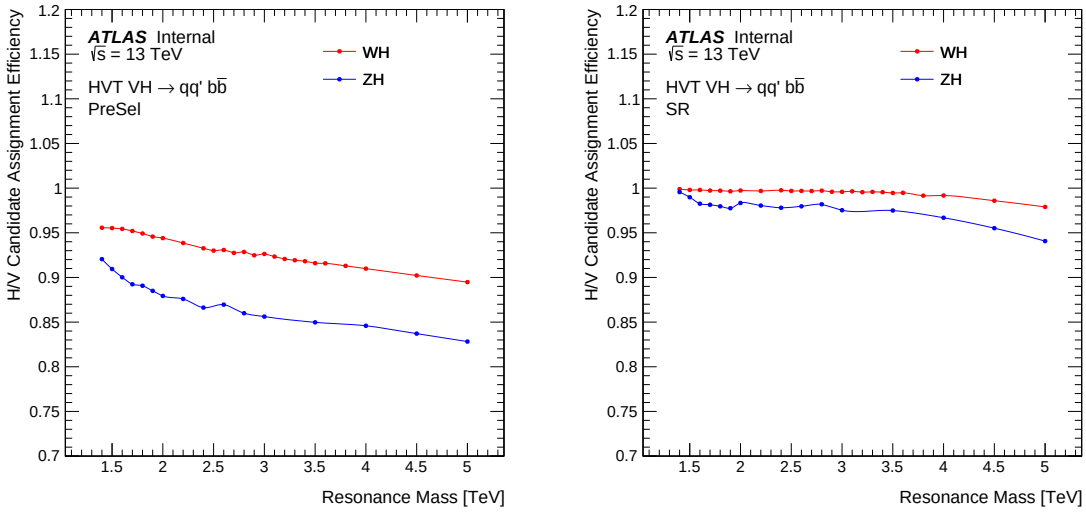

Fig. 5.9 Fraction of correct V/H assignments for TCC large-R jets based on the V/H assignment criteria described in the text, for WH and ZH signal samples, as a function of the resonance mass. Loose pre-selection is used on the left while the combined SRWH/SRZH selection is shown on the right. The difference in efficiency for WH vs. ZH final states is due to the closer proximity of the Higgs and Z boson masses, which produces more overlap between the optimized mass windows (see Figures 5.18 and 5.19).

5.5.2.2 Dijet Mass

The dijet mass of the VH system, labelled m_{JJ} or m_{VH} in this analysis, is required to be greater than 1.3 TeV in order to ensure full trigger efficiency. A comparison of simulated background and signal distributions for m_{JJ} can be found in Figure 5.10.

5.5.2.3 Rapidity Difference

Due to their exclusive s-channel production, signal $W' \to WH$ and $Z' \to ZH$ events are expected to be more centrally produced than QCD dijet events, resulting in a rapidity difference (Δy_{12}) between the two leading large-R jets which peaks near 0

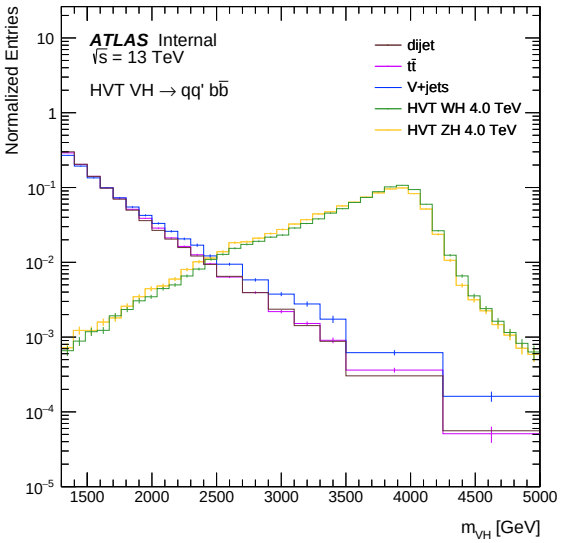

Fig. 5.10 Dijet mass m_{JJ}, as measured in signal and background MC samples, normalized to unity. Only pre-selection is applied, as described in Section 5.5.1.

(see Figure 5.11). Leading jets in this analysis are therefore required to have a small rapidity separation. A fixed cut of $|\Delta y_{12}| < 1.6$ is applied. A comparison of simulated background and signal distributions for Δy_{12} can be found in Figure 5.11.

The sequence of cuts applied and their corresponding efficiencies in data for all elements of the pre-selection data can be found in Table 5.12.

Selection	Data	Efficiency [%]	Total Efficiency [%]
EXOT3	505568676	–	–
GRL + EventCleaning	483433031	95.62	95.62
Jet Cleaning	477623453	98.80	94.47
Trigger	128220751	26.85	25.36
Jet multiplicity	128136392	99.93	25.35
Fatjet EtaPtPreSel	106779224	83.33	21.12
Lead Jet pT	52157511	48.85	10.32
mVH	23981560	45.98	4.74
DeltaY	12497837	52.11	2.47
VR Subjet Overlap Removal	11982215	95.87	2.37

Table 5.12 Preselection cutflow for a subset of Run 2 data. The second column (Efficiency) represents the efficiency relative to the previous cut. The third column (Total Efficiency) represents the cumulative efficiency of all previous cuts.

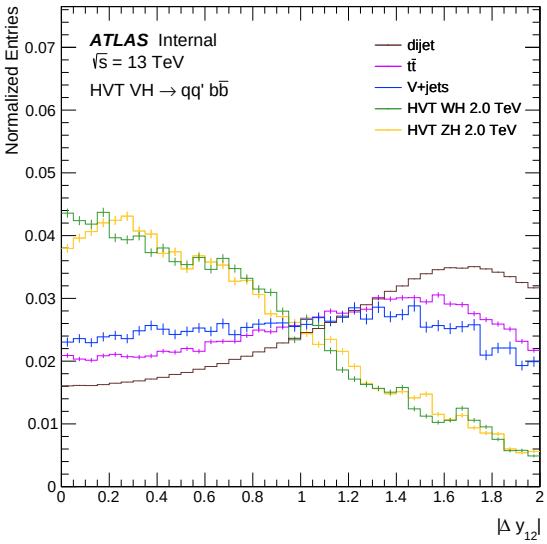

Fig. 5.11 Distributions of the rapidity difference between the two leading p_T large-R jets, as measured in signal and background MC samples, normalized to unity. Only pre-selection is applied, as described in Section 5.5.1.

5.5.3 Boson Tagging

The successful identification of $H \to b\bar{b}$ and hadronically decaying W/Z bosons, as well as the simultaneous rejection of multijet background, relies on additional properties of the H/V candidate large-R jets. These properties are described below along with the tagging optimization method.

- Significant discrimination with minimal signal loss can be achieved by selecting a **jet mass** region around the resonant peak for each of the three relevant bosons. See Figures 5.12 and 5.13.

- D_2 (W/Z tagging only) Jets that correspond to a hadronically decaying boson typically exhibit a two-prong structure, while QCD jets tend to exhibit a more diffuse or one-prong structure. The D_2 **substructure** variable used in this search to discriminate such structure is defined as a ratio of so-called *energy*

correlation functions [54] built from sums over the large-R jet constituent four-momenta. See Figure 5.14. The D_2 variable provides very little additional sensitivity gain for Higgs tagging due to the redundancy with the b-tagging track jet requirements, as shown in Figure 5.17.

- Gluon jets make up the majority of the individual large-R jets found in the QCD multijet background. These gluon jets tend to have high hadron multiplicity compared to quark jets due to the manner in which the QCD color factors influence the showering process. The n_{trk} variable provides a proxy measurement for charged hadron multiplicity. It is computed from tracks passing the "loose" Inner Detector requirement with $p_T > 500$ MeV, $|\eta| < 2.5$, and matched to the event primary vertex. See Figures 5.15 and 5.16.

- The b-hadrons resulting from the $H \to b\bar{b}$ decay provide an additional source of discrimination against QCD jets. The **b-tagging algorithm** as described in Section 5.4.2 is applied to the two leading p_T VR track jets ghost-associated to the Higgs candidate large-R jet.

5.5.3.1 Optimization Method

Three separate taggers are derived for W, Z, and Higgs bosons utilizing a maximum significance expression [80] which is independent of signal cross-section: $\frac{\epsilon}{\frac{a}{2}+\sqrt{B}}$, where ϵ is the signal efficiency, a is the sigma count number corresponding to a one-sided Gaussian significance, and B is the background yield. Smaller values of a are more appropriate for limit-setting, while larger values optimize for maximum discovery potential. A middle ground is chosen here and a value of $a = 3$ is used. The optimization of all relevant variables is performed simultaneously for W, Z and H bosons. In the case of the Higgs boson, separate optimization is performed

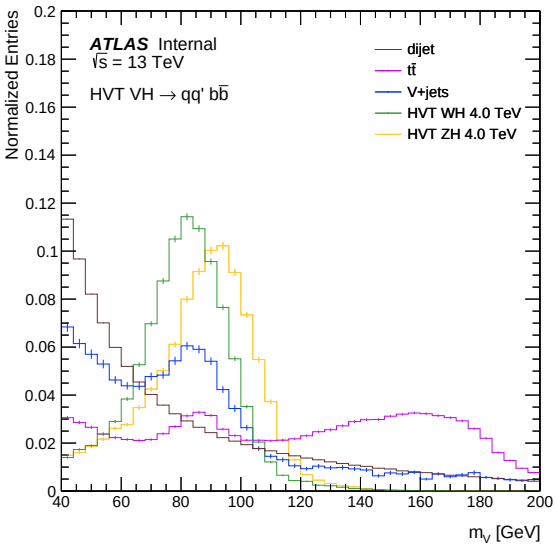

Fig. 5.12 Vector boson candidate jet mass, as measured in signal and background MC samples, normalized to unity. Only pre-selection is applied, as described in Section 5.5.1.

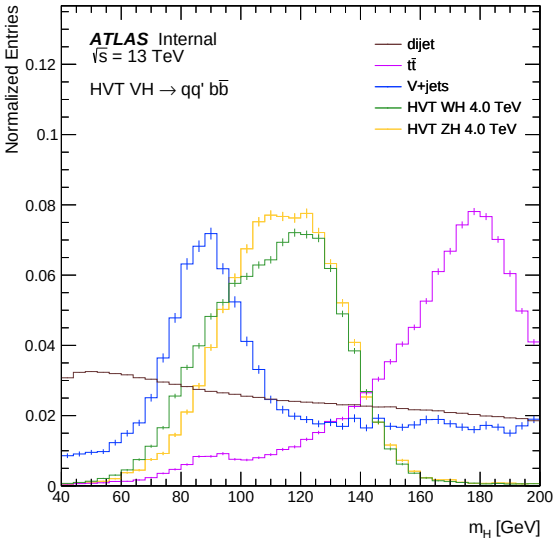

Fig. 5.13 Higgs candidate jet mass, as measured in signal and background MC samples, normalized to unity. Only pre-selection is applied, as described in Section 5.5.1.

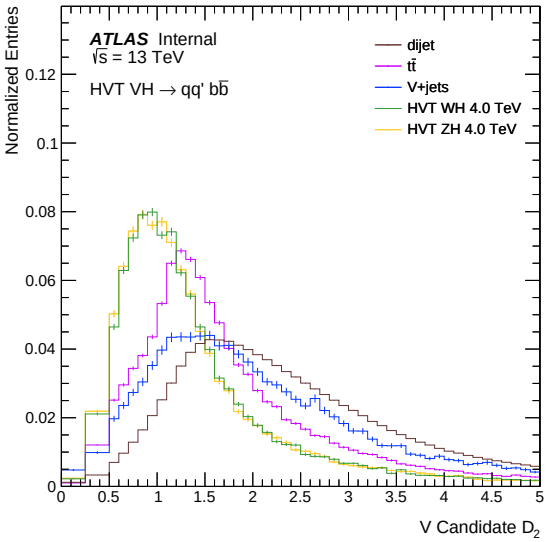

Fig. 5.14 Vector boson candidate jet D_2, as measured in signal and background MC samples, normalized to unity. Only pre-selection is applied, as described in Section 5.5.1.

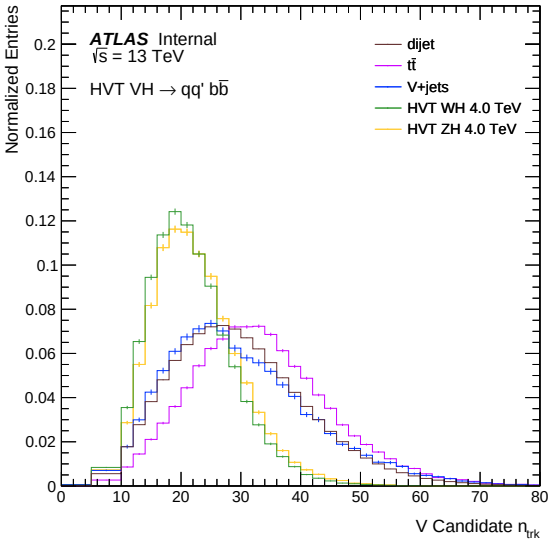

Fig. 5.15 Vector boson candidate jet n_{trk} , as measured in signal and background MC samples, normalized to unity. Only pre-selection is applied, as described in Section 5.5.1.

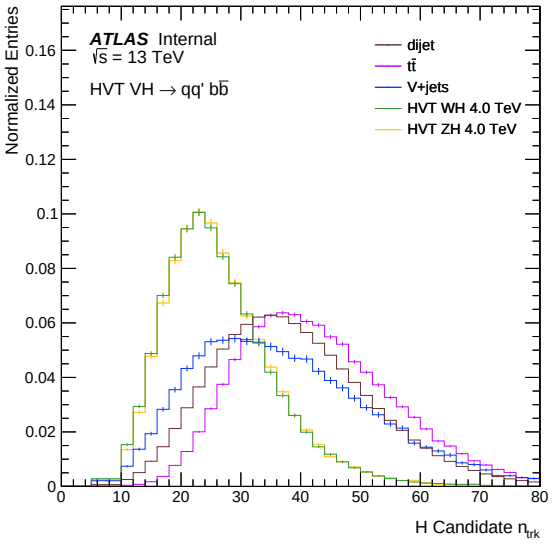

Fig. 5.16 Higgs candidate jet n_{trk} , as measured in signal and background MC samples, normalized to unity. Only pre-selection is applied, as described in Section 5.5.1.

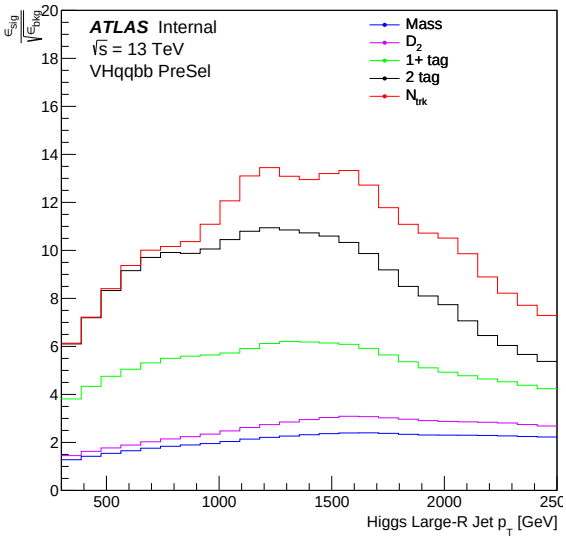

Fig. 5.17 Sensitivity of optimized cuts for Higgs tagging. The optimized D_2 cut (violet) is included only for reference and not used in the final analysis due to lack of discrimination power. The cuts are cumulative, in the order listed in the legend, and the pre-selection described in Section 5.5.1 is also applied.

for the case where 1 or 2 VR track jets pass the b-tagging criteria. The inputs to the optimization include only a loose pre-selection, without any Δy_{12} or m_{JJ} requirements. Only signal events with proper V/H truth matching are included in the optimization, thus ϵ represents the fraction of truth-matched W/Z/H large-R jets passing the selection. The words 'events' and 'jets' here are interchangeable, due to the fact that there is a maximum of one W or Z or H boson per signal event. An example plot of this sensitivity expression for the [750, 950] GeV p_T bin of the Higgs tagger optimization is shown in Figure 5.21.

For W/Z bosons a three-dimensional tagger is derived utilizing jet mass, D_2, and n_{trk} . The D_2 and n_{trk} cuts are both upper bound cuts, while the jet mass cuts form a two-sided window. In the case of Higgs tagging a two-dimensional set of jet mass and n_{trk} cuts is derived. The D_2 observable was not included in the Higgs optimization due to lack of discriminating power in conjunction with b-tagging.

Due to the correlation of each optimization variable with large-R jet p_T, each separate tagger is derived as a set of maximum sensitivity cuts in bins of large-R jet p_T. After optimization of these cuts, they are smoothed by fitting with the following expression: $\sqrt{\frac{A^2}{(p_T-B)^2} + C^2(p_T - D)^2}$. Both terms are first order approximations for different factors impacting the measurement resolution of the jet mass. The first term accounts for energy resolution, which worsens at low p_T, and the second for angular resolution, which worsens at high p_T. While this expression is physically motivated for the mass cut, it works equally well for the n_{trk} cut.

The optimized Higgs mass and n_{trk} cuts are shown in Figure 5.19, and the successive efficiency of each cut is shown in Figure 5.20. The optimized W/Z mass and D_2 cuts from VVJJ are shown in Figure 5.18. The optimized W/Z n_{trk} cuts are shown in Figure 5.22.

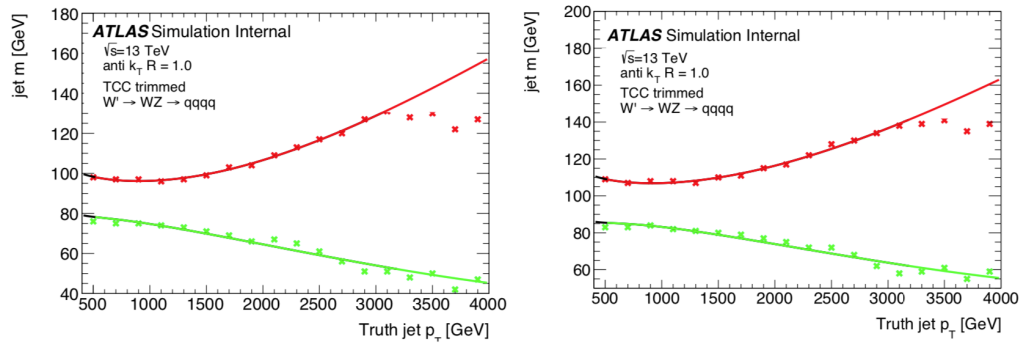

(a) W (b) Z

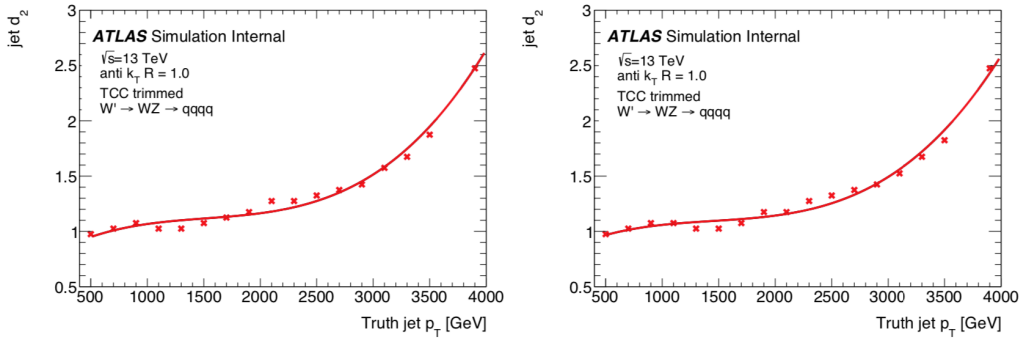

(c) W (d) Z

Fig. 5.18 W/Z boson tagging cuts derived by the VVJJ group for mass (a) (b) and D_2 (c) (d).

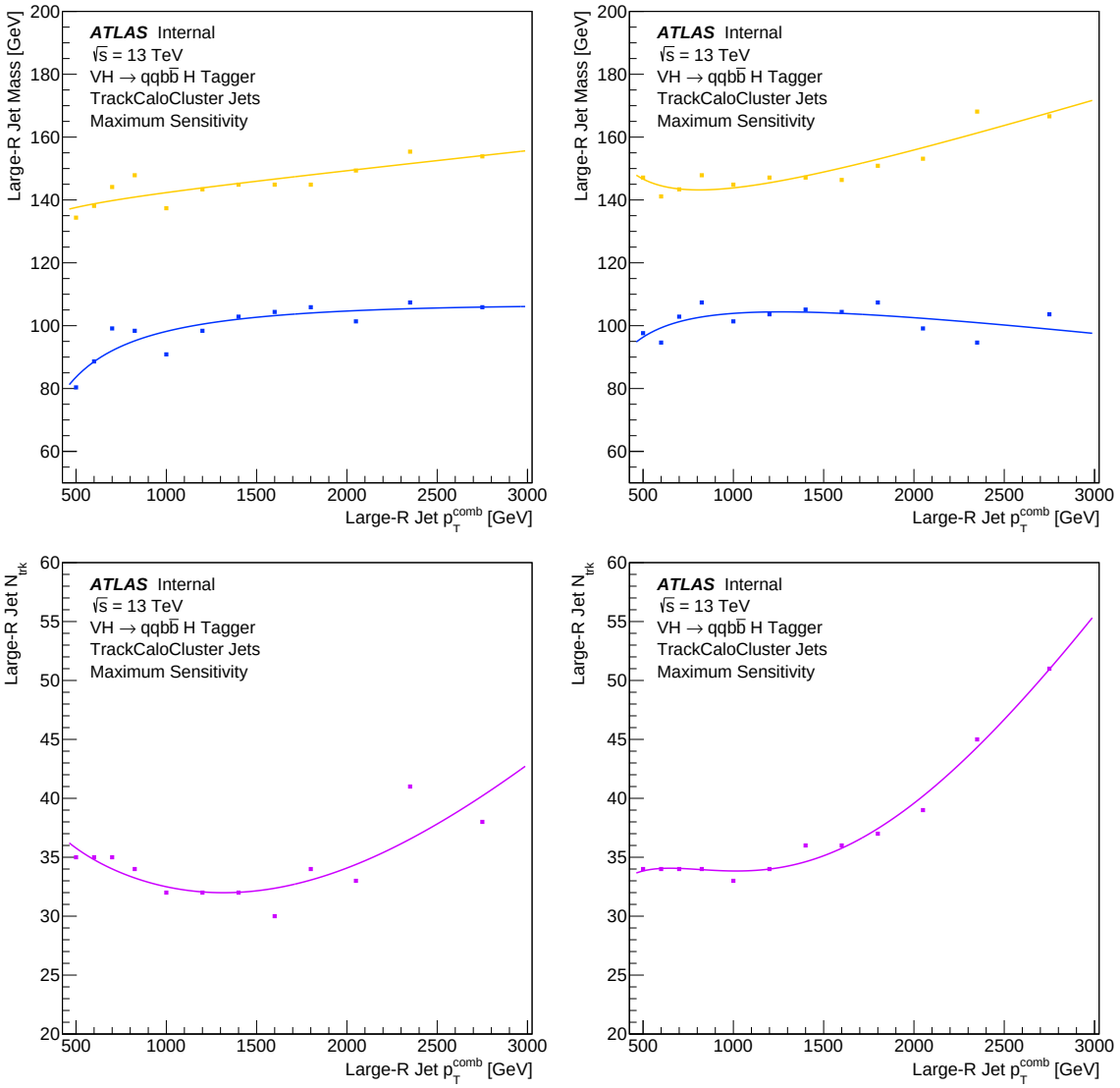

Fig. 5.19 Higgs tagging cuts derived via the method described in Section 5.5.3.1. Both the 1-tag (left) and 2-tag (right) channels are shown for the mass (top row) and n_{trk} (bottom row) cuts.

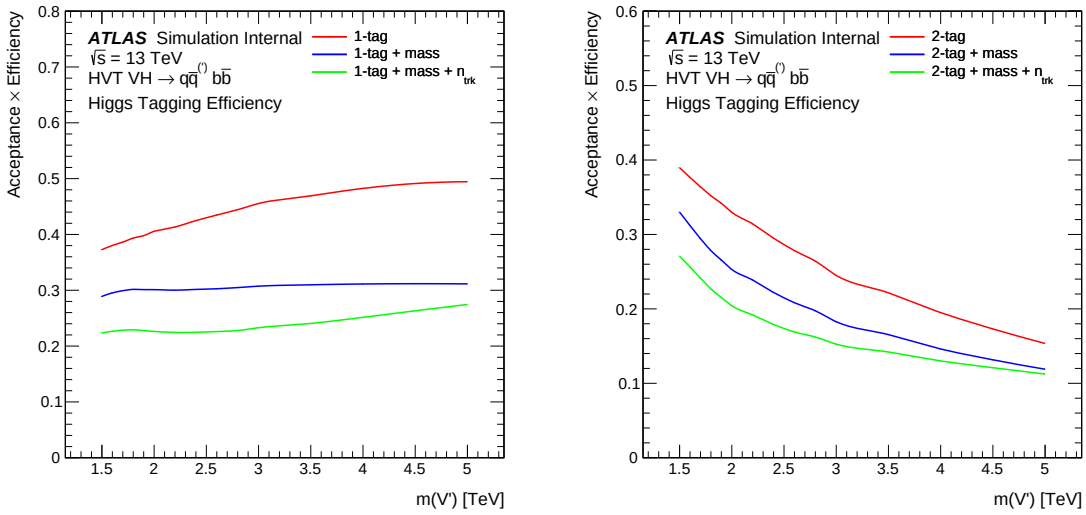

Fig. 5.20 Efficiency times acceptance (relative to pre-selection) for each successive Higgs tagging cut derived via the method described in Section 5.5.3.1. Both the 1-tag (left) and 2-tag (right) channels are shown and b-tagging scale factors are applied.

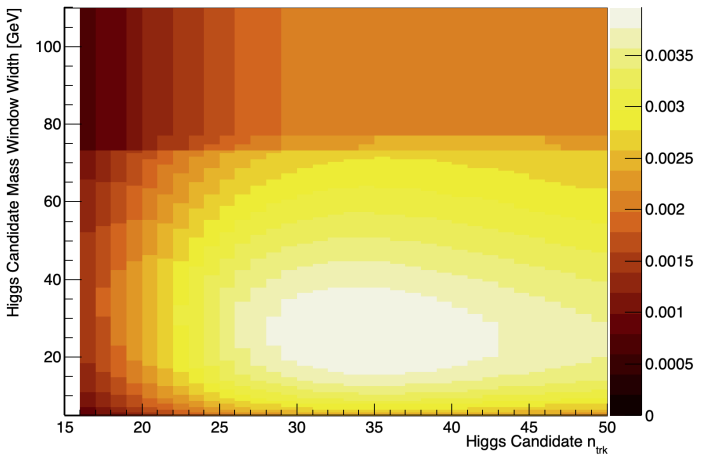

Fig. 5.21 Example sensitivity map for the [750, 950] GeV p_T bin of the Higgs tagger optimization. The location of the maximum of this 2-dimensional distribution determines the mass and n_{trk} cuts for this p_T bin.

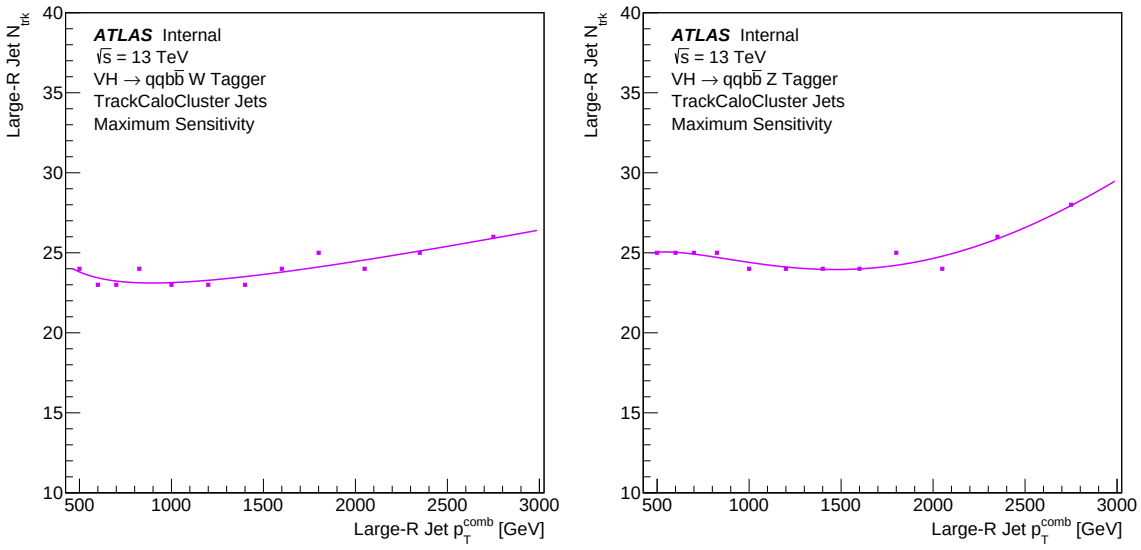

Fig. 5.22 Vector boson n_{trk} cuts derived via the method described in Section 5.5.3.1. Both W boson (left) and Z boson (right) cuts are shown.

5.5.4 Signal Regions

Events passing the event selection cuts and containing a Higgs-boson and a vector-boson candidate, as listed in Table 5.13, are further categorized according to the number of b-tagged VR track-jets that are associated to the H-tagged jet. For each of the WH and ZH final states (non-orthogonal, as identified by the different mass window cuts described in Section 5.5.3.1), two independent signal region channels are defined: 1-tag and 2-tag.

The m_{JJ} distributions for different signal mass points are shown in Figure 5.23, for events selected in the 1-tag and 2-tag signal regions. Figure 5.26 shows the efficiency as measured in the MC simulation for each of the background processes. The efficiency of each selection cut for WH and ZH signal processes is shown on Figure 5.24. In addition, the efficiency curves in the final 1-tag and 2-tag WH and ZH signal regions are shown in Figure 5.25. As one can see, the orthogonal 1-tag and 2-tag signal regions are complementary to each other for the search. A more

detailed breakdown of the cutflow for the WH 2.0 TeV and ZH 4.0 TeV signal samples can be found in Tables 5.14 and 5.15.

While the individual 1-tag/2-tag channels are orthogonal, the WH/ZH signal regions themselves are not. As measured in data there is 38.3% SRWH/SRZH overlap in the 1-tag channel, and 39.6% SRWH/SRZH overlap in the 2-tag channel.

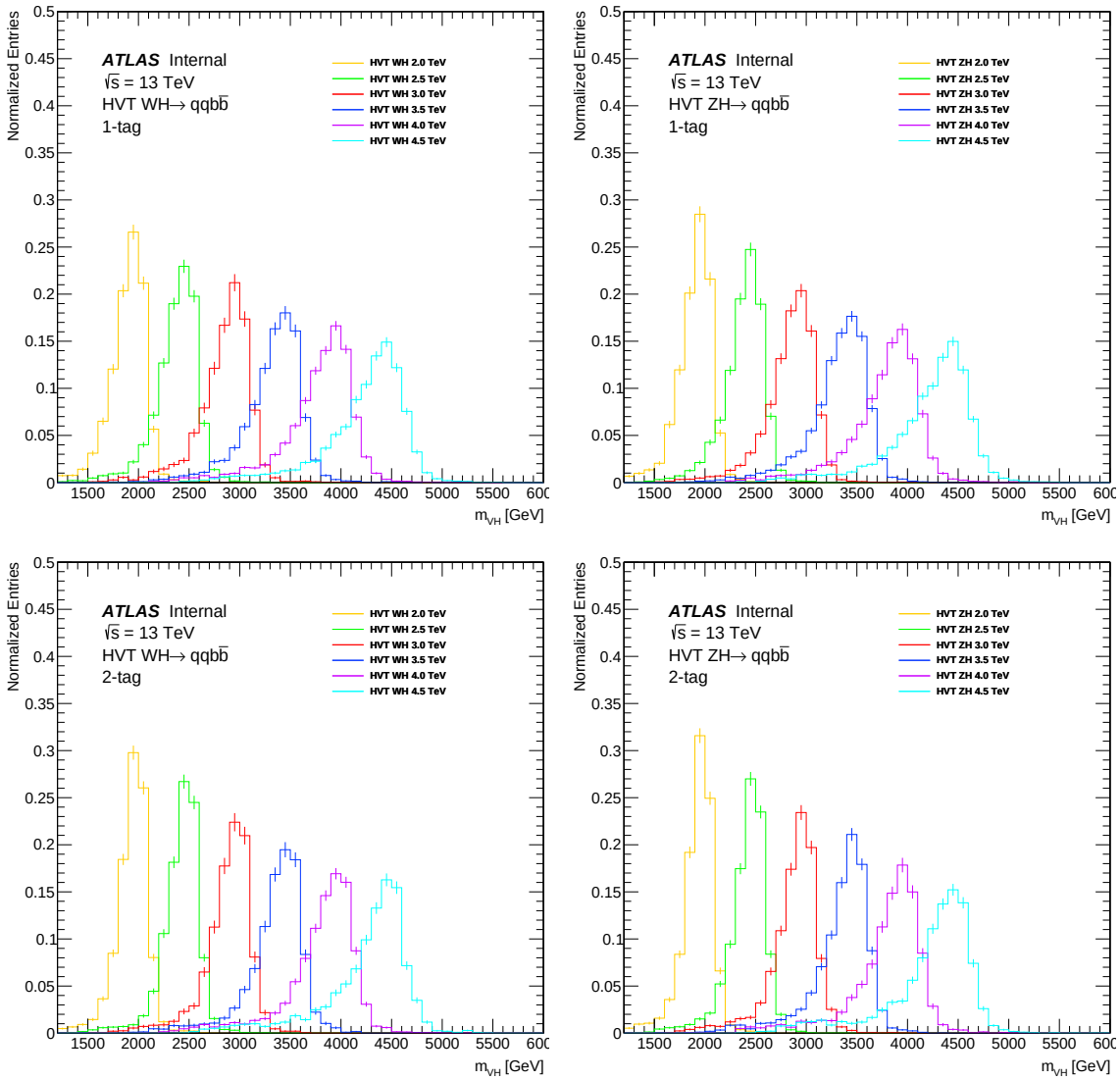

Fig. 5.23 Reconstructed dijet invariant mass distribution of WH (left) and ZH (right) signal MC samples, for selected resonance mass points, in 1-tag (top) and 2-tag (bottom) signal regions. The distributions are normalization to unity.

Cut	Description
EXOT3	5.5.1.1
GRL	See Section 5.3.2
Event Cleaning	See Section 5.5.1.2
Trigger	See Section 5.5.2
$\geq$ 2 large-R jets	$p_T > 200$ GeV, $\lvert\eta\rvert < 2.0$
Leading large-R jet p_T	> 500 GeV
Dijet Mass (m_{JJ})	> 1.3 TeV
Rapidity difference	$\lvert\Delta y\rvert < 1.6$
V/H assignment	Heavier is H-candidate, lighter is V-candidate
W/Z tagging	mass window + D_2 + n_{trk}
Higgs tagging	mass window + n_{trk}

Table 5.13 Summary of event selection.

Cut Name	$\sum$ weights	Cut Efficiency [%]	Cumulative Efficiency [%]
Generated	105000	–	–
EXOT3	99463	94.7	94.7
Jet/Event Cleaning	99112	99.6	94.4
Trigger	98662	99.5	94.0
Jet p_T / η	94114	95.4	89.6
m_{JJ}	90451	96.1	86.1
$\lvert\Delta y_{12}\rvert$	81206	89.8	77.3
W Mass	39540	48.7	37.7
W D_2	22755	57.5	21.7
W n_{trk}	16114	70.8	15.3
H Mass	12569	78.0	12.0
H n_{trk}	9867	78.5	9.4
$\geq$ 1-tag	9303	94.3	8.9
2-tag	4523	48.6	4.3

Table 5.14 Cutflow for the 2.0 TeV WH signal sample. Where appropriate, b-tagging and boson tagging scale factors are included.

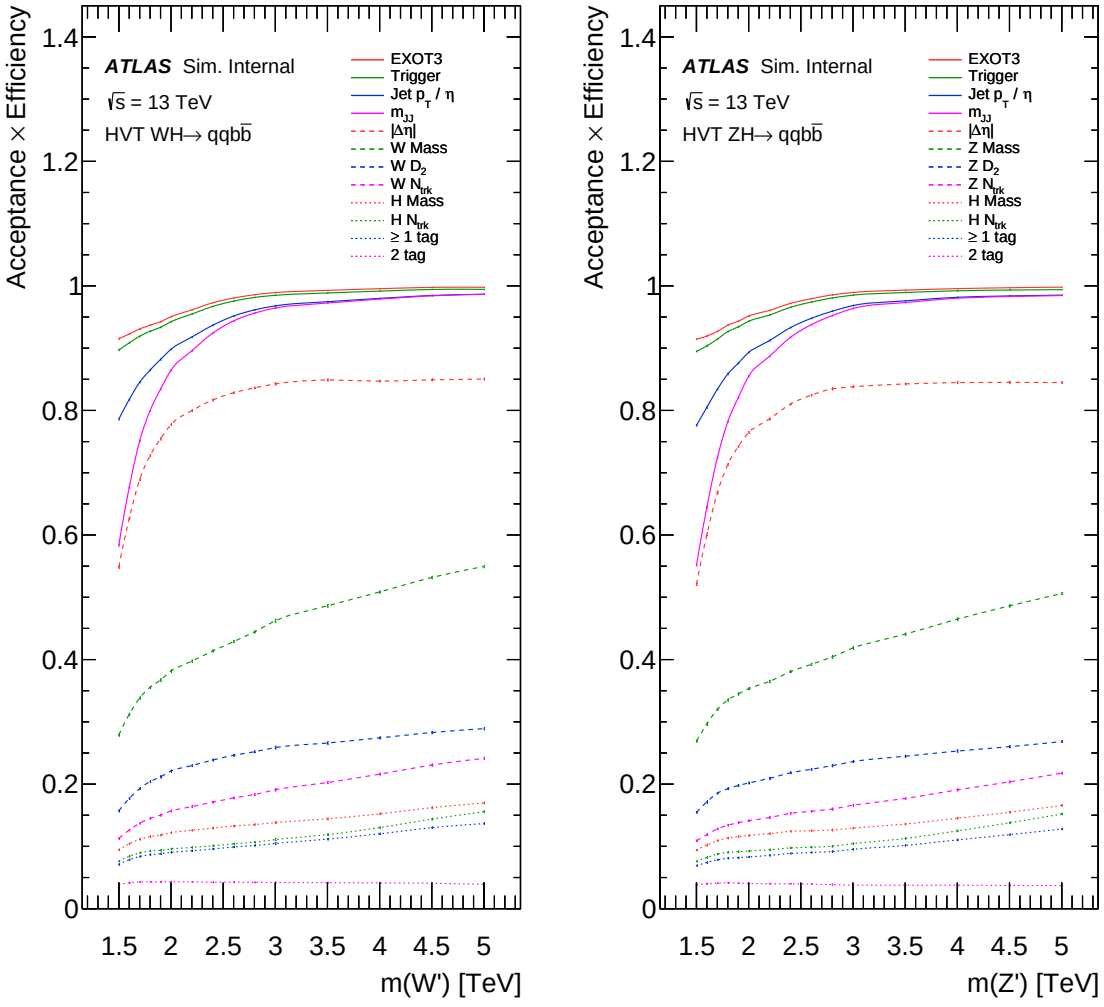

(a) (b)

Fig. 5.24 Signal efficiency at various stages of the event selection as a function of resonance mass for the WH (a) and ZH (b) selections (applied to the corresponding signal sample). Each cut is added to the selection of the previous cut in sequence, from top to bottom.

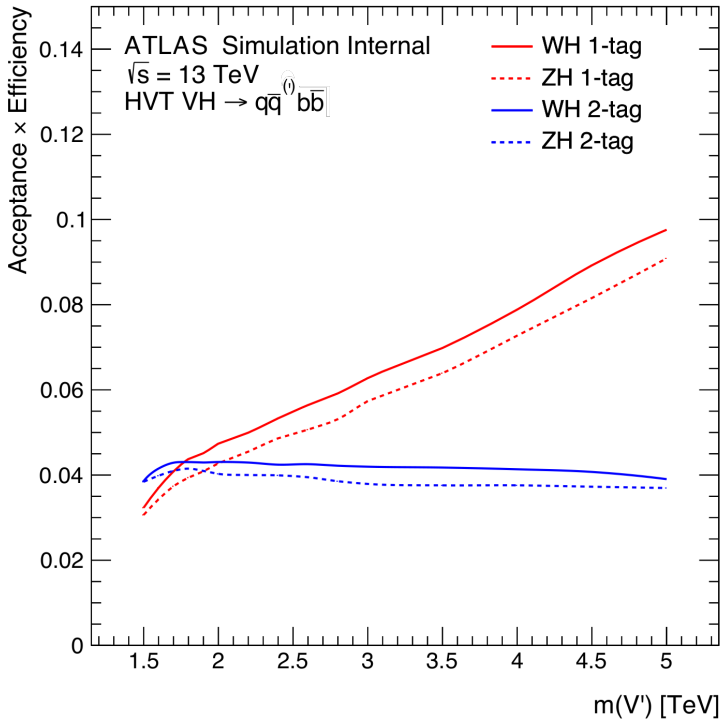

Fig. 5.25 Signal efficiency as function of resonance mass for both WH and ZH signal processes, 1-tag and 2-tag channels.

Cut Name	$\sum$ weights	Cut Efficiency [%]	Cumulative Efficiency [%]
Generated	75000	–	–
EXOT3	74713	99.6	99.6
Jet/Event Cleaning	74463	99.7	99.3
Trigger	74451	100.0	99.3
Jet p_T / η	73644	98.9	98.2
m_{JJ}	73550	99.9	98.1
$\lvert\Delta y_{12}\rvert$	63393	86.2	84.5
Z Mass	34892	55.0	46.5
Z D_2	18830	54.0	25.1
Z n_{trk}	14133	75.1	18.8
H Mass	10752	76.1	14.3
H n_{trk}	9239	85.9	12.3
$\geq$ 1-tag	8151	88.2	10.9
2-tag	2807	34.4	3.7

Table 5.15 Cutflow for the 4.0 TeV ZH signal sample.

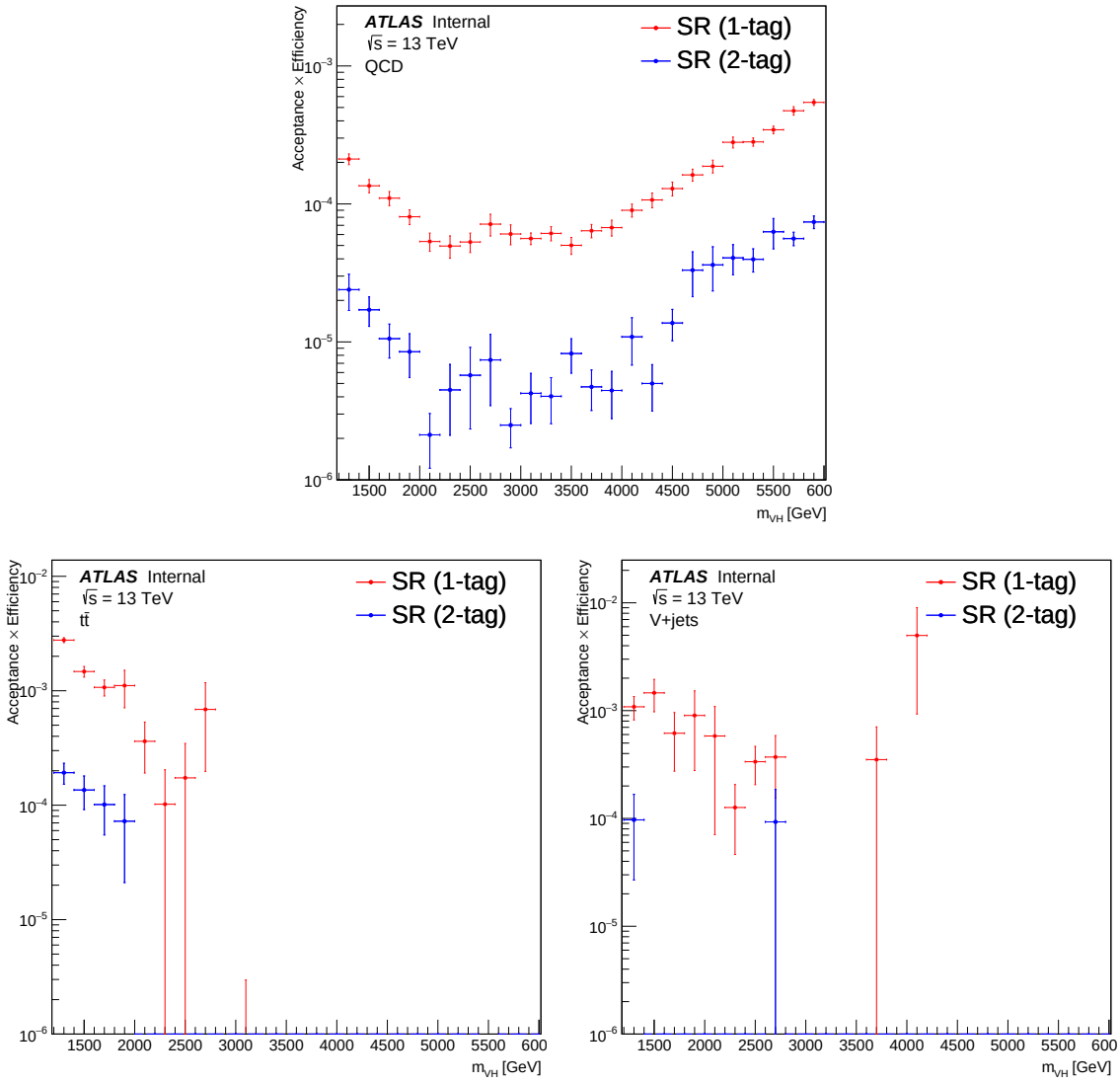

Fig. 5.26 Background efficiencies in the signal regions for dijet, $t\bar{t}$ and V+jets MC. The 1-tag and 2-tag regions correspond to the combined $V = W, Z$ signal regions. The $t\bar{t}$ and V+jets efficiency predictions at high m_{JJ} are hampered by lack of MC statistics.

5.6 Background Estimation

The primary goal of the background estimation is to provide a prediction of the normalization and shape of the combined QCD, $t\bar{t}$, and V+jets backgrounds in the 1-tag and 2-tag signal regions (SR). The variable of most interest is the invariant mass of the combined candidate VH system (m_{JJ}). However, a more complete model of event kinematics is pursued in order to produce comparisons of additional kinematic variables to further validate the complete background description.

The dominant contribution to the background comes from approximately 90% QCD events. The $t\bar{t}$ background is predicted to contribute approximately 10% to all SRs, and a small contribution of less than 1% from V+jets is also present. Other backgrounds such as diboson WW / WZ / ZZ are expected to be present but negligible and are therefore not considered. Modelling the background directly with MC is hampered for two primary reasons: (1) the QCD MC provides only a LO prediction and (2) the high background rejection of the SR selection severely limits the available MC statistics. Therefore a data-driven method is used to extract the background estimation.

Any approach chosen to produce a background estimation needs to mitigate two fundamental competing factors, namely (1) the potential use of high statistics samples from a control region to reduce statistical and high-mass extrapolation uncertainties, and orthogonally (2) the reduction of systematic uncertainties (but increase in statistical uncertainty) by estimating backgrounds as close as possible to (or directly in) the SRs.

As a result of these competing factors, multiple background estimation techniques have been developed and studied during previous iterations of this analysis:

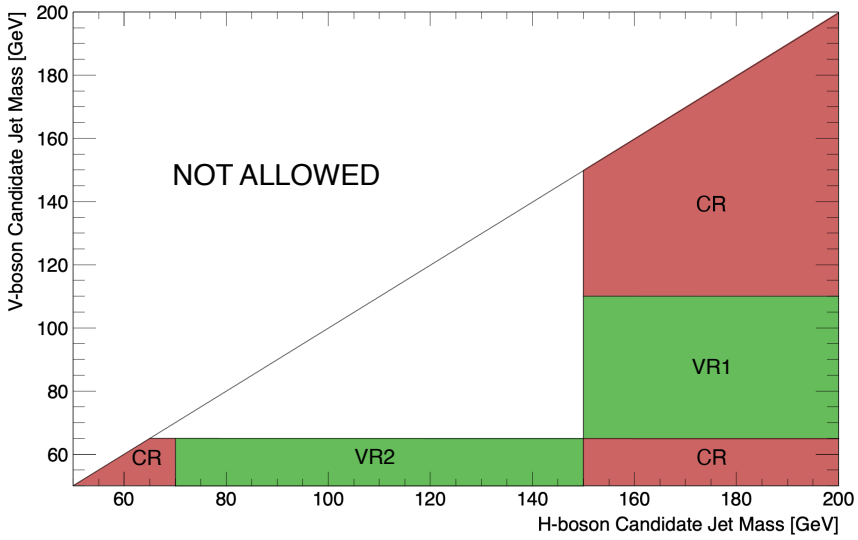

Fig. 5.27 Illustration of the control and validation regions used to derive the background estimations. Signal Regions are not shown as they are not defined by a fixed mass window. The upper left region of the plane is not allowed due to the restriction that $m_V < m_H$.

- **0-Tag Based Re-Weighting Estimation:** Events with 0 b-tags are used as a model for the corresponding 1/2-tag selection. A control region is used to derive a kinematic re-weighting to facilitate the transformation from the 0-tag events to predictions for the corresponding 1/2-tag region. A re-weighting is needed, beyond a simple normalization scale factor, due to the sculpting of the jet p_T distribution that occurs after applying b-tagging requirements. The variables used in the re-weighting are those relevant to the b-tagging, and they are described in more detail in Section 5.6.3. The quality of this prediction is estimated by cross-checking the method with a set of validation regions which are orthogonal to the signal regions.

- **High Mass SB Based Estimation:** Events with a Higgs candidate in the high mass sideband are used as a model for QCD. The 0 b-tag events are used for

validation and/or to derive a normalization scale factor from the high mass sideband to the SRs.

- **Direct Fit based Estimation:** The events in the SR are fit directly with a parameterized function. The 0-tag and high-mass sideband based events are used to validate the method.

The first approach, extrapolation from 0-tag, has been chosen for this analysis. The Direct Fit method is not a reasonable choice due to the lack of statistics in the signal region. The High Mass SB method is strictly worse than the 0-Tag Based Re-Weighting method because it is not applied at an event-by-event level and doesn't optimally use all the available information concerning kinematic sculpting of m_{JJ} between 0-tag and 1/2-tag channels.

Figure 5.31 shows the comparison of normalized shapes for the 0-tag SR[5] to the 1-tag SR and the 2-tag SR in MC. It is evident in both the 1-tag and 2-tag cases that there are shape differences between 0-tag and 1/2-tag, in particular in the high mass tail. This is the primary motivation for the kinematic re-weighting in this analysis, as described in Section 5.6.3.

5.6.1 Control/Validation Regions

Any event that does not meet the signal region requirements is considered for inclusion in a set of additional regions utilized in the kinematic re-weighting process introduced above. These control and validation regions are defined by a set of two-dimensional cuts in the m_V/m_H plane, as shown in Figure 5.27.

Defining the various regions this way is motivated by the relative independence of b-tagging efficiency and large-R jet mass for QCD jets, as demonstrated in Figure 5.29.

[5]We use here the term *0-tag SR*, but it is only used to produce the background estimation and is not actually considered in the final statistical analysis with the 1/2-tag SR channels

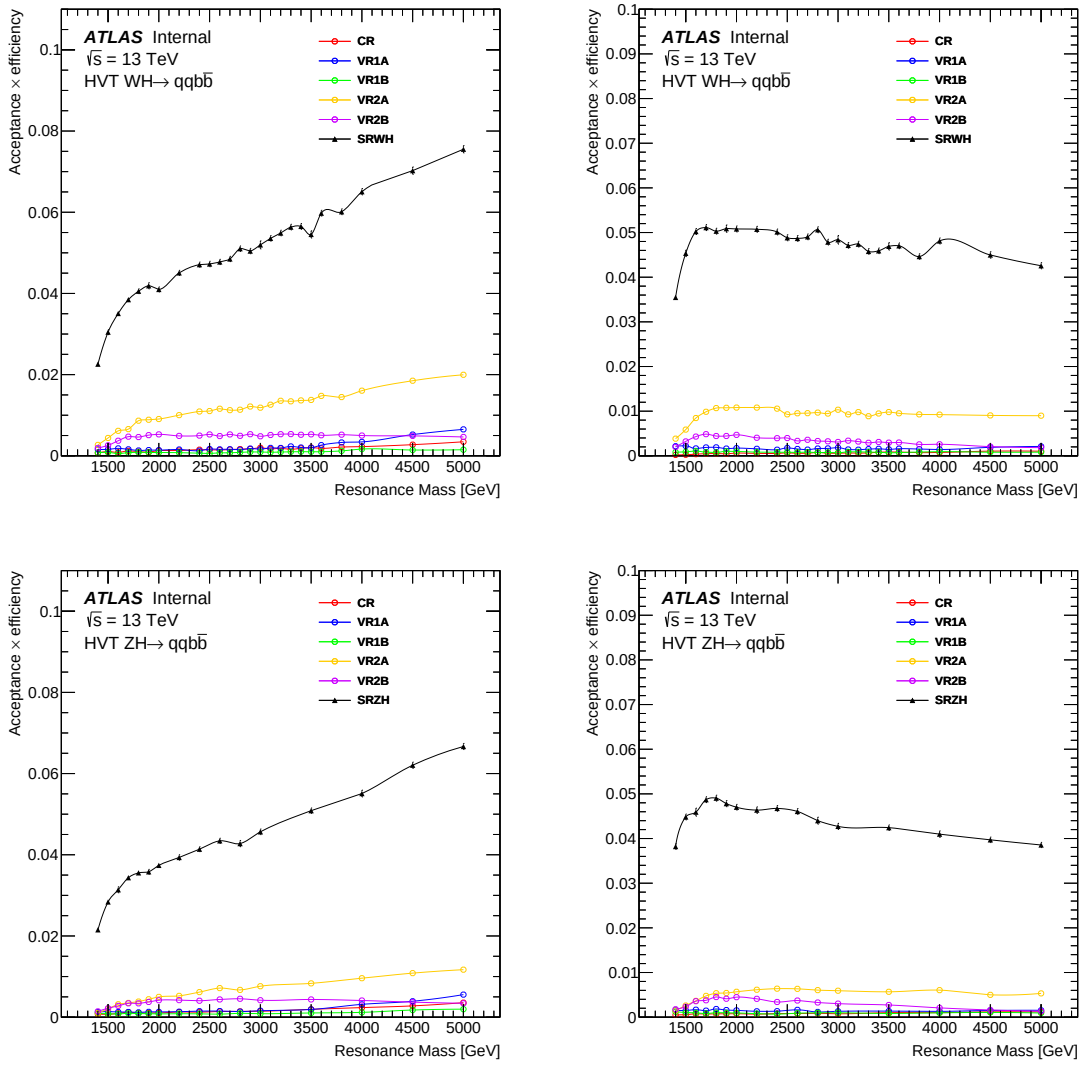

Fig. 5.28 Comparison of signal efficiency for the various control, validation, and signal regions. The WH (top row) and ZH (bottom row) samples are shown for each channel: 1-tag (left column) and 2-tag (right column). The black line shows the corresponding signal region and the colored lines show the control and validation regions.

This independence helps in large part to satisfy the requirement that the re-weighting procedure derived in the control region is applicable to the signal and validation regions. Signal contamination levels in the control and validation regions are small enough to be ignored in all cases, as shown in Figure 5.28.

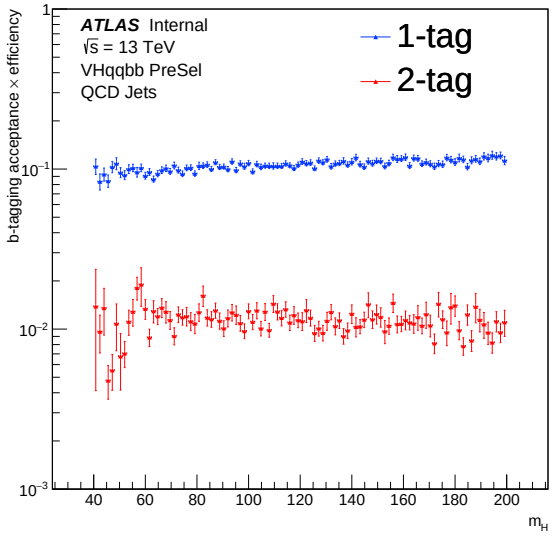

Fig. 5.29 The efficiency of 1/2-tag categorization for QCD MC events as a function of the Higgs candidate Large-R jet mass, starting from the loose pre-selection as described in Section 5.5.1, both for 1-tag and 2-tag.

In order to preserve similarity to the signal regions, the Higgs n_{trk} cut is applied to all control and validation regions as well. The D_2 cut is not applied to the W/Z candidate for the control or validation regions, as it has only a very small correlation with m_{JJ} and reduces the statistics available for re-weighting training/validation. A detailed description of all regions is given in Table 5.16. The estimated relative contribution of each background from MC is given in Table 5.17. The yields for all signal, control and validations regions for the full Run 2 data set are shown in Table 5.18.

Region	Boson Tagger Pass/Fail	Additional Cuts	Comments
WH Signal Region (SRWH)	$W \wedge H$	N/A	Used in the final likelihood fit
ZH Signal Region (SRZH)	$Z \wedge H$	N/A	Used in the final likelihood fit
Control Region (CR)	Fail SRWH/SRZH Cuts Pass H n_{trk} Cut	$(m_V < 65\ GeV \wedge m_H < 70\ GeV) \vee$ $(m_V > 110\ GeV \wedge m_H > 150\ GeV) \vee$ $(m_V < 65\ GeV \wedge m_H > 150\ GeV)$ See Figure 5.27.	Used to train BDT in the kinematic reweighting
Validation Region (VR1A)	Fail SRWH/SRZH Cuts Pass H n_{trk} Cut Pass W or Z n_{trk} cut	$m_H > 150\ GeV$ $m_V > 65\ GeV$ $m_V < 110\ GeV$	Used to validate background estimation and derive associated modeling uncertainties
Validation Region (VR1B)	Fail SRWH/SRZH Cuts Pass H n_{trk} Cut Fail W and Z n_{trk} cuts	$m_H > 150\ GeV$ $m_V > 65\ GeV$ $m_V < 110\ GeV$	Used to validate background estimation and derive associated modeling uncertainties
Validation Region (VR2A)	Fail SRWH/SRZH Cuts Pass H n_{trk} Cut Pass W or Z n_{trk} cut	$m_H > 70\ GeV$ $m_H < 150\ GeV$ $m_V < 65\ GeV$	Used to validate background estimation and derive associated modeling uncertainties
Validation Region (VR2B)	Fail SRWH/SRZH Cuts Pass H n_{trk} Cut Fail W and Z n_{trk} cuts	$m_H > 70\ GeV$ $m_H < 150\ GeV$ $m_V < 65\ GeV$	Used to validate background estimation and derive associated modeling uncertainties

Table 5.16 Definition of all signal, control, and validation regions.

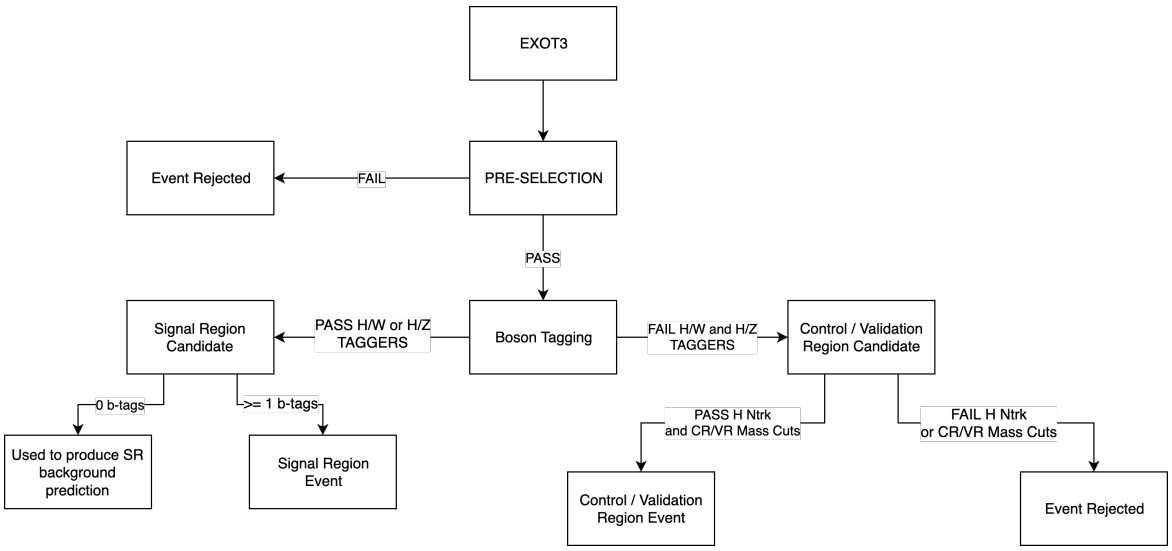

Fig. 5.30 Flowchart outlining the signal, control, and validation region selection.

Region/Channel	QCD Yield [%]	$t\bar{t}$ Yield [%]	V+Jets Yield [%]
CR 0-tag	98.69 ± 0.55	0.73 ± 0.01	0.58 ± 0.03
CR 1-tag	94.39 ± 1.23	5.13 ± 0.07	0.48 ± 0.07
CR 2-tag	94.48 ± 3.77	5.18 ± 0.23	0.34 ± 0.21
VR1A 0-tag	96.58 ± 2.36	0.8 ± 0.05	2.62 ± 0.23
VR1A 1-tag	92.49 ± 5.06	5.49 ± 0.32	2.02 ± 0.45
VR1A 2-tag	95.25 ± 14.05	3.11 ± 0.68	1.64 ± 0.98
VR2A 0-tag	98.38 ± 1.16	0.04 ± 0.01	1.58 ± 0.10
VR2A 1-tag	98.06 ± 2.81	0.31 ± 0.04	1.63 ± 0.22
VR2A 2-tag	97.23 ± 7.4	0.36 ± 0.11	2.41 ± 0.90
VR1B 0-tag	98.49 ± 0.91	0.5 ± 0.01	1.01 ± 0.06
VR1B 1-tag	95.97 ± 1.92	3.35 ± 0.09	0.69 ± 0.11
VR1B 2-tag	95.69 ± 6.0	3.44 ± 0.29	0.87 ± 0.69
VR2B 0-tag	98.37 ± 0.6	0.06 ± 0.01	1.57 ± 0.05
VR2B 1-tag	97.37 ± 1.44	0.38 ± 0.02	2.25 ± 0.14
VR2B 2-tag	97.21 ± 4.13	0.17 ± 0.06	2.62 ± 0.37

Table 5.17 Breakdown of Monte Carlo background composition in each region/channel. The signal regions are not included due to lack of Monte Carlo statistics preventing a meaningful estimate. The errors displayed are purely statistical.

Region	0-tag Events (139 fb^{-1})	1-tag Events (139 fb^{-1})	2-tag Events (139 fb^{-1})
CR	300635	48112	4918
VR1A	26376	4359	495
VR1B	111420	18198	1895
VR2A	77092	11635	1311
VR2B	192257	29064	3015
SRWH	4362	598	57
SRZH	5038	717	84

Table 5.18 Yields in the full Run 2 data set for each signal, control and validation region.

5.6.2 Normalization

As mentioned previously, three channels are distinguished for all regions: 0-tag, 1-tag, and 2-tag. These channels are defined by the b-tagging pass/fail status for each of the two leading p_T ghost-associated track jets of the Higgs candidate large-R

jet. Events from the 0-tag channel are used to estimate the shape of the background in the corresponding 1-tag and 2-tag channels. For all regions the 0-tag channel is $> 98\%$ pure in QCD events, as predicted by MC.

It should be noted that the 0-tag sample has one additional requirement that the Higgs candidate must have at least as many ghost-associated track jets as the number of b-tags in the channel being modeled. So when modeling the 1(2)-tag sample, the 0-tag Higgs candidate must have at least 1 (2) matched track jet(s). This requirement helps to ensure that the kinematics of the 0-tag sample is as close as possible to the tagged SR being modeled.

Separately from the kinematic shape re-weighting, a normalization factor for estimating the yield ratio of the 1/2-tag channel to the 0-tag channel must be derived. We label these scale factors as $\mu_{0\to1}$ and $\mu_{0\to2}$. These scale factors are not identical in all regions, as show in Figure 5.32. The goal is then to develop a strategy for predicting $\mu_{0\to1}$ and $\mu_{0\to2}$ in the signal regions, along with a corresponding statistical and systematic error.

As mentioned previously, modelling the background shape with MC is not a reliable strategy for this analysis. For this reason the data from the control and validation regions are used to estimate the nominal values and uncertainties of $\mu_{0\to1}$and $\mu_{0\to2}$. The nominal values are taken from the control region (CR). A systematic error for each channel is defined conservatively by the largest μ difference between any two regions. The nominal values and errors for both normalization scale factors are:

$$\mu_{0\to1} = 0.160 \pm 0.014\ (\text{syst.}) \pm 7 \times 10^{-4}\ (\text{stat.}) \tag{5.6.1}$$

$$\mu_{0\to2} = 0.0167 \pm 0.0028\ (\text{syst.}) \pm 2 \times 10^{-4}\ (\text{stat.}) \tag{5.6.2}$$

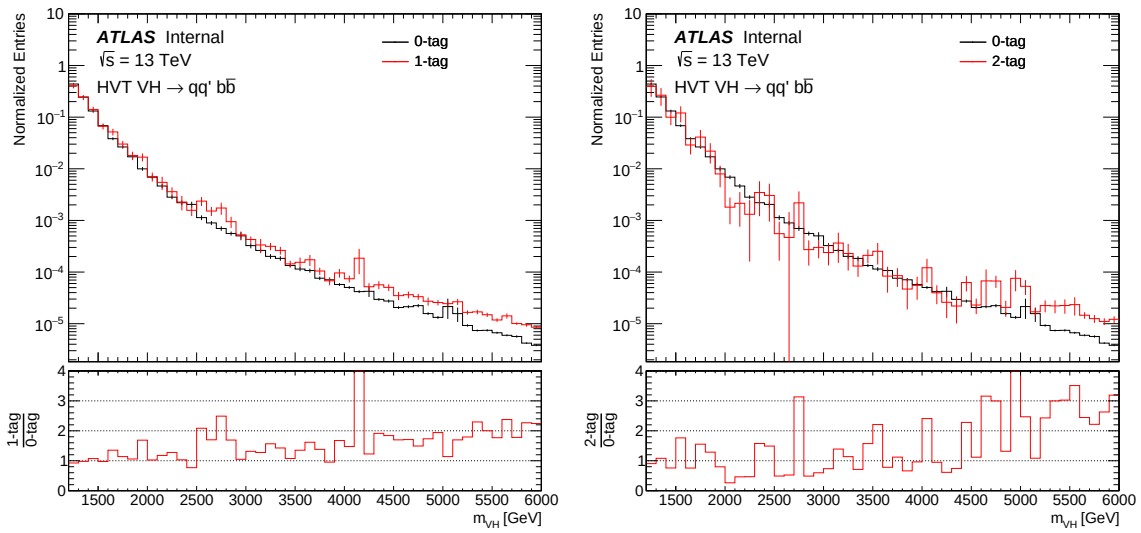

Fig. 5.31 Comparison of 0-tag SR background shape to the 1-tag (left) and 2-tag (right) SR background shapes in simulated multijet data. The SRWH and SRZH signal regions are combined and distributions are normalized to unity. The trends obvious in the ratio plots demonstrate the need for kinematic re-weighting when utilizing the 0-tag data to produce background estimates for 1-tag and 2-tag channels.

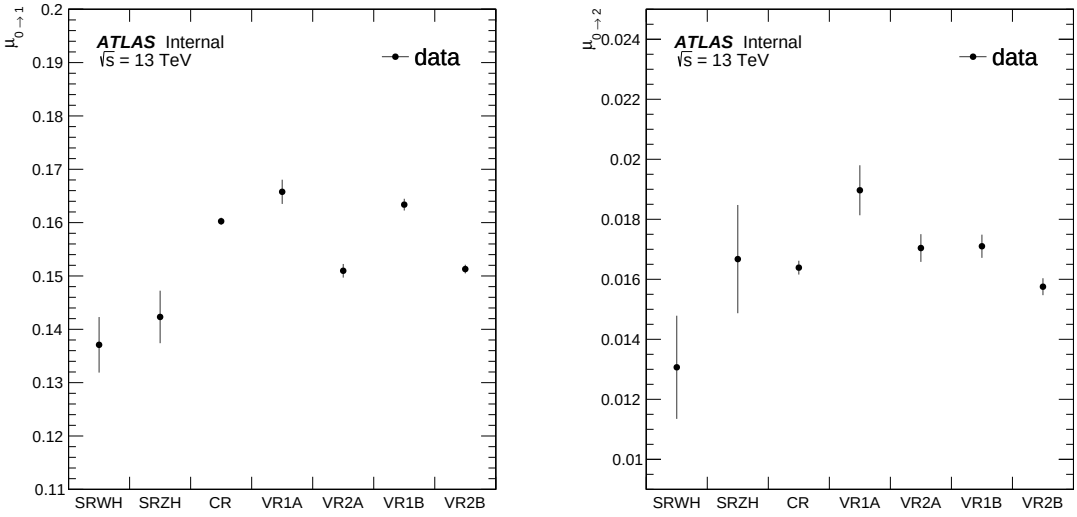

Fig. 5.32 Observed background normalization scale factor values from data for all regions for 1-tag (left) and 2-tag (right) channels. These scale factors ($\mu_{0\to N}$) are defined as the ratio of N-tag to 0-tag yield for each particular control/validation/signal region.

5.6.3 Kinematic Re-weighting

The 0-tag extrapolation method is based on the assumption that most kinematic variables in the 1-tag or 2-tag channels can be well modeled by the corresponding 0-tag channel. However, kinematic distributions can be biased when transferring from 0-tag sample to 1/2-tag sample for two main reasons:

- **Non-trivial kinematic dependency of track jets b-tagging efficiency**. Since the track jet b-tagging efficiency strongly depends on the track jet p_T (and also some dependency on η), the kinematic distributions can be sculpted after applying b-tagging requirements.
- **Change of heavy flavor composition**. For example, when moving from 0-tag to 2-tag samples, the fraction of $g \to bb$ in QCD will increase significantly, which has a different kinematics than the light-quark-dominant 0-tag sample. Similarly, $g \to c\bar{c}$ fractions are like to differ between 0-tag and 1-tag.

A BDT-based approach [81] has therefore been explored which ensures that the most relevant variables are being used for the reweighting. In this method a boosted decision tree is used to predict the weights needed to bring the 0-tag and 1/2-tag regions into agreement. Trees are trained to define single cuts on input variables that maximize the χ^2 value between 0-tag and 1/2-tag samples: this will result in a series of regions that are maximally discrepant between the original and the target samples, in other words, regions of phase-space that most need correction in the original sample.

Each leaf in a tree will have an associated weight which depends on the total number of original and target events that it contains, defined during training. Gradient boosting is performed with a dedicated loss function that gives preference

to trees that find such large imbalances between 0-tag and 1/2-tag regions. The final weight for an event will therefore be a product of weights from each tree, including the chosen learning rate (λ) as a multiplicative factor. The hyperparameter values used for this method are described in Table 5.19. Open source software based upon scikit-learn [82] was used to perform the re-weighting [83].

The following variables are used as inputs to the re-weighting:

- leading track jet p_T, η, ϕ, m and VR radius
- subleading track jet p_T, η, ϕ, m and VR radius
- H/V Candidate Large-R Jet p_T
- H Candidate n_{trk}
- $|\Delta R|$ between leading/subleading track jet
- $\left|\Delta\eta\right|$ between leading/subleading track jet
- $\frac{p_T^1}{p_T^1+p_T^2}$, where p_T^1 and p_T^2 are the leading/subleading track jet p_T.
- Number of track jets ghost-associated to the Higgs candidate

BDT Hyperparameter	Value	Description
Number of Estimators	100	Number of base trees in the ensemble used for boosting.
Learning Rate	0.1	Regularization parameter for the update step of in gradient boosting. Smaller learning rates tend to yield better generalization ability.
Max Depth	3	Maximum depth of the of the base trees.
Min. Samples per Leaf	500	Minimum number of events allowed in each leaf when determining the cuts that separate leaves in the base trees.
Subsample	0.8	Proportion of the training set used for each base tree for 'stochastic' gradient boosting.

Table 5.19 Summary of BDT hyperparameters used in the re-weighting process.

5.6.4 Validation

In order to validate the performance of the BDT re-weighting procedure, comparisons to data are studied in the four validation regions: VR1A, VR1B, VR2A, and VR2B. Figures 5.33 and 5.34 show the m_{JJ} distribution in each of these validations for the 1-tag and 2-tag channels, respectively.

One further way of validating the usefulness of the BDT re-weighting is to train binary classifiers using the re-weighting training variables to differentiate between pre and post reweighted data. Before re-weighting is applied, a properly trained binary classifier should have a (mildly) successful ability to differentiate between, for example, 0-tag and 1-tag. After re-weighting is applied, a properly trained binary classifier should have little success in distinguishing the re-weighted prediction and the actual 1-tag data, and its application should approach the same result as a random coin flip. The relative ability of these two classifiers can be quantified by producing Receiver Operating Characteristic (ROC) curves, and these are shown in Figures 5.35 and 5.36 for 1-tag and 2-tag channels, respectively. The ability of the two classifiers can be distinguished by computing the area under the ROC curve (AUC), where a random chance classifier would have value of AUC = 0.5.

5.6.5 Smoothing

Due to the small number of events in the tail of the re-weighted background templates, smoothing via fitting with a functional form must be applied to produce a well-behaved background description at high m_{JJ}. The first step in this process is to derive a well-motivated binning for the m_{JJ} histograms based upon the experimental m_{JJ} resolution.

First the truth dijet mass (m_{VH}^{truth}) is determined by ΔR-matching both the H and V candidate fat jets to the corresponding `AntiKt10TruthTrimmedPtFrac5SmallR20Jets`

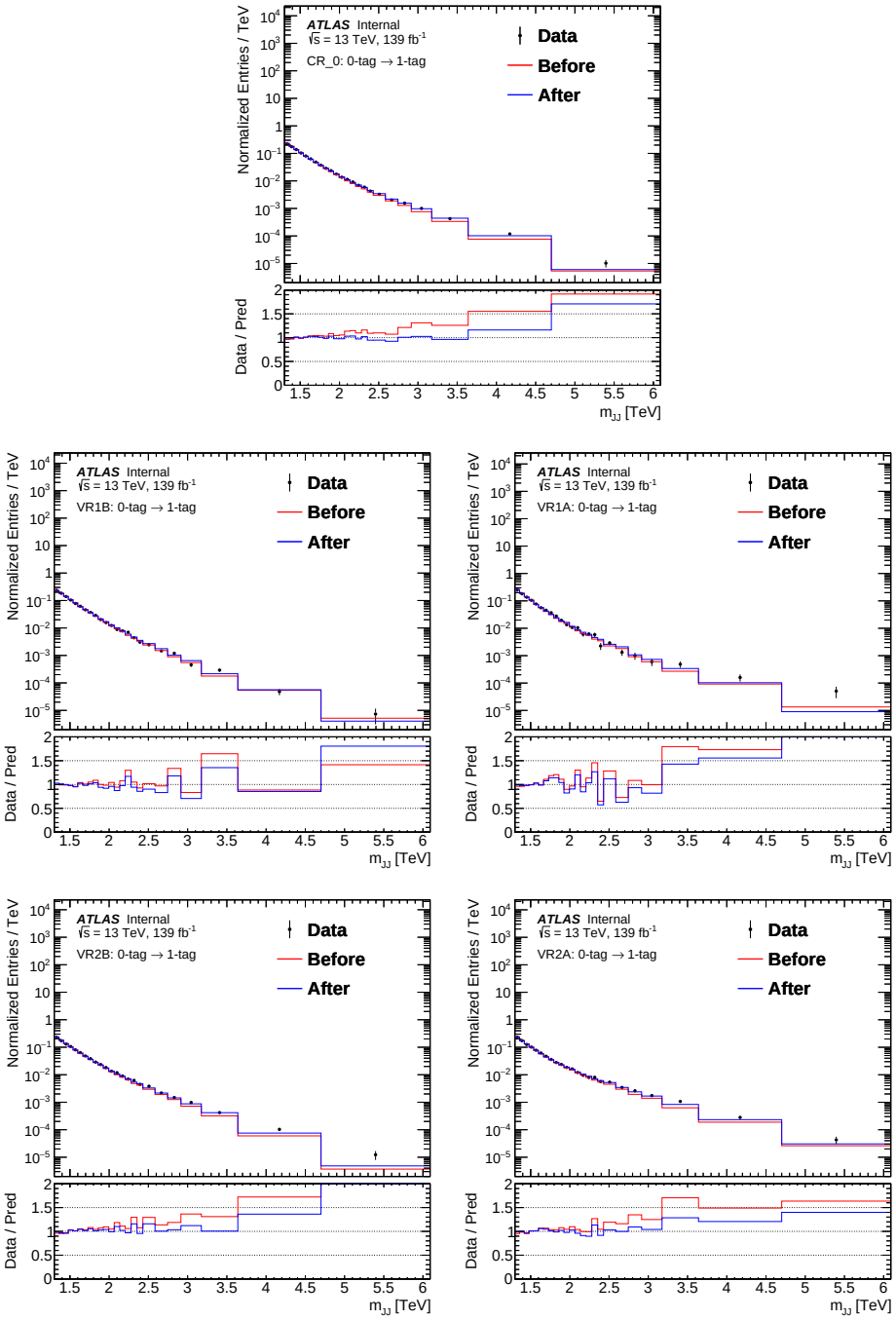

Fig. 5.33 m_{JJ} predictions for the 1-tag region in all control and validation regions. The predictions shown are constructed by scaling 0-tag data, both before (red) and after (blue) kinematic re-weighting is applied.

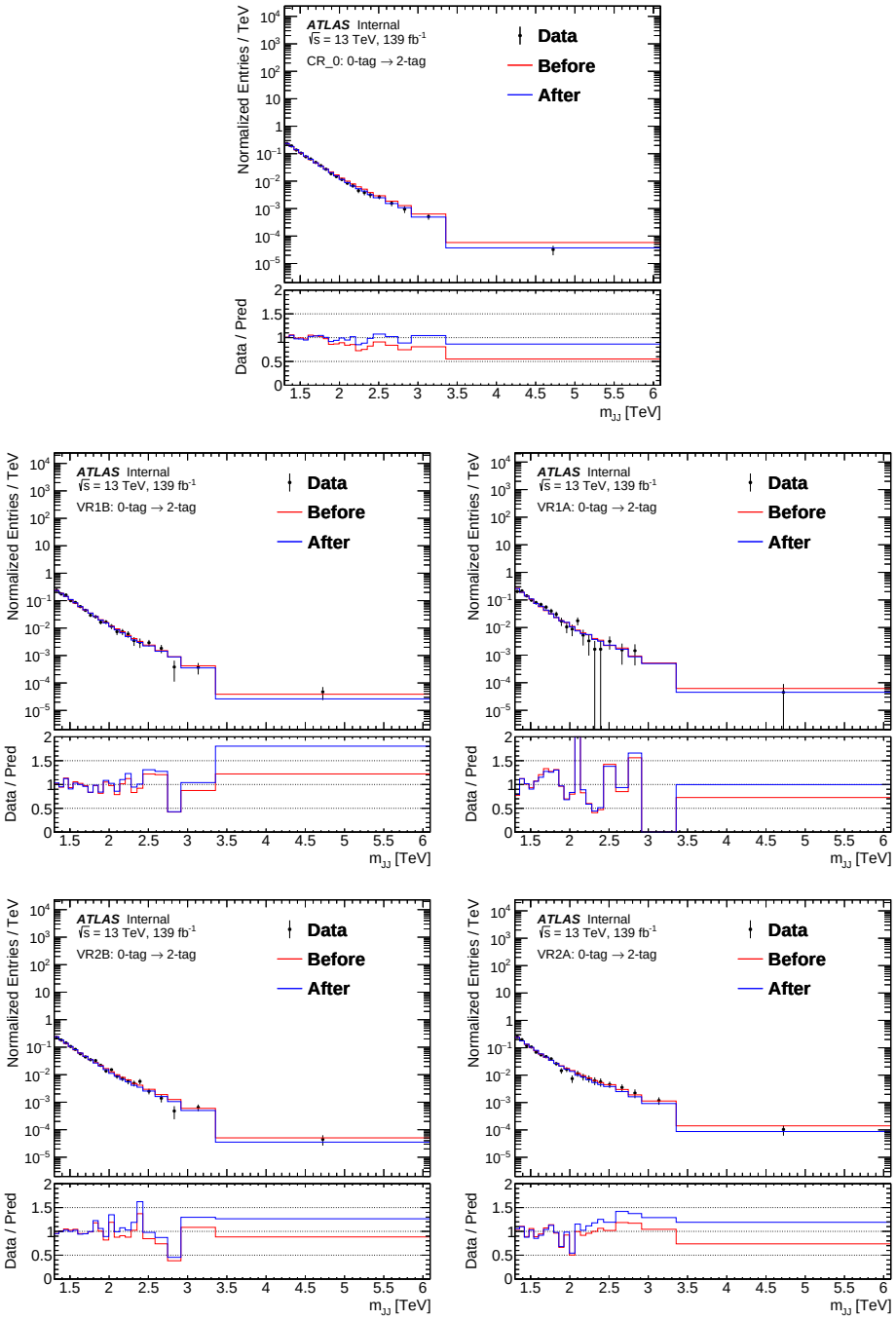

Fig. 5.34 m_{JJ} predictions for the 2-tag region in all control and validation regions. The predictions shown are constructed by scaling 0-tag data, both before (red) and after (blue) kinematic re-weighting is applied.

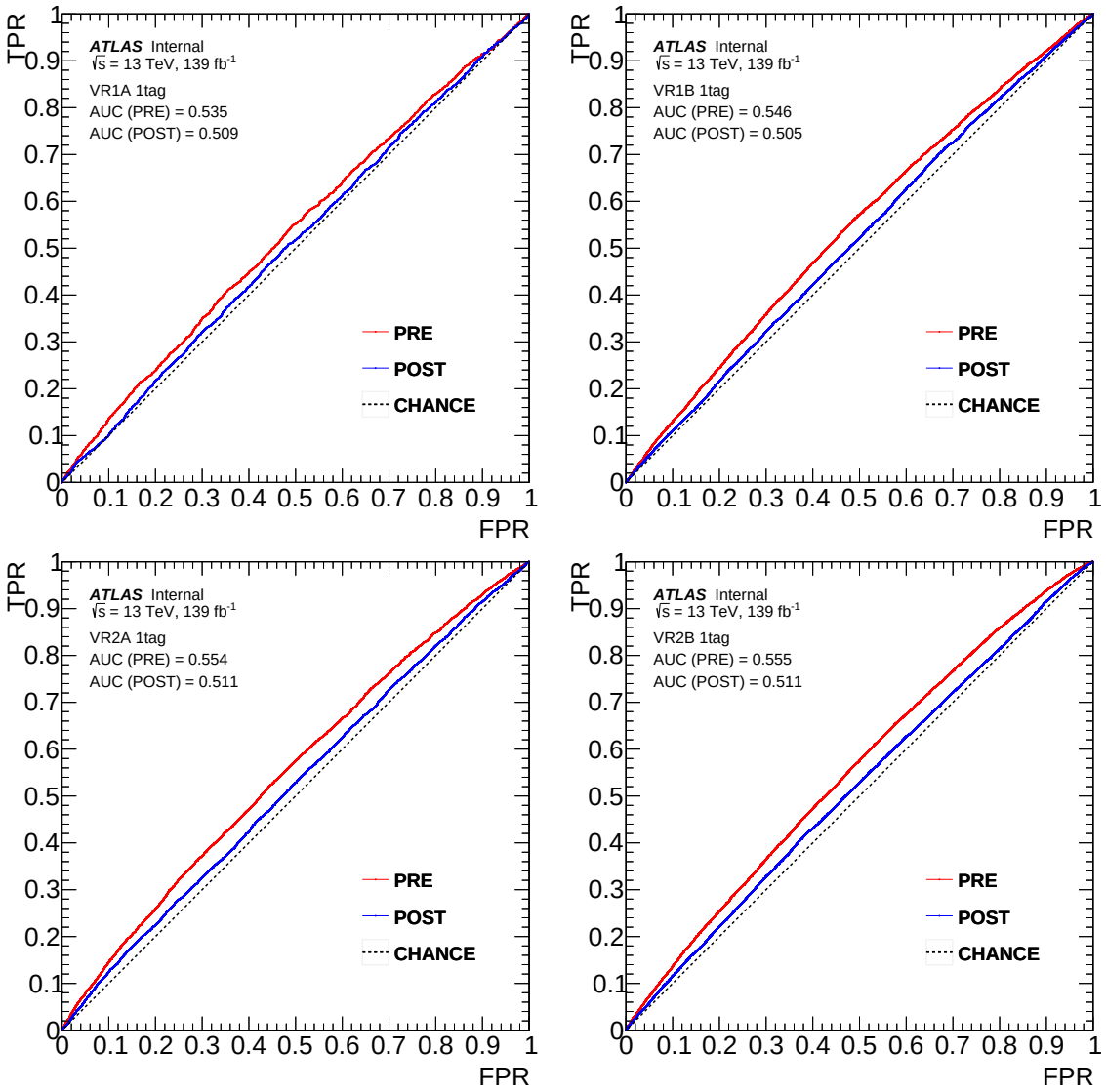

Fig. 5.35 Receiver Operating Characteristic (ROC) curves for each validation region in the 1-tag channel. Two separate binary classifiers are trained using a gradient boosted decision tree. The red (PRE) line corresponds to the case where no re-weighting has been applied and the classifier is trained to discriminate 0-tag from 1-tag events in each region. The blue (POST) line corresponds to the case where re-weighting has been applied and the classifier is trained to discriminate re-weighted 0-tag events from unmodified 1-tag events in each region. Each classifier is trained only the set of variables use in the re-weighting. In the ideal scenario of perfect re-weighting, the blue line would match very closely to the black line which represents a naive 50/50 random chance classifier. The area under the curve (AUC) is shown for each classifier, where a value of 0.5 would correspond to ideal re-weighting.

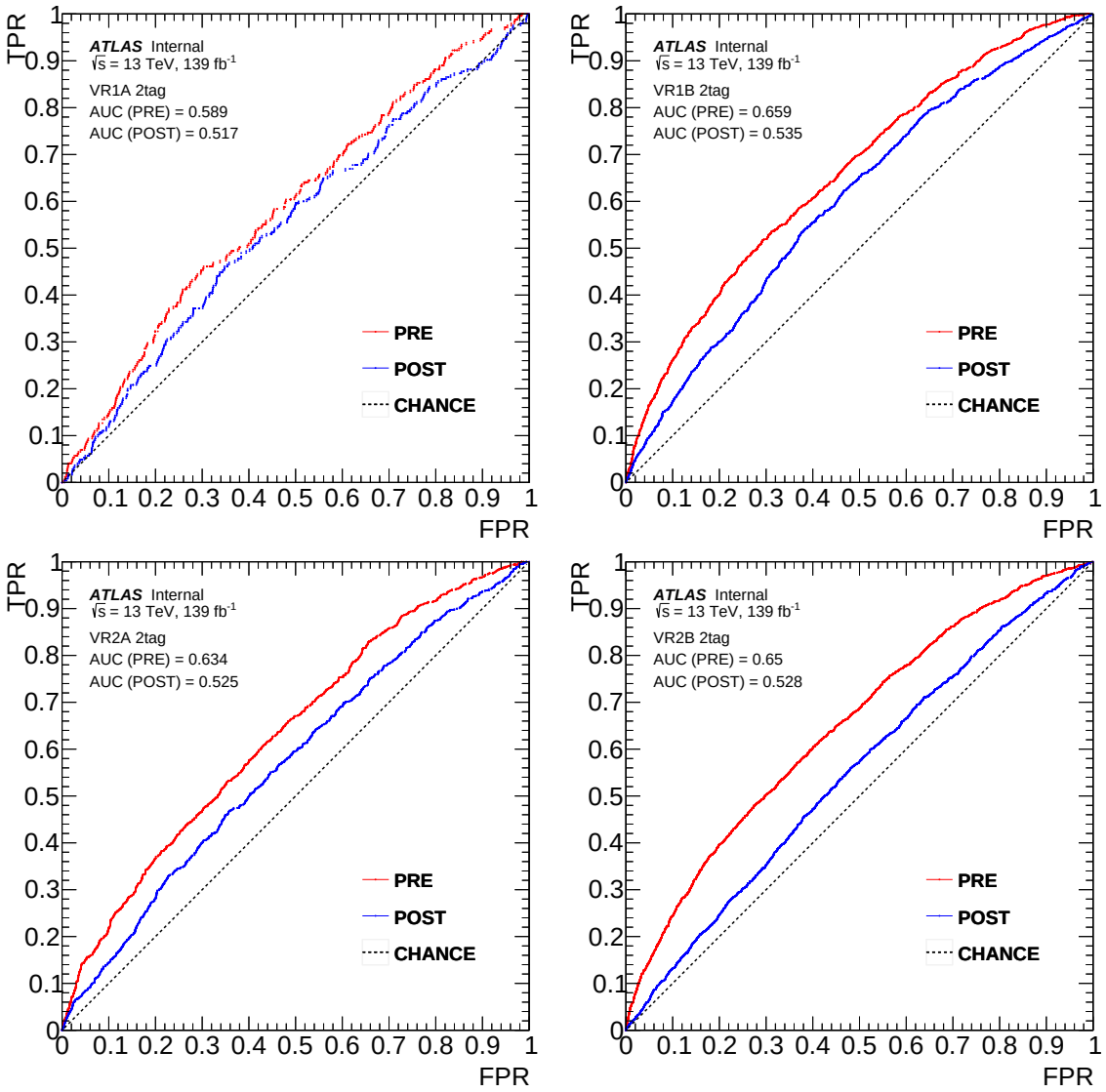

Fig. 5.36 Receiver Operating Characteristic (ROC) curves for each validation region in the 2-tag channel. Two separate binary classifiers are trained using a gradient boosted decision tree. The red (PRE) line corresponds to the case where no re-weighting has been applied and the classifier is trained to discriminate 0-tag from 2-tag events in each region. The blue (POST) line corresponds to the case where re-weighting has been applied and the classifier is trained to discriminate re-weighted 0-tag events from unmodified 2-tag events in each region. Each classifier is trained only the set of variables use in the re-weighting. In the ideal scenario of perfect re-weighting, the blue line would match very closely to the black line which represents a naieve 50/50 random chance classifier. The area under the curve (AUC) is shown for each classifier, where a value of 0.5 would correspond to ideal re-weighting.

large radius truth jet collection. For each WH signal mass value[6] the residuals $(m_{VH} - m_{VH}^{\text{truth}})$ are fitted with a Crystal Ball function, given by

$$f(x;\alpha,n,\bar{x},\sigma) = N \cdot \begin{cases} \exp(-\frac{(x-\bar{x})^2}{2\sigma^2}), & \text{for } \frac{x-\bar{x}}{\sigma} > -\alpha \\ A \cdot (B - \frac{x-\bar{x}}{\sigma})^{-n}, & \text{for } \frac{x-\bar{x}}{\sigma} \leqslant -\alpha \end{cases}, \tag{5.6.3}$$

$$\begin{aligned} A &= \left(\frac{n}{|\alpha|}\right)^n \cdot \exp\left(-\frac{|\alpha|^2}{2}\right), \\ B &= \frac{n}{|\alpha|} - |\alpha|\,, \\ N &= \frac{1}{\sigma(C+D)}, \\ C &= \frac{n}{|\alpha|} \cdot \frac{1}{n-1} \cdot \exp\left(-\frac{|\alpha|^2}{2}\right), \\ D &= \sqrt{\frac{\pi}{2}}\left(1 + \text{erf}\left(\frac{|\alpha|}{\sqrt{2}}\right)\right), \end{aligned}$$

where N is a normalization factor and α, n, $\bar{x}$ and σ are parameters which are fitted with the data.

The resulting fitted σ parameter from the Crystal Ball function is used a measure of the experimental resolution. Only events with correct truth-level H/V candidate assignment are considered. Figure 5.37 shows the result of this fit for four representative mass points. The resulting σ values are then fit as a linear function of resonance mass, as shown in Figure 5.38, and the result is used to derive a set of variable-width bins corresponding to the experimental m_{JJ} resolution for the range of 1.3 to 7 TeV.

[6]No significant different in experimental resolution is observed between simulated WH and ZH signal samples

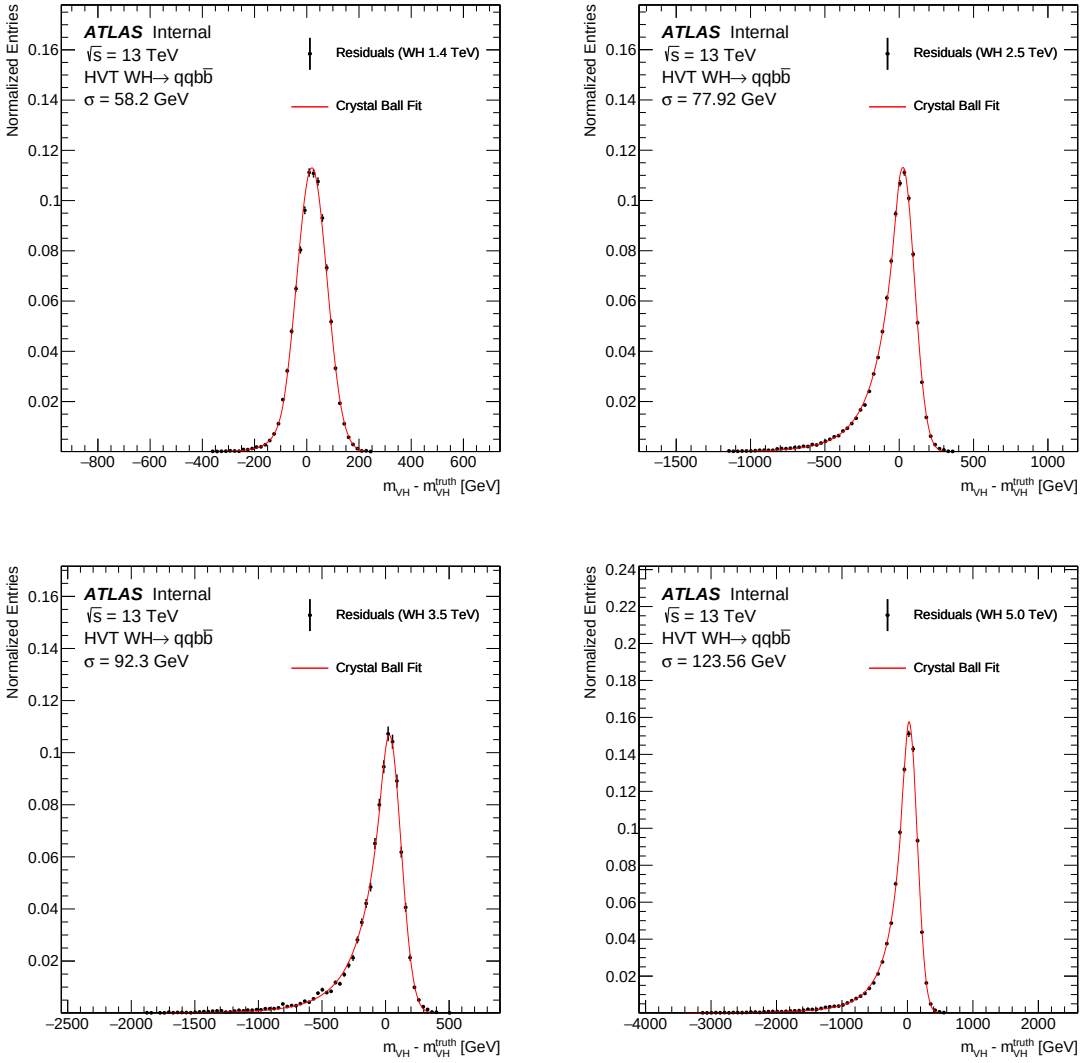

Fig. 5.37 Results for Crystal Ball fits to the HVT WH dijet mass residuals ($m_{VH} - m_{VH}^{\text{truth}}$) for 1.4, 2.5, 3.5 and 5.0 TeV mass values.

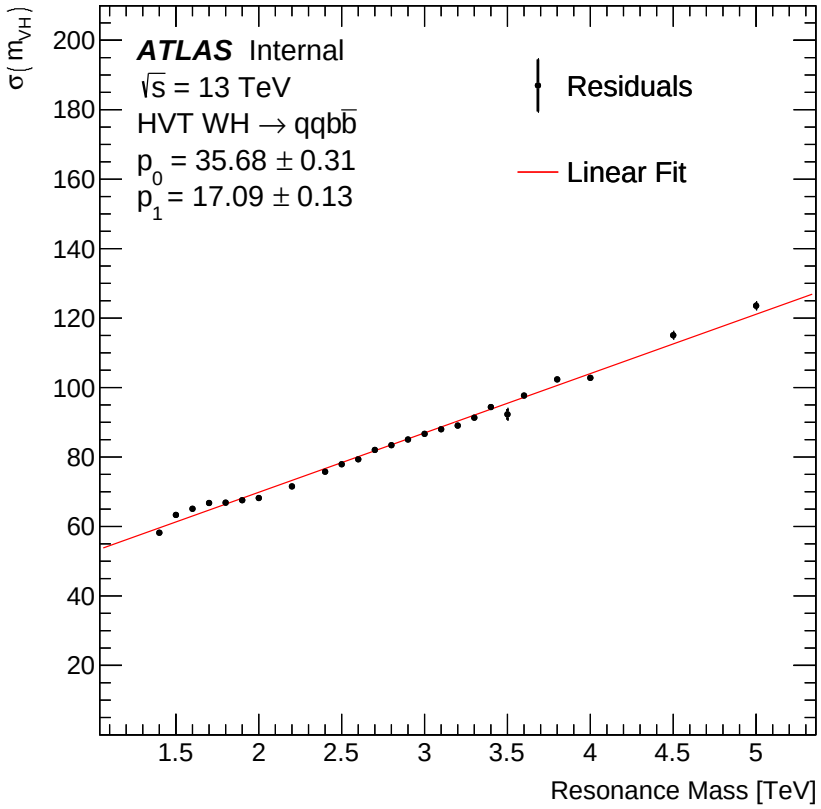

Fig. 5.38 A linear fit to the m_{JJ}resolution trend as a function of signal resonance mass. The result of this fit is used to derive a set of variable width bins to utilize for the final input histograms to the statistical framework.

After the m_{JJ} histograms are produced with the variable-binning described above, Eq. 5.6.4 is fitted to the prediction for each channel with a three parameter function,

$$\frac{dn}{dx} = e^{-p_0}\,(1-x)^{-p_1}\,x^{-p_2}, \tag{5.6.4}$$

where $x = \frac{m_{\mathrm{JJ}}}{\sqrt{s}}$ and p_0 through p_2 are parameters determined by the fit. The normalization parameter is exponentiated as e^{-p_0} to aid in numerical stability by avoiding very small values for p_0. This functional form models changes in the smoothly falling power-law behavior of the background. Fits are performed separately for 1-tag and 2-tag channel background estimates for each signal region.

To achieve further numerical stability of the minimization algorithm used by the fit, the histograms are first normalized before fitting. After fitting, the histograms are re-scaled with the correct propagation of errors applied to both the statistical error of the fit as well as the normalization fit parameter p_0. The fitting method used is a weighted maximum likelihood [7], due to the fact that the bin contents come from the BDT-reweighted prediction with non-unity event weights. This replaces the familiar Poisson likelihood with a modified approximate Poisson likelihood based on the number of *effective entries* in each bin, defined as $(\sum w_i)^2 / \sum w_i^2$, where w_i is the weight of the i-th event in the bin.

The error on the fit is computed by taking the eigenvectors of the covariance matrix which describes the errors on the fit parameters. Each eigenvector is used to produce a new variation of the fit, and the differences between these variations and the nominal are summed in quadrature on a bin-by-bin level to produce the statistical errors associated with the fit as shown by the grey band in Figure 5.39.

The $\frac{\chi^2}{n.d.f.}$ is computed by first rebinning the resulting pre/post-fitted histograms to achieve approximately gaussian statistics in each bin. This is done by searching

[7] This is achieved by supplying the "WL" option to `TH1::Fit`

the bins upwards, starting from 1.3 TeV, and finding the first bin with a number of effective entries (defined above) below five. This bin is then merged with all bins above, up to 7 TeV. The $\frac{\chi^2}{n.d.f.}$ is then computed bin-by-bin with the standard formula.

	SRWH (1-tag)	SRWH (2-tag)	SRZH (1-tag)	SRZH (2-tag)
p_0	14.81 ± 0.47	16.41 ± 0.34	16.21 ± 0.46	17.92 ± 0.32
p_1	7.59 ± 0.56	4.74 ± 0.67	9.28 ± 0.53	6.74 ± 0.65
p_2	8.38 ± 0.11	8.28 ± 0.12	9.0 ± 0.1	8.94 ± 0.12
χ^2_v	1.08	0.94	1.58	2.27

Table 5.20 Fitted parameters, parameter errors ($\pm 1\sigma$), and reduced χ^2 for each signal channel.

5.7 Statistical Method

A frequentist interpretation of the data is applied via a binned maximum-likelihood (ML) fit performed on the m_{VH} distribution, using the standard package RooStats [84]. The parameter of interest is the signal strength μ, defined as the scale factor on the total number of signal events predicted by each of the models. The background only hypothesis corresponds to $\mu = 0$ and the nominal signal plus background hypothesis corresonds to $\mu = 1$. Histogram templates derived from MC simulation are used for the HVT W′ and Z′ processes, while the data-driven estimates are used for the combined $t\bar{t}$, V+jets, and QCD multijet background. The input histogram bounds are [1.3, 6.0] TeV, and signal mass points up to 5 TeV are tested.

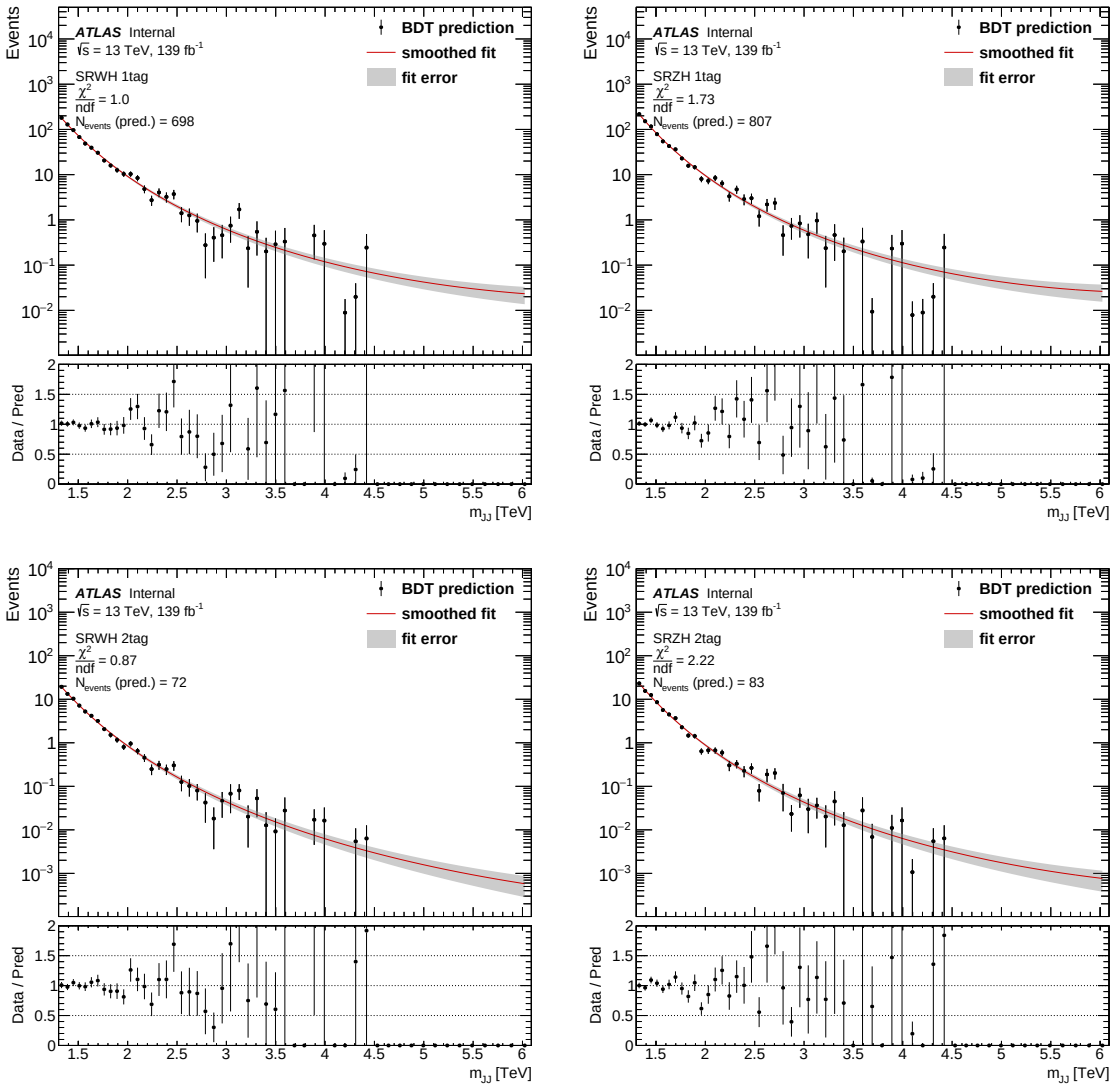

Fig. 5.39 The background predictions for m_{JJ} after kinematic reweighting and fitting for 1-tag (top row) and 2-tag (bottom row) signal regions. The red line shows the final smoothed prediction and the grey band shows the associated statistical error. The black points show the pre-smoothed background prediction after kinematic re-weighting, not the actual signal region events.

5.7.1 Combined Fit

A simultaneous fit is performed to both 1-tag and 2-tag channels, as defined in 5.5.4. This is done separately for each signal region and mass point with the following likelihood formula:

$$L(\mu, \vec{\theta}, \vec{\eta}, \vec{\gamma}) = \prod_{c=1}^{\text{channels}} \prod_{v=1}^{\text{bins}} P_{\text{pois}}\left(N_{cv} | \mu s_{cv} + b_{cv}\right) \times \prod_{j \in \vec{\theta}} \mathcal{N}(\tilde{\alpha}_j | \alpha_j) \times \prod_{k \in \vec{\eta}, \vec{\gamma}} G(\tilde{\beta}_k | \beta_k) \tag{5.7.1}$$

where

- P_{pois} is the Poisson probability distribution function (PDF).
- N_{cv} is the observed number of events in the signal region data for the bin v in the histogram for channel $c \in$ {1-tag, 2-tag}.
- μ is the *signal strength*, a continuous variable that parameterizes a multiplicative factor on the hypothetical signal cross section.
- s_{cv} is the number of signal events for bin v of the histogram for channel c.
- b_{cv} is the expected number of background events for bin v of the histogram for channel c.
- $\vec{\theta}$ is the set of all normalization NPs.
- $\vec{\eta}$ is the set of all shape-related NPs.
- $\vec{\gamma}$ is the set of NPs denoting the statistical error on the individual bin contents of the signal and background histograms.
- $\mathcal{N}(\tilde{\alpha}_j | \alpha_j)$ is the log-normal PDF of the nuisance parameter α_j corresponding to the auxiliary measurement $\tilde{\alpha}_j$.
- $G(\tilde{\beta}_k | \beta_k)$ is the Gaussian PDF of the nuisance parameter β_k corresponding to the auxiliary measurement $\tilde{\beta}_k$.

Both s_{cv} and b_{cv} themselves depend upon a subset of the nuisance parameters $\vec{\theta}$ and $\vec{\eta}$ as described in section 5.8. Nuisance parameters which produce bin variations which are smaller than 1% with respect to the nominal bin contents are pruned away. For each bin in each histogram, interpolation must be performed between the nominal bin prediction and the variations induced by the nuisance parameters to produce the actual value of s_{cv} and b_{cv} used to compute the likelihood. Details on the benefits and drawbacks of various interpolation options, as well as the default options used here, are discussed in [85].

5.7.2 Upper Limits on Cross Section

Upper limits on the signal strength μ are set using a modified frequentist method (CL_s) [86]. The values CL_{s+b} and CL_b are computed using an asymptotic method [87] and correspond to the p-values for the signal-plus-background and background-only hypothesis, respectively. Limits at 95% confidence level on the signal strength can be computed by (1) scanning values of μ (2) computing CL_s and (3) identifying $\mu_{0.05}$ (the value of μ at which $CL_s = 0.05$).

For the calculation of the p-values used in this computation, a test statistic $\lambda(\mu)$ is defined as a profile-likelihood ratio:

$$\lambda(\mu) = \begin{cases} -2\ln\frac{L(\mu,\hat{\hat{\Theta}}(\mu))}{L(\hat{\mu},\hat{\Theta})}, & 0 \leq \hat{\mu} \leq \mu \\ 0, & \hat{\mu} > \mu \\ -2\ln\frac{L(0,\hat{\hat{\Theta}}(0))}{L(\hat{\mu},\hat{\Theta})}, & \hat{\mu} < 0 \end{cases}$$

where L is the likelihood and $\Theta \equiv \{\vec{\theta}, \vec{\eta}, \vec{\gamma}\}$ is the full set of all nuisance parameters, all described in 5.7.1. The global best fit values for μ and Θ are denoted $\hat{\mu}$ and $\hat{\Theta}$,

while the best fit values of Θ for a particular value of μ are denoted $\hat{\hat{\Theta}}(\mu)$. This ratio of likelihoods, for the case of a given μ hypothesis, quantities the compatibility of the data with such a hypothesis.

5.8 Systematic Uncertainties

This section describes the sources of systematic uncertainty considered in this analysis, which are divided into two main categories: experimental uncertainties, which impact only the signal distributions because the background is data-driven, and the uncertainties in the modelling of the background estimate. The impact of these uncertainties is estimated on the final discriminant variable (m_{JJ}).

5.8.1 Experimental Uncertainties

5.8.1.1 Luminosity Uncertainty

The uncertainty in the combined 2015–2018 integrated luminosity is 1.7% [10], obtained using the LUCID-2 detector [88] for the primary luminosity measurements. This uncertainty is applicable only to the simulated signal samples and has only a small impact on this analysis.

5.8.1.2 Large-R Jet p_T scale and resolution

Uncertainty in the jet p_T scale (JpTS) is an important uncertainty to consider in any search for resonant structures with a smoothly falling dijet background. The effect of this uncertainty manifests as a shift in the peak of the expected signal mass spectrum, which alters the significance of any observed excess. The uncertainties on the jet p_T scale (JpTS) are evaluated by the combined performance groups using

track-to-calorimeter double ratios between data and MC. Discrepancies observed between data and MC are assigned as uncertainties on the p_T scale of the jet.

The ratio of the two measures of jet p_T (calorimeter-based and track-based) is expected to be the same (though not equal to one) in both data and MC. Any observed differences are assigned as baseline systematic uncertainties. Additional uncertainties due to the reconstruction and modelling of tracks are taken into account as well. These uncertainties are taken from the inner detector group tools and cover track reconstruction efficiency, impact parameter resolution, tracking in dense environments, track fake rate, and sagitta biases. The size of the total JpTS uncertainty (including baseline ratio, statistical, and tracking uncertainties) varies with jet p_T and is around 5% to 10% for the full mass range. The uncertainties are computed in bins of $\frac{m_{jet}}{p_T^{jet}}$ and η, with one typical example result shown in Figure 5.40.

Due to the unique track-influenced nature of TCC jets, the impact of possible correlations between track-based p_T and calo-based p_T were studied by considering a data/MC comparison method between calo-based (LCTopo) jets and TCC jets. The results are shown in Figure 5.41, and the observed discrepancy was found to have a maximum value of 2% and the effect is thus ignored.

Uncertainties due to jet p_T measurement resolution (JpTR) would lead to a mis-measurement of the width of any observed signal and impact the signal selection efficiency. Additional uncertainties due to the jet energy are estimated by applying a Gaussian smearing which degrades the nominal p_T resolution of jets by an absolute 2%. The changes to the overall yield and m_{JJ} shape are then assigned as 'up' variations, and the corresponding 'down' variation is taken by mirroring the difference between the nominal and 'up' variations.

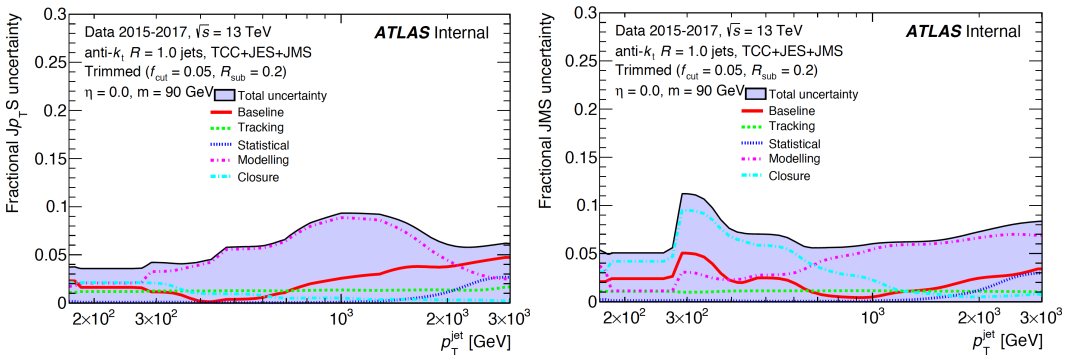

Fig. 5.40 Fractional jet p_T scale (left) and mass scale (right) systematic uncertainty components for anti-k_t, $R = 1.0$ TCC jets in the $\eta = 0$ and $m = 90$ GeV bin, using the TCC+JES+JMS calibration scheme. The total uncertainty (all components summed in quadrature) is shown as a filled blue region topped by a solid black line.

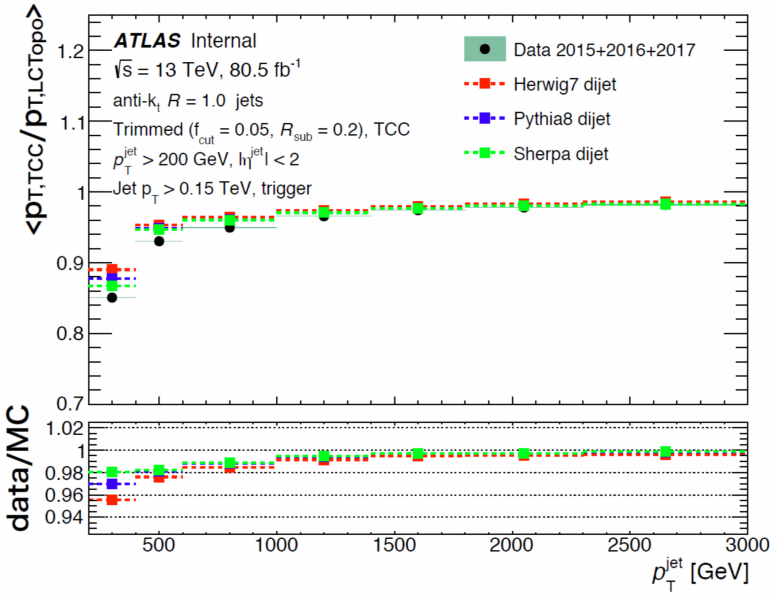

Fig. 5.41 Average ratio of jet p_T for TCC jets to jet p_T for LCTopo jets as a function of p_T for anti-k_t $R = 1.0$ jets with $|\eta| < 2$. © CERN

5.8.1.3 b-tagging Uncertainties

The uncertainties related to the b-tagging efficiency calibrations as measured in $t\bar{t}$ events for track-jets are considered, using the official ATLAS prescriptions [57, 56]. These uncertainties result from three broad categories: *MC generator modelling uncertainty* which impact the kinematic distributions and jet flavour composition in simulated events, *normalisation uncertainty* which account for uncertainties in the cross-section of simulated samples, and *experimental uncertainties* which cover uncertainties in detector effects and reconstruction of physics objects.

These uncertainties enter the analysis through variations on the b-tagging simulation-to-data scale factors. The number of systematic variations is ultimately reduced by summing together the covariance matrices (with respect to jet p_T) for each variation and computing the eigenvectors of this total covariance matrix.

5.8.1.4 Boson Tagging Uncertainties

Additional uncertainties related to boson tagging can impact both the V/H tagging efficiency as well as the resulting dijet mass shape. These uncertainties include jet mass scale (JMS), jet mass resolution (JMR), jet D_2 resolution (D2R) and uncertainties due to the n_{trk} variable. The JMR and JMS systematic uncertainties for TCC jets are officially provided by ATLAS Jet working group and included in the analysis. Since vector boson tagging and Higgs boson tagging implement different selections using different observables, a separate description of the signal systematic uncertainties related to the two taggers is provided in the following paragraphs. In the end the V boson and H boson systematics are treated as uncorrelated.

5.8.1.5 Vector boson tagging scale factor and uncertainties

As already described in Section 5.5.3.1, this analysis uses a modified version of the 3 variables (jet mass, D_2, and n_{trk}) vector-boson tagger optimised by the fully-hadronic diboson resonance search team for the full Run-2 paper [89]. Jet invariant mass and D_2 selections follow exactly the same definitions as the ones used in the fully hadronic diboson resonance search, while the n_{trk} selection has been loosened by the maximum sensitivity optimisation performed for the event selection of this analysis. Given the shape of the n_{trk} distribution for vector bosons, a small change in the n_{trk} selection (VH allows on average 3 more tracks than VVJJ for both W-boson and Z-boson selection) produces a small and almost linear change in signal efficiency. For this reason, the same boson tagging scale factor and relative systematic uncertainty derived in the VVJJ analysis is applied in this analysis. In particular, a data-to-MC SF of 0.92 ± 0.13 is applied to our MC signals, which was derived via studies of W/Z tagging in real V+jets events in data/MC. The 0.13 is considered as signal normalisation scale factor uncertainty. It includes high p_T extrapolation, modelling uncertainties, impact of jet mass scale and resolution, and fitting uncertainties.

5.8.1.6 Systematic uncertainties for Higgs tagging

Given the very small cross section of the Higgs boson, it is not possible to define a H+jets control region where a data-to-MC H-tagging scale factor for n_{trk} selection can be evaluated. In the 2017 fully hadronic diboson resonance search [90], a 1.03 ± 0.05 data-to-MC scale factor for n_{trk} in vector bosons has been measured in a V+jets control region.

Summing in quadrature the 3% scale factor with the 5% systematic uncertainty, the fully hadronic diboson resonance search considered a conservative 6% data-to-MC scale factor for the n_{trk} variable. The impact of this scale factor on the signal

normalisation was observed to be approximately 13%. In the case of applying this result to the n_{trk} selection for H-tagging in this analysis, the 13% result obtained for V-tagging is not directly applicable: phase-space and topology differences need to be taken into account. In order to quantify these differences and assess additional uncertainties for this particular selection, an n_{trk} double ratio has been defined as a function of the jet mass. Eq. 5.8.1 shows the definition of this quantity:

$$R_{\text{ntrk}} = \frac{\frac{\text{jet}_m^{\text{data}}|\text{w/o } n_{\text{trk}}}{\text{jet}_m^{\text{MC}}|\text{w/o } n_{\text{trk}}}}{\frac{\text{jet}_m^{\text{data}}|\text{w/ } n_{\text{trk}}}{\text{jet}_m^{\text{MC}}|\text{w/ } n_{\text{trk}}}} \tag{5.8.1}$$

The purpose of the R_{ntrk} quantity is to compare the jet mass distributions for the mass range [60,150] GeV in both data and multijet MC samples, with and without applying the n_{trk} selection. This comparison has been repeated for different b-tagging conditions in order to check the impact on R_{ntrk} produced by the correlation between n_{trk} and b-tagging. Figure 5.42 shows R_{ntrk} for different b-tagging selections. A 2% difference between the ratio in the Vector boson (red line) and Higgs boson (yellow line) jet mass regions is visible in the top-left plot. This difference can be partially explained by the presence of real W/Z bosons in data that are not included in QCD MC. Both 1-tag (top-right) and 2-tag (bottom plot) channels do not show differences larger that 1%. In order to be conservative while evaluating this difference only on background dominated samples, the 2% observed difference in R_{ntrk} is inflated up to 5% and then added in quadrature to the original 6 % data-to-MC n_{trk} scale factor obtained on 2015-2016 data in V+jets control region. This resulting n_{trk} uncertainty from Higgs tagging resolves to a 10% signal normalisation uncertainty. Any shape effects on the signal peak due to the n_{trk} scale factor are considered as negligible.

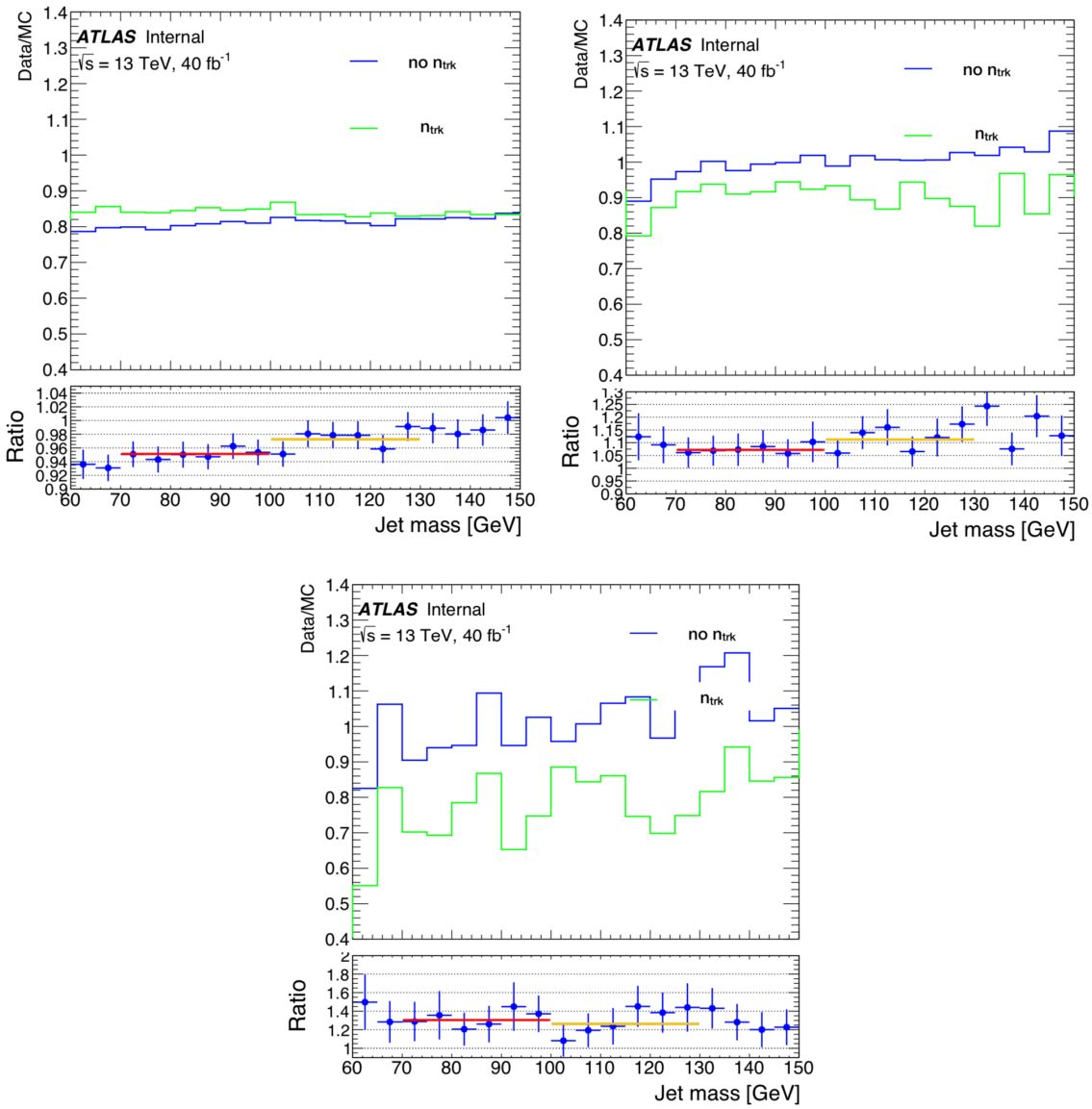

Fig. 5.42 R_{ntrk} for different inclusive b-tagging (top-left), 1 b-tagging (top-right), and 2 b-tagging (bottom) selections. The red and yellow lines in the ratio panels show the average R_{ntrk} values for the vector- and Higgs- boson mass windows, respectively.

5.8.1.7 Large-R Jet Mass Resolution

Jet mass resolution variations are produced by randomly smearing the jet mass by 20% relative to the nominal resolution, using resolution maps provided by the ATLAS jet working group under the assumption of different jet truth origin. For this analysis, the maps for $H \rightarrow b\bar{b}$ large-R jets are used. A comparison of TCC vs. LCTopo large-R Higgs jet mass resolution is shown in Figure 5.43, produced with the signal samples from this analysis.

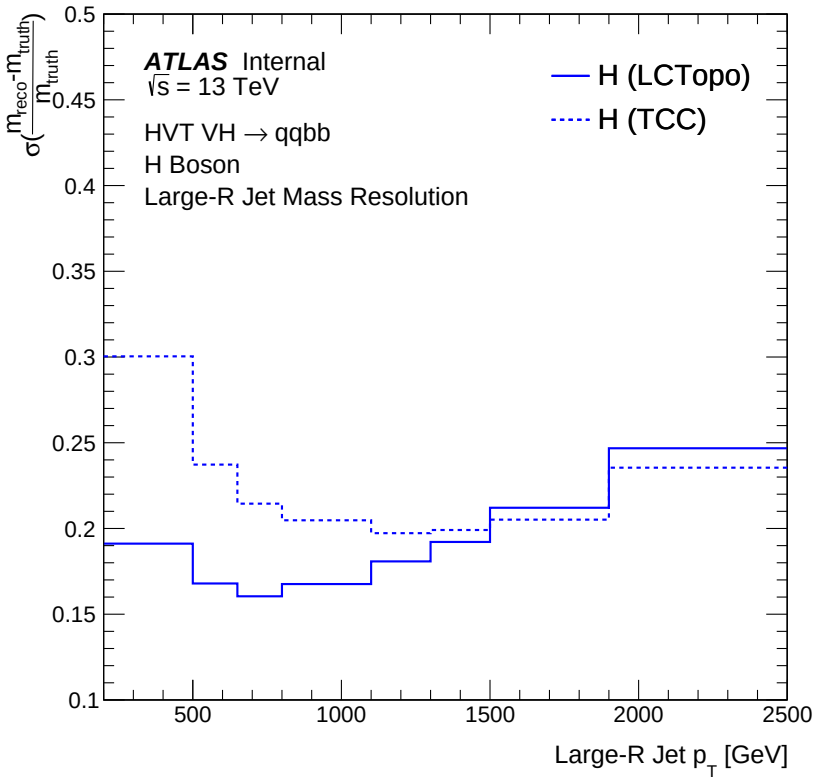

Fig. 5.43 Fractional Jet Mass Resolution (JMR) for truth Higgs jets with pre-selection applied. The JMR is computed here from a Gaussian fit, as opposed to the method from JetEtMiss utilizing the interquartile range (IQR). This yields a larger, more conservative value for the JMR. © CERN

5.8.1.8 μ Uncertainty

The uncertainty on the background normalization estimate from statistical as well as non-closure related uncertainty is described in Section 5.6.2.

5.8.1.9 BDT Re-Weighting Uncertainty

The BDT re-weighting algorithm is trained in the control region (CR) and applied to the validation and signal regions. To account for the uncertainty in this extrapolation, a shape systematic uncertainty is derived by applying the background fitting method outlined in Section 5.6.5 to both the BDT re-weighted prediction as well as the actual data in a particular validation region (VR2B) chosen due to the high event yield. The ratio of the smoothed fits of the BDT prediction and data, shown in Figure 5.44, is used to produce m_{JJ}-dependent weights. These weights are then used to produce up/down shape variations for each signal region and channel. The predominant effect of this uncertainty manifests in the high m_{JJ} tail. To allow more flexibility in the likelihood fit, this systematic is split into two separate low/high mass regions below/above 2.5 TeV.

5.8.1.10 Background Smoothing Function Choice Uncertainty

Systematic uncertainty due to the choice of fit function is considered by applying the same method described in Section 5.6.5, but with a different smoothing function: $e^{-p_0}\,(1-x)^{-p_1}\,(1+x)^{-p_2 \log x}$. Results are shown in Figure 5.45. To allow more flexibility in the likelihood fit, this systematic uncertainty is split into two separate low/high mass regions below/above 2.5 TeV.

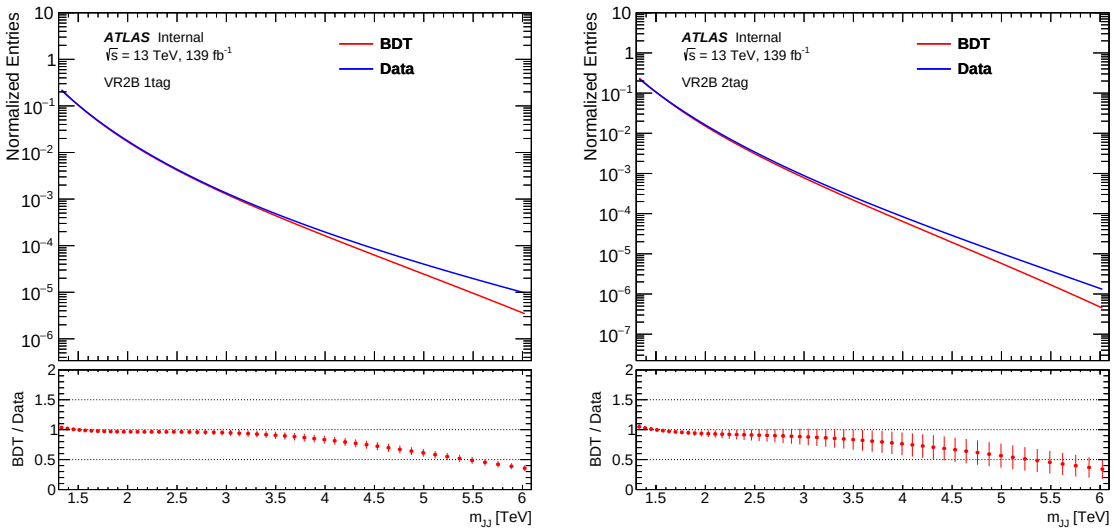

Fig. 5.44 Separate smoothing results for the BDT re-weighted prediction (red) as well as data (blue) for the 1-tag (left) and 2-tag (right) channels in the VR2B validation region. The ratio panel shows the ratio of these two predictions, which is used to derive m_{JJ} dependent weights which are subsequently used to produce up/down variations for each signal region/channel to account for uncertainty in the shape effects resulting from the BDT re-weighting procedure.

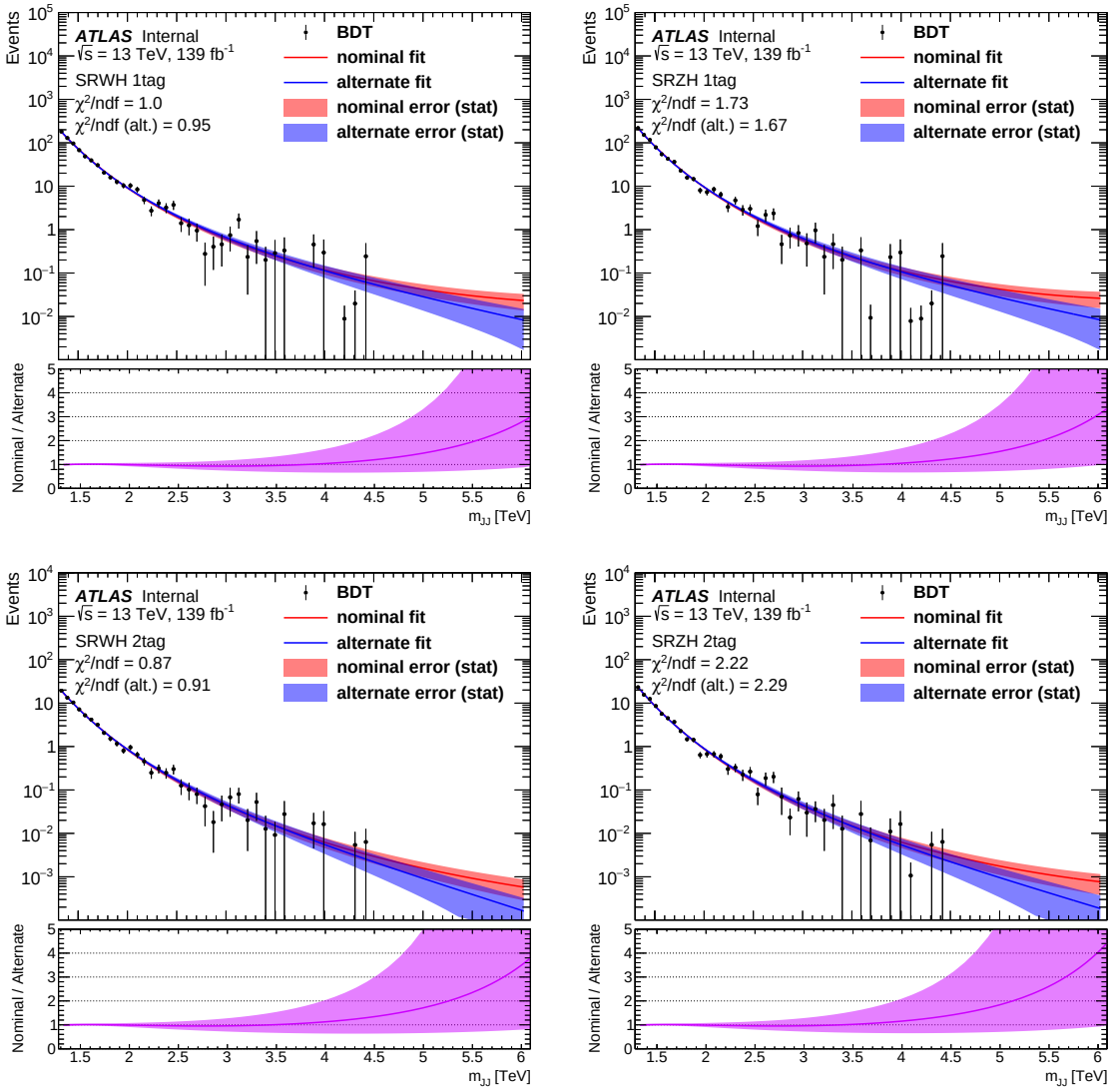

Fig. 5.45 Smoothing fit function variations produced with the alternative fit function: $e^{-p_0}\,(1-x)^{-p_1}\,(1+x)^{-p_2\log x}$.

5.8.2 Theory Uncertainties

5.8.2.1 Parton Distribution Function Uncertainties

Uncertainties in the behavior of the parton distribution functions at the high Q^2 values explored in this analysis can potentially have a large effect on the production rate of any signal. This systematic uncertainty is derived by applying the methodology outlined by the PDF4LHC group using event-level re-weighting[8] to four additional PDF sets[9].

Any systematic error introduced due to PDF variations must be reported as an uncertainty on the signal acceptance rather than the signal cross section. The acceptance is defined as $\frac{\Sigma_{\text{weights}}(\text{signal selection})}{\Sigma_{\text{weights}}(\text{no selection})}$. The uncertainty on signal acceptance is estimated by computing variations in the acceptance ratio, defined as the ratio between the acceptance for a particular PDF variation and the nominal acceptance. The PDF *variations* here can be either a comparison to different PDF sets, as well as comparisons to variations in the error sets of the nominal PDF. For all signal regions and mass points the impact was shown to be less than 1%, so no uncertainties due to PDF variations are included in the results.

5.8.2.2 ISR/FSR Uncertainties

Any choice of MC tune merits the use of additional systematic uncertainties to cover variations in Initial State Radiation (ISR), Final State Radiation (FSR), and Multi-Parton Interactions (MPI). The expected effect on signal efficiency is evaluated at truth level before applying boson tagging cuts, following the same procedure as for the PDF variations described above.

[8] https://lhapdf.hepforge.org
[9] CT14, MMHT2014, NNPDF3.0, and ATLAS-epWZ12

The impact on signal acceptance is demonstrated in Figure 5.46. In the final results a flat systematic uncertainty on the signal normalization of 2%(3%) for WH(ZH) is used.

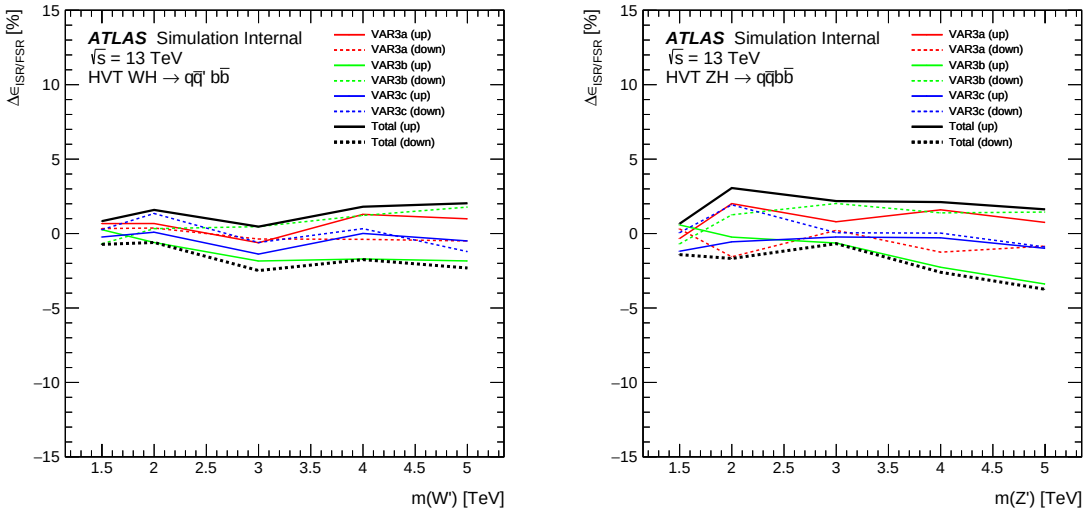

Fig. 5.46 Impact on signal acceptance × efficiency vs. resonance mass for each of the ISR/FSR tune variations under consideration.

Chapter 6

RESULTS

In this section the results of the combined fit with the full 2015, 2016, 2017, and 2018 datasets will be presented, corresponding to a total integrated luminosity of 139 fb^{-1}.

6.1 Post-Fit Dijet Mass

Post-fit studies performed on various mass points for both WH and ZH final states are used to verify the integrity of the fits. In all cases, stable results are obtained and only a representative set of studies is shown in this chapter. Figure 6.1 shows the resulting post-fit m_{JJ} distributions. No significant deviation from the background prediction is observed.

6.2 Nuisance Parameters

The pulls and constraints on the nuisance parameters are shown in Figure 6.2 for the WH 2.6 TeV and ZH 4.0 TeV mass points. The ranking of nuisance parameters is shown in Figures 6.3 and 6.4 for 2.6 TeV and 4.0 TeV signal mass points, respectively. In these ranking plots, the change in the $\hat{\mu}$ value obtained by repeating the fit with a given nuisance parameter (NP) shifted by $+1\sigma$ or -1σ from its nominal value is

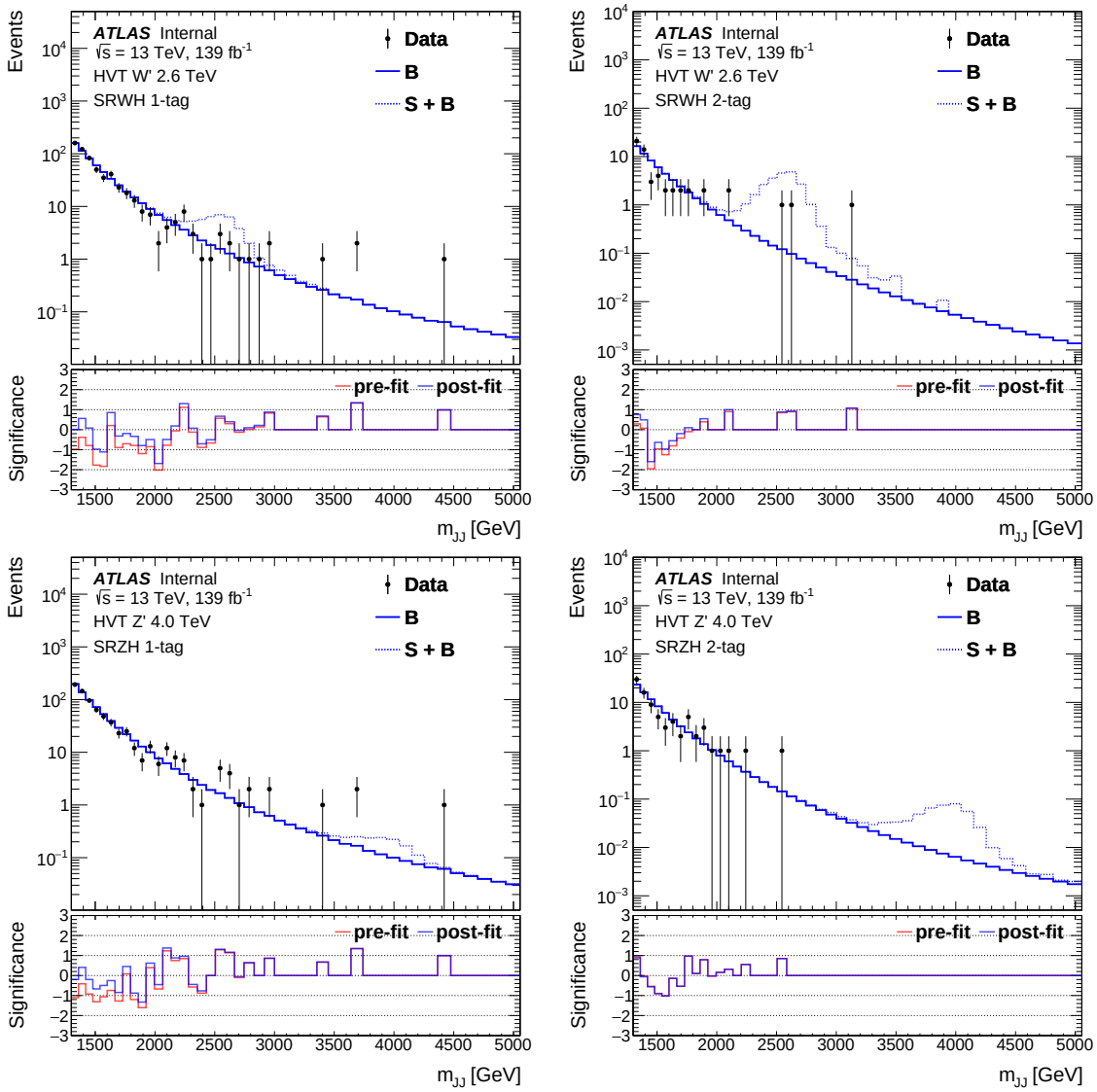

Fig. 6.1 Post-fit m_{JJ} distribution for the 2.6 TeV mass point in SRWH (top row) and SRZH (bottom row) for both the 1-tag (left) and 2-tag (right) channels. The black points correspond to the data, the solid blue histogram corresponds to the post-fit background distribution, and the dashed blue line corresponds to the post-fit signal + background distribution. The bottom panel showcases the Poisson significance of the observed deviations away from the prediction both before (red) and after (blue) the likelihood fit.

determined. This variation in the resulting best-fit value of μ is what *ranks* the NP relative to others. By performing this procedure for each NP, the relative impact of each NP on the results can be estimated.

At a resonance mass of 2 TeV, the background normalization and shape uncertainties dominate, but at the 4 TeV mass point the large-radius jet and boson tagging uncertainties dominate due to the vanishing background expectation in the high m_{JJ} region. The method of estimation for the background normalization NP described in Section 5.6.2 is intentionally conservative, which explains its particularly high ranking for the 2.6 TeV mass point observed in Figure 6.3. However, for the 4.0 TeV mass point the background expectation is small enough (< 0.1 events) that the background normalization uncertainty plays a less prominent role, as seen in Figure 6.4.

The overall quality of the likelihood fit also depends upon the correlation between different NP. If it is the case that two NP are degenerate and represent nearly identical effects, this would result in double-counting and an artificially enhanced variation. To this end a matrix describing the correlations between NP is shown in Figure 6.5 for a pair of WH signal mass points. No significant correlation between any two NP is observed.

6.3 Local Significance

The relevance of any excesses observed in data with respect to the background expectation is quantified by estimating the local significance (p_0) using the asymptotic approximation. The combined local significance of the 1-tag + 2-tag channels is shown for both WH and ZH samples in Figure 6.6. The largest deviation is observed

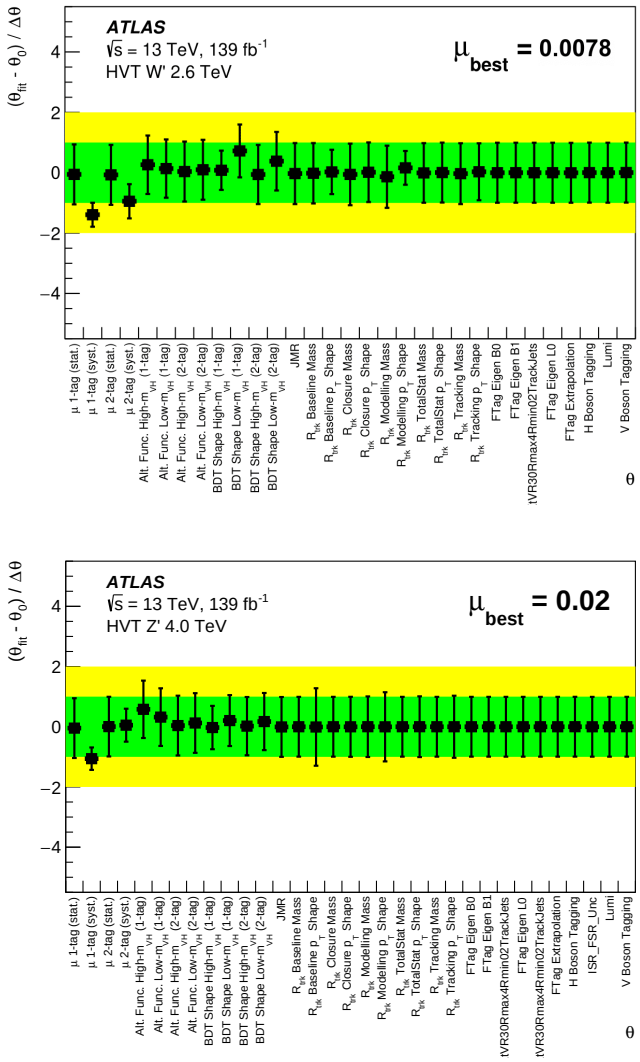

Fig. 6.2 Pulls and constraints on nuisance parameters in the unconstrained-μ fit (described in Section 5.7.1) for the 2.6 TeV WH (top) and 4.0 ZH (bottom) signal mass points.

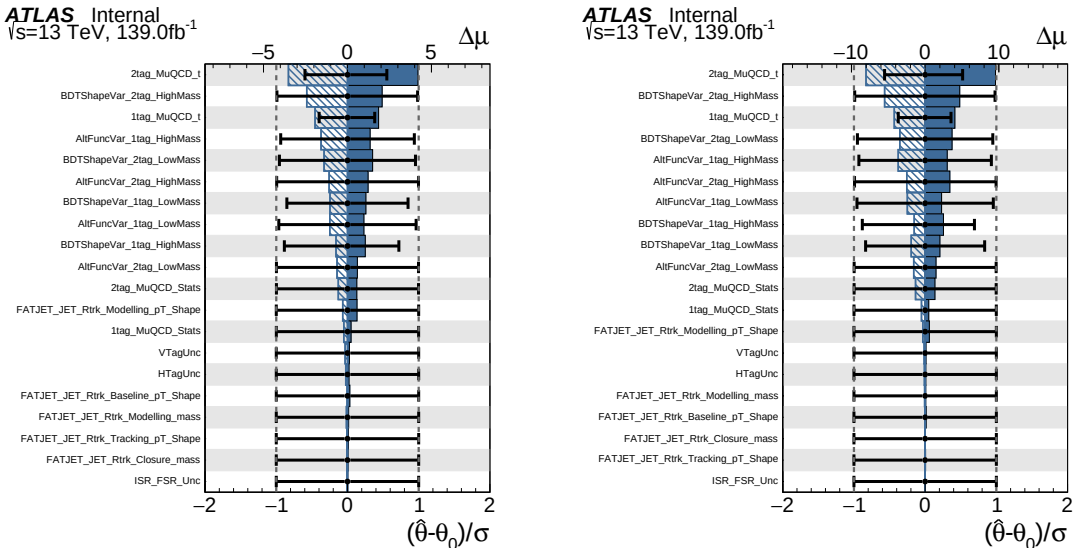

Fig. 6.3 Ranking of nuisance parameters in terms of post-fit impact on $\hat{\mu}$ for the WH (left) and ZH (right) channels for the 2.6 TeV S+B fit. Note that the signal strength μ has been scaled by a factor of $1,000$ for purely numerical reasons.

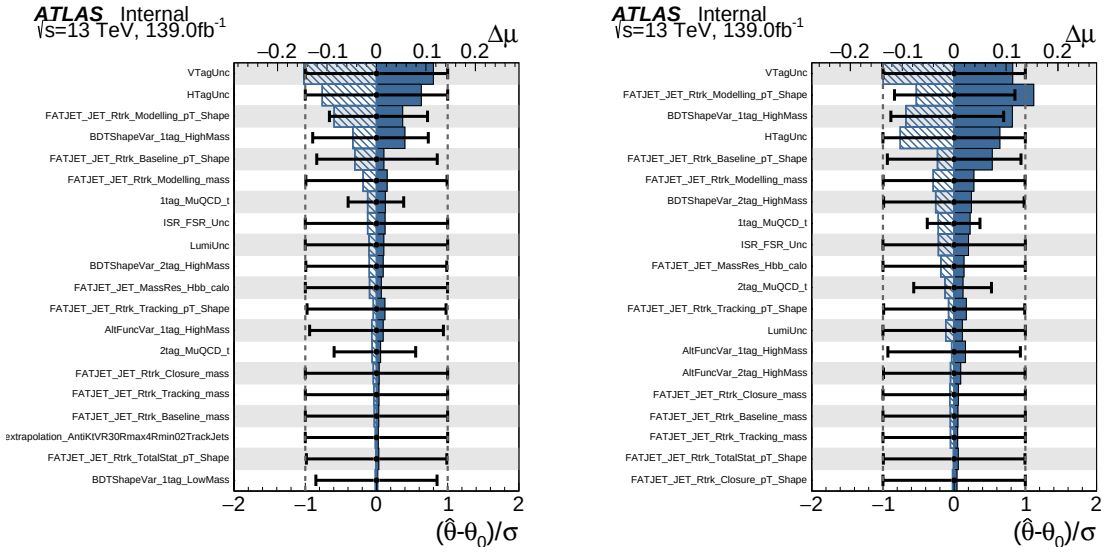

Fig. 6.4 Ranking of nuisance parameters in terms of post-fit impact on $\hat{\mu}$ for the WH (left) and ZH (right) channels for the 4.0 TeV S+B fit.

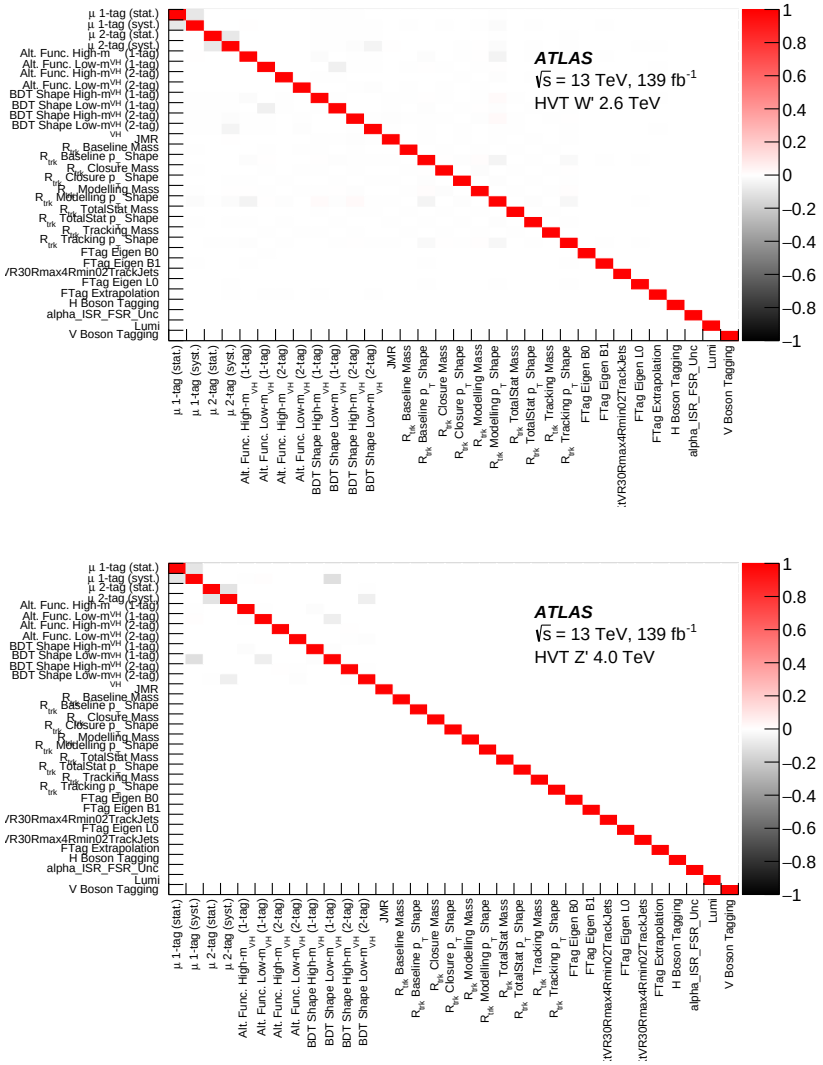

Fig. 6.5 Correlation matrix of nuisance parameters for the 2.6 TeV WH (top) and 4 TeV ZH (bottom) signal mass points.

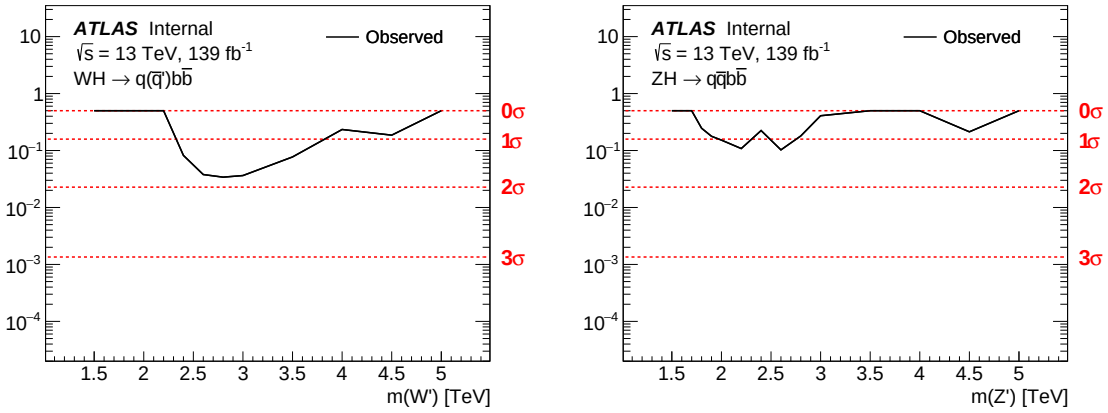

Fig. 6.6 Observed local p_0 values for the combined 1-tag + 2-tag WH (left) and ZH (right) channels.

in the fit to the WH signal region and corresponds to a p_0 value of 0.03 for a resonance mass of 2.8 TeV.

6.4 Upper Limits on Cross Section

Upper limits on the cross section times branching ratio for a resonance decaying to VH are shown in Figure 6.7, for both the WH and ZH signal regions. The expected and observed upper limits are compared to the predictions for HVT Models A and B, from which mass exclusion values can be determined. For Model A, the excluded signal mass ranges are 1500-2900 GeV for WH resonances, and 1500-2200 GeV for ZH resonances. For Model B, the excluded signal mass ranges are 1500-3200 GeV for WH resonances, and 1500-2650 GeV for ZH resonances. These results can also be translated into exclusions in the $\{g_H, g_f\}$ plane, where g_f represents a universal coupling between the V' bosons and fermions. Here, g_q is taken to be equal to g_f. Figure 6.8 shows the 95% CL limits in this plane for several resonance masses. Refer back to Section 5.1 for details concerning the definitions of these coupling parameters.

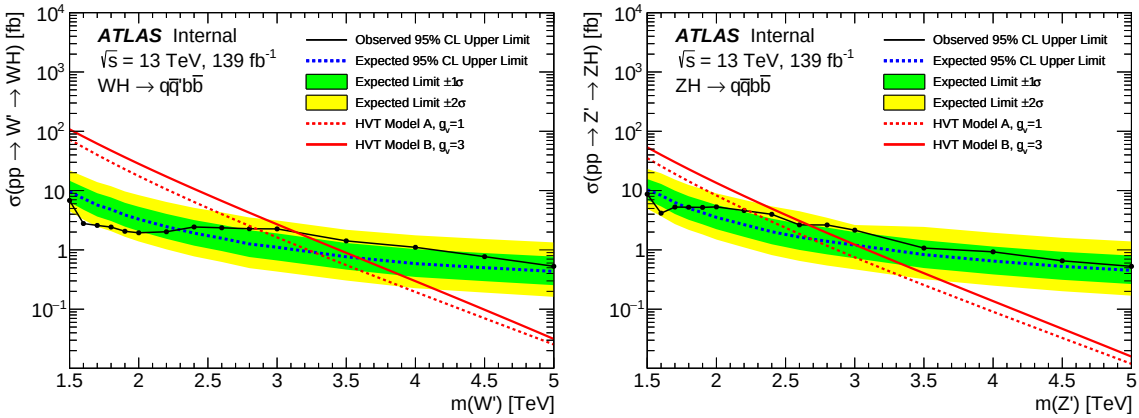

Fig. 6.7 Upper limits on $\sigma(V' \to VH)$ at 95% CL for WH (left) and ZH (right) channels. The figures show the expected limits and predicted cross sections for the HVT Models A and B.

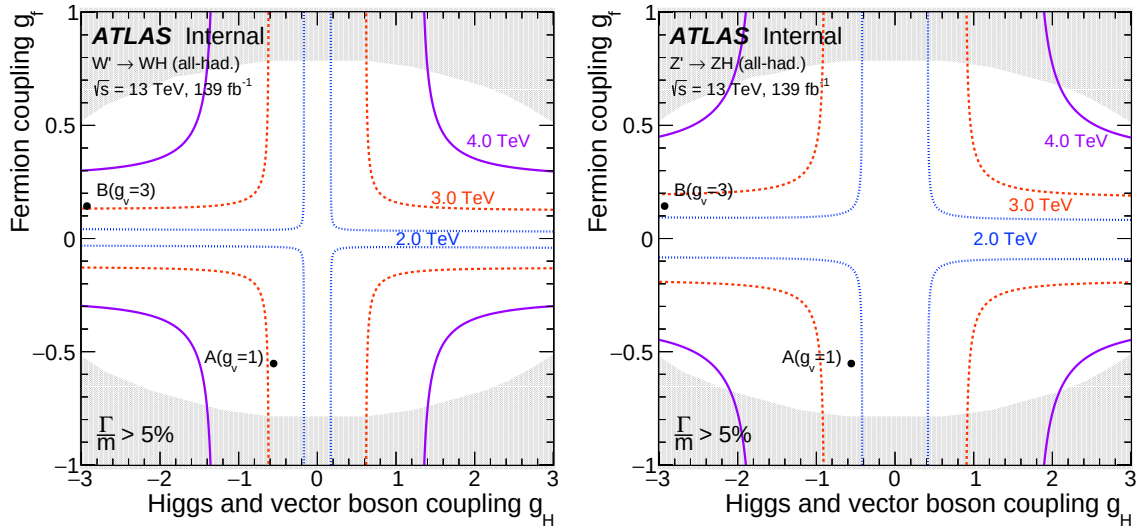

Fig. 6.8 Limits in the g_f vs. g_H coupling plane for resonance masses of 2, 3, and 4 TeV for the WH (left) and ZH (right) channels in the context of the HVT model. The coupling values corresponding to the HVT models A and B are indicated by filled circles. The gray region indicates the values of the couplings corresponding to V' resonances with $\Gamma/m > 5\%$. In that region the assumption that the V' signal m_{JJ} shape is dominated by the experimental resolution is no longer valid.

The relative contribution of the two separate channels to the combined limit is primarily explained by the VR track-jet containment of the two b-hadrons resulting from the Higgs decay. The VR jet clustering algorithm used in this analysis cannot capture the products of each separate b-hadron decay within two separate VR track jets up to arbitrarily high jet p_T. This is because the separation in the $\eta - \phi$ plane of the products of a two body decay is inversely proportional to the p_T of the parent. As Higgs jet p_T increases the probability for both resulting b-hadrons to be fully contained within a single track-jet increases, and the 1-tag channel gradually becomes the channel with dominant sensitivity. Another reason for the increased impact of the 1-tag channel at higher jet p_T is the fact that the b-tagging efficiency decreases with increasing p_T. The cross-over point, as demonstrated in Figure 6.9, is at approximately 4 TeV.

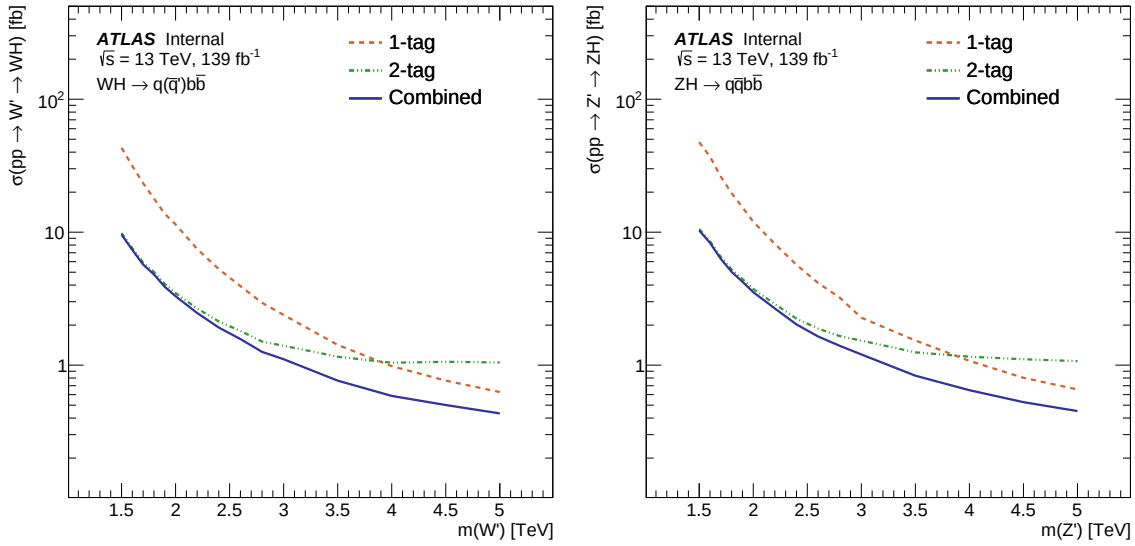

Fig. 6.9 Upper limits on $\sigma(V' \rightarrow VH) \times BR(H \rightarrow b\bar{b})$ at 95% CL for WH (left) and ZH (right) channels. The figures show the expected limits for each channel: 1-tag (dashed orange), 2-tag (dashed green), and combined (solid blue).

The expected limits at 95% confidence level are compared to the previous iteration of the analysis in Figure 6.10, which showcases that the results presented in this thesis

are the strongest constraints to date. The primary sources of improvement in this result are the re-optimized boson tagging criteria, the inclusion of the n_{trk} variable for W/Z and Higgs tagging, the use of VR track jets instead of fixed radius track jets, and the improved background prediction strategy utilizing BDT-reweighting and improved binning/smoothing.

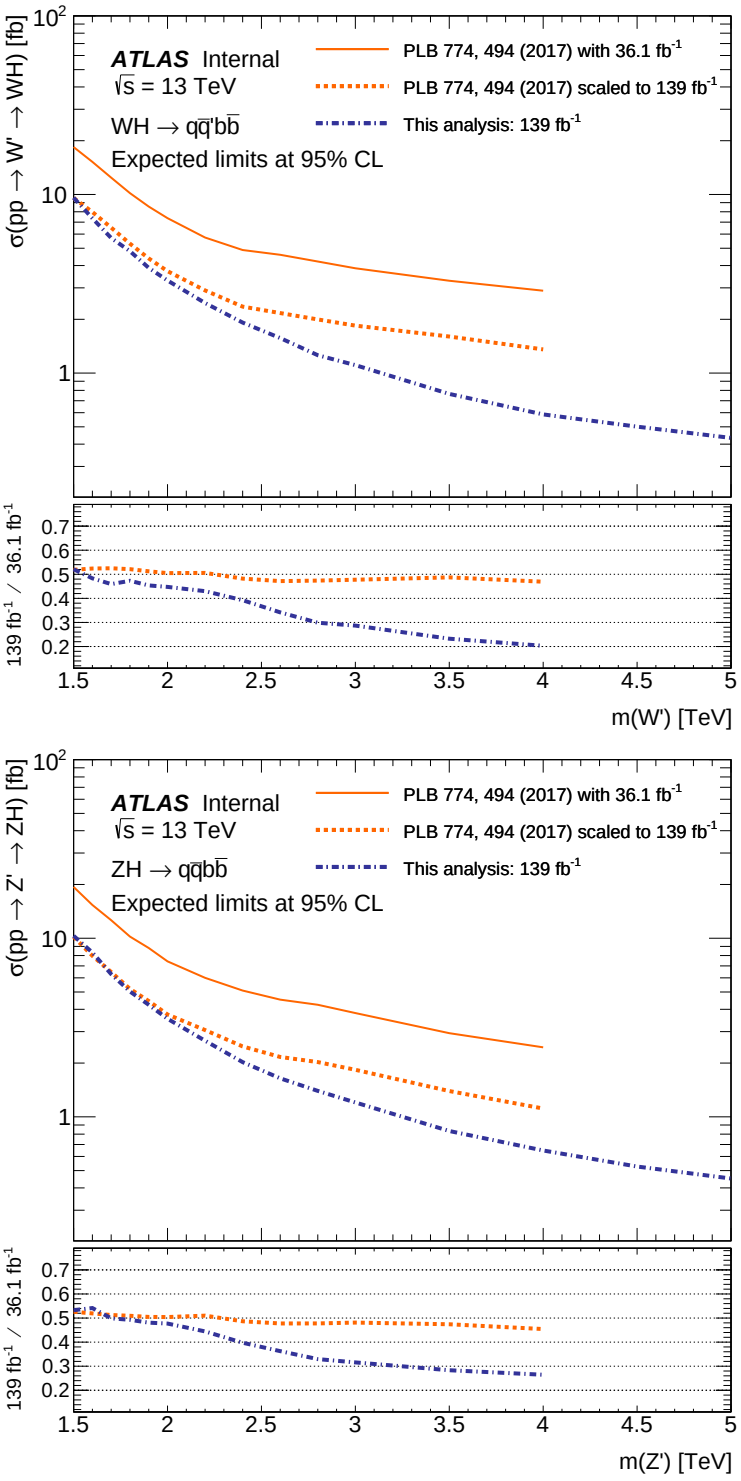

Fig. 6.10 A comparison of expected limits for the WH (top) and ZH (bottom) final states including the previous result [60]. The solid red line shows the published limit, while the dashed red line shows that same with background and signal scaled to match the full Run-2 luminosity. The dashed blue line shows the expected limit results for the current strategy described in this thesis for the full Run-2 luminosity.

Chapter 7

CONCLUSIONS

A search for resonances decaying to a W or Z boson and a Higgs boson has been carried out in the all-hadronic $q\bar{q}^{(\prime)}b\bar{b}$ channel with 139 fb^{-1} of pp collision data collected by ATLAS during 2015-2018 runs of the LHC at $\sqrt{s}$ = 13 TeV. Both the vector boson and Higgs boson candidates are reconstructed using large radius jets, and small radius b-tagged track jets are exploited to tag the Higgs boson candidate jet. The background consists mainly of multijet, $t\bar{t}$, and V+jets events, and is modelled using a data driven method with BDT re-weighting.

No significant excess of events is observed over the expected background and the upper limits set on the crosssection for $pp \rightarrow W' \rightarrow WH$ and $pp \rightarrow Z' \rightarrow ZH$ range from 6.8 fb at m(W′) = 1.5 TeV to 0.53 fb at m(W′) = 5.0 TeV, and from 8.7 fb at m(Z′) = 1.5 TeV to 0.53 fb at m(Z′) = 5.0 TeV, at 95% CL. These results translate into lower limits on the mass of W′ (Z′) bosons of 2.90 TeV (2.20 TeV) in the context of the weakly coupled HVT model A and of 3.20 TeV (2.65 TeV) in the context of the strongly coupled HVT model B, at 95% CL.

REFERENCES

[1] Richard Phillips Feynman. *The principle of least action in quantum mechanics*. PhD thesis, Princeton U., 1942.

[2] V. Bargmann and Eugene P. Wigner. Group Theoretical Discussion of Relativistic Wave Equations. *Proc. Nat. Acad. Sci.*, 34:211, 1948.

[3] Makoto Kobayashi and Toshihide Maskawa. CP Violation in the Renormalizable Theory of Weak Interaction. *Prog. Theor. Phys.*, 49:652–657, 1973.

[4] Nicola Cabibbo. Unitary Symmetry and Leptonic Decays. *Phys. Rev. Lett.*, 10:531–533, 1963.

[5] M. Tanabashi et al. Review of particle physics. *Phys. Rev. D*, 98:030001, Aug 2018.

[6] Michela D'Onofrio and Kari Rummukainen. Standard model cross-over on the lattice. *Phys. Rev. D*, 93(2):025003, 2016.

[7] Florian Bechtel. *The underlying event in proton-proton collisions*. PhD thesis, Hamburg U., 2009.

[8] R. K. Ellis, W. J. Stirling, and B. R. Webber. *QCD and Collider Physics*. Cambridge Monographs on Particle Physics, Nuclear Physics and Cosmology. Cambridge University Press, 1996.

[9] P. Grafström and W. Kozanecki. Luminosity determination at proton colliders. *Prog. Part. Nucl. Phys.*, 81:97–148, 2015.

[10] Luminosity determination in pp collisions at $\sqrt{s}$ = 13 TeV using the ATLAS detector at the LHC. Technical Report ATLAS-CONF-2019-021, CERN, Geneva, Jun 2019.

[11] Matthias Schott and Monica Dunford. Review of single vector boson production in pp collisions at $\sqrt{s}$ = 7 tev. *The European Physical Journal C*, 74(7), Jul 2014.

[12] *ATLAS inner detector: Technical Design Report, 1*. Technical Design Report ATLAS. CERN, Geneva, 1997.

[13] G. Aad et al. The ATLAS Experiment at the CERN Large Hadron Collider. *JINST*, 3:S08003, 2008.

[14] M Capeans, G Darbo, K Einsweiller, M Elsing, T Flick, M Garcia-Sciveres, C Gemme, H Pernegger, O Rohne, and R Vuillermet. ATLAS Insertable B-Layer Technical Design Report. Technical Report CERN-LHCC-2010-013. ATLAS-TDR-19, Sep 2010.

[15] B. Abbott et al. Production and Integration of the ATLAS Insertable B-Layer. *JINST*, 13(05):T05008, 2018.

[16] Heinz Pernegger. The Pixel Detector of the ATLAS Experiment for LHC Run-2. Technical Report ATL-INDET-PROC-2015-001. 06, CERN, Geneva, Feb 2015.

[17] A. Andronic and J.P. Wessels. Transition radiation detectors. *Nuclear Instruments and Methods in Physics Research Section A: Accelerators, Spectrometers, Detectors and Associated Equipment*, 666:130–147, Feb 2012.

[18] M. Aharrouche, J. Colas, L. Di Ciaccio, M. El Kacimi, O. Gaumer, M. Gouanère, D. Goujdami, R. Lafaye, S. Laplace, C. Le Maner, and et al. Energy linearity and resolution of the atlas electromagnetic barrel calorimeter in an electron test-beam. *Nuclear Instruments and Methods in Physics Research Section A: Accelerators, Spectrometers, Detectors and Associated Equipment*, 568(2):601–623, Dec 2006.

[19] Pavol Strizenec and Andrey Minaenko. Performance of the ATLAS liquid argon endcap calorimeter in beam tests. *J. Phys. Conf. Ser.*, 160:012078, 2009.

[20] C. Cojocaru et al. Hadronic calibration of the ATLAS liquid argon end-cap calorimeter in the pseudorapidity region $1.6 < |\eta| < 1.8$ in beam tests. *Nucl. Instrum. Meth. A*, 531:481–514, 2004.

[21] P. Adragna et al. Testbeam studies of production modules of the ATLAS tile calorimeter. *Nucl. Instrum. Meth. A*, 606:362–394, 2009.

[22] *ATLAS muon spectrometer: Technical Design Report*. Technical Design Report ATLAS. CERN, Geneva, 1997.

[23] *ATLAS magnet system: Technical Design Report, 1*. Technical Design Report ATLAS. CERN, Geneva, 1997.

[24] Fabian Kuger. Signal formation processes in micromegas detectors and quality control for large size detector construction for the atlas new small wheel. 08 2017.

[25] Aranzazu Ruiz-Martinez and ATLAS Collaboration. The Run-2 ATLAS Trigger System. Technical Report ATL-DAQ-PROC-2016-003, CERN, Geneva, Feb 2016.

[26] Ian Bird. Computing for the Large Hadron Collider. *Annu. Rev. Nucl. Part. Sci.*, 61:99–118. 20 p, 2011.

[27] Track Reconstruction Performance of the ATLAS Inner Detector at $\sqrt{s} = 13$ TeV. Technical Report ATL-PHYS-PUB-2015-018, CERN, Geneva, Jul 2015.

[28] Andreas Salzburger. Optimisation of the ATLAS Track Reconstruction Software for Run-2. *J. Phys. Conf. Ser.*, 664(7):072042, 2015.

[29] R. E. Kalman. A New Approach to Linear Filtering and Prediction Problems. *Journal of Basic Engineering*, 82(1):35–45, 03 1960.

[30] Thijs G. Cornelissen, M. Elsing, I. Gavrilenko, J.F. Laporte, W. Liebig, M. Limper, K. Nikolopoulos, A. Poppleton, and A. Salzburger. The global chi**2 track fitter in ATLAS. *J. Phys. Conf. Ser.*, 119:032013, 2008.

[31] G. Borissov, D. Casper, K. Grimm, S.Pagan Griso, L.Egholm Pedersen, K. Prokofiev, M. Rudolph, and A. Wharton. ATLAS strategy for primary vertex reconstruction during Run-2 of the LHC. *J. Phys. Conf. Ser.*, 664(7):072041, 2015.

[32] Electron efficiency measurements with the ATLAS detector using the 2015 LHC proton-proton collision data. Technical Report ATLAS-CONF-2016-024, CERN, Geneva, Jun 2016.

[33] Improved electron reconstruction in ATLAS using the Gaussian Sum Filter-based model for bremsstrahlung. Technical Report ATLAS-CONF-2012-047, CERN, Geneva, May 2012.

[34] Morad Aaboud et al. Electron and photon energy calibration with the ATLAS detector using 2015–2016 LHC proton-proton collision data. *JINST*, 14(03):P03017, 2019.

[35] B Lenzi, R Nicolaidou, and S Hassani. TrackInCaloTools: A package for measuring muon energy loss and calorimetric isolation in ATLAS. *Journal of Physics: Conference Series*, 219(3):032049, apr 2010.

[36] J. Illingworth and J. Kittler. A survey of the hough transform. *Comput. Vision Graph. Image Process.*, 44(1):87–116, August 1988.

[37] Georges Aad et al. Muon reconstruction performance of the ATLAS detector in proton–proton collision data at $\sqrt{s}$ =13 TeV. *Eur. Phys. J. C*, 76(5):292, 2016.

[38] Luigi Marchese. Muon reconstruction performance of the ATLAS detector in 2016. *EPJ Web Conf.*, 182:03008, 2018.

[39] Georges Aad et al. Topological cell clustering in the ATLAS calorimeters and its performance in LHC Run 1. *Eur. Phys. J. C*, 77:490, 2017.

[40] M. Aaboud et al. Performance of the ATLAS Track Reconstruction Algorithms in Dense Environments in LHC Run 2. *Eur. Phys. J. C*, 77(10):673, 2017.

[41] Jet mass reconstruction with the ATLAS Detector in early Run 2 data. Technical Report ATLAS-CONF-2016-035, CERN, Geneva, Jul 2016.

[42] Improving jet substructure performance in ATLAS using Track-CaloClusters. Technical Report ATL-PHYS-PUB-2017-015, CERN, Geneva, Jul 2017.

[43] J E Huth, N Wainer, K Meier, N J Hadley, F Aversa, Mario Greco, P Chiappetta, J P Guillet, S Ellis, Zoltán Kunszt, and Davison Eugene Soper. Toward a standardization of jet definitions. (FERMILAB-CONF-90-249-E):7 p, Dec 1990.

[44] S. Catani, Yuri L. Dokshitzer, M.H. Seymour, and B.R. Webber. Longitudinally invariant K_t clustering algorithms for hadron hadron collisions. *Nucl. Phys. B*, 406:187–224, 1993.

[45] Yuri L. Dokshitzer, G.D. Leder, S. Moretti, and B.R. Webber. Better jet clustering algorithms. *JHEP*, 08:001, 1997.

[46] Matteo Cacciari, Gavin P. Salam, and Gregory Soyez. The anti-k_t jet clustering algorithm. *JHEP*, 04:063, 2008.

[47] David Krohn, Jesse Thaler, and Lian-Tao Wang. Jets with Variable R. *JHEP*, 06:059, 2009.

[48] Variable Radius, Exclusive-k$_T$, and Center-of-Mass Subjet Reconstruction for Higgs($\rightarrow b\bar{b}$) Tagging in ATLAS. Technical Report ATL-PHYS-PUB-2017-010, CERN, Geneva, Jun 2017.

[49] Morad Aaboud et al. In situ calibration of large-radius jet energy and mass in 13 TeV proton–proton collisions with the ATLAS detector. *Eur. Phys. J. C*, 79(2):135, 2019.

[50] Monte Carlo Calibration and Combination of In-situ Measurements of Jet Energy Scale, Jet Energy Resolution and Jet Mass in ATLAS. 8 2015.

[51] Georges Aad et al. Performance of jet substructure techniques for large-R jets in proton-proton collisions at $\sqrt{s}$ = 7 TeV using the ATLAS detector. *JHEP*, 09:076, 2013.

[52] J. M. Butterworth, B. E. Cox, and J. R. Forshaw. WW scattering at the cern lhc. *Phys. Rev. D*, 65:096014, May 2002.

[53] Jesse Thaler and Ken Van Tilburg. Identifying Boosted Objects with N-subjettiness. *JHEP*, 03:015, 2011.

[54] Andrew J. Larkoski, Gavin P. Salam, and Jesse Thaler. GEnergy Correlation Functions for Jet Substructure. *JHEP*, 06:108, 2013.

[55] Ian Moult, Lina Necib, and Jesse Thaler. New Angles on Energy Correlation Functions. *JHEP*, 12:153, 2016.

[56] Morad Aaboud et al. Measurements of b-jet tagging efficiency with the ATLAS detector using $t\bar{t}$ events at $\sqrt{s}$ = 13 TeV. *JHEP*, 08:089, 2018.

[57] Georges Aad et al. ATLAS b-jet identification performance and efficiency measurement with $t\bar{t}$ events in pp collisions at $\sqrt{s}$ = 13 TeV. *Eur. Phys. J. C*, 79(11):970, 2019.

[58] S. Dittmaier et al. Handbook of LHC Higgs Cross Sections: 2. Differential Distributions. 1 2012.

[59] Duccio Pappadopulo, Andrea Thamm, Riccardo Torre, and Andrea Wulzer. Heavy Vector Triplets: Bridging Theory and Data. *JHEP*, 09:060, 2014.

[60] Morad Aaboud et al. Search for heavy resonances decaying to a W or Z boson and a Higgs boson in the $q\bar{q}^{(\prime)}b\bar{b}$ final state in pp collisions at $\sqrt{s}$ = 13 TeV with the ATLAS detector. *Phys. Lett.*, B774:494–515, 2017.

[61] ATLAS Collaboration. Search for heavy resonances decaying into a W or Z boson and a Higgs boson in final states with leptons and b-jets in 36 fb^{-1} of $\sqrt{s}$ = 13 TeV pp collisions with the ATLAS detector. 2017.

[62] Vardan Khachatryan et al. Search for a massive resonance decaying into a Higgs boson and a W or Z boson in hadronic final states in proton-proton collisions at $\sqrt{s}$ = 8 TeV. *JHEP*, 02:145, 2016.

[63] Albert M Sirunyan et al. Search for heavy resonances that decay into a vector boson and a Higgs boson in hadronic final states at $\sqrt{s}$ = 13 TeV. *Eur. Phys. J.*, C77(9):636, 2017.

[64] J. Alwall, R. Frederix, S. Frixione, V. Hirschi, F. Maltoni, O. Mattelaer, H. S. Shao, T. Stelzer, P. Torrielli, and M. Zaro. The automated computation of tree-level and next-to-leading order differential cross sections, and their matching to parton shower simulations. *JHEP*, 07:079, 2014.

[65] Torbjorn Sjostrand, Stephen Mrenna, and Peter Z. Skands. A Brief Introduction to PYTHIA 8.1. *Comput. Phys. Commun.*, 178:852–867, 2008.

[66] Richard D. Ball, Valerio Bertone, Francesco Cerutti, Luigi Del Debbio, Stefano Forte, Alberto Guffanti, Jose I. Latorre, Juan Rojo, and Maria Ubiali. Impact of Heavy Quark Masses on Parton Distributions and LHC Phenomenology. *Nucl. Phys.*, B849:296–363, 2011.

[67] ATLAS Run 1 Pythia8 tunes. Technical Report ATL-PHYS-PUB-2014-021, CERN, Geneva, Nov 2014.

[68] Georges Aad et al. Measurements of the Higgs boson production and decay rates and coupling strengths using pp collision data at $\sqrt{s}$ = 7 and 8 TeV in the ATLAS experiment. *Eur. Phys. J. C*, 76(1):6, 2016.

[69] ATLAS Collaboration. Improved luminosity determination in pp collisions at sqrt(s) = 7 TeV using the ATLAS detector at the LHC. *Eur. Phys. J.*, C73(8):2518, 2013.

[70] T. Gleisberg, Stefan. Hoeche, F. Krauss, M. Schonherr, S. Schumann, et al. Event generation with SHERPA 1.1. *JHEP*, 0902:007, 2009.

[71] Jun Gao, Marco Guzzi, Joey Huston, Hung-Liang Lai, Zhao Li, Pavel Nadolsky, Jon Pumplin, Daniel Stump, and C.-P. Yuan. CT10 next-to-next-to-leading order global analysis of QCD. *Phys. Rev. D*, 89(3):033009, 2014.

[72] Stefano Frixione and Bryan R. Webber. Matching NLO QCD computations and parton shower simulations. *JHEP*, 0206:029, 2002.

[73] D. J. Lange. The EvtGen particle decay simulation package. *Nucl. Instrum. Meth.*, A462:152–155, 2001.

[74] Michal Czakon and Alexander Mitov. Top++: A Program for the Calculation of the Top-Pair Cross-Section at Hadron Colliders. *Compt/ Phys. Commun.*, page 2930, 2014.

[75] ATLAS Collaboration. Comparison of Monte Carlo generator predictions for gap fraction and jet multiplicity observables in top-antitop events. Technical Report ATL-PHYS-PUB-2014-005, CERN, Geneva, May 2014.

[76] ATLAS Collaboration. Topological cell clustering in the ATLAS calorimeters and its performance in LHC Run 1. *Eur. Phys. J. C*, 77:490, 2017.

[77] David Krohn, Jesse Thaler, and Lian-Tao Wang. Jet Trimming. *JHEP*, 02:084, 2010.

[78] Matteo Cacciari, Gavin P. Salam, and Gregory Soyez. The Catchment Area of Jets. *JHEP*, 04:005, 2008.

[79] ATLAS Collaboration. Selection of jets produced in 13 TeV proton-proton collisions with the ATLAS detector. 2015.

[80] Giovanni Punzi. Sensitivity of searches for new signals and its optimization, 2003.

[81] A. Rogozhnikov. Reweighting with Boosted Decision Trees. *J. Phys. Conf. Ser.*, 762(1):012036, 2016.

[82] F. Pedregosa, G. Varoquaux, A. Gramfort, V. Michel, B. Thirion, O. Grisel, M. Blondel, P. Prettenhofer, R. Weiss, V. Dubourg, J. Vanderplas, A. Passos, D. Cournapeau, M. Brucher, M. Perrot, and E. Duchesnay. Scikit-learn: Machine learning in Python. *Journal of Machine Learning Research*, 12:2825–2830, 2011.

[83] A. Rogozhnikov. hep_ml. https://github.com/arogozhnikov/hep_ml, 2020.

[84] L. Moneta et al. The RooStats Project. In *Proceedings of the 13th International Workshop on Advanced Computing and Analysis Techniques in Physics Research, ACAT2010*, Proceedings of Science, 2010.

[85] HistFactory: A tool for creating statistical models for use with RooFit and RooStats. Technical Report CERN-OPEN-2012-016, CERN, Geneva, Jan 2012.

[86] A L Read. Modified frequentist analysis of search results (the CL_s method). (CERN-OPEN-2000-205), 2000.

[87] Glen Cowan, Kyle Cranmer, Eilam Gross, and Ofer Vitells. Asymptotic formulae for likelihood-based tests of new physics. *Eur. Phys. J. C*, 71:1554, 2011.

[88] G. Avoni et al. The new lucid-2 detector for luminosity measurement and monitoring in atlas. *JINST*, 13(07):P07017, 2018.

[89] Georges Aad et al. Search for diboson resonances in hadronic final states in 139 fb^{-1} of pp collisions at $\sqrt{s}$ = 13 TeV with the ATLAS detector. *JHEP*, 09:091, 2019.

[90] Morad Aaboud et al. Search for diboson resonances with boson-tagged jets in pp collisions at $\sqrt{s}$ = 13 TeV with the ATLAS detector. *Phys. Lett.*, B777:91–113, 2018.